

学位論文

**Seismic anisotropy of the oceanic lithosphere/asthenosphere
system elucidated by the array analysis of surface waves**

(表面波アレイ解析による
海洋リソスフェア/アセノスフェアの地震波速度異方性の解明)

平成 2 5 年 1 2 月博士 (理学) 申請

東京大学大学院理学系研究科

地球惑星科学専攻

竹尾 明子

Abstract

I propose a new multi-band method for the “broadband ocean bottom seismology”. The method utilizes seismic surface waves at periods of 3–100 s recorded by arrays of seafloor instruments. The measured phase velocities are inverted for obtaining one-dimensional anisotropic structure beneath the array including its uncertainty.

The uppermost mantle structure beneath the oceanic basins is essential to discuss the oceanic lithosphere/asthenosphere system, the most simple and representative system of the theory of plate tectonics. Seismic anisotropy within the oceanic lithosphere and asthenosphere is especially important, as it reflects the flow and deformation in the uppermost mantle. Previous structural studies have been, however, limited in terms of the depth range: the top of lithosphere at depths of ~ 10 – 20 km by refraction surveys, and the structure at depths deeper than ~ 30 km by surface-wave tomography studies. There has been no discussion from the top of the lithosphere continuously to the asthenosphere, which needs the broadband analysis of surface waves at periods of 3–100 s. In addition, there has been limited discussion about the intensity of seismic anisotropy because of the difficulty of estimating the absolute value of seismic anisotropy by surface-wave tomography studies.

I analyzed seafloor records quantitatively to discuss the anisotropic structure in the oceanic lithosphere and asthenosphere beneath five oceanic regions: the Shikoku Basin, French Polynesia, northwest Shatsky, southeast Shatsky and southwest Shatsky regions. The datasets are those obtained by the 1–3 years deployment of the broadband ocean bottom seismometers and the differential pressure gauges at 7–11 stations in each region from 2005 to 2013.

I first developed methods to analyze broadband surface waves in seafloor records by improving existing array-analysis methods: the ambient noise cross-correlation analysis at periods of 3–30 s, and the teleseismic surface-wave array analysis at periods of 30–100 s. There were many improvements especially for the ambient noise cross-correlation analysis including the estimation of the clock delay and instrumental responses, the simultaneous estimation of the average phase velocities of multi-mode surface waves by developing a waveform fitting method, and the correction for the effects of water-depth and source heterogeneity to the phase-velocity anomalies. By the overall improvement in the study, the methods became applicable to almost all broadband array records acquired in the seafloor.

By applying the method to the datasets of five oceanic regions, I could measure phase velocities of both Rayleigh and Love waves at periods of 3–100 s, and could estimate the azimuthal anisotropy of phase velocities of Rayleigh waves at periods of 5–70 s. The period range is broad compared to previous studies, and could be used to estimate radially and azimuthally anisotropic structures beneath each region at depths of ~ 10 – 150 km except for the southwest Shatsky region, where I only analyzed surface waves at periods shorter than

30 s and could constrain structures at depths shallower than ~ 40 km. The errors of each estimated values were carefully discussed in each measurement procedure, and also used to estimate the uncertainty of the obtained models.

The smooth radially anisotropic models were estimated after showing the insufficiency of the isotropic model and after carefully discussing the scaling relationship between anisotropic parameters. In addition, the non-smooth radially anisotropic models were estimated to compare them with the thermal models beneath oceanic basins by focusing on parameters such as the velocity gradient in the high-velocity LID and the gradient in the transition zone between the LID and the low velocity zone (LVZ). The depth of the middle of the transition zone is estimated to be thicker for the older seafloor region in the range of 40–90 km, which indicates that the LID is corresponding to the lithosphere. The velocity gradient in the LID is zero or positive and is inconsistent with the negative velocity gradient predicted by thermal models of the oceanic uppermost mantle. The discrepancy indicates the effect of phase transition to produce the apparent positive velocity gradient in the LID. The velocity gradient in the transition zone between LID and LVZ is steeper than those given by thermal models. This result invokes mechanisms for producing the velocity reduction in the transition zone, in addition to the thermal effect, such as decreasing grain size, partial melting, or the presence of water in the LVZ.

The intensity of radial anisotropy is 3%–6% with the velocity of horizontally propagating and horizontally polarized S-wave higher than that of vertically polarized S-wave ($V_{SH} > V_{SV}$). This result indicates the presence of lattice-preferred orientation of olivine crystals and/or the presence of horizontal layers or pockets of partial melts. The depth change in radial anisotropy was not required from the data.

The azimuthally anisotropic structures of V_{SV} were estimated from the azimuthal anisotropy of Rayleigh waves. Although the intensity of anisotropy depends on the region, the intensity at depths of 10–50 km was estimated to be higher (2%–6%) than the intensity at depths of 50–100 km (0%–3%). This result indicates that the viscosity is low and the shear deformation is accumulated in the top of the asthenosphere. The fastest azimuth was estimated to be NW–SE direction in the Shikoku Basin, French Polynesia and northwest Shatsky regions, whereas it was E–W in the southeast Shatsky region and was SW–NE in the southwest Shatsky region. The S-wave splitting analysis was further applied to reveal the lateral heterogeneity of azimuthal anisotropy in the French Polynesia region. The result indicates the perturbation of mantle flow by the presence of a hot plume beneath the hotspot in the French Polynesia region.

The average fastest azimuth estimated in the French Polynesia region is not perpendicular to the magnetic lineations, but is parallel to ancient plate motion, where the rate of seafloor spreading was low. On the other hand, the fastest azimuth was estimated to be perpendicular to magnetic lineations in the southwest Shatsky region, where the rate of seafloor spreading was high. The result is same in the northwest Shatsky regions, whereas it is oblique in the

southeast Shatsky region, where the rate of seafloor spreading is the middle. These results indicate that the flow in the uppermost mantle is parallel to the ancient plate motion when the plate motion is fast, whereas the flow is perpendicular to the ancient mid ocean ridge when the seafloor spreading is fast. The emergence of Shatsky Rise might have also affected the mantle flow beneath the southeast Shatsky region.

The intensity of azimuthal and radial anisotropy could be directly compared for the first time in this study. The intensity of radial anisotropy higher than that of azimuthal anisotropy indicates that the anisotropy is produced by the AG-type fabric of olivine crystals and/or by the presence of layers or pockets of partial melts.

The multi-band analysis in this study proved that the broadband array analysis of surface waves contributes to estimate the radially and azimuthally anisotropic models in the uppermost mantle to discuss the structure and flow in the oceanic lithosphere/asthenosphere system. It means that this study could establish a new field to the structural analysis in oceanic regions, the broadband ocean bottom seismology, which estimate the uppermost mantle anisotropic structure beneath oceanic regions by the broadband surface-wave analysis of seafloor records. This new field can elucidate the uppermost mantle structure at depths deeper than those by refraction surveys and the reliability higher than the surface-wave tomography studies, although the area is limited to the regions in which broadband ocean bottom seismometers were deployed. The results obtained by applying the method to current seafloor datasets invoke the needs and possibilities for future observation and analysis in other oceanic regions to reveal the universality and regionality of the oceanic lithosphere/asthenosphere system.

Contents

1	GENERAL INTRODUCTION	4
1.1	Plate Tectonics in Oceanic Regions	4
1.2	Uppermost Mantle Structure beneath Oceanic Regions	5
1.3	Recent Discussion about Oceanic Lithosphere/ Asthenosphere System	6
1.4	Surface-Wave Array Analysis	8
1.5	The Birth of the Broadband Ocean Bottom Seismology	10
2	STUDY AREA and DATA	13
2.1	Introduction	13
2.2	Five Oceanic Regions	13
2.2.1	Shikoku Basin	13
2.2.2	French Polynesia	16
2.2.3	Northwest and Southeast Shatsky Rise	18
2.2.4	Southwest Shatsky Rise	21
2.3	Characteristics of Seafloor Records	24
3	SURFACE WAVE ANALYSIS	26
3.1	Introduction	26
3.2	Uniqueness of Surface Waves in Oceanic Regions	27
3.3	Ambient Noise Cross-Correlation Analysis	28
3.3.1	Calculation of Cross Spectra	28
3.3.2	Cross Correlation Functions	33
3.3.3	Correction for Clock Delays and Instrumental Responses	35
3.3.4	Measurement of Average Phase Velocities	45
3.3.5	Measurement of Phase Velocity Anomalies and Corrections	51
3.3.6	Estimation of Azimuthal Anisotropy	58
3.4	Teleseismic Event Array Analysis	59
3.4.1	Measurement of Average Phase Velocities	59
3.4.2	Estimation of Azimuthal Anisotropy	63
3.5	Discussions of Surface-Wave Analysis	67
3.5.1	Broadband Phase Velocity Measurements	67

3.5.2	Amplitude of the Ambient Noise	67
4	1D RADially ANISOTROPIC STRUCTURES	70
4.1	Introduction	70
4.2	Model Parameters and Assumptions	70
4.3	Smooth Isotropic Structures	72
4.3.1	Four Regions	72
4.3.2	SW Shatsky Rise	73
4.4	Anisotropic Parameter Scalings	76
4.5	Smooth Radially Anisotropic Structures	78
4.6	Non-smooth Radially Anisotropic Structures	83
4.7	Discussions of the Radially Anisotropic Models	88
4.7.1	Assumption of 1D Structure	88
4.7.2	Comparison with Previous Models	90
4.7.3	Lid, Low Velocity Zone and the Transition Zone	92
4.7.4	Possible Depth Changes in Radial Anisotropy	95
5	1D AZIMUTHALLY ANISOTROPIC STRUCTURES	97
5.1	Introduction	97
5.2	Model Parameters and Inversion Method	98
5.3	Smooth Azimuthally Anisotropic Structures	99
5.4	Shear Wave Splitting Analysis	103
5.5	Discussions of the Azimuthally Anisotropic Models	107
5.5.1	Lateral Heterogeneity of Isotropic and Anisotropic Structures	107
5.5.2	Effect of P-wave Anisotropy	111
5.5.3	Depth Changes in Azimuthal Anisotropy	116
5.5.4	Azimuth of Maximum S-wave Velocity	119
6	GENERAL DISCUSSIONS	122
6.1	Intensities of Radial and Azimuthal Anisotropies	122
6.2	Summary of Results for Each Region	127
6.2.1	Shikoku Basin	127
6.2.2	French Polynesia	128
6.2.3	Northwest Shatsky	128
6.2.4	Southeast Shatsky	129
6.2.5	Southwest Shatsky	130
6.3	Broadband Ocean Bottom Seismology in This Study	130
6.4	Broadband Ocean Bottom Seismology in the Future Studies	132
7	SUMMARY	134

A	NOTATIONS	136
B	BOOTSTRAP METHOD	141
C	SIMULATED ANNEALING METHOD	143

Chapter 1

GENERAL INTRODUCTION

1.1 Plate Tectonics in Oceanic Regions

The seafloor in oceanic basins is the most simple appearance of the theory of plate tectonics. The oceanic crust with a thickness of 5–6 km emerges at the mid ocean ridge (MOR) and records the ancient geomagnetic field. The age of formation is then given by the pattern of magnetic lineation produced by the reversals of the geomagnetic field (*Vine and Matthews, 1963*). The motion of oceanic crust relative to the underlying mantle can be estimated from the movement of hotspot chain (e.g., *Gripp and Gordon, 2002*). Based on these observations at the surface, the current and ancient ages of seafloor have been reconstructed by a number of researchers, and are recently compiled by *Müller et al. (2008)* and *Seton et al. (2012)*.

The oceanic uppermost mantle including the oceanic lithosphere and asthenosphere is also a representative system of the theory of plate tectonics. The oceanic lithosphere (plate) is the stiff part of the surface of earth formed by the oceanic crust and the top of the underlying upper mantle. The motion of oceanic lithosphere, thus, causes flow in the underlying oceanic asthenosphere.

The structure of the oceanic lithosphere can be estimated from the sea topography. The thickness of the lithosphere increases with seafloor age as described by a half-space cooling model (e.g., *Davis and Lister, 1974*). The depth of the ocean then deepens with seafloor age by the isostatic response to the increasing thickness of the lithosphere, which is cooler and denser than the underlying asthenosphere (e.g., *Parsons and Sclater, 1977*). This concept has been evaluated by determining the uppermost mantle structure beneath oceanic regions by seismologists.

1.2 Uppermost Mantle Structure beneath Oceanic Regions

The reflection and refraction surveys in oceanic regions have revealed the crustal and uppermost mantle structure at depth shallower than ~ 20 km. Although the deeper structure can be determined by using body waves from nearby earthquakes in continental and island regions, the similar analysis is difficult in oceanic regions because of the limited data and seismicity.

The uppermost mantle structure beneath oceanic regions have, therefore, been determined by using surface waves propagating in oceanic regions, whose phase and group velocities mainly reflect S-wave velocity structure at shallow (deeper) depths at short (long) periods (*Ewing et al.*, 1957). The dispersion curve, the period dependence of velocities of surface waves, gives one-dimensional S-wave velocity structures, and were used to point out the presence of a low velocity zone (LVZ) at depths of ~ 50 – 200 km beneath oceanic basins in 1950s (e.g., *Press*, 1959; *Gutenberg*, 1959). *Dorman et al.* (1960) later determined the structure including the LVZ and an overlying high-velocity LID. The thickening of the LID with seafloor age was further shown by *Leeds et al.* (1974) by using the regionalized dispersion curves. The recent development of surface-wave tomography provided three-dimensional upper-mantle structure in the whole earth, which clearly shows the correlation between seafloor age and the uppermost mantle structure (*Ritzwoller et al.*, 2004; *Maggi et al.*, 2006a; *Nettles and Dziewonski*, 2008). The LVZ and the LID have been, therefore, interpreted as the oceanic asthenosphere and lithosphere, respectively.

Seismic anisotropy in the uppermost mantle has also been investigated by using surface waves: the radial anisotropy and the azimuthal anisotropy. Azimuthal anisotropy is the simple one meaning the dependence of the seismic velocity on the azimuth of propagation. The presence of azimuthal anisotropy of Pn-wave velocity in oceanic uppermost mantle was first pointed out by refraction surveys (*Raith et al.*, 1969; *Morris et al.*, 1969). The azimuthal anisotropy of surface waves reflects that of S-wave velocity (e.g., *Montagner and Nataf*, 1986). The early surface-wave researchers used the relationship to infer the presence of azimuthal anisotropy at deeper depths (e.g., *Forsyth*, 1975), which was later determined by surface-wave tomography studies with the increasing number of available datasets (*Tanimoto and Anderson*, 1984; *Montagner*, 2002; *Maggi et al.*, 2006b).

The lattice preferred orientation (LPO; same as crystal preferred orientation, CPO) of olivine crystals is usually considered to be the main cause of the azimuthal anisotropy (e.g., *Forsyth*, 1975). The plate motion causes shear deformation in the uppermost mantle, which provides growth of olivine grains in a particular axis, the a-axis. The a-axes of the olivine grains then align in a direction of mantle flow under the shear deformation. As the elastic waves propagate faster along a-axis compared to other axes (b- and c- axes), the seismic waves consequently propagate faster in the direction of mantle flow. The azimuth of max-

imum velocity of Pn-wave perpendicular to the MOR, therefore, implies that the flow is perpendicular to MOR in the setting of the seafloor spreading (*Raitt et al.*, 1969; *Francis*, 1969). The similar fastest azimuth is observed at depths shallower than ~ 50 km, and considered to be the ancient mantle flow frozen in the oceanic lithosphere (e.g., *Forsyth*, 1975), whereas the fastest direction in the current oceanic asthenosphere at depths deeper than ~ 100 km is parallel to the current plate motion (e.g., *Tanimoto and Anderson*, 1984). This difference between anisotropy in the oceanic lithosphere and asthenosphere was clearly shown by a recent surface-wave tomography study by using group velocities of Rayleigh waves at periods of 25–150 s (*Smith et al.*, 2004).

The concept of radial anisotropy is complicated compared to azimuthal anisotropy, but has long history for surface-wave studies. The early studies obtained dispersion curves of Rayleigh and Love waves for limited azimuths of propagations, which were insufficient for estimating the azimuthal anisotropy. The dispersion curves, however, could not be explained by one-dimensional isotropic structures both in continental (*Anderson*, 1962), island (*Aki and Kaminuma*, 1963) and oceanic (*Forsyth*, 1975; *Schlue and Knopoff*, 1977; *Yu and Mitchell*, 1979; *Nishimura and Forsyth*, 1989) regions. This phenomenon was called the “Rayleigh/Love wave discrepancy”, and solved by introducing the radial anisotropy (RA), which is also referred to the vertical transverse isotropy (VTI), with the velocity of horizontally-propagating and vertically-polarized S-wave (V_{SV}) lower than the velocity of horizontally-propagating and horizontally-polarized S-wave (V_{SH}). The same concept was imposed in the reference model of earth, the PREM model by *Dziewonski and Anderson* (1981). The subsequent tomography studies have determined three-dimensional upper mantle structure including radial anisotropy (*Ekström and Dziewonski*, 1998; *Shapiro and Ritzwoller*, 2002; *Nettles and Dziewonski*, 2008; *Fichtner et al.*, 2010).

The origin of radial anisotropy is first considered to be thin layer or pockets of partial melt in the uppermost mantle (*Backus*, 1962; *Aki*, 1968; *Schlue and Knopoff*, 1976). After the discovery of azimuthal anisotropy, however, the LPO was also considered to be the cause of radial anisotropy. During horizontal shearing, the fast axes (a-axes) of olivine crystals align along the horizontal flow direction and/or the slow axes (b-axes) align vertically, leading to the azimuthal average of V_{SH} becoming faster than V_{SV} (*Estey and Douglas*, 1986).

1.3 Recent Discussion about Oceanic Lithosphere/ Asthenosphere System

The difference between oceanic lithosphere and asthenosphere have been especially focused since the discovery of the G-discontinuity, a discontinuity between the LID and LVZ, by the reflections and/or conversions of body waves (e.g., *Revenaugh and Jordan*, 1991; *Kawakatsu et al.*, 2009; *Rychert and Shearer*, 2011). Although the spatial coverage is limited by the

locations of earthquakes and stations, those studies have determined the depth and the velocity reduction at the G-discontinuity, which has been interpreted as the lithosphere–asthenosphere boundary (LAB). *Gaherty et al.* (1996) and *Kato and Jordan* (1999) analyzed both body and surface waves, and obtained path-average one-dimensional structures with the G-discontinuity beneath the central Pacific and Philippine Sea regions, respectively. These structures have been used to discuss the origin of the LVZ, such as its thermal structure (*Stixrude and Lithgow-Bertelloni*, 2005), grain size variations (*Faul and Jackson*, 2005), and the presence/absence of partial melt (e.g., *Anderson and Sammis*, 1970) or of water (*Karato*, 2012). However, the employed long-path averaging of these studies appears inadequate for evaluating the various models proposed for the origin of the LVZ.

The presence of strong seismic anisotropy in the uppermost mantle beneath oceanic basins further complicates the situation. Recent tomographic studies have shown that the intensity of radial anisotropy ($V_{SH} > V_{SV}$) is stronger in the LVZ than in the LID (e.g., *Ekström and Dziewonski*, 1998; *Nettles and Dziewonski*, 2008), which leads to two potential interpretations: the enhancement of LPO in the LVZ (e.g., *Podolefsky et al.*, 2004; *Becker et al.*, 2008; *Behn et al.*, 2009); or the presence of pockets or layers of partial melt under shear stress in the LVZ (e.g., *Schlue and Knopoff*, 1976; *Kawakatsu et al.*, 2009). As far as radial anisotropy concerned, the usage of body waves is not so effective, as the velocities of nearly vertical propagation S-waves used by body-wave analyses are close to that of V_{SV} that Rayleigh waves are sensitive (e.g., *Takeuchi and Saito*, 1972). One exception is the observation of the long duration of Po and So waves, which indicates the presence of laterally elongated heterogeneity in the oceanic lithosphere (*Furumura*, 2005; *Shito et al.*, 2013) that might produces the apparent radial anisotropy. For directly estimating the intensity of radial anisotropy, however, we need to analyze the Love waves to determine the V_{SH} structure, and consequently to discuss the origins of the radial anisotropy and LAB.

The oceanic lithosphere itself is an interesting target for several researchers. *Lizarralde et al.* (2004) determined the P-wave velocity structure beneath the mid-ocean-ridge region in the northern Atlantic Ocean by a refraction survey, and concluded that the velocity gradient is positive at the top of the mantle at depths shallower than ~ 20 km. In addition, surface-wave studies have often assumed the constant velocity in the LID (e.g., *Leeds et al.*, 1974; *Gaherty et al.*, 1996; *Kato and Jordan*, 1999). These positive or zero velocity gradients in the LID are inconsistent with the negative velocity gradient in the LID predicted by the pressure and temperature dependence of the seismic velocity and thermal model in the oceanic uppermost mantle as discussed by several studies (e.g., *Shapiro and Ritzwoller*, 2004; *Stixrude and Lithgow-Bertelloni*, 2005). There is, however, no detailed discussion about the velocity gradient in the LID because of the difficulty of determine the structure in the LID.

The structure at the top of the LID at depths shallower than ~ 20 km can be determined by refraction surveys, whereas the analysis of surface waves at periods shorter than ~ 40 s is needed to determine the structure at deeper depths of 20–50 km as well as to minimize

the tradeoff between the shallow structure and the radial anisotropy at depths of ~ 100 km (e.g., *Bozdog and Trampert*, 2008). The measurement of phase velocities of surface waves at the period range is usually difficult because the waveforms are complicated due to the multipathing under the presence of strong heterogeneity at depths shallower than 50 km (e.g., *Forsyth and Li*, 2005). *Shapiro and Ritzwoller* (2002) solved this problem by using group velocities of surface waves at periods of 16–200 s, which are easier to measure than the phase velocities. The depth resolution in the LID was, however, still insufficient to discuss the the velocity gradient in the LID (*Shapiro and Ritzwoller*, 2004) probably due to lack of the first higher-mode Rayleigh waves that have sensitivities to the top of the LID in oceanic regions (e.g., *Harmon et al.*, 2007)

Smith et al. (2004) also used group velocities of Rayleigh waves to reveal azimuthal anisotropy in the uppermost mantle by a tomography method. As a result, they revealed that the fastest azimuths in the LID at depths shallower than ~ 50 km is perpendicular to the ancient MOR shown by the magnetic lineations, whereas the azimuths in the LVZ at depths deeper than ~ 100 km is parallel to the current plate motion. The typical resolution of ~ 2000 km obtained by tomography studies are, however, still insufficient to compare their results with the tectonics of seafloor, which has typical scale for the heterogeneity of ~ 500 km due to the presence of transform faults, seamounts and the rapid change in the seafloor age. In addition, the intensity of azimuthal anisotropy cannot be estimated quantitatively as it depends on the assumed smoothing or damping parameters (*Smith et al.*, 2004). We cannot even compare the intensity of azimuthal anisotropy at depths deeper than 20 km with that at shallower depths quantitatively determined by refraction surveys to be up to 10% (*Song and Kim*, 2012). *Song and Kawakatsu* (2012) suggested that the radial anisotropy of S-wave is stronger than the azimuthal anisotropy of S-wave based on the pattern of shear-wave splitting at global subduction zones. The quantitative comparison of intensity between two types of anisotropy also needs quantitative estimation of the intensity of azimuthal anisotropy.

1.4 Surface-Wave Array Analysis

There is one solution to analyze broadband surface waves quantitatively with a required lateral resolution: the array analysis of surface waves, where an array means an aggregate of observation stations. The obtained phase velocities of surface waves at periods of 1–100 s can be then used to constrain various parameters discussed above: the radially anisotropic structure including the LID and LVZ, the velocity gradient in the LID, the azimuthally anisotropic structure comparable to seafloor tectonics, and the intensity of azimuthal anisotropy.

The array analysis methods for analyzing surface waves can be classified into two groups: the array analysis of teleseismic surface waves, and the cross-correlation analysis of ambient noise. The former analyzes array records of surface waves derived from teleseismic events and

evaluate the effects of ray bending and multipathing at short periods to precisely measure phase velocities of surface waves (e.g., *Forsyth and Li*, 2005).

The cross-correlation analysis of ambient noise uses continuous records of “ambient noise” for an array of stations and extracts background surface-wave propagation by cross-correlating the records for a pair of stations (e.g., *Aki*, 1957; *Shapiro and Campillo*, 2004; *Bensen et al.*, 2008; *Nishida et al.*, 2008b; *Ekström et al.*, 2009). This method is especially required at periods shorter than ~ 10 s, where the multipathing is highly complicated due to the presence of strong lateral heterogeneity at depths shallower than 20 km. The effect of ray bending and multipathing outside the array can be neglected because this method assumes a random wave-field in which surface waves arrives from all the direction. Recent studies have shown that each cross-correlation function (CCF) is mainly sensitive to the structure along the path between the pair of stations (*Snieder*, 2004; *Tromp et al.*, 2010; *Nishida*, 2011), which allow us the regional tomography to determine S-wave velocity structure of the crust and the uppermost mantle (e.g., *Bensen et al.*, 2008; *Nishida et al.*, 2008b) including azimuthal anisotropy (*Lin et al.*, 2010).

In oceanic regions, the array records have been extensively analyzed in the East Pacific Rise (EPR) region, where many ocean bottom seismometers (OBSs) have been deployed. For example, *Dunn and Forsyth* (2003) measured phase velocities of fundamental-mode Love waves at periods of 4–17 s using local seismic events, and obtained a two-dimensional V_{SH} structure. *Forsyth and Li* (2005) and *Weeraratne et al.* (2007) measured phase velocities of fundamental-mode Rayleigh waves at periods of 18–100 s by using teleseismic events, and obtained a three-dimensional V_{SV} structure including the azimuthal anisotropy. *Harmon et al.* (2007) and *Yao et al.* (2011) also analyzed both fundamental- and first higher-mode Rayleigh waves at periods of 2–30 s by applying the noise correlation method to OBS records. By using phase velocities of Rayleigh waves measured from teleseismic waveforms at longer periods, *Harmon et al.* (2007) and *Yao et al.* (2011) obtained a one-dimensional structure of V_{SV} from the crust to a depth of ~ 100 km with a depth resolution that was much higher than that in global tomographic studies. The presence of azimuthal anisotropy at depths of ~ 10 –15 km was further inferred by *Harmon et al.* (2007) from phase velocities of higher-mode Rayleigh waves at periods of 3.5–6 s for the EPR region. At shorter periods of 0.5–3 s, *Mordret et al.* (2013b) analyzed fundamental-mode Rayleigh waves, and estimated horizontal distribution of azimuthal anisotropy within the sediment layer in the North Sea.

The period range of surface-wave analysis in previous studies is, however, still limited in terms of discussing the structure within the LID and LVZ. For example, the azimuthal anisotropy is estimated quantitatively only from the fundamental-mode Rayleigh waves (*Weeraratne et al.*, 2007). The anisotropy is inferred qualitatively for the first higher-mode Rayleigh wave (*Harmon et al.*, 2007). The quantitative analysis of the first higher-mode Rayleigh wave is needed to estimate azimuthal anisotropy at the top of the LID at depths of 10–20 km. In addition, the analysis of Love wave is limited to the short period range of 4–17

s (e.g., *Dunn and Forsyth*, 2003), which can only constrain V_{SH} (thus the radial anisotropy) at depths shallower than ~ 20 km.

What is now desired and possible by using the state-of-the-art OBS array is to analyze both Rayleigh and Love waves simultaneously in a broadband period range of ~ 3 –100 s to constrain the in-situ uppermost mantle structure including the radial and azimuthal anisotropy with the depth resolution sufficient to discuss the structure including the LID and LVZ.

1.5 The Birth of the Broadband Ocean Bottom Seismology

Several problems must be solved to accomplish the “broadband ocean bottom seismology”, the broadband surface-wave analysis to estimate seismic anisotropy in the uppermost mantle from seafloor records: the unknown clock delays and instrumental responses at part of stations, the unknown source distribution of ambient noise, the limited variation in station-to-station (interstation) distances due to limited number of stations, the high noise level and the limited amount of datasets.

The first problem is the unknown clock delay. As the GPS signal is unavailable in the ocean, seafloor instruments are equipped with inner high-quality crystal clocks, whose drifts are typically one second per year or less and can be corrected after the recovery by comparison to GPS signals. If the clock stops during the observation period or if the clock drift is non-linear, however, the clock delay cannot be corrected by the ordinal method. *Hannemann et al.* (2013) recently used the temporal changes in CCFs to estimate the clock delay as done by *Sens-Schönfelder* (2008) for the land station without GPS reception.

The second problem is the accuracy of the instrumental response when differential pressure gauges (DPGs) are used instead of OBSs. The DPG is an instrument that records the difference between seafloor pressure and low-pass filtered pressure, and gives relative pressure change at periods shorter than about 1000 s with some phase delay (*Cox et al.*, 1984). The instrumental responses of DPGs are usually imperfectly known because they depend on the viscosity of the fluid and the diameter (and the cleanness) of the capillary tube (*Cox et al.*, 1984). Although *Araki and Sugioka* (2009) estimated the response by comparing the DPG record with a record of a quartz pressure gauge, the responses of almost all DPGs have been kept unknown.

The third problem is the unknown source distribution of the ambient noise. The assumption that each CCF reflects the structure between the pair of stations is valid only when the interstation distance is much larger than the wavelength as shown practically by *Yao and van der Hilst* (2009) and theoretically by *Weaver et al.* (2009). Although the source distribution is extensively investigated in the southern California region by *Harmon et al.*

(2010), the source distribution should be evaluated in oceanic regions to reduce the bias of the effect to the estimation of azimuthal anisotropy.

The fourth problem is the overlap between multi-mode surface waves when the interstation distances are comparable to the wavelength. For example, higher-mode Rayleigh waves are observable and important in oceanic regions at periods shorter than $\sim 10\text{--}20$ s, where the fundamental-mode Rayleigh wave is mainly sensitive to P-wave velocity in the ocean and higher-mode Rayleigh waves are sensitive to S-wave velocity in the crust and uppermost mantle (*Ewing et al.*, 1957). Previous studies analyzed each mode of Rayleigh wave separately by applying group velocity filters (*Harmon et al.*, 2007; *Yao et al.*, 2011). The separation, however, becomes difficult for shorter interstation distances due to overlap between different modes. Although plenty of studies have considered this effect at frequency higher than 1 Hz to estimate the sedimental structure in land regions (e.g., *Beatty et al.*, 2002), the effect have not been considered to obtain the mantle structure.

The separation of Rayleigh and Love waves in horizontal components is also difficult for short interstation distances or at long periods, where the Rayleigh and Love waves appear in the both radial and transverse components (*Aki*, 1957; *Haney et al.*, 2012). Although both Rayleigh and Love waves have been analyzed in land (*Bensen et al.*, 2008; *Nishida et al.*, 2008b) and oceanic regions (*Mordret et al.*, 2013a), this effect has not been accounted.

The last problem is the amount of records less than the onland record in terms of both the number of stations and the observation period. The number of available teleseismic events are then smaller, and the signal-to-noise ratio of cross-correlation functions are lower (*Bensen et al.*, 2007). Recent tomography studies have spent less effort to evaluate the uncertainty of each measurement because they use thousands to millions of measurements and average out the error of measurements. In comparison, the uncertainty should be evaluated thoroughly for the seafloor records to avoid bias from one anomalous measurement. In addition, there are large variation in seafloor records, especially the noise level that highly depends on the observation sites and the state of installations. The quantitative evaluation of the uncertainty of each measurement is, therefore, needed to be confident for each measurement.

In this study, I overcome the above five problems to analyze broadband surface waves recorded by seafloor instruments, and estimate the radially and azimuthally anisotropic structures beneath five oceanic regions to discuss the unsolved problems in the uppermost mantle decried in Section 1.3. Chapter 2 summarizes the datasets used in this study, which is obtained in five oceanic regions by four projects: the Shikoku Basin, French Polynesia, northwest Shatsky, southeast Shatsky and southwest Shatsky regions. Chapter 3 describes the methods to analyze broadband surface waves including the solutions to overcome five problems above. I analyzed surface waves at periods of 3–30 s by the ambient noise cross-correlation method, and at periods of 30–100 s by the array analysis of teleseismic surface waves. Chapter 4 is about the estimation of one-dimensional (1D) radially anisotropic structure beneath each region, whereas Chapter 5 is about the 1D azimuthally anisotropic

structures. The uncertainty of measurements and models will be described carefully in each section to show their reliabilities. The comparison between radially and azimuthally anisotropic structures will be given in Chapter 6 as well as the summary of the broadband ocean bottom seismology developed in this study and its possibility in future studies. The notations and detail of algorithm used in this study are summarized in Appendix.

There are one published article and two submitted articles related to this study. *Takeo et al.* (2013) obtained the average phase velocities of broadband surface waves and a radially anisotropic structure beneath the Shikoku Basin, which is in Chapters 3–4 in this thesis. *Takeo et al.* (submitted) obtained the azimuthal anisotropy of phase velocities of Rayleigh waves by improving the methods, which is in Chapters 3–5 in this thesis. *Isse et al.* (accepted) estimated the clock delays for the northwest and southeast Shatsky regions, which is in Chapter 3 in this thesis.

Chapter 2

STUDY AREA and DATA

2.1 Introduction

Recent seafloor observation projects have deployed broadband OBSs (BBOBSs) and DPGs in various tectonic settings. The first large-scale deployment was on a MOR, the East Pacific Rise between Nazca and Pacific plates, with a seafloor age of ~ 0 Ma by the MELT project (*MELT Seismic Team*, 1998). The GLIMPSE project later investigated the western side with an older seafloor age but still younger than 8 Ma (*Weeraratne et al.*, 2007). Other groups have deployed BBOBSs in the hotspot regions such as the French Polynesia region in the south Pacific Ocean by the PLUME project (*Barruol*, 2002; *Suetsugu et al.*, 2005) and the Hawaii region by the Hawaiian PLUME (*Laske et al.*, 2009) project. The TIARES project (*Suetsugu et al.*, 2012) re-investigated the French Polynesia region by a denser deployment of BBOBSs. There are many OBS deployments in the subduction regions, for example, the large-scale BBOBS deployment by the SSP project (*Shiobara et al.*, 2009). On the other hand, recent projects have focused on the oceanic basins to investigate oceanic lithosphere/asthenosphere structure such as the northwestern Pacific Ocean by the PLATE (*Shintaku et al.*, submitted) and NOMan (*Baba et al.*, 2013) projects, and the south of Hawaii by the NOMELT project. As the aim of this study is to discuss the structure of oceanic lithosphere/asthenosphere system, the records from mid-ocean-ridge regions and subduction regions are not suitable. In this study, therefore, five oceanic basins are chosen from the available datasets as summarized in Table 2.1 and shown in Figures 2.1–2.2. The details and tectonic settings of each datasets are summarized in the following section.

2.2 Five Oceanic Regions

2.2.1 Shikoku Basin

The Shikoku Basin (SB) is a back-arc basin in the northwestern Pacific Ocean and in south of Japanese Islands formed at 15–30 Ma (*Okino et al.*, 1999), and is surrounded by the

Table 2.1: Summary of datasets.

Region	Shikoku Basin	French Polynesia	NW Shatsky	SE Shatsky	SW Shatsky
Project	SSP	TIARES	NOMan	NOMan	PLATE
Seafloor age (Ma)	15-30	50-70	125-135	135-145	150-160
No. of stations	7	9	7	7	11
Observation Period	'05-'08	'09-'10	'10-'13	'10-'13	'10-'11
Sampling Rate (Hz)	100/200	100	100	100	40/50
for Ambient Noise Analysis (Hz)	10	10	100	100	10
for Teleseismic Event Analysis (Hz)	100	10	100	100	10

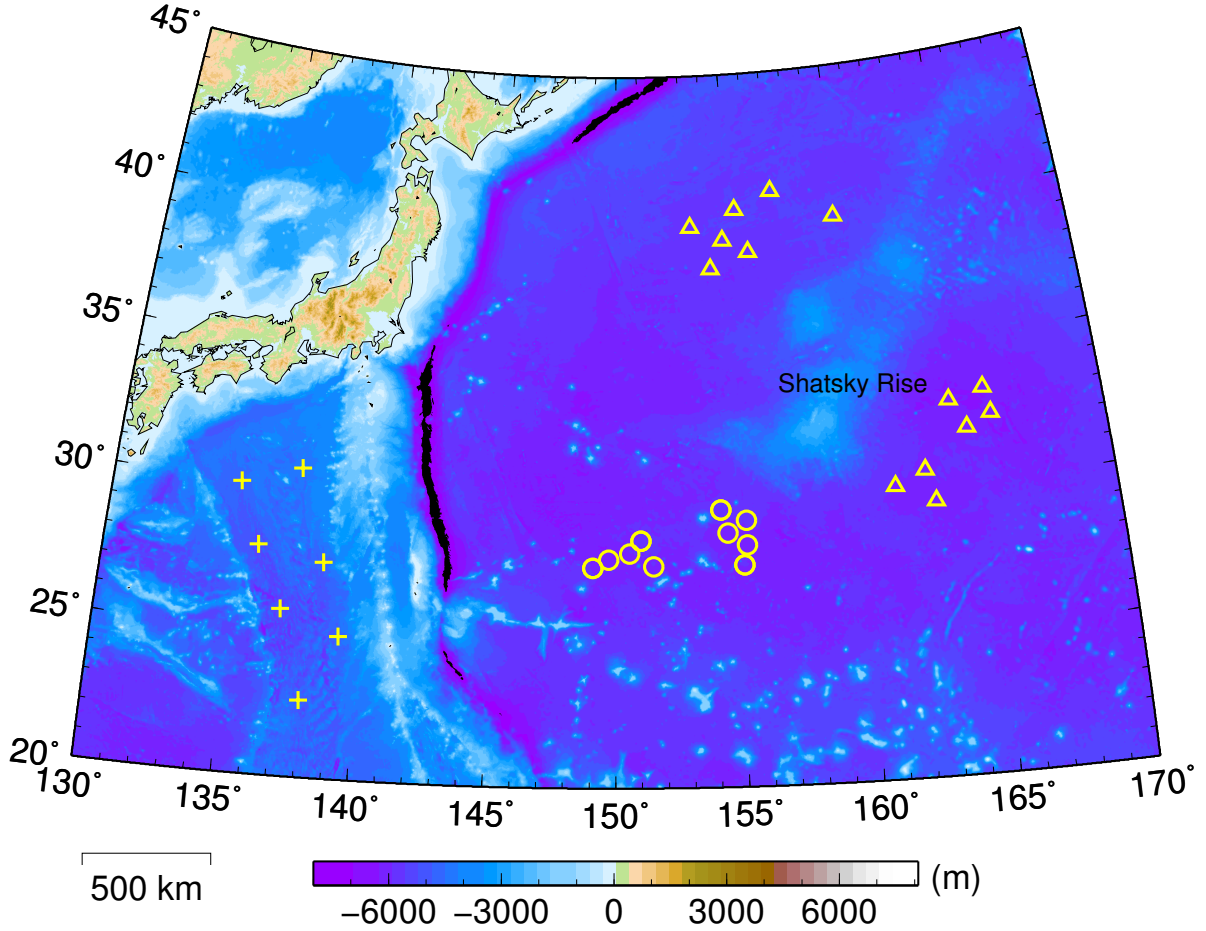


Figure 2.1: Topography map showing the locations of BBOBSs used in this study in the Shikoku Basin by the SSP project (crosses), SW Shatsky by the PLATE project (circles), NW and SE Shatsky by the NOMan project (triangles).

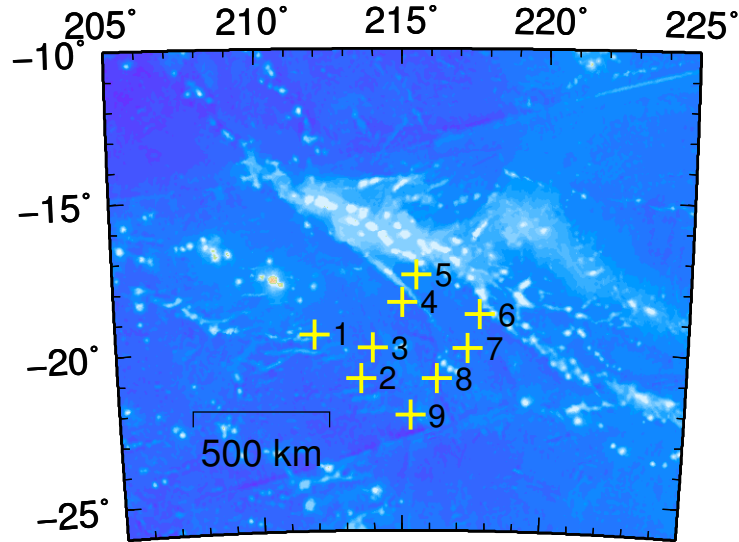


Figure 2.2: Same as Figure 2.1, but for BBOBSs in the French Polynesia region by the TIARES project (crosses).

Nankai Trough, Izu–Bonin–Mariana arc, Kyusyu–Palau ridge, and Parece–Vela basin. The Shikoku Basin is now moving northwestward as a part of the Philippine Sea Plate, and the northern end is subducting beneath southwest Japan. Although the tectonic setting of the Shikoku Basin is complicated, the uppermost mantle structure beneath the Shikoku Basin is expected to be similar to that in other oceanic basins (*Isse et al.*, 2009), as it has normal oceanic crust (*Nishizawa et al.*, 2011).

Several surface-wave studies have been investigated the upper-mantle structure beneath the Philippine Sea region including the Shikoku Basin (e.g., *Kanamori and Abe*, 1968; *Oda and Senna*, 1994; *Kato and Jordan*, 1999). *Nakamura and Shibutani* (1998) first performed regional surface-wave tomography for obtaining three-dimensional V_{SV} structure beneath the Philippine Sea region. The horizontal resolution of three-dimensional structure was gratefully improved by *Isse et al.* (2009, 2010) by using BBOBS records acquired by the Stagnant Slab Project (SSP) from 2005 to 2008 (*Shiobara et al.*, 2009).

The purpose of SSP was to reveal subduction structure including the Pacific Plate, the Philippine Sea Plate (including IBM island arc, back-arc basins, ridges; see detail in Fig. 2.3 and Table 2.2) from the trench to the transition zone. The BBOBSs were equipped with Guralp CMG-3T sensors with a flat velocity response from 0.02 to 360 s (*Kanazawa et al.*, 2009). One-year observations were repeated once, twice, or three times at each of the 17 stations. *Isse et al.* (2009) used the BBOBS records as well as onland records, and improved the lateral resolution of the V_{SV} structure in the Philippine Sea region. They revealed three strong, slow anomalies in the mantle wedge along the Izu–Bonin (Ogasawara)–Mariana arc (IBM). *Isse et al.* (2010) also identified azimuthally and radially anisotropic structure in the same region, and showed that the fast direction of azimuthal anisotropy is consistent

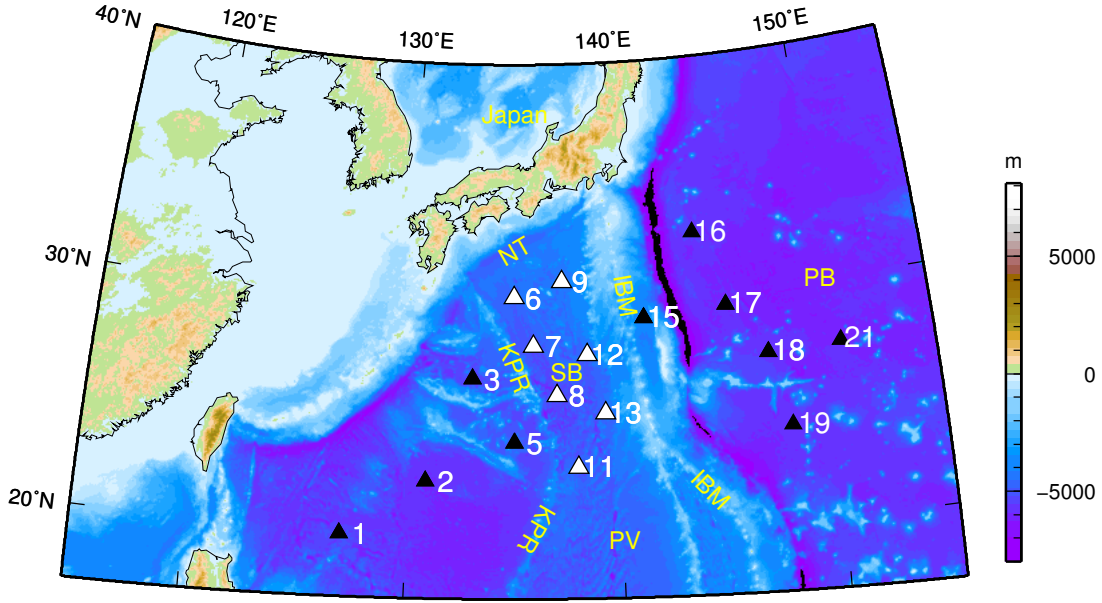


Figure 2.3: Topographic map and BBOBS stations of the Stagnant Slab Project (triangles). Open triangles show stations in the SB used in this study. IBM, Izu–Bonin–Mariana arc; KPR, Kyushu–Palau ridge; NT, Nankai Trough; PB, Pacific Basin; PV, Parece–Vela basin; SB, Shikoku Basin.

with ancient seafloor spreading at depths shallower than 100 km and with the current plate motion at greater depths. However, these previous studies only analyzed surface waves at periods longer than 30 s and, as such, the depth resolution of their obtained structures at shallow depths is limited.

In the present study, I focused on obtaining a robust one-dimensional structure in order to compare it with thermal models for oceanic basins to discuss the origin of the LVZ. Although the arrays of BBOBSs were deployed in the Shikoku Basin (seven stations) and Pacific Basin (five stations), I only used data from the Shikoku Basin because the data from the Pacific Basin are not suited for our analysis due to high noise levels.

2.2.2 French Polynesia

The French Polynesia region in the south Pacific consists old and active hotspot islands (McNutt, 1998; Adam and Bonneville, 2005). Duncan and McDougall (1976) determined the age of hotspot islands, and revealed the movement of younger hotspot islands with ages younger than ~ 10 Ma. The direction of motion is parallel to the present-day plate motion. Schlanger *et al.* (1984) further determined the movement of older hotspot islands from the youngest Tuamotu islands (~ 45 Ma) to the north (~ 90 Ma). The direction of motion is sub-parallel to the present-day plate motion, reflecting the change in the motion of Pacific Plate at ~ 43 Ma. The change in the direction is smaller for the south Pacific than that for

Table 2.2: Summary of stations by the Stagnant Slab project.

Station No.	Sampling rate (Hz)	Longitude (°)	Latitude (°)	Depth (m)
from October 2005 to November 2006				
06	200	134.98	29.99	4614
07	200	135.92	27.90	5259
08	200	137.01	25.77	4894
09	200	137.32	30.67	4260
11	200	137.98	22.67	4770
12	200	138.51	27.50	4679
13	200	139.30	24.97	4786
from November 2006 to November 2007				
06	200	134.97	29.99	4626
07	200	135.92	27.90	5265
08	200	137.01	25.77	4896
09	200	137.32	30.67	4266
11	200	137.98	22.67	4786
12	200	138.51	27.50	4688
13	200	139.30	24.97	4793
from November 2007 to November 2008				
06	100	134.97	29.99	4621
07	100	135.92	27.90	5261
08	100	137.01	25.77	4896
09	100	137.32	30.67	4259
11	100	137.98	22.67	4792
12	100	138.51	27.50	4692
13	100	139.30	24.97	4784

Table 2.3: Summary of stations by the TIARES project.

Station No.	Sampling rate (Hz)	Longitude (°)	Latitude (°)	Depth (m)
from February 2009 to July 2010				
1	100	-148.05	-19.47	4398
2	100	-146.44	-20.96	4766
3	100	-146.02	-19.93	4632
4	100	-144.99	-18.43	4457
5	100	-144.51	-17.50	4031
6	100	-142.29	-18.81	4483
7	100	-142.69	-19.94	4467
8	100	-143.76	-20.95	4779
9	100	-144.70	-22.17	4513

the north Pacific recorded by the difference between the Emperor seamounts and Hawaiian seamounts as pointed out by *Lonsdale* (1988).

The BBOBS observation in this region was first conducted from 2003 to 2005 as a part of Polynesian Lithosphere and Upper Mantle Experiment (PLUME) project (*Barruol, 2002; Suetsugu et al., 2005*). The experiment revealed a root of hotspot by the local surface-wave tomography (*Isse et al., 2006a*), flow in the mantle by the shear-wave splitting analysis (*Barruol et al., 2009*), and the structure of the mantle transition zone by the receiver-function analysis (*Suetsugu et al., 2009*). The typical interstation distance of the project was 500 km, which was too large and too inhomogeneous for the surface-wave study at periods shorter than 30 s.

Nine BBOBSs were later deployed more densely from 2009 to 2010 as a part of Tomographic investigation by seafloor array experiment for the Society hotspot (TIARES) project (*Suetsugu et al., 2012*) to reveal the detailed structure of the Pacific Superswell in the upper mantle. The selected observation area (Figure 2.2 and Table 2.3) was not above the active hotspot island itself, but above the nearby seafloor in an effort to image the root of hotspot from the side. The area, therefore, lacks lateral heterogeneity compared to surrounding regions (*Isse et al., 2006a*), and is suitable for this study to obtain structure within the oceanic lithosphere and asthenosphere.

2.2.3 Northwest and Southeast Shatsky Rise

The northwestern Pacific Ocean around the Shatsky Rise is the oldest seafloor in the Pacific Plate emerged at 100–180 Ma by the activity of a triple ridge-ridge-ridge triple junctions. There were three plates at ~ 200 Ma, the Izanagi, Phoenix and Farallon plates, which formed a ridge-ridge-ridge triple junction at around the opposite side of a supercontinent, the Pangea

(*Seton et al.*, 2012). The emergence of the Pacific Plate occurred at the triple junction at ~ 180 Ma, which formed the triple ridge-ridge-ridge triple junctions (*Hilde et al.*, 1976; *Sager et al.*, 1988; *Nakanishi et al.*, 1989, 1992), i.e., there were six ridges: the Pacific–Izanagi, Pacific–Phoenix, Pacific–Farallon, Izanagi–Phoenix, Phoenix–Farallon and Farallon–Izanagi ridges. Although *Hilde et al.* (1976) first referred to the Izanagi Plate as the Kula Plate, *Woods and Davies* (1982) later discovered that it is different from the Kula Plate, and called the old plate as “Izanagi” after one of the creators of the Japanese islands in Japanese mythology.

The Izanagi and Phoenix plates have already subducted beneath the western and southern ends of the Pacific Ocean, whereas the Farallon plate still exists by breaking up into the Kula, Cocos, Nazca and Juan De Fuca plates in the eastern Pacific Ocean after ~ 70 Ma, where the Kula plate has already subducted beneath the north end of Pacific Ocean. The present magnetic lineations in the seafloor show the ancient Pacific–Izanagi ridge called the Japanese Lineation set, the ancient Pacific–Farallon ridge called the Hawaiian Lineation set, and the ancient Pacific–Phoenix ridge called the Phoenix Lineation set (*Nakanishi et al.*, 1992).

The Shatsky Rise is an old oceanic plateau formed at the Izanagi–Farallon–Pacific triple junction during the Late Jurassic and Early Cretaceous at 127–146 Ma (*Hilde et al.*, 1976; *Sager et al.*, 1988; *Nakanishi et al.*, 1989). The formation is complicated with the jumps of the ridge axis at least nine times (*Nakanishi et al.*, 1999). Although the formation of the Shatsky Rise may have affected the oceanic lithosphere/asthenosphere system around the region, the seafloor depth of oceanic basins surrounding the rise is considered “normal” compared to the Mid-Pacific Mountains region located at the southern end of Figure 2.1 (*Korenaga and Korenaga*, 2008).

The oceanic basins around the Shatsky Rise, thus, can be a valuable sample for the seafloor older than 120 Ma. The Normal Oceanic Mantle (NOMan) project, therefore, deployed BBOBSs in around the NW and SE Shatsky Rise (Fig. 2.4 and Table 2.4) for revealing the structure of oceanic lithosphere/asthenosphere system as well as the water content in the mantle transition zone. I hereafter refer to the two regions as the NW and SE Shatsky region, respectively, and investigate one-dimensional structures beneath each regions separately. The NW Shatsky region is located on the Japanese Lineation set with a seafloor age of ~ 130 Ma, whereas the SE Shatsky region is on the Hawaiian Lineation set with a seafloor age of ~ 140 Ma.

The types of BBOBSs are as same as the Shikoku Basin and French Polynesia regions (*Kanazawa et al.*, 2009) for most of stations. Another type of OBSs deployed at station 2 and 3 is the recently developed broadband OBSs, the BBOBS-NX, which buries the seismometer lightly in the sediment by the free-fall and provides a high-quality record with the noise level much lower than that of BBOBS especially for the horizontal components. The first observation started in 2009, and one-year records were recovered at station 2–5 in 2011–2012.

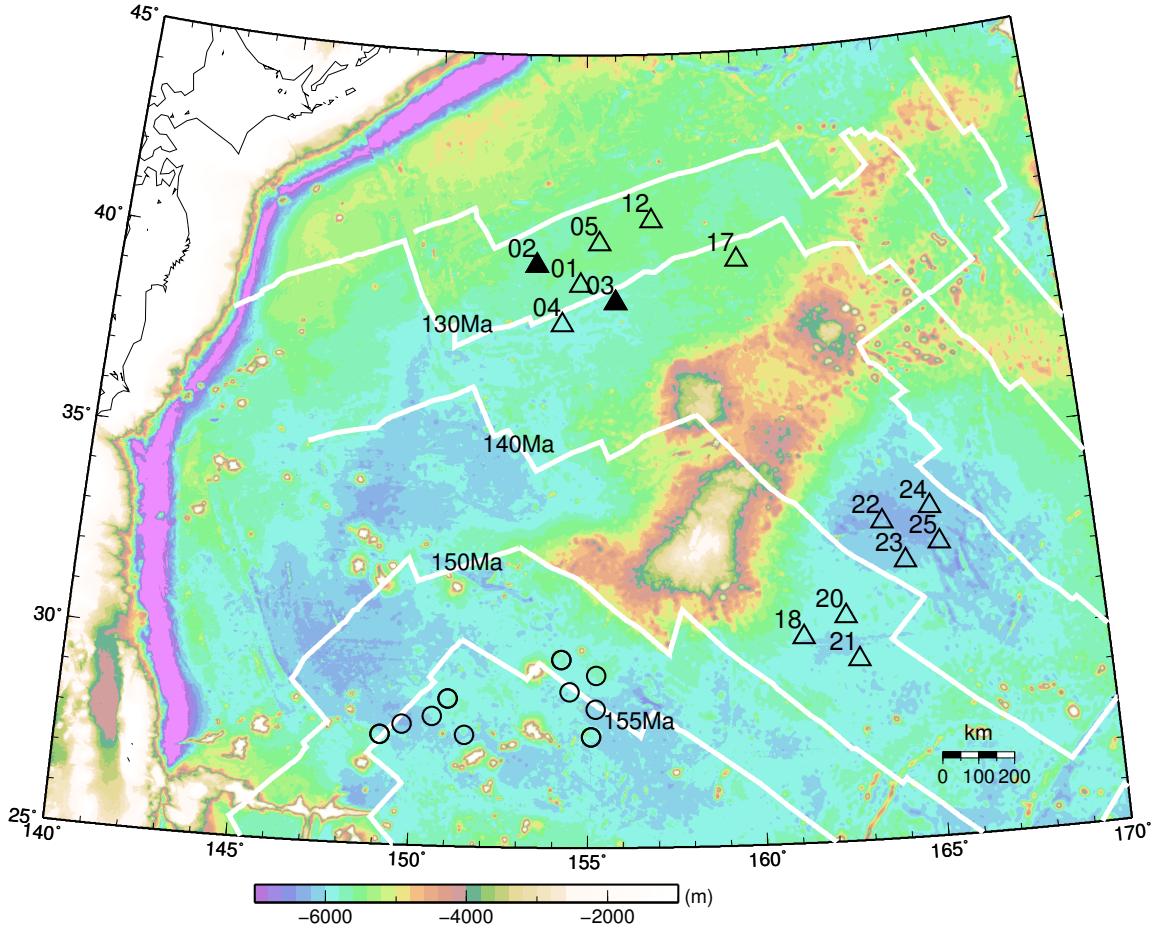


Figure 2.4: Locations of BBOBSs (open triangles) and BBOBS-NXs (filled triangles) by the Noman project. The NW and SE Shatsky regions are defined by the area of station 1–17 and 18–25, respectively. The stations in the SW Shatsky region is also shown by circles (see detail in Figure 2.5). White lines shows the magnetic lineations compiled by *Müller et al.* (2008).

The second observation started in 2011, and 1.5-year records were recorded at station 18 and 20–25 in 2013. The third observation started in 2012, and one-year records were recovered at station 1, 4, 5, 12 and 17 in 2013. The final observation cruise is planned in 2014 for the recovery of BBOBSs at eleven stations and BBOBS-NXs at six stations.

There are several previous studies in this region especially around a borehole seafloor station, the WP2 station (*Shinohara et al.*, 2006), in the northeastern end of NW region. *Shinohara et al.* (2008) conducted a refraction survey around WP2 station, and estimated the Pn- and Sn -wave anisotropies, which are about 5% and 4%, respectively. The maximum velocity directions are almost perpendicular to the magnetic lineation. *Kawakatsu et al.* (2009) and *Kumar and Kawakatsu* (2011) estimated the depth and the velocity reduction of the lithosphere-asthenosphere boundary by the receiver-function analysis, which are 7%–8%

Table 2.4: Summary of stations by the NOMan project.

Station No.	Sampling rate (Hz)	Longitude (°)	Latitude (°)	Depth (m)
from June 2010 to June 2011				
02 (NX)	100	153.35	39.70	5704
03 (NX)	100	155.91	38.76	5737
04	100	154.20	38.21	5923
05	100	155.41	40.25	5598
from November 2011 to July 2013				
18	100	161.29	30.19	5927
20	100	162.55	30.64	5913
21	100	162.86	29.54	5936
22	100	163.81	32.95	6118
23	100	164.41	31.92	6011
24	100	165.26	33.22	6059
25	100	165.44	32.32	6057
from August 2012 to August 2013				
01	100	154.78	39.20	5179
04	100	154.21	38.21	5916
05	100	155.41	40.25	5593
12	100	157.11	40.82	5501
17	100	159.85	39.77	5519

velocity reduction at a depth of ~ 80 km.

2.2.4 Southwest Shatsky Rise

The fifth area is the SW Shatsky region, where 16 OBSs (each with three component seismometers and a differential pressure gauge; DPG) were deployed in two arrays of eight OBSs by the Pacific Lithosphere Anisotropy and Thickness Experiment (PLATE) from 2009 to 2010. The region has the oldest identifiable magnetic anomalies in the Pacific, ~ 150 -160 Ma, and is in an area not affected by subsequent Cretaceous intraplate volcanism (*Nakanishi et al.*, 1989, 1992). While this location was specifically chosen for its old seafloor age of ~ 150 Ma, the location required deployment at great water depths (~ 6000 m) and high pressures that lead to failure of several instruments. The final array of working instruments is indicated in Figure 2.5 and was reduced to eight OBSs and nine DPGs, which were not necessarily coincident at any one station.

I use five stations (stations 1-8) in the western array, and six stations (stations 10-16) in the eastern array. The western and eastern arrays are located on the Japanese and Hawaiian

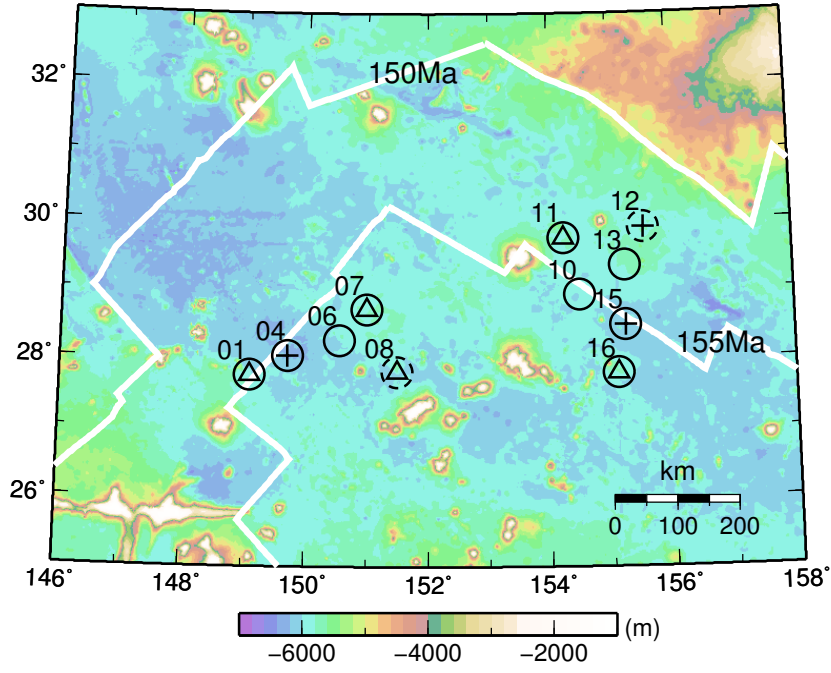


Figure 2.5: Station map of the PLATE project. Triangles and crosses show three-component OBSs. Circles show DPGs. The horizontal-component records of OBSs shown by crosses and the DPGs shown by broken circles are not used in this study due to low data quality. White lines show the magnetic lineations.

Table 2.5: Summary of stations by the PLATE project.

Station No.	OBS	Sampling rate (Hz)	Longitude (°)	Latitude (°)	Depth (m)
from October/November 2009 to November 2010					
01	T-240	50	149.09	27.77	5982
04	T-40	50	149.71	28.05	6249
06	-	50	150.55	28.27	5964
07	T-240	50	151.00	28.72	5898
08	LDEO	40	151.49	27.81	5906
10	-	50	154.49	28.93	6002
11	T-240	50	154.24	29.75	5996
12	LDEO	40	155.56	29.90	5834
13	-	50	155.24	29.35	5750
15	T-40	50	155.24	28.49	6156
16	T-240	50	155.11	27.80	5665

Lineation sets, respectively. The interstation distances range from 60 to 600 km. There are three types of OBSs as summarized in Table 2.5: OBSs with a velocity-flat response at periods shorter than 240 s (Trillium 240; T-240) or shorter than 40 s (Trillium 40; T-40), and OBSs with an acceleration-flat response at periods longer than 1 s developed in Lamont-Doherty Earth Observatory (L-DEO) (*Webb et al.*, 2001). If the pressure change is only caused by seismic surface waves, the phase of the pressure is theoretically the same as that of the vertical displacement (see §3.3.1 for the detail). I therefore regarded the DPG records as displacement waveforms, and estimated the unknown instrumental phase responses of DPGs from the CCFs between DPG and OBS records in Section 3.3.3. The amplitude response of DPG was roughly estimated with an accuracy of $\sim 10\%$ by comparing the amplitude of teleseismic surface waves recorded by DPGs and OBSs at periods of 50–100 s. The amplitude response may be inappropriate at shorter periods, although the estimation is difficult and could not be achieved in this study. As the sampling rate is 50 Hz for 8 stations and 40 Hz for 3 stations and I am interested in surface wave dispersion at periods greater than 1 s, I first down-sampled all records to 10 Hz. The sampling rate used for the analysis in the next Section (§3) is summarized in Table 2.1.

The previous study of mantle structure in this region is limited. For the western array of the SW Shatsky region, *Oikawa et al.* (2010) showed that the Pn wave propagating in the direction perpendicular to the magnetic lineations is faster than that in the direction parallel to the magnetic lineations. *Baba et al.* (2010) obtained a one-dimensional electrical conductivity model for the region between the western array and the westside region of the western array and the trench by using the electromagnetic records obtained at the stations in the Pacific Basin by the SSP project (Fig. 2.3). They revealed that the model is highly

resistive compared to the model beneath the Philippine Sea region, where the seafloor age is younger than ~ 60 Ma.

2.3 Characteristics of Seafloor Records

Several points should be emphasized as the characteristics or the problems of seafloor records compared to the onland records as already introduced in Section 1. I here re-emphasize the problems for the case of datasets used in this study.

The first point is the noise level of BBOBS. The typical noise spectra of a BBOBS is shown in Figure 2.6, which suggests that the noise level of the vertical component is comparable to that of onland records, but the noise level of the horizontal component is higher. At periods longer than 10 s, especially, the noise level becomes higher at longer periods. Given that the noise level strongly depends on the site, the component and the observation period, the employment of proper methods of seismic data analysis appears to be essential.

Other problems are the unknown clock delays and unknown instrumental responses. For the records used in this study, the precise clock delays information were not available for one station in the NW Shatsky region, one station in the SE Shatsky region and two station in the SW Shatsky region, which was corrected by using the temporal change of cross-correlation functions (see §3.3.3 for detail). The instrumental responses of DPGs deployed in the SW Shatsky were also unknown. They were also corrected by using the cross-correlation functions between the DPG and BBOBS records (see §3.3.3).

The last point is that the amount of seafloor records is less than the onland records in terms of both the number of stations and the period of record. The typical number of stations and the observation period for each region in this study are 5–10 and 1–2 years, respectively. These values are about one order lower than those of onland projects. The number of available teleseismic events are then smaller, and the signal-to-noise ratio of cross-correlation functions are lower (*Bensen et al.*, 2007). Although recent tomography studies spend less effort to evaluate the uncertainty of each measurement because they use thousands to millions of measurements and average out the error of measurements. In comparison, the uncertainty should be evaluated thoroughly for the seafloor records to avoid bias from one anomalous measurement. The rest of this thesis, therefore discusses the uncertainty of measurements and estimated structure somewhat pertinaciously compared to previous studies.

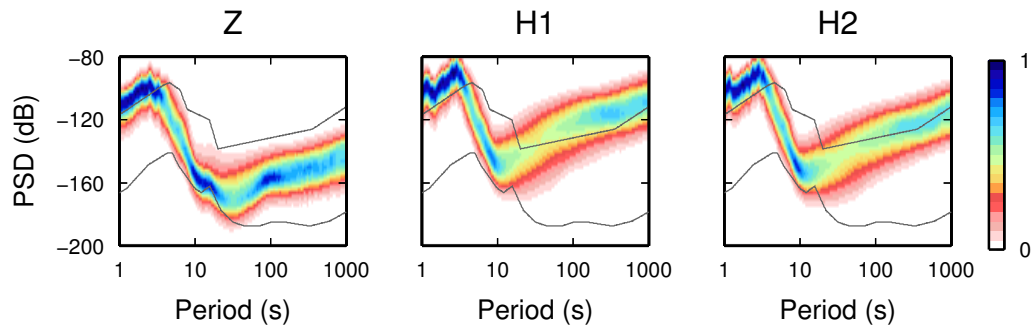


Figure 2.6: Colors show the probability density of acceleration power spectrum density (PSD) of vertical (Z) and horizontal (H1 and H2) components at a typical station in the Shikoku Basin region normalized to the maximum probability density. The gray lines show New Low and High Noise Models (*Peterson, 1993*).

Chapter 3

SURFACE WAVE ANALYSIS

3.1 Introduction

The broadband analysis of surface waves at periods of ~ 3 -100 s is essential for obtaining uppermost mantle structure from the crust to depths of ~ 150 km. This chapter summarizes the method to analyze broadband surface waves including higher modes from the records of BBOBSs and DPGs. The discussion on the error and uncertainty will be presented in each section for each measurement procedure.

Section 3.2 first describes the relationship between surface-wave velocities and S-wave/P-wave velocities, especially the difference between Rayleigh waves in oceanic and continental regions. For example, the first higher mode of Rayleigh wave is frequently observed and important in oceanic regions (*Harmon et al.*, 2007; *Yao et al.*, 2011). There is, however, no consensus even on the name of fundamental-mode and higher-mode Rayleigh waves yet. The concept of ocean-mode and solid-mode Rayleigh waves will be presented to simplify the discussion.

The cross-correlation analysis of ambient noise at periods of 2–30 s will be summarized in Section 3.3. It includes the uncertainty of cross spectra (§3.3.1), the obtained cross-correlation functions (§3.3.2), the corrections for the clock delays and instrumental responses (§3.3.3), the measurement of average phase velocities of multi-mode surface waves for each array of stations by the waveform fitting (§3.3.4), and the measurement of phase-velocity anomalies for each pairs of stations (§3.3.5).

The array analysis of teleseismic surface waves at periods of 30–100 s will be summarized in Section 3.4, including the average phase-velocity measurement (§3.4.1), and the estimation of azimuthal dependence (§3.4.2).

3.2 Uniqueness of Surface Waves in Oceanic Regions

This section summarizes the nature of surface wave dispersions and their sensitivity to the mantle structure in oceanic regions for simplifying the subsequent analyses and discussions. Five modes of surface waves are considered: the fundamental-mode Rayleigh wave (0S mode), the first higher-mode Rayleigh wave (1S mode), the second higher-mode Rayleigh wave (2S mode), the fundamental-mode Love wave (0T mode), and the first higher-mode Love wave (1T mode). Figures 3.1–3.2 show phase and group velocities for the PREM-OCEAN4.6 model, a model based on PREM (*Dziewonski and Anderson, 1981*) where the thickness of the ocean is changed from 3.0 to 4.6 km and the thickness of the crust is reduced from 22 to 6 km. The figure also includes the phase velocities for the PREM-SOLID model, which is same as the PREM-OCEAN4.6 model but without the ocean layer. The calculation for phase and group velocities (dispersion curves) is based on the Fortran package DISPER80 (*Saito, 1988*) with the physical dispersion (*Kanamori and Anderson, 1977*). I used the calculated eigen-periods of spheroidal and toroidal modes for obtaining phase velocities of Rayleigh and Love waves, respectively.

The difference between oceanic and continental regions is reflected in the sudden decrease of phase velocity of 0S mode for the PREM-OCEAN4.6 model at a period of ~ 14 s. This decrease corresponds to the transition of modal energy from the solid to the ocean (*Ewing et al., 1957*). The period of the phase velocity drop is related to the ocean depth as shown by the comparison between the PREM-OCEAN4.6 model and the PREM-OCEAN6 model, a model similar to PREM-OCEAN4.6 model with a thickness of the ocean of 6 km (Figure 3.1). The group velocities govern energy arrival, which depends on the derivative of the phase velocity. At the periods of phase-velocity drops, therefore, the group velocities take the minimum values, and sometimes becomes lower than the mode of lower order, i.e., the group velocity of 1S mode is lower than that of 0S mode at periods of ~ 2 –4 s for the PREM-OCEAN4.6 model.

Figure 3.3 summarizes the sensitivities of phase velocities to S-wave and P-wave velocities. The sensitivity of phase velocity (c) at a period of T to a parameter p at a depth of z , $K_p(z, T)$, is defined as follows:

$$\frac{\Delta c(T)}{c(T)} = \int \left[\sum_p K_p(z, T) \frac{\Delta p(z)}{p(z)} \right] dz \quad (3.1)$$

where Δc is the perturbation of the phase velocity when Δp is added to the parameter p . The sensitivities can be calculated from the variational equation of the energy integral equation (*Takeuchi and Saito, 1972*). In a radially anisotropic media, the Rayleigh waves mainly reflect velocity of horizontally propagating S-wave with vertical polarization, V_{SV} , whereas Love waves mainly reflect velocity of horizontally propagating S-wave with horizontal polarization, V_{SH} . As well known, surface waves at long periods have greater sensitivities at deeper depths, and Love waves have sensitivities to shallower depths than Rayleigh waves

do.

The detail is, however, more complicated in oceanic regions. At periods shorter than ~ 14 s, the 0S mode has sensitivity to S-wave velocity in the crust, but the sensitivity to S-wave velocity is smaller than that to P-wave velocity in the ocean (Figure 3.3). In contrast, the 1S mode for the PREM-OCEAN4.6 model corresponds to the 0S mode for the PREM-SOLID model for both phase velocities and the sensitivities. At periods shorter than ~ 5 s, the phase velocities of 1S mode for the PREM-OCEAN4.6 model suddenly decreases, and 2S mode corresponds to the 0S mode for the PREM-SOLID model. In summary, the Rayleigh waves with a velocity lower than ~ 2 km/s mainly reflect P-wave velocity in the ocean, ~ 1.5 km/s, whereas the waves with a velocity higher than ~ 2 km/s mainly reflect S-wave velocity in the solid (Ewing et al. 1957). As Rayleigh wave intrinsically means surface wave propagating the surface of solid, *Ewing et al.* (1957) called these waves generalized Rayleigh waves. *Yao et al.* (2011) recently called the 0S and 1S modes as Scholte-Rayleigh waves by considering the Scholte wave, which propagates near the interface between solid and liquid layers. The name is, however, not suited for the 2S mode because the energy of 2S mode concentrates in the ocean layer and not at the interface, the seafloor. I choose to refer to them as Rayleigh waves for simplicity. In addition, I call the Rayleigh waves with a velocity lower than ~ 2 km/s ocean-mode Rayleigh waves and the faster waves solid-mode Rayleigh waves. For example, 0S mode transitions from ocean-mode Rayleigh wave to solid-mode Rayleigh wave at periods of ~ 10 -20 s.

Only 0S and 0T modes are enough to constrain structure from the crust to the upper mantle beneath continental and island regions. In oceanic regions with a thickness of ocean greater than ~ 4 km, however, 1S mode must be analyzed to constrain structure in the uppermost mantle at depths of ~ 10 –20 km. The 2S mode is further needed to constrain V_{SV} structure in the crust. Both modes need to be considered and analyzed to obtain the V_{SV} structure in the uppermost mantle and crust.

3.3 Ambient Noise Cross-Correlation Analysis

3.3.1 Calculation of Cross Spectra

At periods shorter than 30 s, I extracted the background surface wave propagation between pairs of stations by cross-correlating continuous records of ambient noise (*Aki*, 1957). I first calculated CCFs between every pair of stations and components by calculating the cross spectra in the frequency domain and by taking the inverse Fourier transform. The cross-spectrum is defined as,

$$S_{ij}^{kl}(\omega) = \frac{\langle W_{ij}^{kl}(\omega) \cdot (F_i^k(\omega))^* \cdot F_j^l(\omega) \rangle}{\langle W_{ij}^{kl}(\omega) \rangle}, \quad (3.2)$$

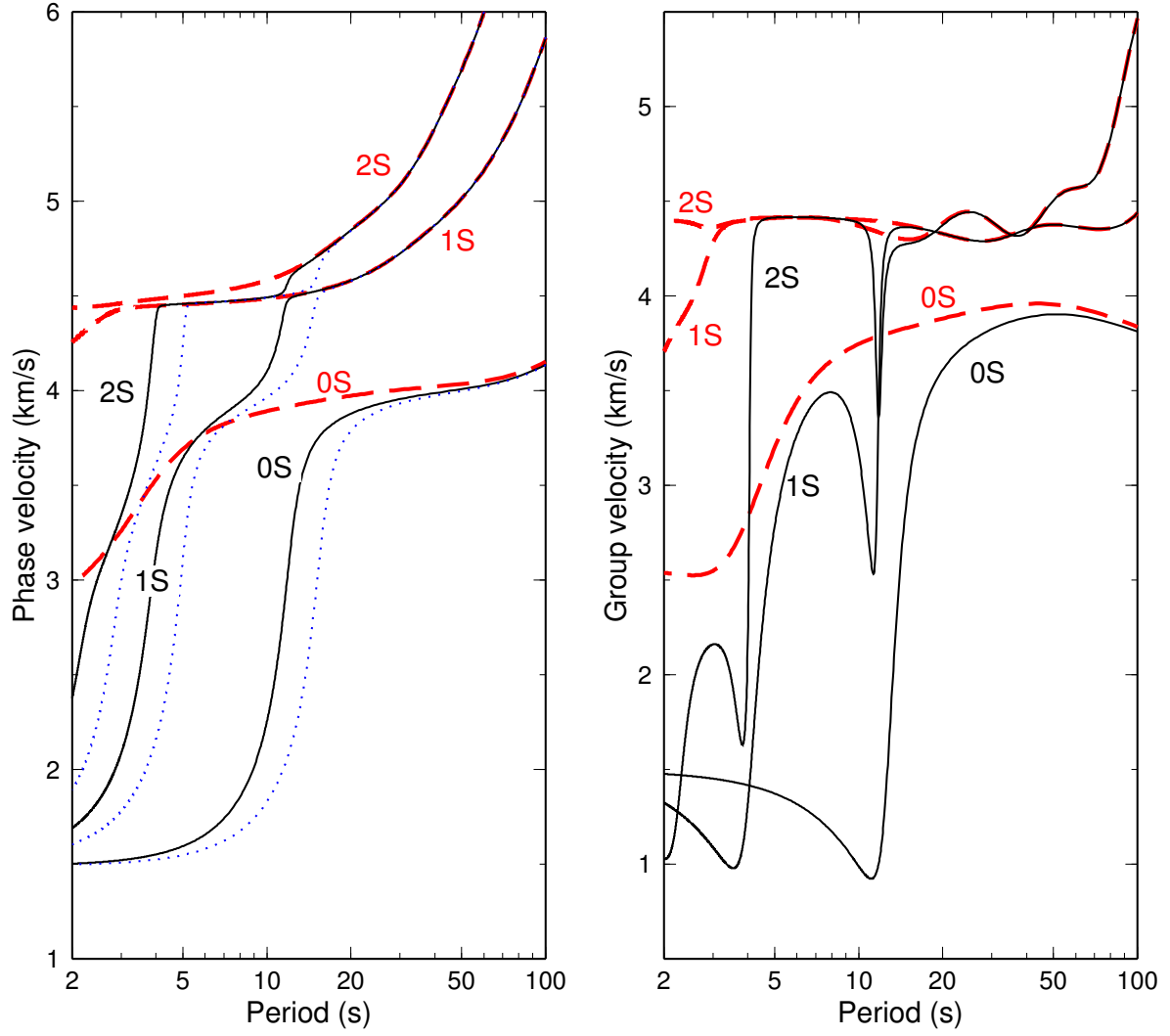


Figure 3.1: Phase and group velocities of 0S, 1S and 2S modes for the PREM-OCEAN4.6 model (black solid lines) and the PREM-SOLID model (red dashed lines). Blue dotted lines show phase velocities for the PREM-OCEAN6 model.

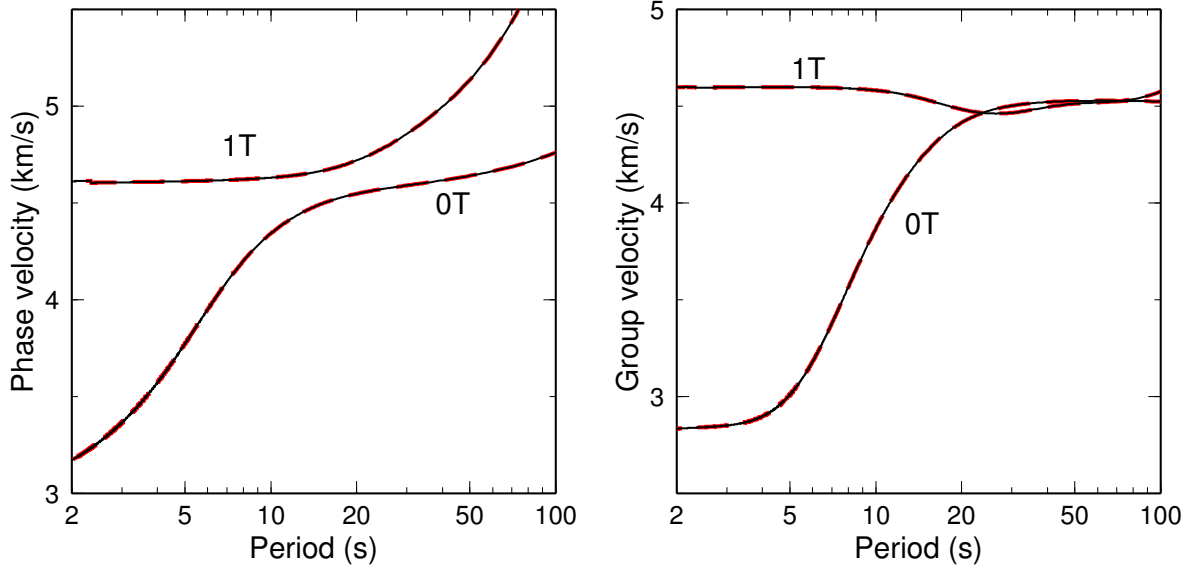


Figure 3.2: Same as Fig. 3.1, but for the 0T and 1T modes.

where $\langle \rangle$ means the ensemble average, and F_i^k is a Fourier spectrum of the component k record at the i th station with a time window of 1638.4 s for the 10 Hz sampling records (Shikoku Basin, French Polynesia and SW Shatsky regions), and 1310.7 s for the 100 Hz sampling records (NW and SE Shatsky regions). Each time window is half overlapped with the adjacent time windows. I discarded any segments containing earthquake signals. The Fourier spectrum for the OBS record was divided by the instrumental response calculated from poles and zeros to be the displacement spectrum, whereas the spectrum for the DPG record was not divided because of the unknown instrumental response of DPGs. The estimation of the instrumental responses by using CCFs will be described in Section 3.3.3. The weighting term, W_{ij}^{kl} , is given by:

$$W_{ij}^{kl}(\omega) = \frac{1}{|\tilde{F}_i^k(\omega)|} \cdot \frac{1}{|\tilde{F}_j^l(\omega)|}. \quad (3.3)$$

The normalized amplitude is $|\tilde{F}_i^P| = |F_i^P|$ for the DPG record, $|\tilde{F}_i^Z| = |F_i^Z|$ for the vertical component of OBS, and $|\tilde{F}_i^T| = |\tilde{F}_i^R| = \sqrt{(|F_i^T|^2 + |F_i^R|^2)/2}$ for the two horizontal components of OBS.

The definition of cross spectrum in equation (3.2) is similar to the conventional definition of cross spectrum:

$$S'_{ij}{}^{kl}(\omega) = \left\langle \frac{(F_i^k(\omega))^*}{|\tilde{F}_i^k(\omega)|} \cdot \frac{F_j^l(\omega)}{|\tilde{F}_j^l(\omega)|} \right\rangle = \langle W_{ij}^{kl}(\omega) \cdot (F_i^k(\omega))^* \cdot F_j^l(\omega) \rangle, \quad (3.4)$$

which is called spectrum normalization or whitening (*Bensen et al., 2007*). If the continuous records only contain signals (background surface waves), then the spectrum normalization is equivalent to the deconvolution of source spectrum (*Nakahara, 2006*). If the noise level

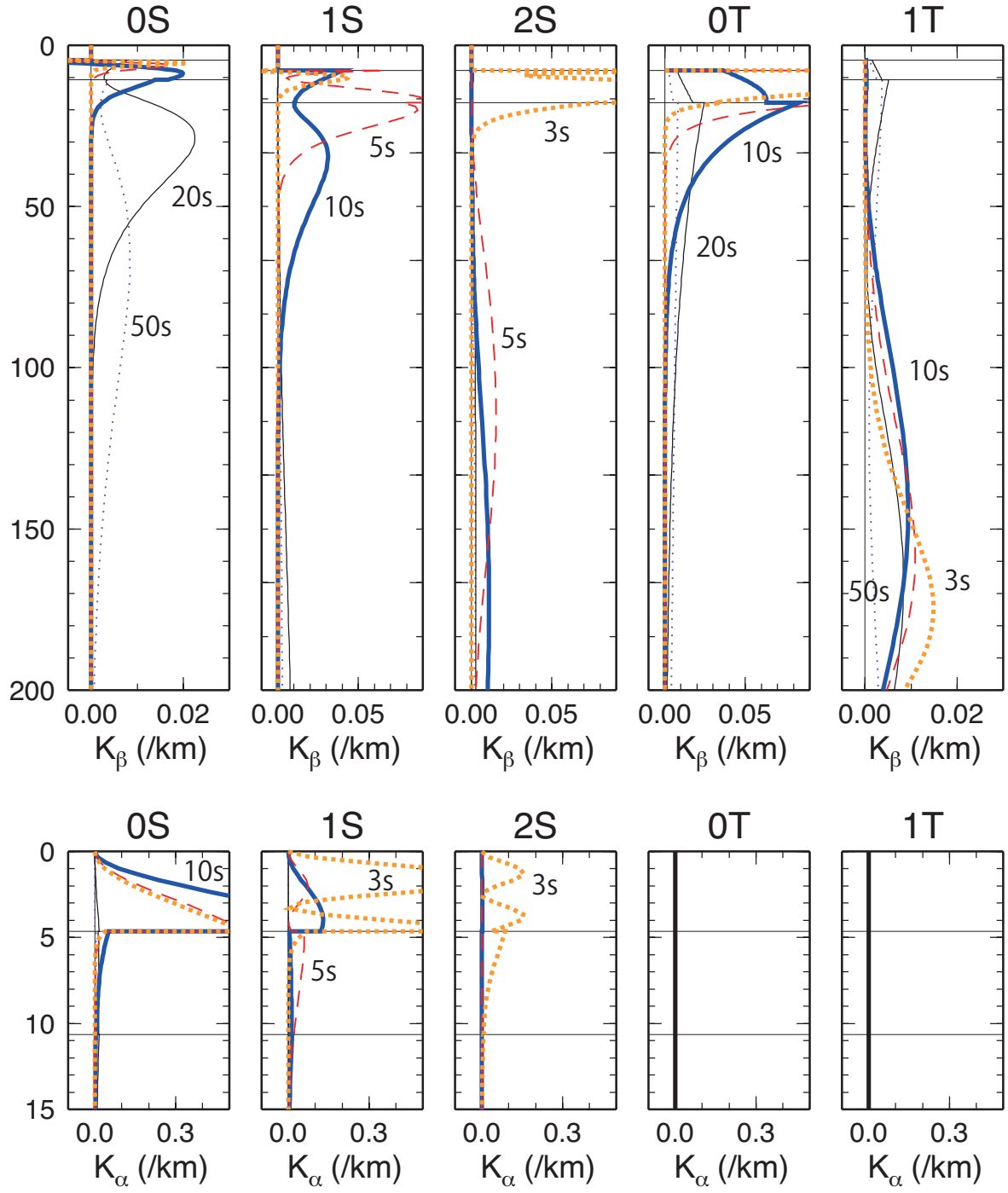


Figure 3.3: Sensitivities of phase velocities to S-wave and P-wave velocities (K_β and K_α , respectively) at periods of 20 s (thin solid lines), 10 s (thick solid lines), 5 s (broken lines), and 3 s (dotted lines). The two lines in each panel show the depths of the seafloor and Moho.

is much higher than the signal level, as is the case with the BBOBS records used in this study, then the amplitude of each Fourier spectrum reflects the noise level. In this latter case, the normalization is not equivalent to the source deconvolution, but simply suppresses the contribution of noisy data. The equation (3.4), however, decreases the amplitude of the cross spectrum for the pair of stations with the higher noise levels. This study, therefore, uses equation (3.2) to compensate for the effect of weighting.

The signal-to-noise ratio of cross-correlation function is previously discussed by *Bensen et al.* (2007), but the uncertainty has not been obtained quantitatively yet. The estimation of uncertainty is discussed here by considering that the continuous records of ambient noise contain both signal (background surface waves) and noise components. The noise is produced by local phenomena such as oceanic currents, and is incoherent with other stations. The noise level of the BBOBS record used in this study is higher than the signal level and depends on the site and observation period. The uncertainty of a cross spectrum is expected to be higher for a pair of stations with higher noise levels, which will be obtained by expressing the Fourier spectrum of each segment ($F_i^k(\omega)$) as a summation of signal ($s_i^k(\omega)$) and noise ($n_i^k(\omega)$). The cross spectrum between the i th and j th stations ($S_{ij}^{kl}(\omega)$) obtained by equation (3.2) can be written as:

$$\begin{aligned} S_{ij}^{kl} = & \frac{\langle W_{ij}^{kl} \cdot s_i^{k*} \cdot s_j^l \rangle}{\langle W_{ij}^{kl} \rangle} + \frac{\langle W_{ij}^{kl} \cdot s_i^{k*} \cdot n_j^l \rangle}{\langle W_{ij}^{kl} \rangle} \\ & + \frac{\langle W_{ij}^{kl} \cdot n_i^{k*} \cdot s_j^l \rangle}{\langle W_{ij}^{kl} \rangle} + \frac{\langle W_{ij}^{kl} \cdot n_i^{k*} \cdot n_j^l \rangle}{\langle W_{ij}^{kl} \rangle}. \end{aligned} \quad (3.5)$$

When the noise level is much higher than the signal level, the second and third terms are negligible compared with the fourth term. In addition, the amplitude of the numerator of the fourth term is almost one ($W_{ij}^{kl} \cdot n_i^{k*} \cdot n_j^l \sim 1$) before taking the ensemble average, and becomes approximately $1/\sqrt{N}$ upon taking the average of N ensembles. The number of ensembles is the observation period divided by the length of time window times two, where the multiplication by two corresponds to the half overlapping of time windows. As the number is almost constant for all the cross spectra for the same region, the above equation becomes:

$$S_{ij}^{kl} \simeq \frac{\langle W_{ij}^{kl} \cdot s_i^{k*} \cdot s_j^l \rangle}{\langle W_{ij}^{kl} \rangle} + \frac{1}{\langle W_{ij}^{kl} \rangle} \mathcal{O}\left(\frac{1}{\sqrt{N}}\right). \quad (3.6)$$

where the first and second terms are the signal and uncertainty of each cross spectrum, respectively. The signal level of each cross spectrum is proportional to the source spectrum (s^2), whereas the uncertainty is proportional to $\langle W_{ij}^{kl} \rangle^{-1} \sim |\tilde{F}_i^k| \cdot |\tilde{F}_j^l|$, which is the product of noise levels at the i th and j th stations. Fig. 3.4 shows the actual value of $\langle W_{ij}^{kl} \rangle^{-1}$. The noise level of one pair of stations differs from others by up to a factor of 100. The variation in uncertainties of cross spectra is therefore large.

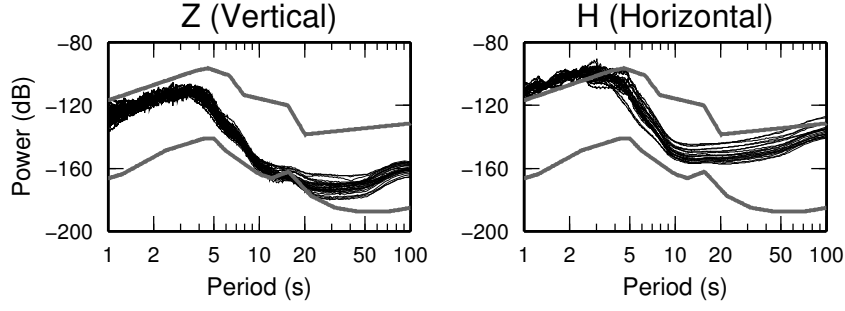


Figure 3.4: Variation in site-dependent noise level for each pair of stations ($\langle W_{ij}^{kl} \rangle^{-1}$; thin black lines) in the Shikoku Basin region with the New Low and High Noise Models (Peterson, 1993) (thick gray lines).

3.3.2 Cross Correlation Functions

The CCFs are useful for recognizing various modes of surface waves contained in the cross spectra. Figures 3.7–3.10 show the CCFs for four regions obtained by the inverse-Fourier transformation of cross spectra calculated from the vertical ($k = l = Z$, ZZ component), radial (RR) and transverse (TT) components of OBS records. The CCFs for the SW Shatsky region shown in Figure 3.11 includes the CCFs between DPGs (PP), DPG and vertical components of OBS (PZ) in addition to the three components of OBS records (ZZ, RR and TT). The use of PZ component is necessary for increasing the number of available pairs because three stations only have DPG records and two stations only have OBS records. The TT-component CCFs show the propagation of 0T mode, whereas the PP-, PZ-, ZZ- and RR- component CCFs show the propagation of multi-mode Rayleigh waves: 0S, 1S and 2S modes. At periods of 3-5 s in this water depth, the 1S mode arrives later than the 0S mode due to the sudden decrease of the phase velocity of 1S mode (Ewing *et al.*, 1957) as indicated by Figure group velocities of the PREM-OCEAN4.6 model in Figure 3.1.

The amplitudes of Rayleigh waves in PP, PZ, ZZ and RR components are notable. The PP and PZ components mainly show the ocean-mode Rayleigh waves, whereas the RR component mainly shows the solid-mode Rayleigh waves. The ZZ component shows both modes simultaneously except for the Shikoku Basin region where the ocean-mode Rayleigh waves dominates the ZZ component (Fig. 3.7). The difference between appearances can be understood by considering the eigenfunctions of Rayleigh waves at the seafloor. Figure 3.5 shows the eigenfunctions for the 0S and 1S modes at a period of 7 s, which correspond to the ocean-mode and solid-mode Rayleigh waves, respectively. The displacement exists both in the oceanic and solid layers for the solid-mode Rayleigh wave, whereas it concentrates in the oceanic layer for the ocean-mode Rayleigh wave. As the vertical displacement is continuous at the seafloor, the vertical displacement exists in both solid and ocean part of the seafloor. As the horizontal displacement is discontinuous at the seafloor, on the other

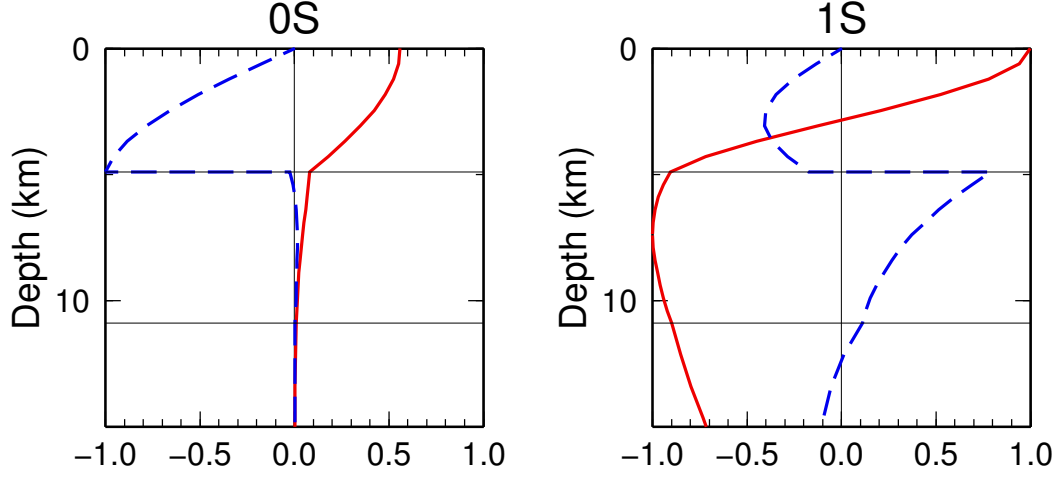


Figure 3.5: Horizontal (dotted blue lines) and vertical (red solid lines) displacements normalized by the maximum value for 0S and 1S modes at a period of 7 s calculated for a smooth radially-anisotropic model for the Shikoku Basin region shown in Figure 4.10. Two horizontal lines show the depth of the seafloor and the Moho.

hand, the displacement at the solid part of the seafloor is small compared to that at the ocean part of the seafloor for the ocean-mode Rayleigh wave. By further considering that an OBS records the displacement at the solid part of the seafloor, the amplitude of ocean-mode Rayleigh waves is expected to be smaller for the horizontal components than for the vertical components. Figure 3.6 shows the energy ratio between the horizontal displacement (U) and the vertical displacement (V) represented by $U^2/(U^2 + V^2)$. The ratio is almost zero for the ocean-mode Rayleigh waves with a phase velocity lower than 2 km/s, whereas the ratio is larger for the solid-mode Rayleigh waves. The amplitude for the DPG can be considered as same as the vertical component of OBS, although the DPG records the displacement at the ocean part of the seafloor. The ocean-mode Rayleigh waves, thus, appear mainly in the DPGs and the vertical components of OBSs.

Figure 3.11 further shows an unknown phase marked by a black arrow in the positive lag-time of the PZ component at periods of 5-10 s and interstation distances longer than 300 km. The apparent group velocity at the interstation distance range of 300-700 km is ~ 3.5 km/s, which is close to the group velocity of 1S mode at this period range, 3.6 km/s. The simplest interpretation is that the signal corresponds to the conversion of 0S mode to 1S mode at seamounts located between two arrays in our study (see Fig. 2.5). As I pointed out already, the ocean-mode Rayleigh waves tend to appear in DPGs, whereas the solid-mode Rayleigh waves tend to appear in the vertical components of OBSs. At periods of 5-10 s, 0S and 1S modes appear in DPGs and vertical components of OBSs, respectively. The converted waves are therefore expected to appear in the CCFs between the DPGs and the vertical components of the OBSs.

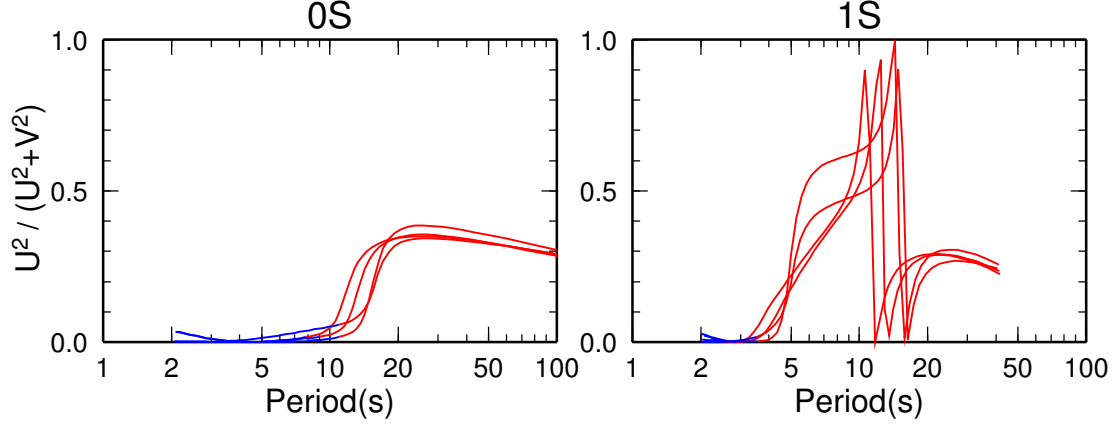


Figure 3.6: The energy ratio between the horizontal (U) and vertical (V) displacements represented by $U^2/(U^2 + V^2)$ at the solid part of the seafloor calculated by using smooth radially-anisotropic models for four oceanic regions (Shikoku Basin, French Polynesia, NW Shatsky and SE Shatsky regions) shown in Figure 4.10. Blue and red lines show the ratio for the ocean-mode and solid-mode Rayleigh waves, respectively.

3.3.3 Correction for Clock Delays and Instrumental Responses

The accuracy of clock is essential for the accurate measurement of phase velocities. For the dataset used in this study, the typical travel time is about 30-150 s. The travel-time accuracy of about 0.3 s is then required to achieve phase-velocity accuracy of 1% and to discuss seismic anisotropy quantitatively. The two typical problems in seafloor records, however, obstruct the accurate phase-velocity measurement: the unknown clock delays and the unknown instrumental responses. This section summarizes the methods to overcome such problems by using CCFs for each of three regions: SW Shatsky, NW Shatsky and SE Shatsky regions.

The records obtained in the SW Shatsky region included two problems, unknown clock delays at two stations and unknown instrumental responses of DPGs, which were estimated by the three steps described below.

In the first step, I corrected the clock delays at station 4 and station 12. At station 4, the total delay of the clock at the end of the project was ~ 20 s, which is an order of magnitude larger than other stations, implying the possibility of significant non-linear drift or a clock jump. At station 12, the drift correction was not possible due to the cessation of recording during the observation period. I therefore estimated the clock delays at these two stations from the temporal changes of CCFs as done by *Sens-Schönfelder* (2008) for land seismic records without GPS reception. *Hannemann et al.* (2013) recently applied the similar method to estimate clock delays of OBS records. Figure 3.12a shows the CCFs calculated from five-day records and the CCFs averaged over the whole year with a band-pass filter of 3-10 s. Although the waveforms seem identical, the lag time of the signal slightly varies with

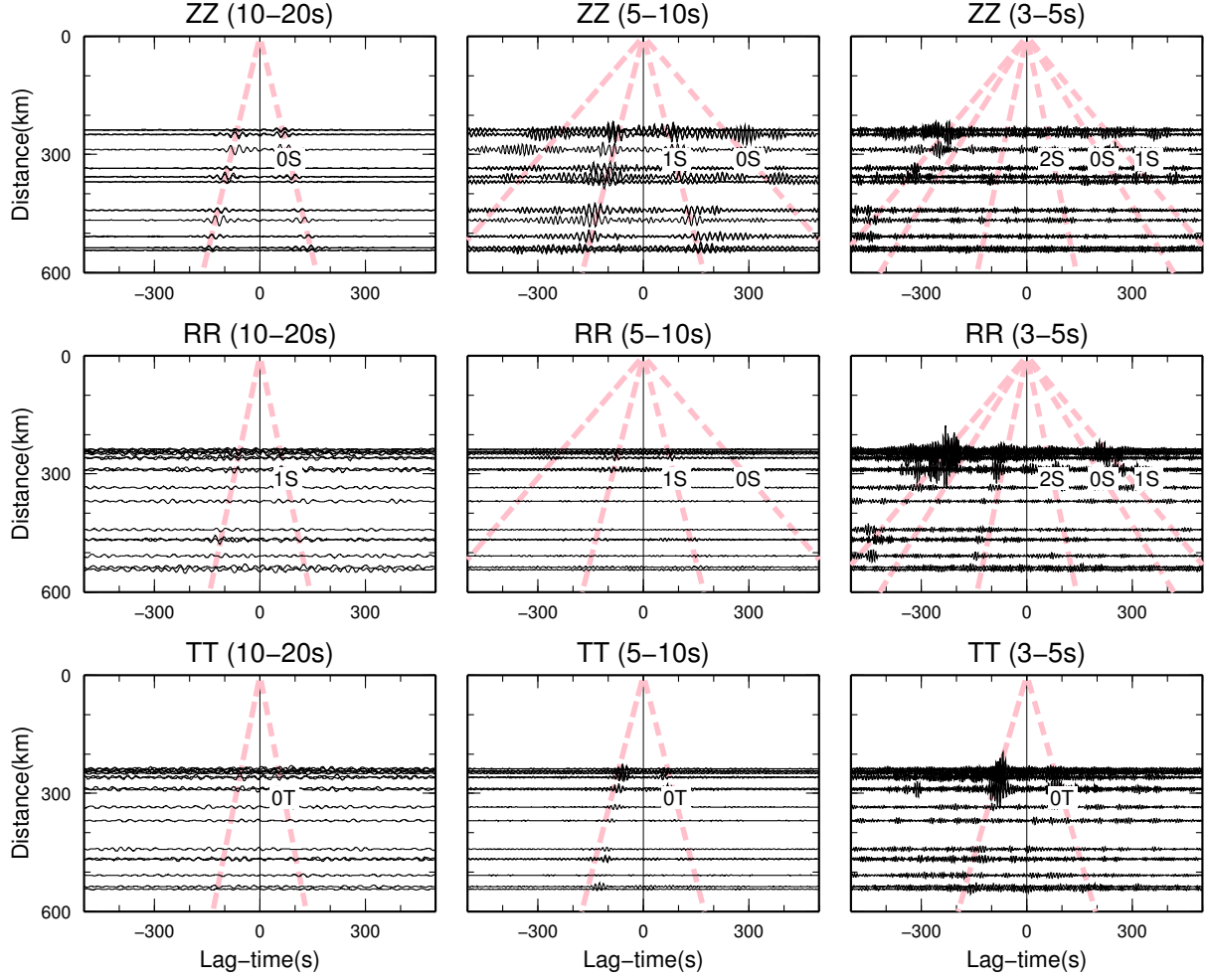


Figure 3.7: CCFs band-pass filtered at 10-20 s, 5-10 s, and 3-5 s for the Shikoku Basin region. I multiplied each cross spectrum by $\langle W_{ij}^{kl} \rangle$ before calculating the CCF for reducing the CCF amplitude with large uncertainties. The amplitude of the two horizontal components (10-20 s) is exaggerated by a factor of five as compared with the vertical component. Dashed pink lines show the arrival of each mode at a typical period.

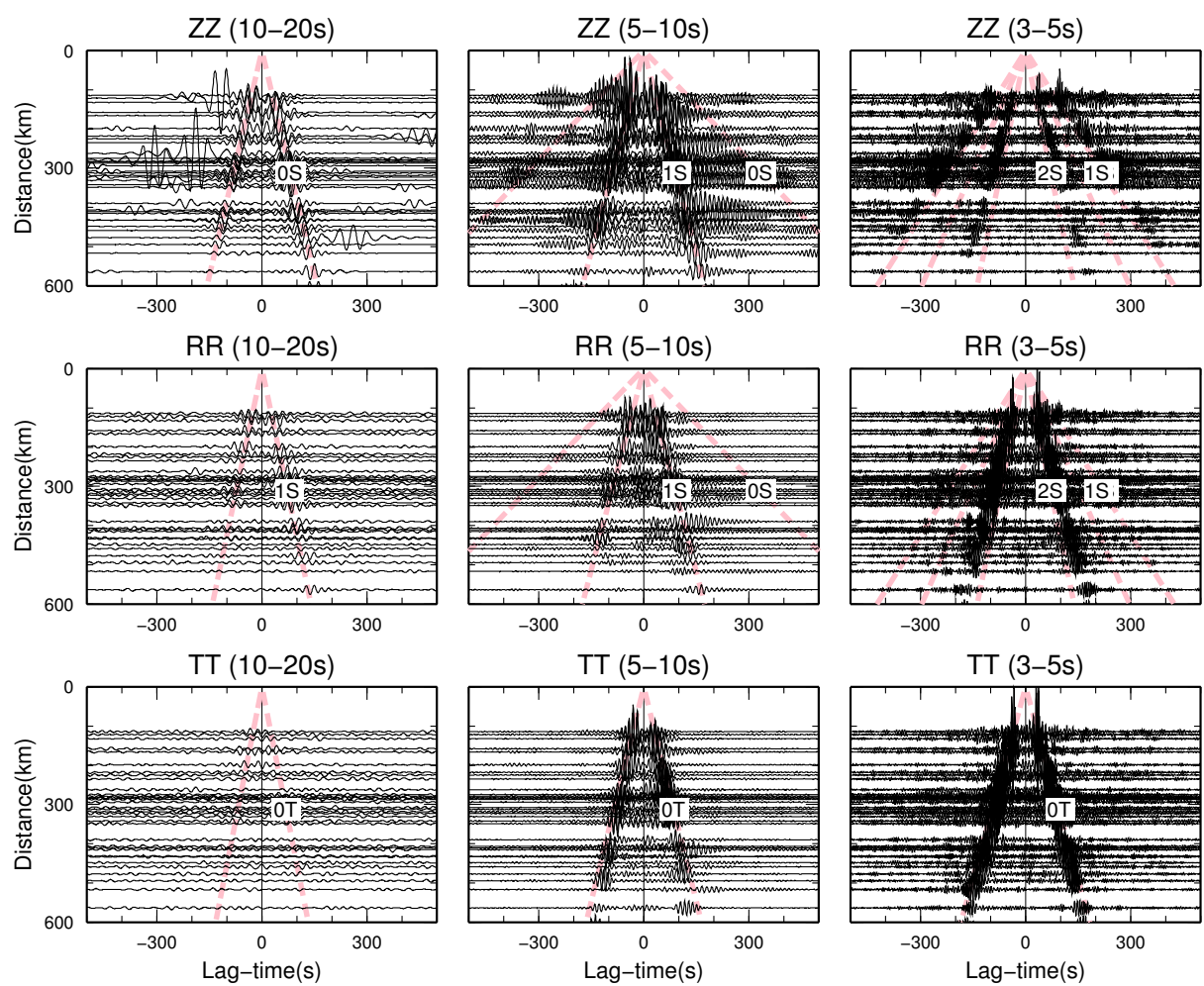


Figure 3.8: Same as Fig. 3.7, but for the French Polynesia region.

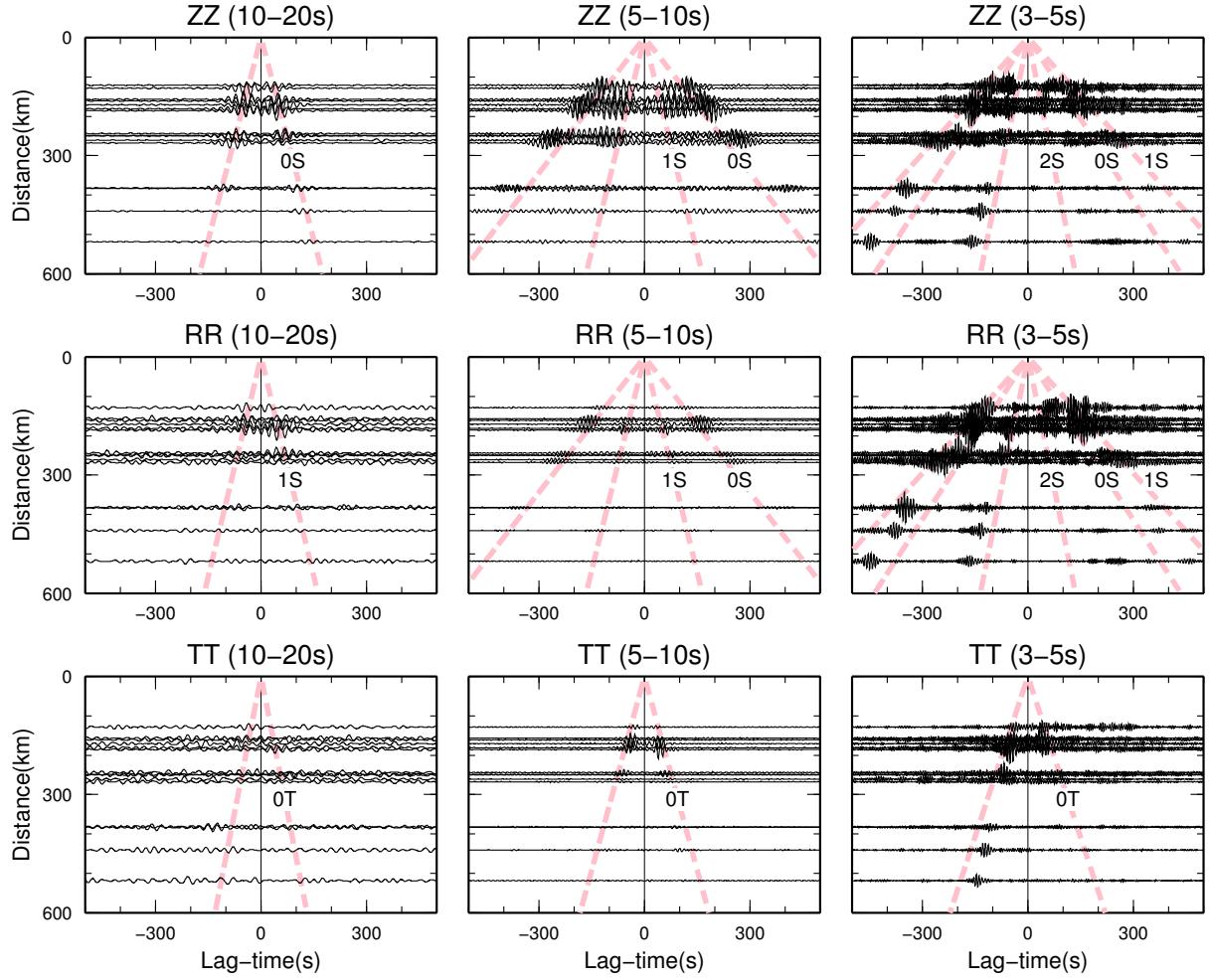


Figure 3.9: Same as Fig. 3.7, but for the NW Shatsky region. The amplitude of the two horizontal components (10-20 s) is exaggerated by a factor of eight as compared with the vertical component.

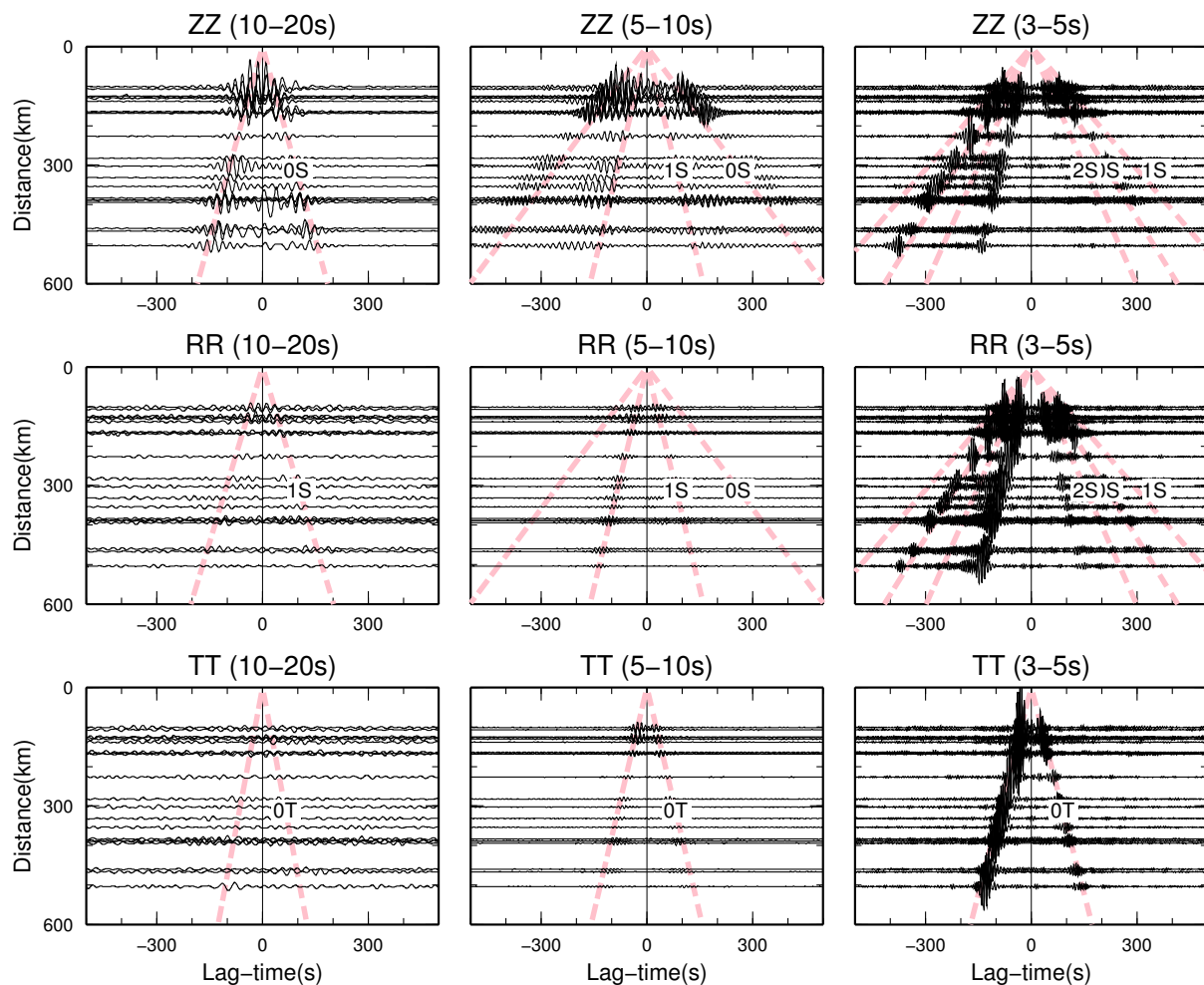


Figure 3.10: Same as Fig. 3.7, but for the SE Shatsky region. The amplitude of the two horizontal components (10–20 s) is exaggerated by a factor of eight as compared with the vertical component.

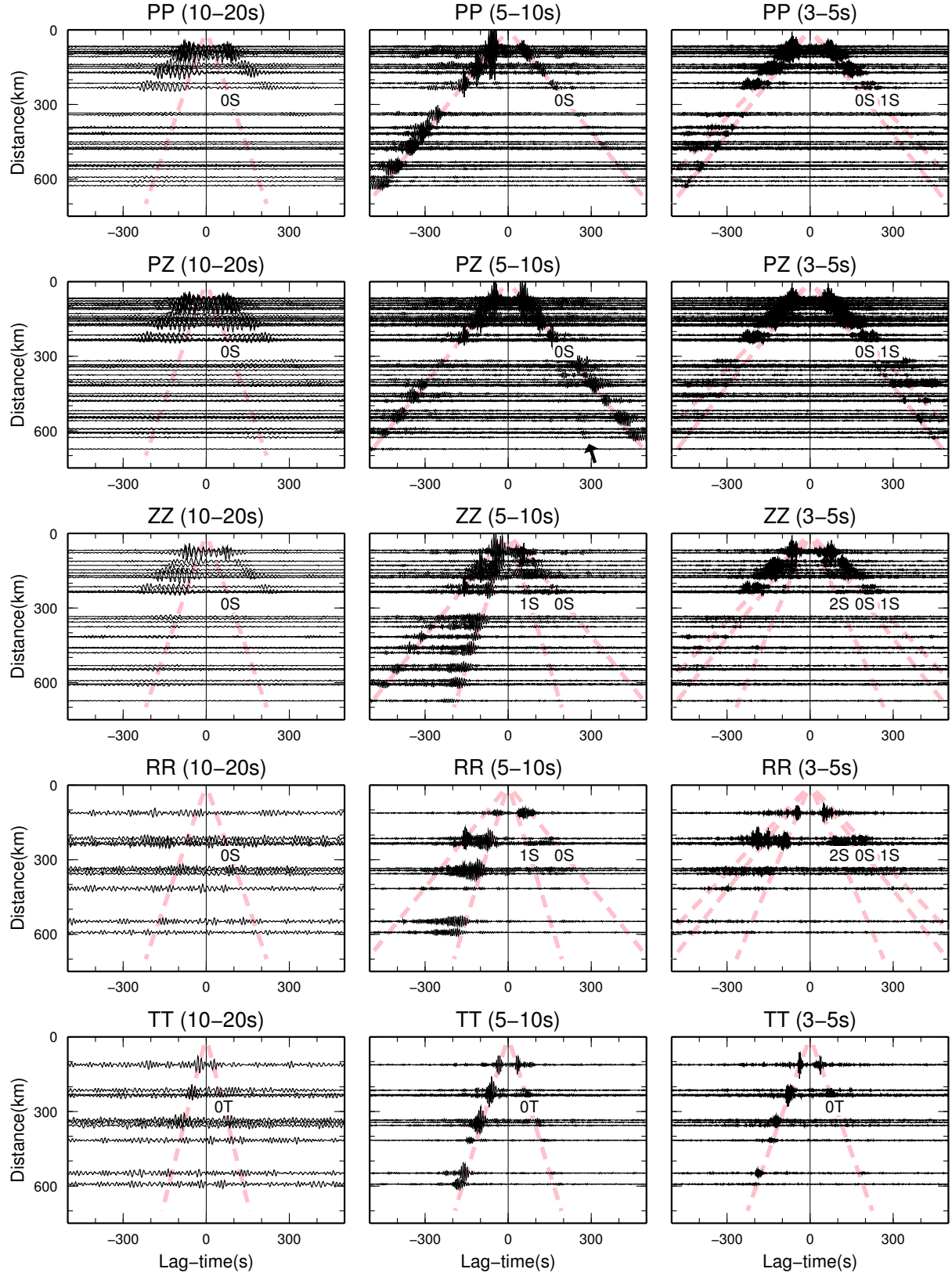


Figure 3.11: Same as Fig. 3.7, but for the SW Shatsky region. The amplitude of the two horizontal components (10–20 s) is exaggerated by a factor of ten as compared with the vertical component. Arrow in PZ component shows unknown phase.

day. Figure 3.12b shows the time shifts, $\Delta\tau$, that maximize cross-correlation coefficients between five-day CCFs and the whole-year CCFs for PP, PZ and ZZ components with a time-window from -300 s to 300 s. For pairs of stations in the western array, the time shift varies with day for pairs including station 4, but there is no discernible variation from zero for other pairs of stations (Figure 3.12b). For pairs of stations in the eastern array, the time shift varies with day for pairs including station 12, but is zero for other pairs of stations (Figure 3.12c). I fitted the temporal change by a linear function of time for station 12. On the other hand, the temporal change for station 4 is not linear. I fitted the change by an empirical summation of a linear function and an exponential function with time. A low-order polynomial function works equally well. The CCFs between all the pairs of stations are then re-calculated by assuming the clock delay at the start of the observation period to be zero. This assumption is valid with an accuracy of ~ 1 ms because the clock at the start of the observation is fixed to the time estimated by using the GPS.

The apparent time shift due to inhomogeneous source distribution cannot be neglected especially when the interstation distances are comparable to the wavelength (*Yao and van der Hilst, 2009*). The absence of a temporal change for pairs without station 4 or 12, however, suggests that the effect of seasonal variation of source distribution to the estimation of clock delay is small. If the temporal changes of time shifts for the pairs including station 4 or 12 are caused by seasonal variation of source distribution, the same pattern should appear in the time shifts for the pairs without station 4 or 12.

In the second step, I estimated the response of each DPG. In previous study, *Araki and Sugioka (2009)* estimated the response by comparing the DPG record with a record of a quartz pressure gauge. In this study, I estimated the response from CCFs between the DPG record and the vertical-component record of the OBS deployed in the same station. If both DPG and OBS records only contain background surface-waves, the phase of the CCF, $\Delta\phi$, reflects the instrumental response of DPG because the phase of DPG (phase of stress at the bottom of the oceanic layer) is as same as the phase of the vertical component of OBS (phase of displacement at the top of the solid part of the earth) for surface waves. It can be explained by regarding that the surface wave is the summation of normal modes. For each normal mode, the phase of stress and displacement synchronize each other from the oceanic layer to the solid part of the earth because the stress becomes zero when the displacement is zero. The synchronization is also evident from the absence of complex number in the formulation of normal mode (e.g., *Takeuchi and Saito, 1972*). The surface wave, the summation of normal modes, also produce the same phase for both the stress and the displacement. Figure 3.13a shows the phase for all pairs of stations. At frequency of 0.1-0.3 Hz, the curves are stable and have slight offsets from zero, which seem to reflect the instrumental responses of the DPGs. On the other hand, the curves are unstable at frequencies higher than 0.3 Hz, where the wavelength is shorter than the water-depth and reverberation of body waves between the seafloor and the sea surface is possible. I therefore fitted the phase curves at frequencies

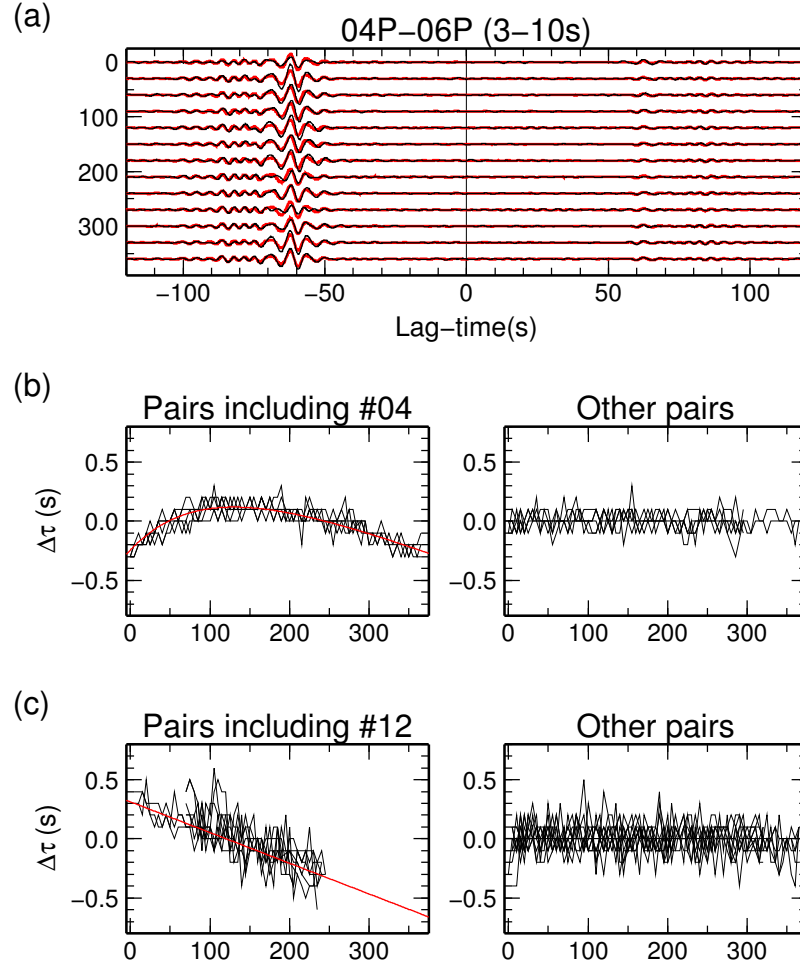


Figure 3.12: (a) CCFs calculated from five-day records (black) and the whole-year records (red) as a function of day from the start of observation. (b, c) Time shifts between five-day and the whole-year CCFs as a function of the day for pairs of stations in western and eastern arrays, respectively. Red lines show the fitting lines.

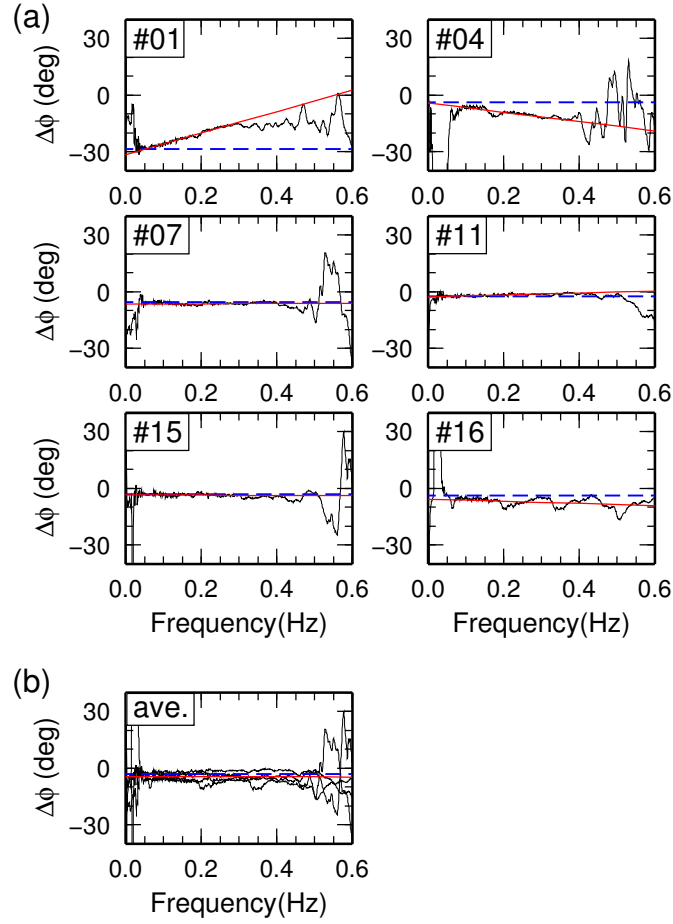


Figure 3.13: (a) Phase difference between DPG and vertical component of OBS as a function of frequency. Red solid lines show the linear fitting line, whereas blue dashed lines show the constant value obtained from teleseismic waveforms at periods of 20-60 s. (b) Same as (a) but for the average of four stations (7, 11, 15 and 16), which is used for DPGs station without OBS records (station 6, 10 and 13).

of 0.1-0.3 Hz for obtaining the instrument response of DPGs. Figure 3.13 shows the fitting line and the constant phase delay obtained by cross-correlating the DPG and the vertical records of teleseismic Rayleigh waves at the frequency range of 0.016-0.05 Hz (periods of 20-60 s). For the DPG stations without any working OBS (6, 10 and 13), I assume that the response is given by the average of the responses for four stations (7, 11, 15 and 16), which give similar responses (Figure 3.13b).

In the third step, I evaluated the effectiveness of the response correction from the time symmetry of CCFs between different stations. I applied band-pass filters with a width of 0.05 Hz for each CCFs, and measured the time shifts that maximize the cross-correlation coefficients between positive and negative lag time of each CCFs. The time shift becomes zero if the CCF is time symmetric and becomes $2\Delta\tau'$ if the clock of one station delays by $\Delta\tau'$ or the phase of one station delays $2\pi\Delta\tau'/T$, where T is period. The half amplitudes of

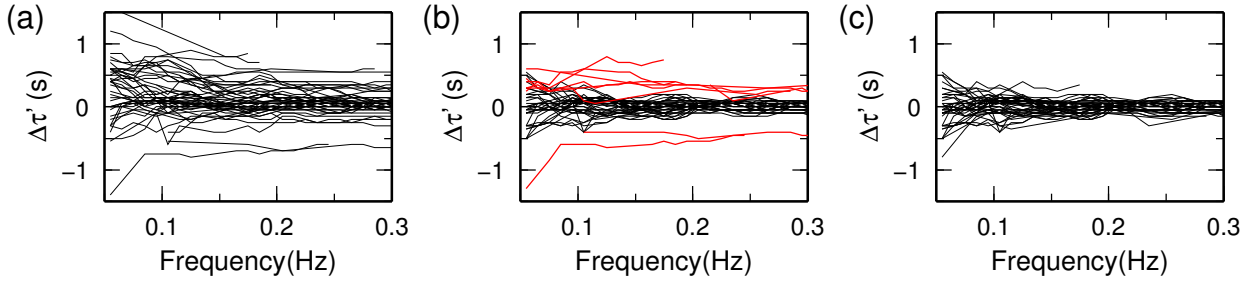


Figure 3.14: Half the time-shifts needed to obtain time-symmetric CCFs for each PP, PZ and ZZ component CCFs as a function of frequency (a) after the correction of clock delays with time and before the correction of DPG responses, (b) after the correction of DPG responses, and (c) after the corrections of DPG responses and the timing delay of 0.5 s at station 8 and 12. Red lines in (b) show the pairs including station 8 or 12.

time shifts are non-zero before the correction of DPG responses (Figure 3.14a), but become smaller than 0.2 s after the correction of DPG responses even for the DPG station without a corresponding OBS (Figure 3.14b). This result indicates that the assumed response for DPG without an OBS is valid with the uncertainty smaller than 0.2 s. Time shifts of about 0.5 s, however, still exist for the pairs including stations 8 and 12 (red lines in Figure 3.14b). I concluded that these time shifts are due to recording systems such as the FIR filter because these two stations were operated by a different institutions recording at a different sampling rate on a different recording system, and corrected the timing of these stations by 0.5 s. Figure 3.14c shows the time shifts after the DPG responses and the timing of 0.5 s were corrected. The amplitudes of time shifts are almost all smaller than 0.2 s, and indicate that the phase and timing of records are corrected with uncertainties smaller than 0.2 s.

The unknown clock delays also existed for two other records: station 2 in the NW Shatsky region deployed by the first observation cruise of Noman project, and station 20 in the SE Shatsky region deployed by the second observation cruise of Noman project. For the station 2, the drift correction was impossible probably due to trouble in recording system after the end of seismic record in 2011 and before the recovery in 2012. The drift of clock was, therefore, estimated from the differential arrival times of teleseismic P-waves between the station 2 and nearby stations (stations 3–5; Fig. 2.4) with an accuracy of ~ 0.7 s by *Isse et al.* (accepted). After the drift correction, I re-estimated the clock drift from the temporal change of CCFs as shown in Figure 3.15. The linear trend was used for the clock correction by assuming that the delay of clock is zero at the start of observation, where the time is fixed to that estimated by using GPS. For the station 20, the trouble in recording system occurred just after the installation. I estimated the clock drift from the temporal change of CCFs between the station 20 and nearby stations (stations 18 and 21; Fig. 2.4). The linear trend was used for the clock correction by assuming that the delay of clock is zero at the

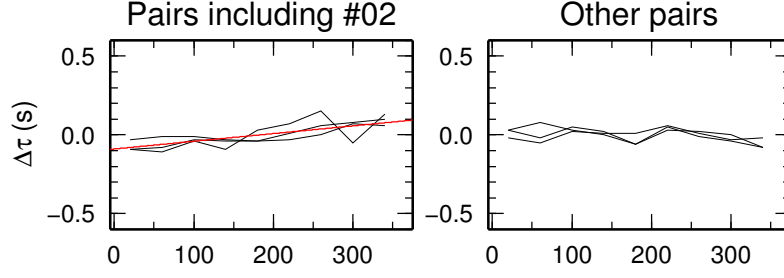


Figure 3.15: Time shifts between 40-day and the whole-year CCFs as a function of day from the start of observation for the first year of observation period for the NW Shatsky region. The drift estimated from teleseismic P-waves by *Isse et al.* (accepted) have already applied.

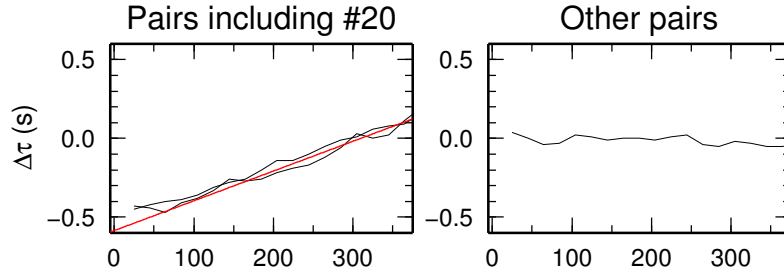


Figure 3.16: Time shifts between 40-day and the 1.5-year CCFs as a function of day from the start of observation for the SE Shatsky region.

end of observation, where the time is fixed to that estimated by using GPS. The estimation error of timing is less than 0.1 s as indicated by the deviation of measurements from the fitting in Figures 3.15–3.16.

3.3.4 Measurement of Average Phase Velocities

The present section describes the methods to obtain average phase velocities and average amplitudes of multi-mode surface waves. The theoretical cross-spectra follow the formulation of spatial autocorrelation method by *Aki* (1957). Four modes of surface waves are considered: 0S, 1S, 2S and 0T modes. The average phase velocities and average amplitudes of each mode beneath the array can be obtained by fitting the synthetic CCFs to the observed CCFs under the assumption of a constant phase velocity and amplitude at each mode for all pairs of stations. The model parameters are phase velocities (c_m) and amplitudes (a_m^{kl}) of each modes (m) in each component (k, l) at each frequency ($f = \omega/2\pi$). According to the equation by *Aki* (1957), the synthetic cross-spectra, $S_{ij}''^{kl}$, are given by,

$$S_{ij}''^{PP} = a_{0S}^{PP} J_0 \left(\frac{\omega d_{ij}}{c_{0S}} \right) + a_{1S}^{PP} J_0 \left(\frac{\omega d_{ij}}{c_{1S}} \right), \quad (3.7)$$

$$S_{ij}''^{PZ} = a_{0S}^{PZ} J_0 \left(\frac{\omega d_{ij}}{c_{0S}} \right) + a_{1S}^{PZ} J_0 \left(\frac{\omega d_{ij}}{c_{1S}} \right), \quad (3.8)$$

$$S_{ij}''^{ZZ} = a_{0S}^{ZZ} J_0 \left(\frac{\omega d_{ij}}{c_{0S}} \right) + a_{1S}^{ZZ} J_0 \left(\frac{\omega d_{ij}}{c_{1S}} \right) + a_{2S}^{ZZ} J_0 \left(\frac{\omega d_{ij}}{c_{2S}} \right), \quad (3.9)$$

$$S_{ij}''^{RR} = a_{0S}^{RR} J_{0-2} \left(\frac{\omega d_{ij}}{c_{0S}} \right) + a_{1S}^{RR} J_{0-2} \left(\frac{\omega d_{ij}}{c_{1S}} \right) + a_{2S}^{RR} J_{0-2} \left(\frac{\omega d_{ij}}{c_{2S}} \right) \\ + a_{0T}^{TT} J_{0+2} \left(\frac{\omega d_{ij}}{c_{0T}} \right), \quad (3.10)$$

$$S_{ij}''^{TT} = a_{0S}^{RR} J_{0+2} \left(\frac{\omega d_{ij}}{c_{0S}} \right) + a_{1S}^{RR} J_{0+2} \left(\frac{\omega d_{ij}}{c_{1S}} \right) + a_{2S}^{RR} J_{0+2} \left(\frac{\omega d_{ij}}{c_{2S}} \right) \\ + a_{0T}^{TT} J_{0-2} \left(\frac{\omega d_{ij}}{c_{0T}} \right), \quad (3.11)$$

where d_{ij} is the distance between the i th and the j th stations, J_n is the n th Bessel function of the first kind, $J_{0-2}(x) = J_0(x) - J_2(x)$, and $J_{0+2}(x) = J_0(x) + J_2(x)$.

Previous studies have measured the phase velocities of each mode of surface waves by isolating each mode by applying group-velocity filters (e.g., *Harmon et al.*, 2007; *Yao et al.*, 2011; *Takeo et al.*, 2013). The example of phase-velocity measurement by fitting the Bessel function is shown by *Takeo et al.* (2013). The group velocities of ocean-mode Rayleigh waves, however, strongly depend on the mode, frequency and the depth of the ocean as shown in Figure 3.1, which causes difficulty of choosing appropriate group-velocity filter especially for the interstation distance closed to the wavelength.

I, therefore, fitted the complete synthetic cross-spectra, $S_{ij}''^{kl}$ to the real components of observed cross-spectra, $\Re_e(S_{ij}^{kl})$, by the waveform fitting in this study. By using the method, compared to the fitting procedure with the assumption of single mode described above, phase velocities of multi-mode surface waves can be obtained without applying group-velocity filters. I express phase velocities of mode m as a summation of B-spline functions, $g_m^n(f)$,

$$c_m(f) = \sum_n p_m^n g_m^n(f), \quad (3.12)$$

and determine the values of coefficients, p_m^n . I estimated the optimal phase velocity that minimize the mean square misfit between observed and synthetic cross-spectra,

$$L(\omega, \mathbf{c}) = \sum_{kl} \frac{\sum_{ij} \langle W_{ij}^{kl}(\omega) \rangle^2 [\Re_e(S_{ij}^{kl}(\omega)) - S_{ij}''^{kl}(\omega, \mathbf{c}, \mathbf{a})]^2}{\sum_{ij} \langle W_{ij}^{kl}(\omega) \rangle^2 [\Re_e(S_{ij}^{kl}(\omega))]^2}, \quad (3.13)$$

by the simulated annealing method (*Ingber*, 1989) (see Appendix C for detail): I assumed 40,000 combinations of p_m^n , calculated the optimal amplitude of each mode and each component, a_m^{kl} , for each frequency for each assumed combination of p_m^n by the least squares method, and searched for the minimum of the misfit. For PP, PZ and ZZ components of the SW Shatsky region, pairs with interstation distance shorter than 250 km are used in the

essence of reducing the number of CCFs and avoiding the unknown phase in the PZ component (shown by an arrow in Figure 3.11). The above equation (3.13) can also be written as:

$$L(\omega, \mathbf{c}) = \sum_{kl} \frac{\sum_{ij} [\Re_e(S'_{ij}{}^{kl}(\omega)) - \langle W_{ij}^{kl}(\omega) \rangle S''_{ij}{}^{kl}(\omega, \mathbf{c}, \mathbf{a})]^2}{\sum_{ij} [\Re_e(S'_{ij}{}^{kl}(\omega))]^2}, \quad (3.14)$$

by using another definition of cross spectrum, $S'_{ij}{}^{kl} = \langle W_{ij}^{kl} \rangle S_{ij}^{kl}$, called normalization or the spectrum whitening and used in previous studies (§3.3.1). To fit the cross spectrum (S_{ij}^{kl}) to the synthetic spectrum ($S''_{ij}{}^{kl}$) with the weighting by $\langle W_{ij}^{kl} \rangle^2$ is equivalent to fit the cross spectrum ($S'_{ij}{}^{kl}$) to the modified synthetic spectrum ($\langle W_{ij}^{kl} \rangle S''_{ij}{}^{kl}$) without the weighting term.

Figure 3.17 shows the assumed B-spline functions, the obtained phase velocities, c_m and amplitudes, a_m^{kl} . The measurement error is estimated using the bootstrap method (Efron, 1979) (see Appendix B for detail) where 100 dispersion curves ($c_m^1(\omega), c_m^2(\omega), \dots, c_m^{100}(\omega)$) were estimated for each of 100 bootstrap samples. A bootstrap sample is the aggregate of station pairs randomly selected from all station pairs allowing for overlaps. For each component, the number of CCFs in each bootstrap sample is the same as the number of all CCFs. I defined the error of phase-velocity measurement ($\Delta c_m(\omega)$) as one standard deviation of 100 dispersion curves. Figure 3.18 shows the optimal phase velocity curve the error range ($\bar{c}_m(\omega) \pm \Delta c_m(\omega)$), where $\bar{c}_m(\omega) = \sum_n c_m^n(\omega)/100$ is the average value taken from the 100 dispersion curves obtained using the bootstrap method. The bootstrap average (\bar{c}) deviates from the estimated value by using all the measurements (c_m) probably because one or two anomalous measurements biases the measurement, c_m . I, therefore, define the uncertainty range by $\bar{c}_m \pm \Delta c_m$ instead of $c_m \pm \Delta c_m$ to avoid the bias.

Figure 3.19 shows the synthetic and observed CCFs for the SW Shatsky region. Phases are matched very well and three modes of Rayleigh waves are fitted even at short distances. Although the amplitudes are not matched well especially for the ocean-mode Rayleigh waves at short periods, it does not affect the later estimation of structure and anisotropy in the solid earth based on phase velocities of solid-mode Rayleigh waves.

In the measurement procedure, I assumed a homogeneous source distribution and structure, which may induce bias to the average phase velocities. The CCFs shown in Fig. 3.7–3.11 indicate that the source distribution is anisotropic. The larger amplitude of the negative lag time as compared with that of positive lag time indicates that the amplitude of the source coming from the northwest, west, or southwest is larger than those coming from the opposite directions. The effect of heterogeneous source distribution can be evaluated by expanding the azimuthal dependence of sources by the Fourier series (Cox, 1973; Weaver *et al.*, 2009). I removed the effect of Fourier components with odd orders by only using the real component of each cross spectrum (Ekström *et al.*, 2009; Weaver *et al.*, 2009). I minimized the effect of Fourier components with even orders by using station pairs with different azimuths

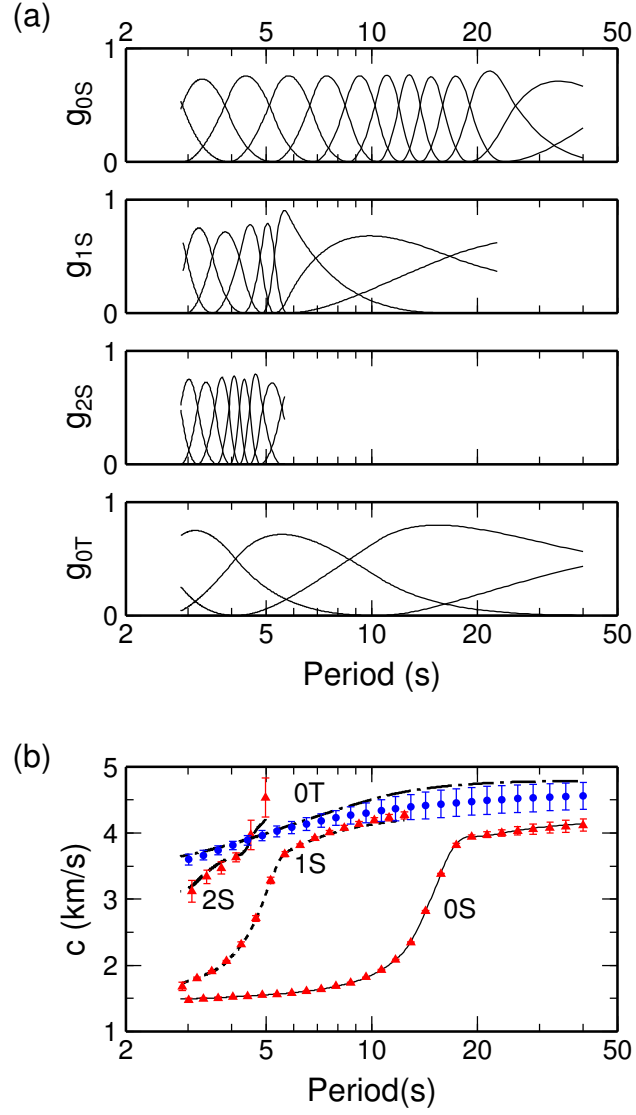


Figure 3.17: (a) B-spline functions of four modes of surface waves for the SW Shatsky region. (b) Curves shows the measured phase velocities, c_m . The red triangles and blue circles with error bars shows the uncertainty range estimated by the bootstrap method, $\bar{c}_m \pm \Delta c_m$, for the Rayleigh and Love waves, respectively.

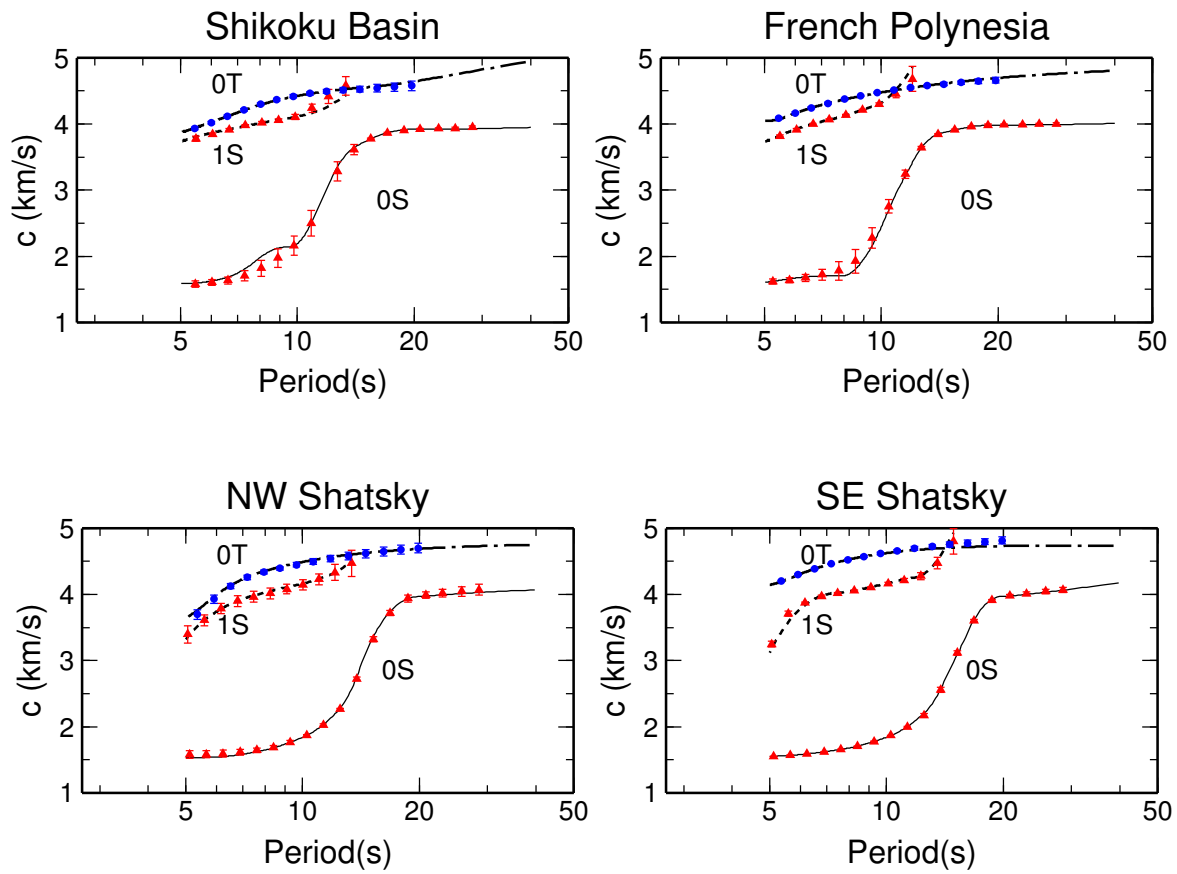


Figure 3.18: Same as Figure 3.17b, but for four regions other than the SW Shatsky region.

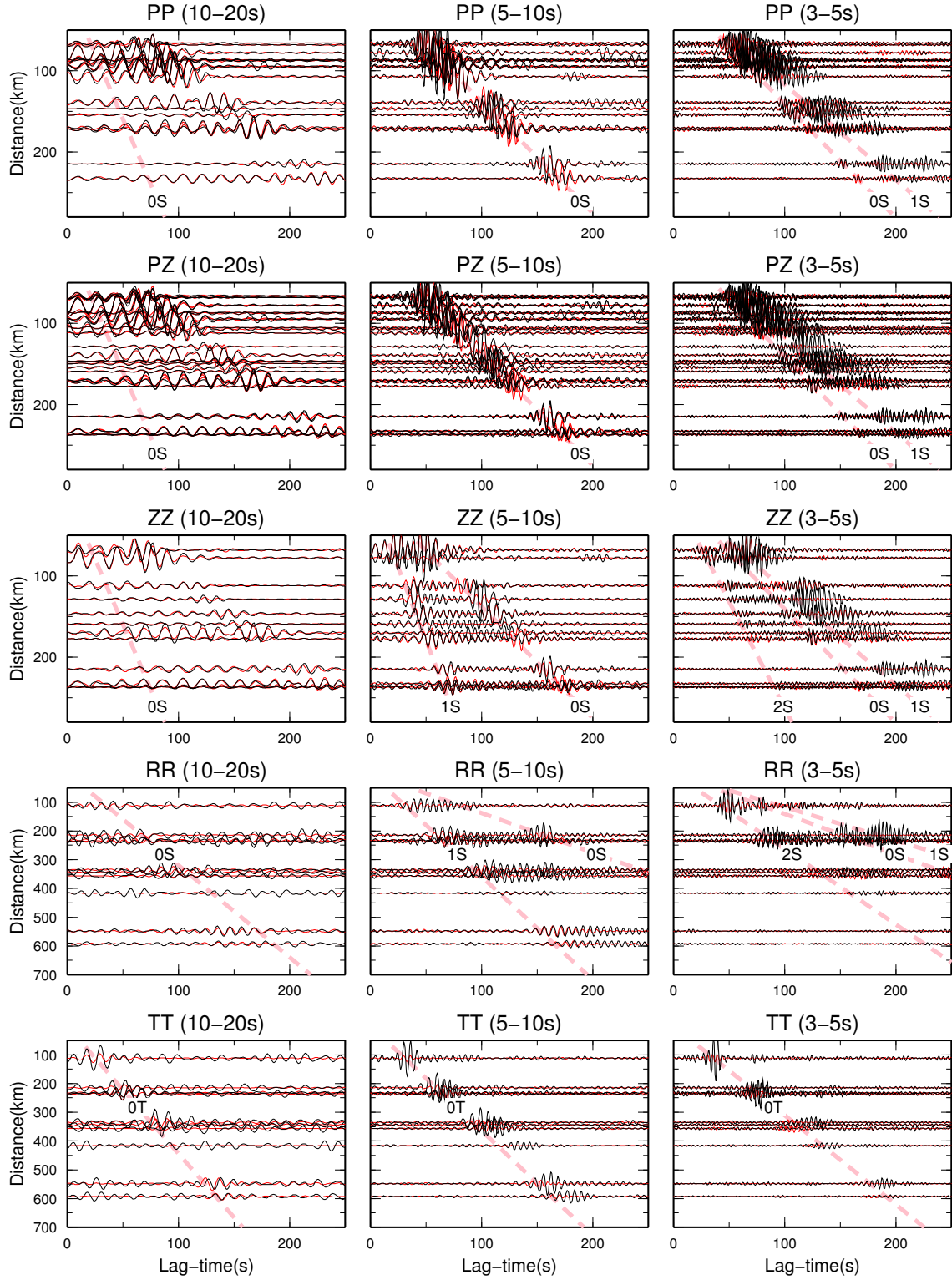


Figure 3.19: An example of fitting between time-symmetric components of observed CCFs (black) and synthetic CCFs (red) for the SW Shatsky region. Dashed pink lines show the arrival of each mode at a typical period. Although the gradients of pink lines for RR component are same as those for PP, PZ and ZZ components, they may seem different due to the difference between distance coverages.

Table 3.1: Summary of the period range (s) of average phase velocities measured in this study.

Mode	Shikoku Basin	French Polynesia	NW Shatsky	SE Shatsky	SW Shatsky
Ambient Noise Analysis					
0S	5–40	5–40	5–40	5–40	3–40
1S	5–14	5–14	5–15	5–15	3–12
2S	-	-	-	-	3–5
0T	5–20	5–20	5–20	5–2	3–40
Teleseismic Event Analysis					
0S'	30–110	30–100	30–100	30–100	-
0T'	30–60	30–100	50–80	50–80	-

(Nakahara, 2006). In addition, our estimation of measurement error includes the uncertainty related to the lateral heterogeneity within the array because each CCF mainly reflects structure between the stations and I estimated the error by randomly selecting CCFs. If the structure and the source of ambient noise were laterally homogeneous, the measurement error only reflects the effect of noise in CCFs and becomes smaller than the values estimated in this study.

The period range of precise phase velocity measurements is limited to 3–40 s for Rayleigh waves and 3–20 s for Love waves as summarized in Table 3.1. At shorter periods, the signal may be difficult to extract probably due to high apparent attenuation due to small lateral heterogeneity in the crust. At longer periods, the signal-to-noise ratio of CCFs is low due to high noise levels of BBOBSs (Fig. 2.3), especially for the horizontal components, which causes the difficulty of the analysis of Love waves at periods longer than 20 s. The Rayleigh waves at periods longer than 30 s is difficult because of the long wavelength equivalent to the interstation distances. At long periods, therefore, surface waves originating from large teleseismic events are useful.

3.3.5 Measurement of Phase Velocity Anomalies and Corrections

The estimation of azimuthal anisotropy requires the measurements of phase-velocity anomalies for each pair of stations, which give phase-velocity anomalies for various azimuths of surface-wave propagations. I measured phase velocity anomalies and amplitude anomalies of 0S and 1S modes at periods of 5–35 s by fitting the synthetic CCF to the observed CCF for each pair of stations and each band-pass filter. The frequency range is from $0.9f_0$ to

1.1 f_0 , where f_0 is the mean frequency. The synthetic cross-spectra for analyzing 0S mode is,

$$S_{ij}'''^{kl} = (1 + \zeta_{ij}^{kl})a_{0S}^{kl}J_0\left(\frac{\omega d_{ij}}{(1 + \gamma_{ij}^{kl})c_{0S}}\right) + a_{1S}^{kl}J_0\left(\frac{\omega d_{ij}}{c_{1S}}\right) + a_{2S}^{kl}J_0\left(\frac{\omega d_{ij}}{c_{2S}}\right), \quad (3.15)$$

and that for 1S mode is,

$$S_{ij}'''^{kl} = a_{0S}^{kl}J_0\left(\frac{\omega d_{ij}}{c_{0S}}\right) + (1 + \zeta_{ij}^{kl})a_{1S}^{kl}J_0\left(\frac{\omega d_{ij}}{(1 + \gamma_{ij}^{kl})c_{1S}}\right) + a_{2S}^{kl}J_0\left(\frac{\omega d_{ij}}{c_{2S}}\right), \quad (3.16)$$

where ζ_{ij}^{kl} and γ_{ij}^{kl} are the amplitude anomaly and phase-velocity anomaly, respectively. The synthetic and observed CCFs were obtained by applying band-pass filters to cross-spectra in the frequency domain, and by calculating inverse Fourier transforms. For applying group velocity window to isolate each mode, the envelope of synthetic waveform of 0S and 1S modes was obtained by the Hilbert transformation. The optimal values of ζ_{ij}^{kl} and γ_{ij}^{kl} are then searched. For several pairs of stations, more than two components exist, and give different phase-velocity anomalies. The following discussion uses the value with the highest signal-to-noise ratio, R_{SN} , where the signal amplitude is obtained from the root mean square of CCFs in the time window including the analyzing mode, and the noise amplitude is obtained from the time window without the mode.

Figure 3.20a shows the examples of phase-velocity anomalies for the SW Shatsky region. The large deviations occur at periods of ~ 10 -20 s for 0S mode, where the transition from the ocean-mode to solid-mode occurs, and seem to reflect the water-depth variations. I estimated the effect of water depth, γ_w , by modifying the 1D isotropic model of each region (will be shown in Section 4) to various water depths, and by calculating phase velocities corresponding to the models. Figure 3.20b shows the correction value with respect to the water-depth of 5.9 km as a function of period and water-depth, which is the largest at periods of ~ 10 -15 s. After calculating the correction value as a function of longitude and latitude based on the sea topography by ETOPO 2.0, the correction terms for each pair of stations was estimated by taking the average within the area where the distance from the great-circle path between pairs of stations is less than 10 km. Figure 3.20c shows the phase-velocity anomalies after the correction, $\gamma - \gamma_w$. The deviation is much smaller than before the correction (Figure 3.20a) especially at periods of 10-17 s for 0S mode. The same corrections were applied to other regions based on the one-dimensional radially anisotropic model for each region shown in Section 4.

The effect of inhomogeneous source distribution also needs to be corrected. The former analyses in this study are based on the theoretical cross-spectrum with the assumption of homogeneous source distribution obtained by *Aki* (1957). *Cox* (1973) derived the theoretical cross-spectrum for the case of inhomogeneous source distribution, which is given by,

$$B(\phi) = B_0 + \sum_n B_n \cos[n(\phi - \phi_n)], \quad (3.17)$$

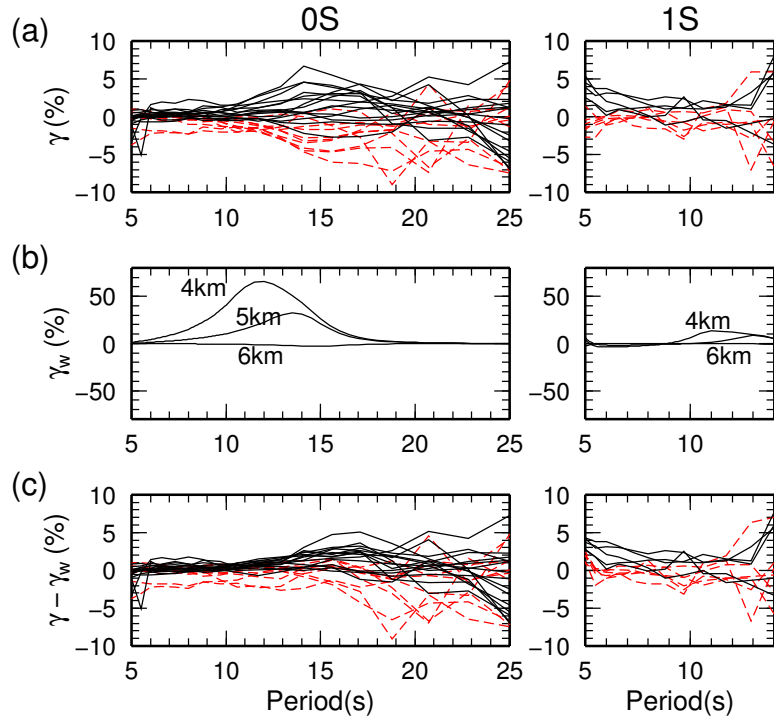


Figure 3.20: (a) Phase-velocity anomalies as a function of period for the SW Shatsky region. Solid black lines and dashed red lines correspond to pairs in eastern and western arrays, respectively. (b) The perturbations of phase velocities with respect to the water-depth of 5.9 km. (c) Phase-velocity anomalies after the correction of water-depth.

as a function of back-azimuth, ϕ . The theoretical cross spectrum for the vertical component is then given by,

$$S(\phi) = B_0 J_0 \left(\frac{\omega d}{c} \right) + 2 \sum_n i^n B_n \cos [n(\phi - \phi_n)] J_n \left(\frac{\omega d}{c} \right), \quad (3.18)$$

where ϕ is the station-to-station azimuth, the azimuth of the great circle between the pair of stations. The symbol i here remarks the imaginary unit. The odd-order components of inhomogeneous source distribution (B_1, B_3, B_5, \dots), therefore, only causes imaginary term. We can avoid the effects of odd-order components by only using real components of obtained cross-spectra. The next step is to evaluate the effects of even-order components of inhomogeneous source distribution (B_2, B_4, B_6, \dots).

Weaver et al. (2009) recently estimated the effects of inhomogeneous source distribution to the phase-velocity measurement. They focused on a method for phase-velocity measurement, the zero-crossing method by *Ekström et al.* (2009). By assuming the source distribution same as equation (3.17), they calculated the change in the zero-crossing frequency, and the change in travel-time anomaly caused by the second term in equation (3.18). The apparent phase-velocity anomaly is,

$$\gamma_s = \frac{1}{2\omega^2 \tau^2} \frac{B''(\phi)}{B(\phi)} = \frac{1}{8\pi^2} \left(\frac{\lambda'}{d} \right)^2 \frac{B''(\phi)}{B(\phi)} \sim \frac{1}{8\pi^2} \left(\frac{\lambda'}{d} \right)^2 \sum_n n^2 \frac{B_n}{B_0} \cos [n(\phi - \phi_n)], \quad (3.19)$$

where $\lambda' = u/f$ is almost equivalent to the wavelength $\lambda = c/f$. This anomaly cannot be neglected when the interstation distance is comparable or shorter than the wavelength, or when the source distribution is highly inhomogeneous.

Figures 3.21-3.23 show the measured amplitude anomalies, ζ_{ij}^{kl} , as a function of station-to-station azimuth. The fitting curves are obtained by considering B_0 , B_2 and B_4 terms in equation (3.17), i.e., $B = B_0 + B_2 \cos 2(\phi - \phi_2) + B_4 \cos 4(\phi - \phi_4)$. The amplitude anomalies for the SW Shatsky region cannot be estimated because of the unknown amplitude responses of DPGs. Figure 3.24 shows the intensity of source heterogeneity represented by B_2/B_0 and B_4/B_0 . The typical values are $B_2/B_0=0.3$ and $B_4/B_0=0.15$ for the 0S mode at periods of 15–25 s, and $B_2/B_0=0.5$ and $B_4/B_0=0.2$ for the 1S mode at periods of 5–15 s. The maximum effects of source heterogeneity to the phase-velocity anomalies are, thus, $\gamma_s \sim (\lambda'/d)^2 \times 5\%$ for 0S mode, and $\gamma_s \sim (\lambda'/d)^2 \times 6\%$ for 1S mode from equation (3.19). For the four regions except for the SW Shatsky, the typical value of γ_s is smaller than 1% because the interstation distances (> 100 – 200 km) are longer than the twice of the wavelength at periods shorter than ~ 20 s. For several pairs in the SW Shatsky region, γ_s may exceed 1% because of shorter interstation distances (50–100 km), but cannot be corrected because of the unknown amplitude responses of DPGs.

Figures 3.25-3.27 show the phase-velocity anomalies after the correction of water-depth and inhomogeneous source distribution for regions except for the SW Shatsky region. The values with the signal-to-noise ratio smaller than 3 or the error larger than 2% were discarded,

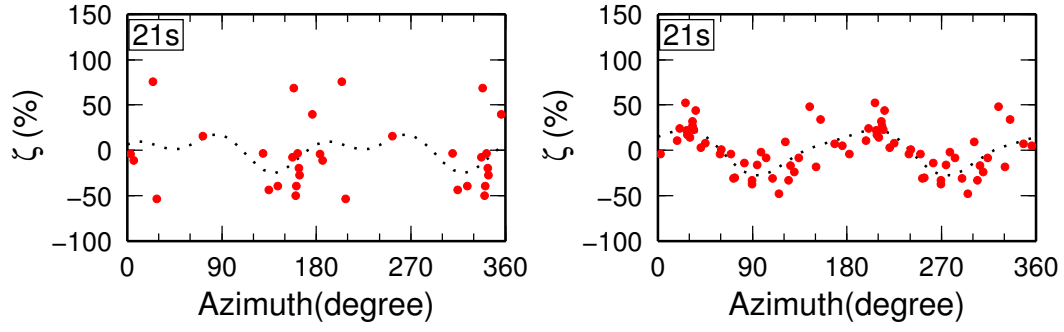


Figure 3.21: Amplitude anomalies of 0S mode for the Shikoku Basin (left) and French Polynesia (right) regions. The dotted curve is the fitting curve.

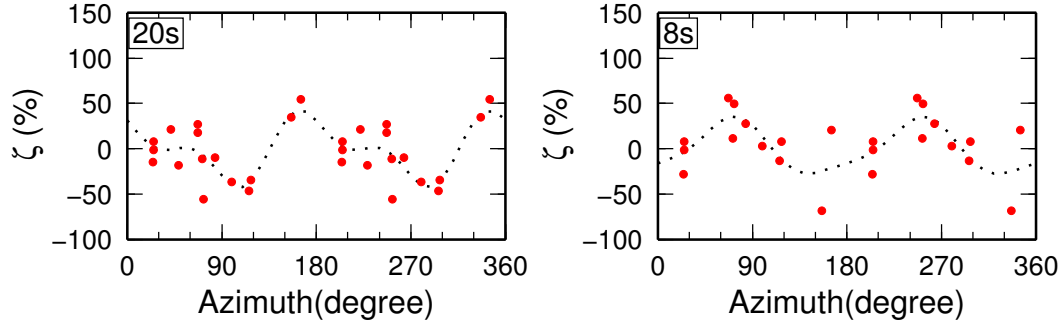


Figure 3.22: Amplitude anomalies of 0S (left) and 1S (right) modes for the NW Shatsky region. The dotted curve is the fitting curve.

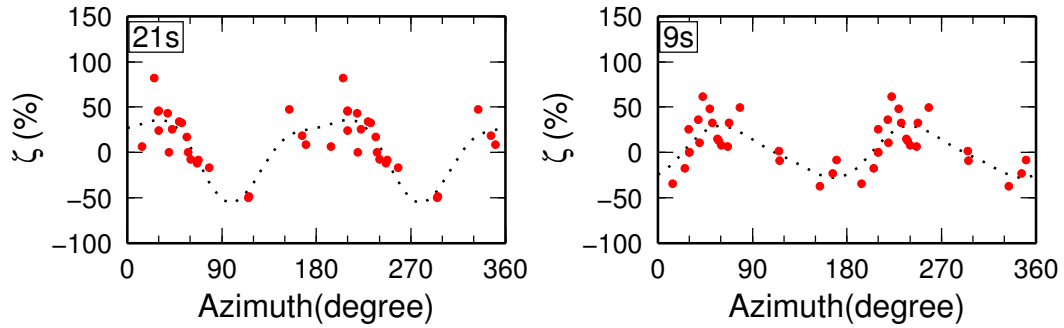


Figure 3.23: Same as Figure 3.22, but for the SE Shatsky region.

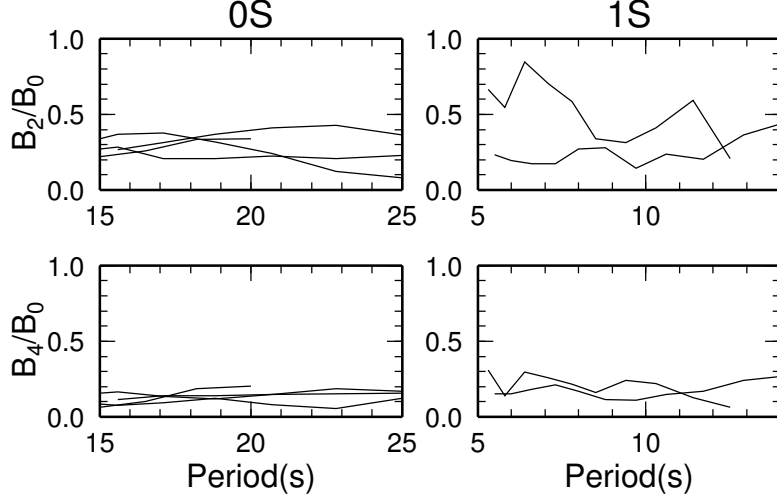


Figure 3.24: The intensity of source heterogeneity represented by B_2/B_0 and B_4/B_0 .

where the errors of phase-velocity anomalies were estimated by considering two factors: signal to noise ratio of each CCF, R_{SN} , and the uncertainty of the clock delay or instrumental response, $\Delta\tau'$ (§3.3.3). The presence of noise in each CCF causes bias to the phase of signal by about $\tan^{-1}(1/(2R_{\text{SN}}))$. The error in the phase-velocity anomaly is then,

$$\Delta\gamma_1 = \tan^{-1}\left(\frac{1}{2R_{\text{SN}}}\right) \times \frac{1}{\omega\tau} = \tan^{-1}\left(\frac{1}{2R_{\text{SN}}}\right) \times \left(\frac{\lambda'}{d}\right), \quad (3.20)$$

where $\tau = d/u$ is the travel time and u is the group velocity of one-dimensional model given in Chapter 4. The value, $\lambda' = u/f$, is almost equivalent to the wavelength, $\lambda = c/f$. The error of the clock and response can similarly be estimated to be,

$$\Delta\gamma_2 = \frac{\Delta\tau'}{\tau}. \quad (3.21)$$

The value of $\Delta\tau'$ is 0.2 s for the SW Shatsky, 0.1 s for the NW and SE Shatsky, and 0 s for the Shikoku Basin and French Polynesia regions (§3.3.3). The total error of the phase-velocity anomaly is $\Delta\gamma = \Delta\gamma_1 + \Delta\gamma_2$.

Figure 3.28 shows the phase-velocity anomalies after the correction of water-depth for the eastern area of SW Shatsky region. I only used the records from the eastern area because the azimuth of magnetic lineation is different for the eastern and western areas and there is only five stations in the western area. The maximum number of measurements for the 1S mode is 6 because the mode is only remarkable in the vertical components of OBSs and only four OBS records were recovered in the eastern array. For using almost all measurements, therefore, the minimum signal-to-noise ratio is set to be 2, whereas the threshold is 3 for 0S mode and for other regions. The estimation of error is also different from other regions. As the source distribution cannot be estimated for this region, the third term is added to the

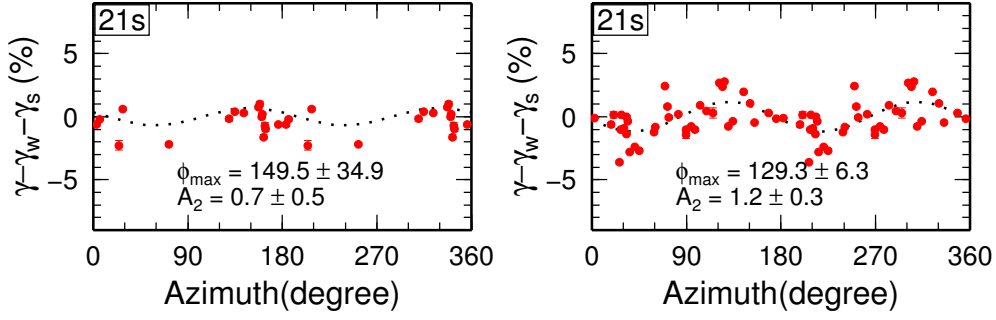


Figure 3.25: Phase-velocity anomalies of 0S mode for the Shikoku Basin (left) and French Polynesia (right) regions. The dotted curve is the fitting curve.

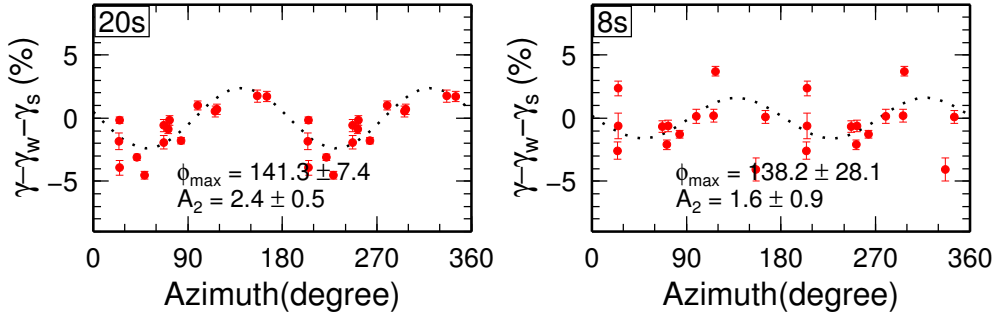


Figure 3.26: Phase-velocity anomalies of 0S (left) and 1S (right) modes for the NW Shatsky region. The dotted curve is the fitting curve.

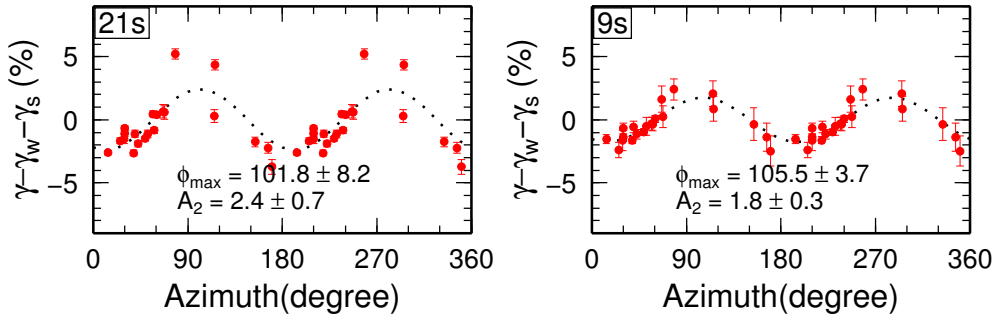


Figure 3.27: Same as Figure 3.26, but for the SE Shatsky region.

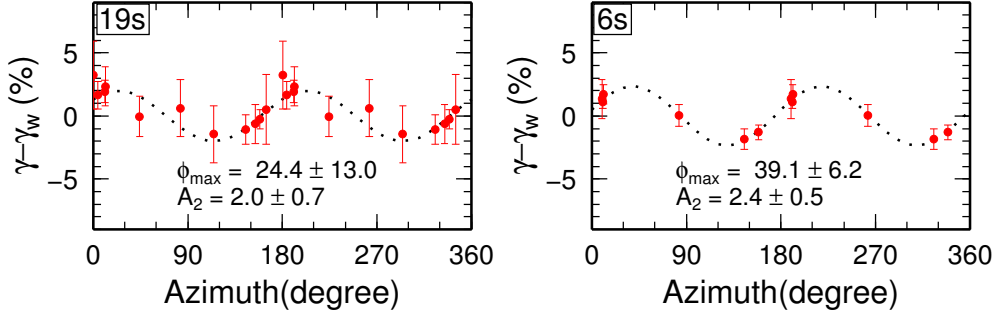


Figure 3.28: Same as Figure 3.26, but for the SW Shatsky region.

errors of phase-velocity anomalies, $\Delta\gamma_3$ defined by,

$$\Delta\gamma_3 = |\gamma_s| \sim \left(\frac{\lambda'}{d}\right)^2 \times 5\%, \quad (3.22)$$

based on the typical source distribution discussed above (Fig. 3.24). The total error of the phase-velocity anomaly is $\Delta\gamma = \Delta\gamma_1 + \Delta\gamma_2 + \Delta\gamma_3$ for this region.

3.3.6 Estimation of Azimuthal Anisotropy

Figures 3.25–3.28 show clear azimuthal dependence of phase-velocity anomalies especially for the 0S mode at NW Shatsky region (Fig. 3.26 left) and the 1S mode at SE Shatsky region (Fig. 3.27 right). The azimuthal dependence seems to be dominated by $\cos 2\phi$ term, and is consistent with the theoretical estimation for the Rayleigh waves (e.g., *Smith and Dahlen, 1973; Montagner and Nataf, 1986*), indicating the presence of azimuthal anisotropy of V_{SV} . The fitting lines by $\gamma = A_2 \cos 2(\phi - \phi_{\max})$ are shown in Figures 3.25–3.28, where A_2 means the half intensity of azimuthal anisotropy, and ϕ_{\max} means the fastest azimuth, the azimuth of maximum velocity. The errors of A_2 and ϕ_{\max} were obtained by the bootstrap method (Appendix B) for four regions except for the SW Shatsky region (Fig. 3.25–3.27). The bootstrap method is difficult to apply to the region because of the small number of station pairs (about ten for the 0S mode, and five for the 1S mode). The error for the SW Shatsky region is, therefore, obtained by adding gaussian noise with a variance of half the uncertainty ($\Delta\gamma/2$) to the measurements, estimating 100 fitting curves, and taking one standard deviation (Fig. 3.28). The fitting by $\cos 2\phi$ seems appropriate especially for Shatsky Rise regions (Fig. 3.26–3.28) compared to the Shikoku Basin (Fig. 3.25 left) and the French Polynesia (Fig. 3.25 right) regions. This difference can be understood by considering the seafloor homogeneity. The sea topography is homogeneous for the Shatsky Rise regions (Fig. 2.1) compared to that for the Shikoku Basin (Fig. 2.3) and the French Polynesia (Fig. 2.2) regions. The crustal and mantle heterogeneities are expected to be stronger in the Shikoku Basin and French Polynesia regions compared to the Shatsky Rise regions. As each phase-velocity anomaly reflects both the azimuthal anisotropy and the lateral heterogeneity,

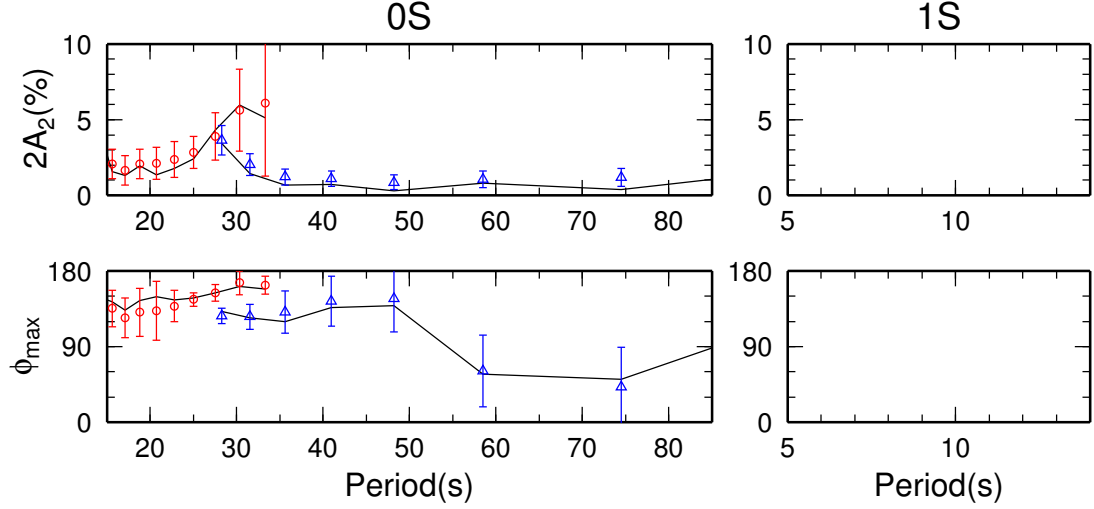


Figure 3.29: The peak-to-peak intensity ($2A_2$) and the fastest direction (ϕ_{\max}) estimated from ambient noise (red circles) and teleseismic surface waves (blue triangle) for the Shikoku Basin region as a function of period. The solid lines show the measurements, whereas the symbols with error bars show the uncertainty range estimated by the bootstrap method.

the variation from the $\cos 2\phi$ fitting for the Shikoku Basin and French Polynesia regions indicate the presence of crustal and mantle heterogeneity beneath these regions.

Figures 3.29–3.33 summarize the peak-to-peak intensity ($2A_2$) and the fastest direction (ϕ_{\max}) as a function of period. The phase-velocity anomalies of the 1S mode could not be analyzed for the Shikoku Basin and French Polynesia regions because of strong 2π ambiguity, i.e., two phase velocities with the difference of $\sim 3\%$ can fit the waveforms similarity because of short wavelength (~ 20 – 40 km) compared to the interstation distances (~ 200 – 600 km) in these regions. The period range of analysis for each mode is summarized in Table 3.2. Figure 3.34 shows an example of phase-velocity anomalies of the ocean-mode Rayleigh wave for the SW region. The anomalies are almost constant for various azimuths, and indicate that no anisotropy or lateral heterogeneity exists for the P-wave velocity in the ocean layer. The depth structure of azimuthal anisotropy will be discussed in Section 5 by using the estimation of azimuthal anisotropy from teleseismic waves at longer periods in addition to the estimation in this section.

3.4 Teleseismic Event Array Analysis

3.4.1 Measurement of Average Phase Velocities

At periods longer than 30 s, the phase velocities were measured by using surface waves derived from teleseismic events with moment magnitudes larger than Mw 5.5, focal depths shallower than 200 km, and great-circle distances greater than 3000 km. Although the effect

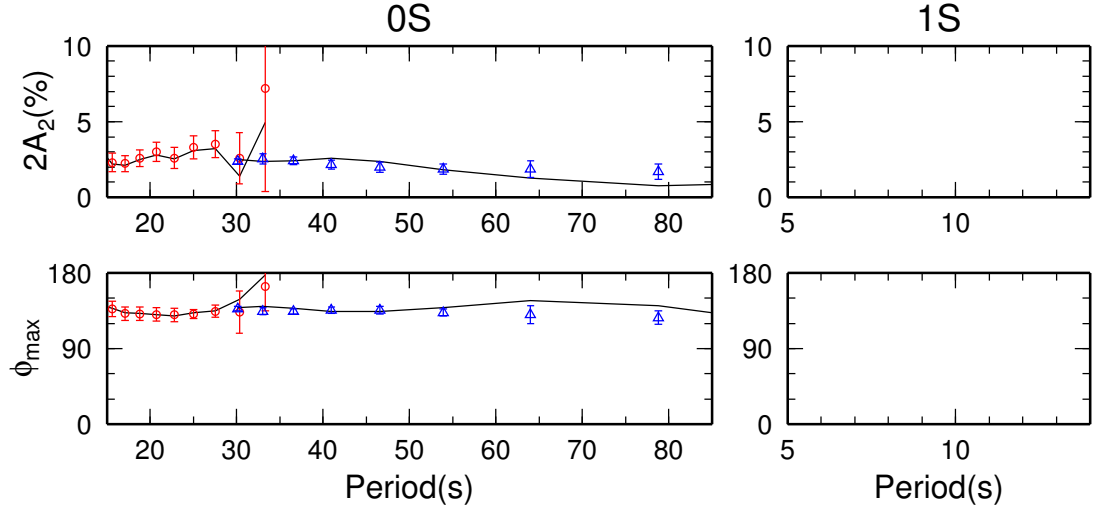


Figure 3.30: Same as Figure 3.29, but for the French Polynesia region.

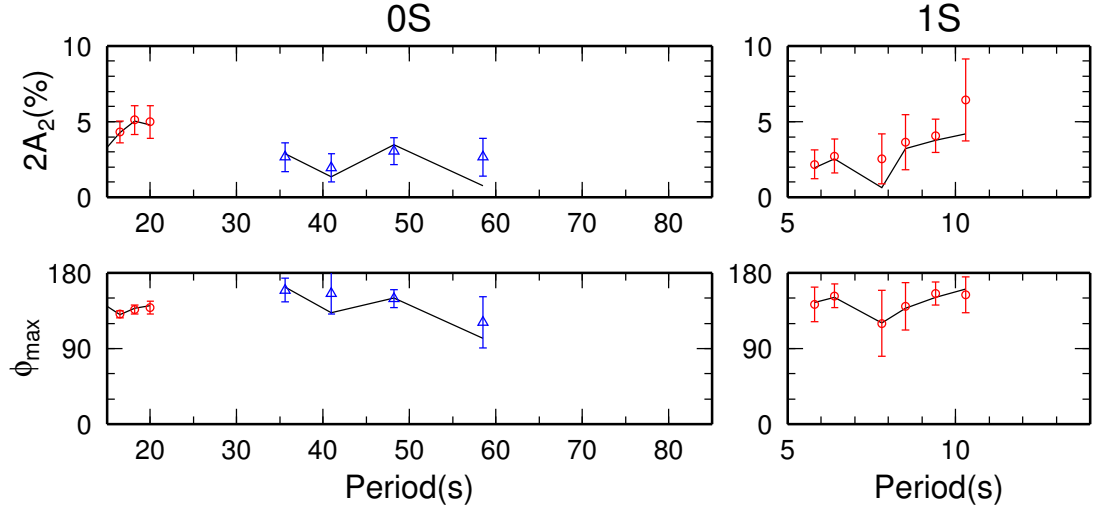


Figure 3.31: Same as Figure 3.29, but for the NW Shatsky region.

Table 3.2: Summary of the period range (s) for the azimuthal anisotropy of phase velocities estimated in this study.

Mode	Shikoku Basin	French Polynesia	NW Shatsky	SE Shatsky	SW Shatsky
Ambient Noise Analysis					
0S	10–35	10–35	10–20	10–30	10–25
1S	-	-	5–10	5–15	5–12
Teleseismic Event Analysis					
0S'	30–100	30–100	35–50	35–60	-

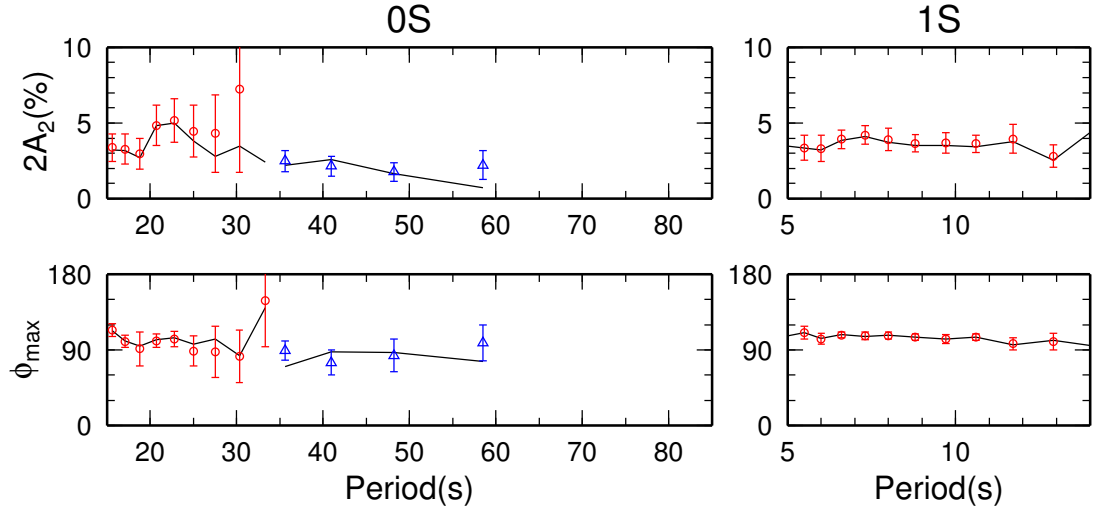


Figure 3.32: Same as Figure 3.29, but for the SE Shatsky region.

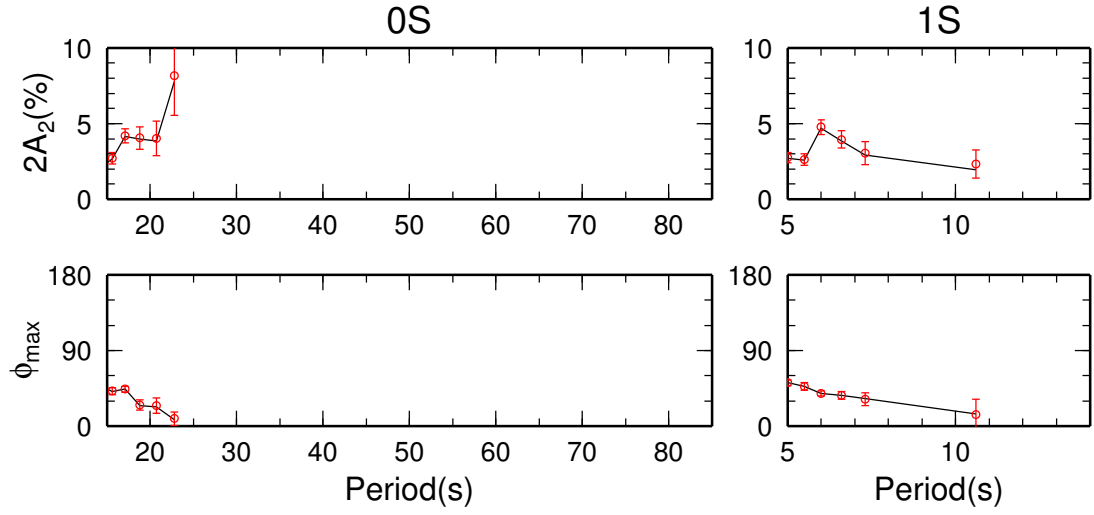


Figure 3.33: Same as Figure 3.29, but for the eastern array of SW Shatsky region. The uncertainty ranges were estimated by adding gaussian noise to measured phase-velocity anomalies.

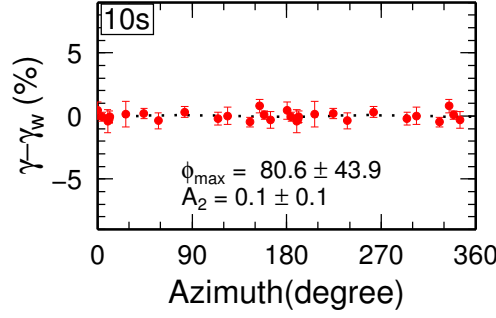


Figure 3.34: Phase-velocity anomalies of the ocean-mode Rayleigh wave (the 0S mode at 10 s) for the SW Shatsky region.

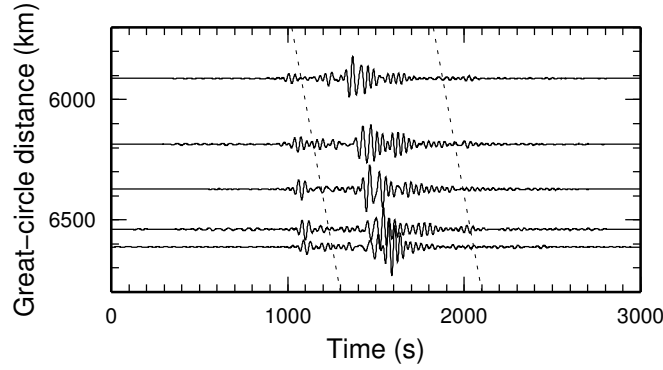


Figure 3.35: An example of teleseismic Love wave propagation at periods of 29–59 s recorded by BBOBSs in the Shikoku Basin region for an event with a moment magnitude of 7.3 that occurred at 12:46 on 9 April 2008 (UT). Dashed lines mark the time interval used for analysis.

of multipathing is small in this long period range especially at periods longer than 40 s (*Forsyth and Li, 2005*), the effect of ray bending cannot be neglected. The back azimuth of incoming surface waves are, therefore, estimated by using the array of BBOBSs. The surface-wave records with the signal-to-noise ratio higher than 10 were first selected for each event. The signal amplitude was estimated from the peak of the envelope function, and the noise amplitude was estimated from the root mean square amplitude of 800-s-long records 2 h after the origin time of the event. Figure 3.35 shows an example of Love wave propagation recorded by the BBOBSs in the Shikoku Basin region.

The procedure for the average phase-velocity measurement consists of two steps. The first step estimates the phase velocity ($c = \sum_n p_m^n g_m^n(\omega)$) and the perturbation of incident direction from the great circle ($\theta = \sum_n q_m^n g_m^n(\omega)$) of each mode (m) for each event (E) by maximizing the average of cross-correlation coefficients (C_E) defined as:

$$C_E(\mathbf{p}, \mathbf{q}) = \frac{1}{N_E^k} \sum_{i,j} \frac{\sum_{\omega} \Re_e \left[F_i^k \cdot (F_j^k)^* \cdot e^{i\Delta\varphi_{ij}(\omega, c, \theta)} \right]}{\sqrt{\sum_{\omega} |F_i^k|^2} \sqrt{\sum_{\omega} |F_j^k|^2}}, \quad (3.23)$$

where \Re_e is the real component, $F_i^k(\omega)$ is the Fourier spectrum of component k for the j th station, N_E is the number of station pairs, and $g_m^n(\omega)$ is a n th B-spline function. The phase difference between the i th and j th stations, $\Delta\varphi_{ij}$, is estimated using the coordinate system proposed by *Forsyth and Li* (2005) with that assuming a propagation of one plane wave in local coordinates (x, y) where: $x = x' - x'_0$, and x' is the great circle distance between source and point, x'_0 is the great circle distance between source and reference station, and y is the small circle distance from the point to the great circle connecting the source and the reference station. In this coordinate system, the phase difference between the i th and j th pair of stations is given by:

$$\Delta\varphi_{ij}(\omega, c, \theta) = \frac{\omega(r_i - r_j)}{c}, \quad (3.24)$$

where $r_i = \sqrt{x_i^2 + y_i^2} \cos(\tan^{-1} y_i/x_i - \theta)$, and (x_i, y_i) are the coordinates of the i th station. Using equation (3.23) and (3.24), I obtained the optimal phase velocity ($c = c_E = \sum_n p_E^n g_m^n(\omega)$) and optimal incident direction ($\theta = \theta_E = \sum_n q_E^n g_m^n(\omega)$) for each event (E) by the simulated annealing method (Appendix C). The next step only uses events whose average cross-correlation coefficient ($C_E(\mathbf{p}_E, \mathbf{q}_E)$) larger than 0.7.

In the second step, I searched for the optimal phase velocity curve ($c_m(\omega) = \sum_n p^n g_m^n(\omega)$) that maximizes the summation of cross-correlation coefficients for each mode:

$$C(\mathbf{p}) = \sum_E N_E^k C_E(\mathbf{p}, \mathbf{q}_E) \quad (3.25)$$

where the incident direction is fixed by the optimal value for each event ($\theta_E = \sum_n q_E^n g_m^n(\omega)$) obtained in the first step. Figure 3.36 shows phase velocities of 0S and 0T modes obtained from the vertical and transverse components, respectively. I hereafter describe the 0S and 0T modes as $m=0S'$ and $m=0T'$ modes to distinguish them with the measurements from the ambient noise ($m=0S$ and $m=0T$). The number of available events for Love waves is smaller than that for Rayleigh waves due to the higher noise level of the horizontal-component records as summarized in Table 3.3. Figure 3.37 summarizes the locations of epicenters used for the analysis. Figure 3.36 also shows the range of errors estimated by the bootstrap method (Appendix B), where the bootstrap sample was constructed using a randomly selected aggregate of events that allowed overlaps. The errors for Rayleigh waves are much smaller than those for Love waves. The phase velocity of Rayleigh waves at a period of 30 s is consistent with that determined by the noise correlation analysis.

3.4.2 Estimation of Azimuthal Anisotropy

Figures 3.38–3.39 show the azimuthal dependence of phase velocities of the 0S mode for four regions. They seem to be dominated by $\cos 2\phi$ term similarly to the case of ambient-noise analysis (Fig. 3.25–3.28). The estimation of azimuthal dependence from these measurements is, however, difficult because of the unstable frequency dependence of signal amplitudes,

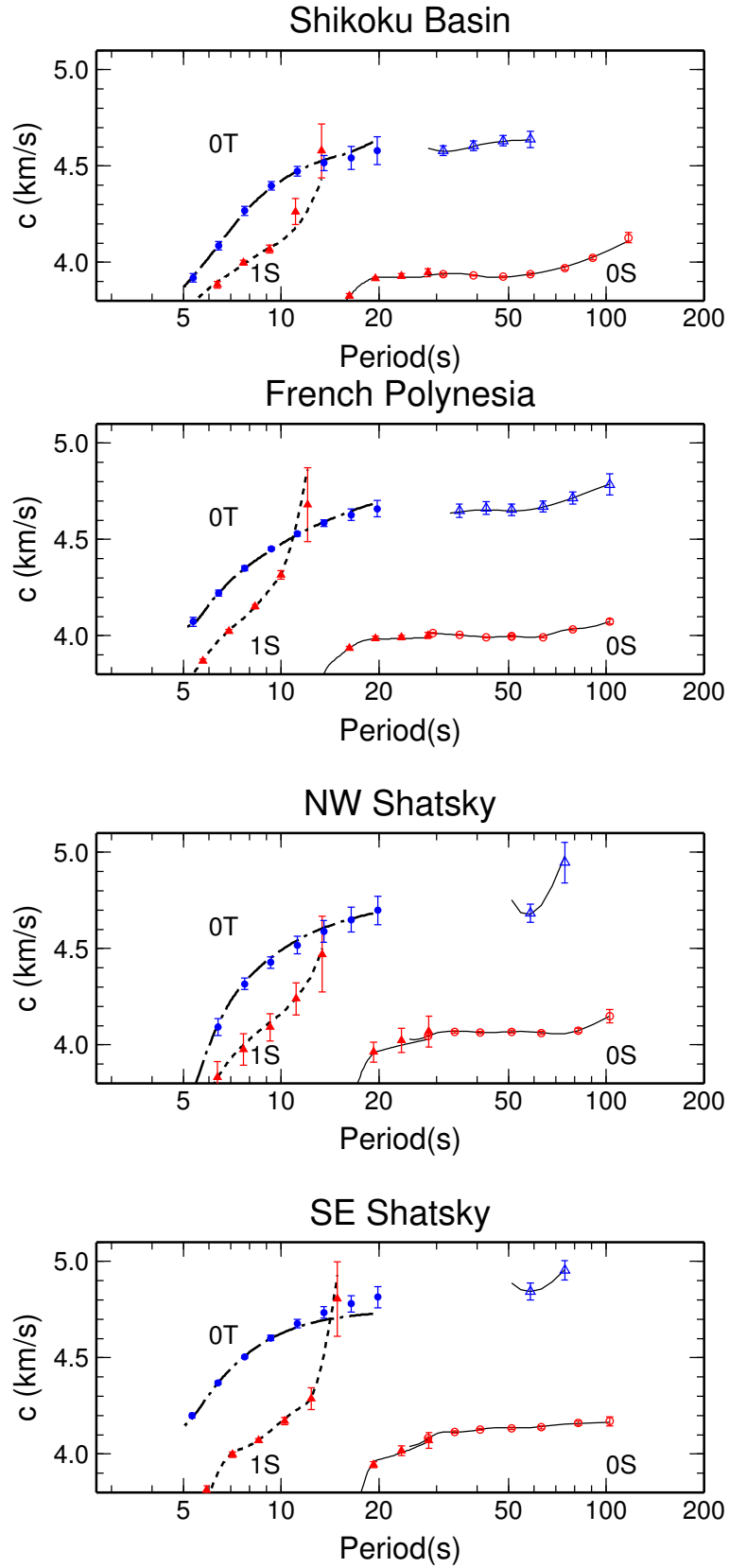


Figure 3.36: Phase velocities measured from ambient noise (color-filled symbols) and from teleseismic surface waves (white-filled symbols) for four regions other than the SW Shatsky region.

Table 3.3: Numbers of teleseismic events used for measuring average phase velocities.

Region	0S mode	0T mode
Shikoku Basin	137	29
French Polynesia	172 or 227	17
NW Shatsky	130	19
SE Shatsky	187	21

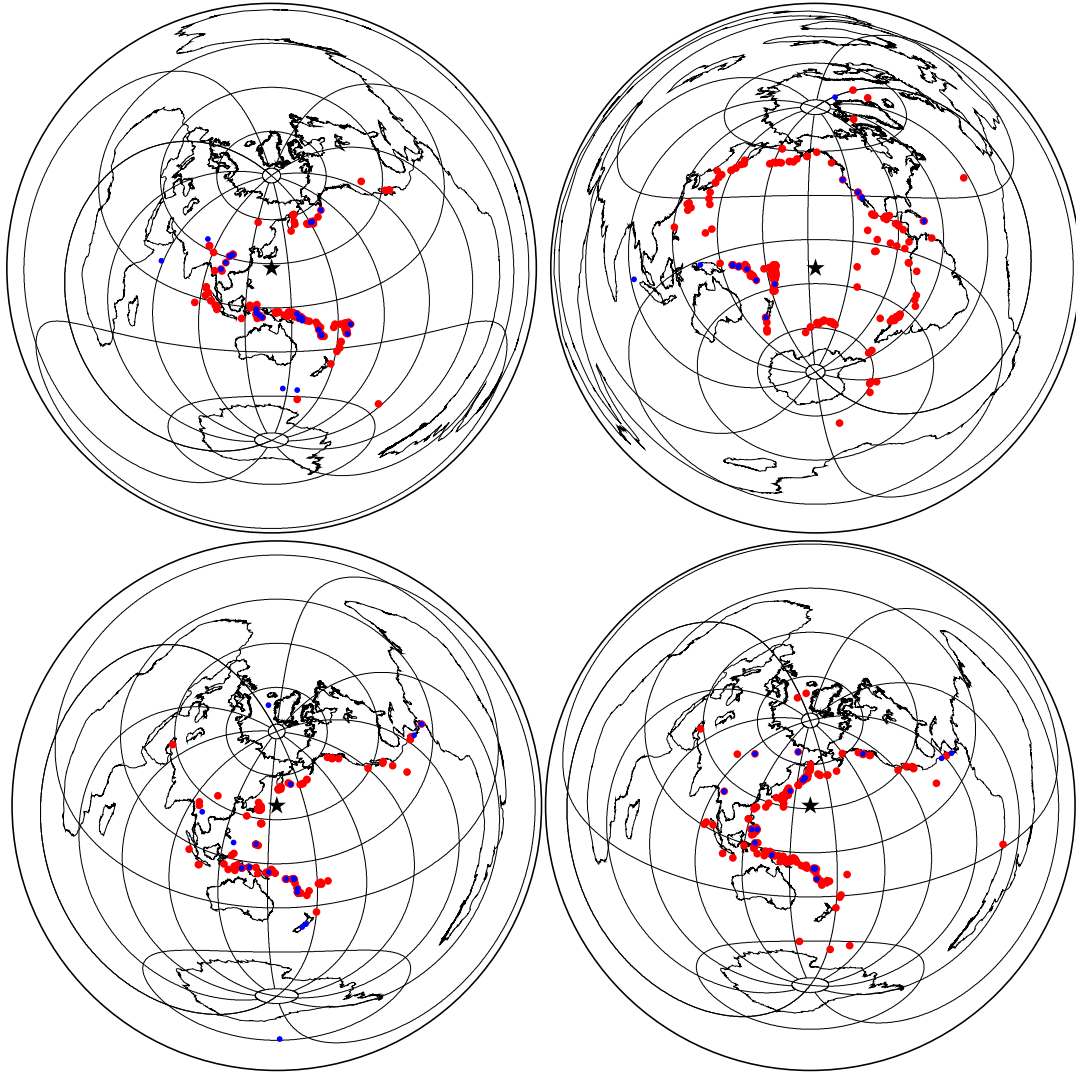


Figure 3.37: Red and blue circles show the epicenters of teleseismic events used for measuring average phase velocities of 0S and 0T modes beneath each array in the Shikoku Basin (top left), French Polynesia (top right), NW Shatsky (bottom left) and SE Shatsky (bottom right) regions. Stars show the locations of arrays.

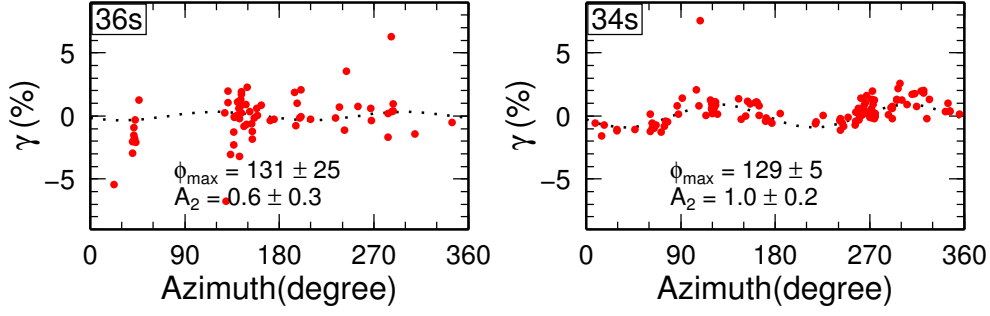


Figure 3.38: Phase-velocity anomalies of 0S mode for the Shikoku Basin (left) and French Polynesia (right) regions estimated from teleseismic surface waves. The dotted curve is the fitting curve.

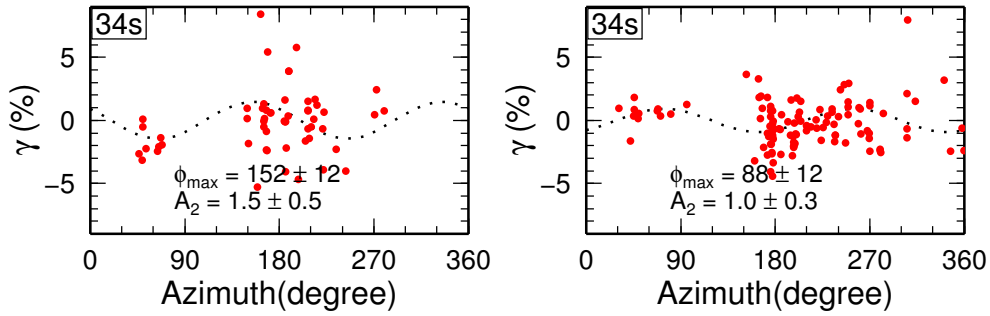


Figure 3.39: Same as Figure 3.38, but for the NW (left) and SE (right) Shatsky regions.

which may be reflecting high noise level of OBSs. I therefore estimated the frequency dependence of azimuthal anisotropy that maximizes the cross-correlation coefficients defined in equation (3.25). The azimuthal dependence can be represented by

$$c(\omega) = c_0(\omega) [1 + a \cos(2\phi) + b \sin(2\phi)], \quad (3.26)$$

where $c_0(\omega) = \sum_n p'_n g_m^n(\omega)$, $a(\omega) = \sum_n a'_n g_m^n(\omega)$ and $b(\omega) = \sum_n b'_n g_m^n(\omega)$. The half intensity and the fastest direction of azimuthal anisotropy are then given by $A_2 = \sqrt{a^2 + b^2}$ and $\phi_{\max} = \tan^{-1}(b/a)$, respectively.

Figures 3.29–3.32 summarize the obtained values as well as the values obtained from the ambient noise. Figure 3.40 summarizes the locations of epicenters used for the analysis. The measurement error shown in Figures 3.29–3.32 is smaller for the French Polynesia region (Fig. 3.30) compared to other regions, reflecting the scattering of the measurements especially for the NW Shatsky region (Fig. 3.39 left). It can be understood by considering the size of each array. As the phase-velocity anomaly is proportional to the ratio between the travel-time anomaly and the travel time within the array, the accuracy of the phase-velocity anomaly is better for the larger array that provides larger travel time. The size of array is larger than ~ 500 km for various propagation azimuth for the French Polynesia region (Fig. 2.2),

whereas it is larger than ~ 500 km for the limited propagation azimuth for other regions due to elliptical deployment of OBSs (Fig. 2.1). The accuracy of the phase-velocity anomaly is, therefore, higher for the French Polynesia region compared to other regions.

3.5 Discussions of Surface-Wave Analysis

3.5.1 Broadband Phase Velocity Measurements

The broadband surface-wave analysis was summarized in this chapter: the ambient noise cross-correlation analysis at periods of 3–30 s (§3.2), and the teleseismic surface-wave array analysis at periods of 30–100 s (§3.3). Although the period range of analysis depends on the mode of surface waves and the region, the broadband analysis at periods of 5–100 s could be almost achieved for both Rayleigh and Love waves, except for the SW Shatsky region, where I only applied the ambient-noise method. The period range for the Love wave (3–100 s) is especially broad compared to the range by the previous study in the EPR region, 4–17 s (*Dunn and Forsyth, 2003*). By using the phase velocities of Rayleigh waves as well, we can now estimate the radially anisotropic structure at depths of ~ 0 –150 km. The quantitative estimation of azimuthal anisotropy of the 1S mode (§3.2.5) also should be focused because previous studies could estimate anisotropy only qualitatively (*Harmon et al., 2007*). By using the azimuthal anisotropy of phase velocities of the 0S and 1S modes, we can now estimate the azimuthally anisotropic structure at depths of ~ 10 –100 km. Although the region is limited to the SW Shatsky region, the phase-velocity measurement of the 2S mode is also remarkable, while previous studies have analyzed the 0S and 1S modes (*Harmon et al., 2007; Yao et al., 2011*).

3.5.2 Amplitude of the Ambient Noise

The amplitude of ambient noise is one of the interesting topic for many researchers. Although I only obtained the azimuthal dependence of the ambient-noise source for the even-order terms of Fourier expansions (Figures 3.21–3.23; §3.3.5), the estimation of both even-order and odd-order terms will reveal the azimuth to the source of ambient noise in the future studies as done in southern California by *Harmon et al. (2010)*.

I could quantitatively estimate the average amplitude of the ambient noise represented by a_m^{kl} in equation (3.7–3.11) (§3.3.4) by correcting the effect of noise level to the calculation of cross-spectra (§3.3.1). Although obtained value are not shown because of the difficulty of showing all the amplitudes for each mode, component and region as a function of frequency, the amplitude can be roughly discussed from the waveforms shown in Figures 3.7–3.11. For example, the ZZ component shows both ocean-mode and solid-mode Rayleigh waves simultaneously except for the Shikoku Basin region where the ocean-mode Rayleigh waves dominates the ZZ component (Figure 3.7). Previous studies have also reported the

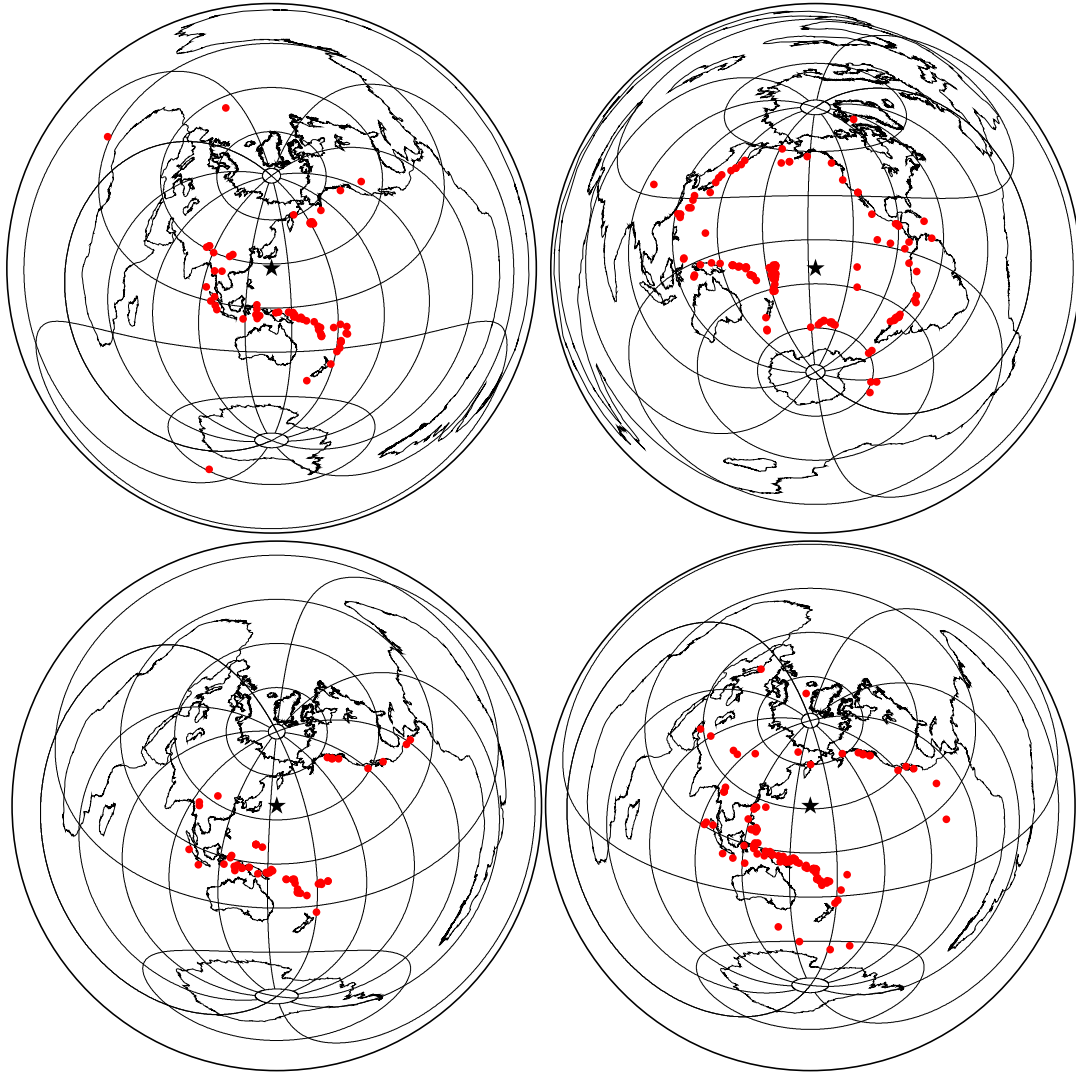


Figure 3.40: Red circles show the epicenters of teleseismic events used for estimating azimuthal anisotropy of OS mode beneath each array in the Shikoku Basin (top left), French Polynesia (top right), NW Shatsky (bottom left) and SE Shatsky (bottom right) regions. Stars show the locations of arrays.

simultaneous appearance of the ocean-mode and solid-mode Rayleigh waves in the vertical component at the EPR region (*Harmon et al.*, 2007; *Yao et al.*, 2011). These differences in vertical components may be reflecting the difference between shallow structures such as the velocity and thickness of shallow crustal layers (e.g., *Tanimoto and Alvizuri*, 2006). For more detailed discussion, we need to consider the excitation of two modes and the sensitivity of amplitude ratio to the structure in oceanic regions, which is beyond the scope of this study. The amplitude ratio between the Rayleigh and Love waves is also interesting to consider the excitation mechanism of the microseisms, which have been estimated in an island region (*Nishida et al.*, 2008a), but have not been done in oceanic regions yet.

Chapter 4

1D RADIALY ANISOTROPIC STRUCTURES

4.1 Introduction

The average phase velocities measured in the previous chapter can be used to estimate one-dimensional structure beneath each region. After summarizing the model parameters and assumptions (§4.2), the isotropic model for each region will be discussed first (§4.3). The scaling relationship between anisotropic parameters are then discussed (§4.4) for obtaining one-dimensional smooth radially anisotropic structures (§4.5), which are needed to account for the discrepancy between the measured phase velocities and the phase velocities corresponding to isotropic models. The smooth structures, however, are not suited for estimating parameters such as the velocity gradient in the LID or the velocity difference between the LID and LVZ because these values depend on the value of smoothing parameter. I therefore estimated these values and their uncertainty directly by inverting for the non-smooth radially anisotropic structure including the LID and LVZ structures (§4.6). These obtained structures will be discussed and compared to thermal models for the oceanic basins (§4.7).

4.2 Model Parameters and Assumptions

Radially anisotropic media can be described by eight parameters: density, attenuation coefficients for P- and S-waves, P-wave velocity (V_{PH}), S-wave velocity (V_{SV}), and three anisotropic parameters ($\phi = V_{PV}^2/V_{PH}^2$, $\xi = V_{SH}^2/V_{SV}^2$, and η) (e.g., *Takeuchi and Saito, 1972*) (see Appendix A for detail). V_{PV} and V_{PH} denote the velocities of vertically and horizontally propagating P-waves, respectively, and V_{SV} and V_{SH} are the velocities of horizontally propagating S-waves with vertical and horizontal polarizations, respectively. The parameter η is defined by $F/(A - 2L)$ by using three elastic constants (F , A and L) for a radially anisotropic media (*Takeuchi and Saito, 1972*) and affects the velocities of P- and

S-waves with incident angles between 0° and 90° . The phase velocities of Rayleigh waves are largely controlled by variations in V_{SV} , with the phase velocities of Love waves being mainly controlled by variations in V_{SH} . The phase velocity of a fundamental-mode Love wave has a high sensitivity to shallow depths even at long periods, whereas the phase velocities of Rayleigh waves have high sensitivities to deeper depths at longer periods (Fig. 3.3). The resolution of V_{SV} is thus higher than that of V_{SH} at depths greater than ~ 50 km.

The phase-velocities measured in this study mainly reflect S-wave velocity and its anisotropy from the crust to the depth of ~ 150 km. In addition, the depth of ocean is reflected to the period of transition from the solid-mode to the ocean-mode Rayleigh waves (§3.2). I therefore estimated V_{SV} and $\delta V = V_{SH}/V_{SV} - 1$ in each of nine layers from the Moho to a depth of 150 km, V_S in the three isotropic crustal layers, and the depth of ocean. The crust is assumed to be isotropic because the dependence of crustal P-wave velocity to the propagation azimuth is smaller than that for the mantle velocity, and indicates that the anisotropy in the crust is smaller than that in the mantle (*Christensen and Salisbury, 1975*). *Dunn and Toomey (2001)* also reported that the P-wave anisotropy in the crust is limited to upper ~ 2 km with a intensity of up to 4%. Such a small anisotropy can be neglected in this study because the measured phase velocities of Rayleigh waves have less sensitivity to the crustal structure compared to that to the mantle structure (Fig. 3.3). Although other parameters have a slight influence on the phase velocities of Rayleigh and Love waves, independent estimation of these parameters is difficult. I constrained the P-wave velocity ($V_P = (V_{PV} + V_{PH})/2$) in the mantle to be 1.73 times larger than the S-wave velocity ($V_S = (V_{SV} + V_{SH})/2$) based on results by an experimental study (*Anderson and Bass, 1984*) and a refraction survey in NW Pacific (*Shinohara et al., 2008*). The P-wave velocity and density in the crustal layers were estimated by using their relationship with S-wave velocity in the oceanic crust given by *Christensen and Salisbury (1975)*:

$$V_P = 1.75 \times V_S + 0.375 \text{ km/s}, \quad \rho = 0.5 \text{ g/cc}/(\text{km/s}) \times V_S + 1.25 \text{ g/cc}. \quad (4.1)$$

Other parameters are fixed to the Oceanic Reference Model (ORM) model by (*Maggi et al., 2006a*), including mantle density, attenuation coefficients, and structure deeper than 225 km. *Maggi et al. (2006a)* derived the ORM model by obtaining a global three-dimensional structure by using the fundamental and higher modes of Rayleigh waves, and by averaging their model for oceanic regions between the seafloor ages of 30 and 70 Ma. The model can be representative for the oceanic regions with the seafloor age between 0 and 180 Ma at depths deeper than 225 km, where the dependence of S-wave velocity structure on the seafloor age is small compared to the shallower structure. The model is similar to the PREM model by *Dziewonski and Anderson (1981)*, but has no discontinuity at the depth of 220 km. One layer at a depth range of 150–225 km is set to be lineally connected to the values at the depth of 150 km and the depth of 225 km.

4.3 Smooth Isotropic Structures

4.3.1 Four Regions

I again used the simulated annealing method (*Ingber*, 1989) (Appendix C) to search for optimal model parameters that led to a small misfit function defined by,

$$E_{\text{RA}} = \sqrt{\sum_{m,\omega} \left[\frac{\bar{c}_m(\omega) - c_m^{\text{model}}(\omega)}{\Delta c_m(\omega)} \right]^2 / \sum_m N_m}, \quad (4.2)$$

where N_m is the number of measurements for each mode m , $\bar{c}_m(\omega)$ is the bootstrap average of the measured phase velocity, $\Delta c_m(\omega)$ is the error on the phase velocity measurements, and $c_m^{\text{model}}(\omega)$ is the phase velocity calculated by DISPER80 (*Saito*, 1988) using the model parameters. The frequency interval of the measurements is set to be constant on a log scale.

To reduce the uncertainty related to the trade-off between adjacent layers, I introduce a smoothing term, $\epsilon_{\text{sv}} R_{\text{sv}}$, to the misfit function and minimize the summation:

$$E'_{\text{RA}} = E_{\text{RA}} + \epsilon_{\text{sv}} R_{\text{sv}}, \quad (4.3)$$

$$R_{\text{sv}} = \sum_{i=1}^{N-1} \left(V_{SV}^{i+1} - V_{SV}^i \right)^2, \quad (4.4)$$

where ϵ_{sv} is a constant, V_{SV}^i is V_{SV} in the i -th layer and $N = 10$ is the number of layers. The model uncertainty was evaluated by using dispersion curves obtained by the bootstrap method (Appendix B) where one hundred dispersion curves ($c_m^l(\omega)$, ($l = 1, \dots, 100$)) were obtained for each mode $m = 0\text{S}$, 1S and 0T by from the ambient noise and for each mode $m = 0\text{S}$ and 0T from teleseismic events as described in the previous chapter. The l th model was obtained by substituting the l th combination of dispersion curves ($c_{0\text{S}}^l$, $c_{1\text{S}}^l$, $c_{0\text{T}}^l$, $c_{0\text{S}'}^l$, $c_{0\text{T}'}^l$) in the place of average phase velocities (\bar{c}_m) in equation (4.2). For each layer, I then discarded the uppermost and lowermost five values from the 100 values and define this 90% confidence interval range as the model uncertainty.

Figure 4.1 is an example of model estimation for the Shikoku Basin region. Figure 4.1a shows the data misfit (E) and the average of V_{SV} uncertainties in 10 layers as a function of the smoothing parameter (ϵ_{sv}). There is a tradeoff between the data misfit and the model uncertainty. In more detail, the misfit function is almost constant for ϵ_{sv} less than 10, and the uncertainty increases as ϵ_{sv} decreases. This result means that the fitting does not improve, but the model uncertainty increases, for ϵ_{sv} less than 10. The optimal ϵ_{sv} value is equal to or larger than 10. The solid lines in Figure 4.1b show the model corresponding to $\epsilon_{\text{sv}} = 10$ (SB-ISO10), the isotropic structure beneath the Shikoku Basin. The phase velocities of model SB-ISO10 almost fit the measured phase velocities of Rayleigh waves as shown in Figure 4.1d. On the other hand, broken lines in Figure 4.1b shows a smoother model (SB-ISO100) corresponding to $\epsilon_{\text{sv}} = 100$. but the phase velocities of model SB-ISO100 do not fit the phase

velocity measurements even for the Rayleigh waves as shown in Figure 4.1e. I therefore chose $\epsilon_{sv} = 10$ as the final value and SB-ISO10 as our preferred isotropic model.

Figure 4.2 shows models for four regions: Shikoku Basin, French Polynesia, NW Shatsky and SE Shatsky. The seafloor ages are about 20, 60, 130 and 140 Ma, respectively. The smoothing parameters are the same as SB-ISO10, $\epsilon_{sv} = 10$, for all regions, which give the model uncertainty of $\sim 0.5\%$. The S-wave velocity is higher than 4.5 km/s at depths shallower than ~ 50 km, whereas it is lower at deeper depths except for the SE Shatsky region, where the velocity is almost constant value of 4.6 km/s from the Moho to the depth of 150 km. The correlation between the S-wave velocity and the seafloor ages is obvious at depths of 50–150 km.

The isotropic models in Figure 4.2, however, cannot fit the measured phase velocities of the 0T mode as shown by the misfit in Figure 4.1d and Figures 4.3–4.5. The misfit for the 0T mode exceeds 2% for the Shikoku Basin 4.1d, French Polynesia (Fig. 4.3), SE Shatsky (Fig. 4.5) regions, whereas the misfit is smaller for the NW Shatsky region (Fig. 4.4). The misfit for the Rayleigh waves is smaller than that for the Love wave because the error of phase-velocity measurement is smaller for the Rayleigh waves and the misfit function is normalized by the error of phase-velocity measurement in equation (4.2). The misfit for the 0T mode increases from the period of ~ 10 s to the period of ~ 100 s, and indicates that the S-wave velocity in the mantle is not isotropic. For reducing the misfit, we need to introduce radial anisotropy to the mantle structure.

4.3.2 SW Shatsky Rise

The estimation of structure for the SW Shatsky region is different from other four regions by considering the narrower period range (3–30 s) for the SW Shatsky region. In addition, the 2S at periods of 3–5 s could be analyzed for the SW Shatsky region, which has sensitivity mainly to the S-wave velocity structure in the crust. The model parameters are, therefore, set to be the depth of the seafloor (d1), the depths of the bottom of three crustal layers (d2, d3, d4), S-wave velocity in the three crustal layers (v1, v2, v3), and the S-wave velocity in the uppermost mantle from the Moho to a depth of 220 km (v4). The single mantle layer is assumed because there is little resolution of mantle structure deeper than 40 km with the available period range. The monotonic increase of S-wave velocity with depth is assumed. The density and P-wave velocity in the crust are scaled to S-wave velocity by the scaling relationship based on natural rocks (Christensen and Salisbury 1975).

Figure 4.6b shows the obtained structure. The phase velocities corresponding to the obtained model are shown in Figure 4.6a. The model phase velocities match well to the measured phase velocities, fitting within the range of error bars. As average phase velocities of both the Rayleigh and Love waves were satisfied with an isotropic structure, there is no requirement for radial anisotropy given the limited period range measured. The model

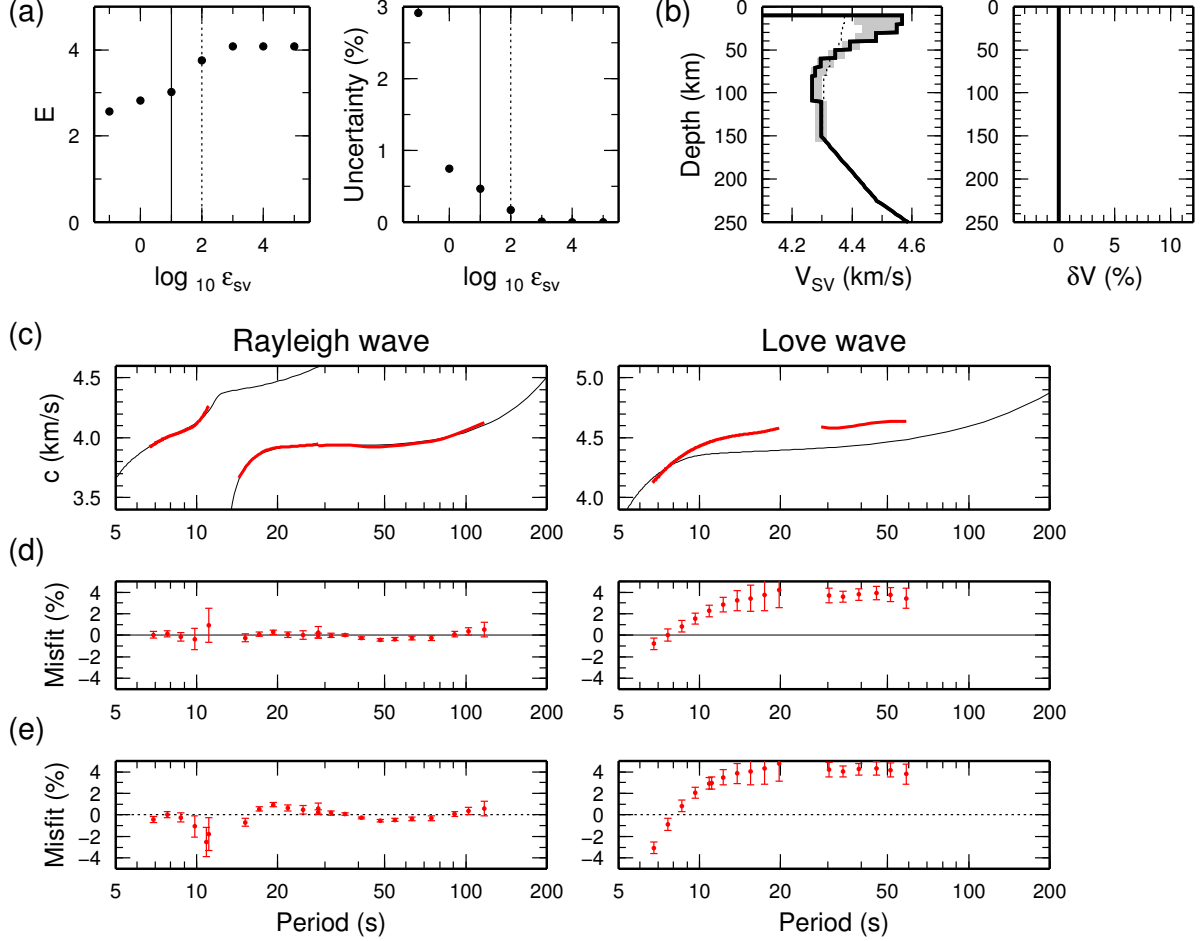


Figure 4.1: An example of isotropic-model inversion for the Shikoku Basin region. (a) Minimum misfit function, E , and the uncertainty of V_{SV} averaged for 10 layers as a function of ϵ_{sv} . (b) Solid lines show our final isotropic model (SB-ISO10) corresponding to $\epsilon_{sv} = 10$ at a frequency of 1 Hz. The depth of 0 km corresponds to the ocean surface. Gray areas show the model uncertainty. Broken lines show SB-ISO100, which is a smoother structure corresponding to $\epsilon_{sv} = 100$. (c) Phase velocities of SB-ISO10 (thin black line) and measurements (thick red line). (d) Misfit between measurements and phase velocities of SB-ISO10. (e) Misfit between measurements and phase velocities of SB-ISO100.

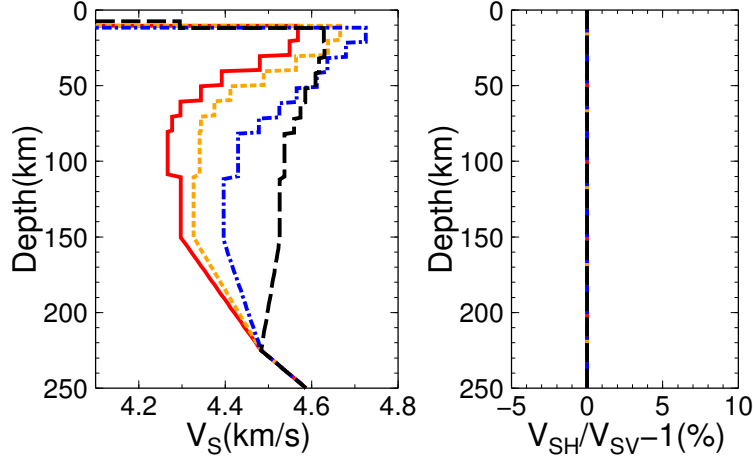


Figure 4.2: Isotropic models for the Shikoku Basin (red solid lines; 20Ma), French Polynesia (orange short-dashed lines; 60 Ma), NW Shatsky (blue chain lines; 130 Ma) and SE Shatsky (black long-dashed lines; 140 Ma) regions.

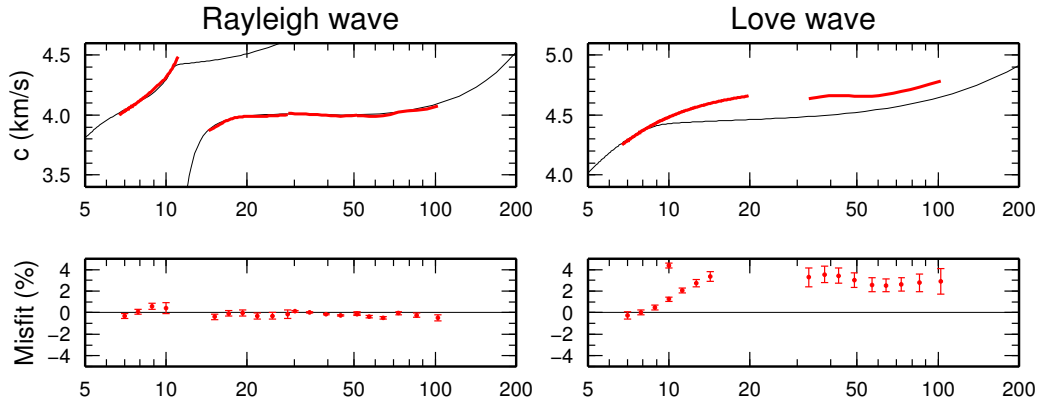


Figure 4.3: Same as Figure 4.1c-d, but for the French Polynesia region.

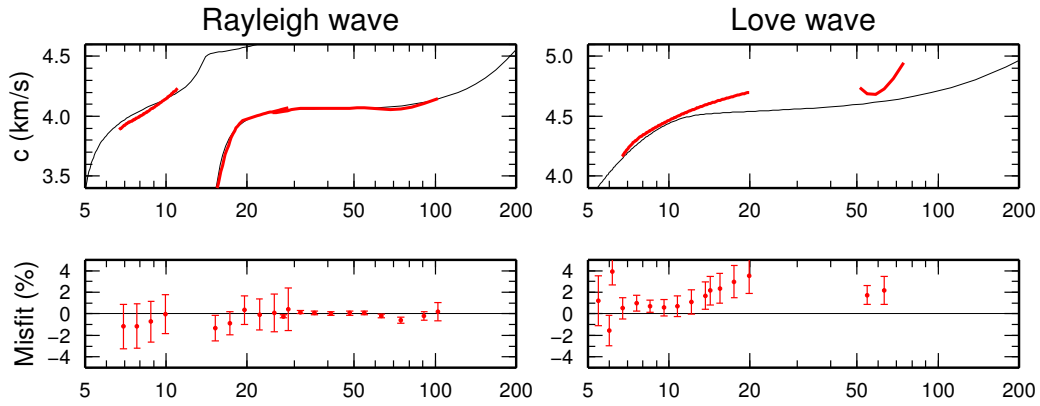


Figure 4.4: Same as Figure 4.1c-d, but for the NW Shatsky region.

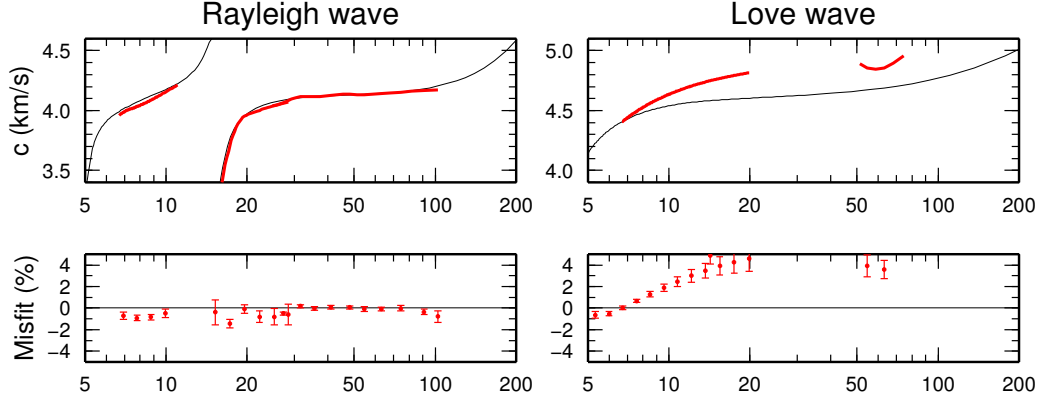


Figure 4.5: Same as Figure 4.1c–d, but for the SE Shatsky region.

uncertainty was further estimated by obtaining one hundred models corresponding to one hundred pairs of dispersion curves obtained by the bootstrap method (Appendix B). The distribution of one hundred models are shown by the histograms in Figure 4.6c and Figure 4.6d. As S-wave velocities in the second and third crustal layers (v_2 and v_3) are close to each other (Figure 4.6d), we cannot recognize the boundary between the two layers in Figure 4.6b. The depth of the seafloor and the S-wave velocity in the mantle are well determined, whereas other parameters have larger uncertainty due to trade-off between parameters.

4.4 Anisotropic Parameter Scalings

There are 21 independent elastic constants for general anisotropic structure, which will be reduced to five for a radially anisotropic structure: two velocity parameters, $\alpha = V_{PH}$ and $\beta = V_{SV}$; and three anisotropic parameters ($\xi = N/L = (V_{SH}/V_{SV})^2$, $\phi = C/A = (V_{PV}/V_{PH})^2$, and $\eta = F/(A - 2L)$) (Takeuchi and Saito, 1972) (Appendix A). Although phase velocities of Rayleigh and Love waves mainly have sensitivity to β and $\xi = (1 + \delta V)^2$, other parameters slightly affect the phase velocities. Figure 4.7 shows sensitivity kernels of phase velocities for each parameter for the PREM-OCEAN4.6 model, a model based on PREM (Dziewonski and Anderson, 1981) (see detail in §3.2). We cannot recognize the sensitivity of Rayleigh waves to ξ and that of Love waves to α , ϕ , and η because they are zero or almost zero. The most important relationship here is that the sensitivities of Rayleigh waves to ϕ and η are negative of each other. As a result, $\phi + \eta$ has almost no effect on the phase velocity, whereas $\phi - \eta$ has a minor effect. It is necessary to constrain $\phi - \eta$ with an accuracy of 10% for estimating β and $\delta V = \sqrt{\xi} - 1$ with an accuracy of 1%.

Montagner and Anderson (1989) first discussed the correlations between anisotropic parameters when the mantle has a LPO. Their results for olivine can be parameterized as,

$$\phi \sim \xi^{-1.5}, \quad \eta \sim \xi^{-2.5}, \quad (4.5)$$

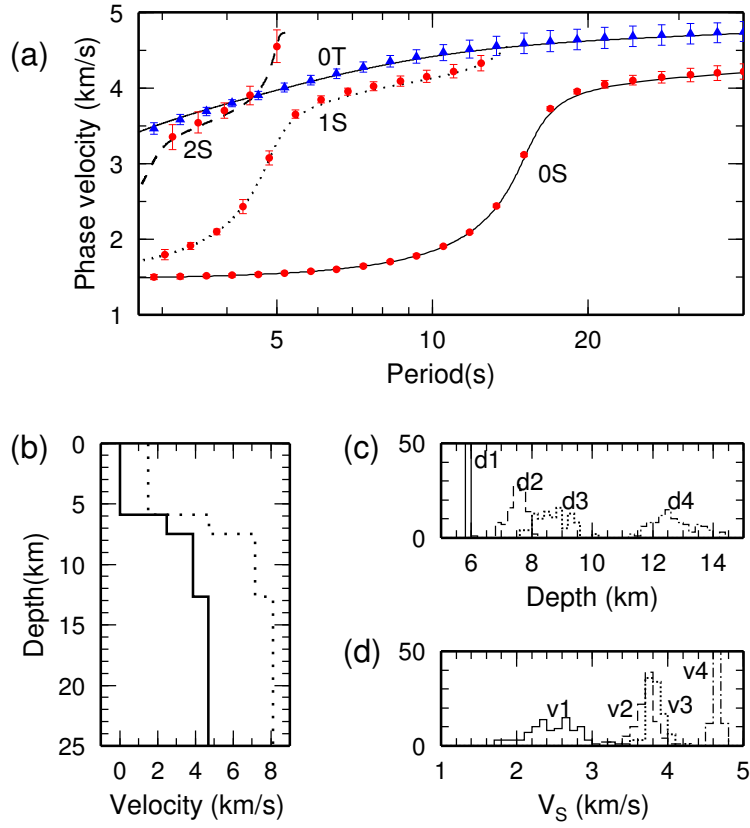


Figure 4.6: (a) Measured phase velocities of Rayleigh (red circles) and Love (blue triangles) waves, and model phase velocities (black curves). (b) One-dimensional S-wave and P-wave velocity model shown by solid and dotted lines, respectively. (c) Histograms showing the uncertainty of the top depths of the three crustal layers and the mantle. (d) Same as (c) but for S-wave velocities in the four layers.

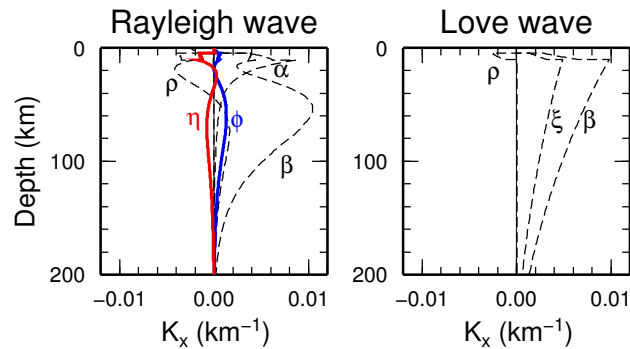


Figure 4.7: Sensitivity of the parameter p to the phase velocities of fundamental-mode surface waves at a period of 40 s (K_p) for the PREM-OCEAN4.6 model (§3.2).

by *Gung et al.* (2003). *Becker et al.* (2008) also considered this topic and obtained a different relationship,

$$\phi \sim \xi^{-1.4}, \quad \eta \sim \xi^{-2.0}, \quad (4.6)$$

by considering a mixture of olivine and enstatite crystals. These equations show that P-wave anisotropy is larger than S-wave anisotropy. However, if radial anisotropy is caused by the presence of pockets or layers of partial melt, then the S-wave anisotropy should be larger than the P-wave anisotropy because the velocity reduction caused by melting is greater for S-waves than for P-waves.

I obtained a new relationship when anisotropy originates from melt layering. This calculation is based on a simple melt layering model in which layers of partial melt are horizontal and thin as compared with the surrounding solid rock layers. Such a model can be represented using three parameters: (i) the reduction of rigidity in layers containing partial melt as compared with the rock layers (a); (ii) the reduction of the bulk modulus as compared with the reduction in rigidity (b); (iii) the thickness of layers containing partial melt as compared with that of the rock layers (f). The Poisson ratio is set to 0.25 for melt-free layers. By varying combinations of these parameters between $0 < a < 1$, $0.4 < b < 0.6$, and $0 < f < 0.1$, I calculated long wavelength equivalent elastic constants with the formulation by *Backus* (1962). Figure 4.8a shows three anisotropic parameters for $b = 0.5$ and Figure 4.8b shows the correlations between these parameters. I scaled these parameters using,

$$\phi \sim \xi^{-0.2}, \quad \eta \sim \xi^{-1.7}. \quad (4.7)$$

The dependence of ϕ to ξ is small for this melt-layering model than for the LPO models (equations 4.5–4.6) because the reduction of P-wave velocity by the presence of partial melt is smaller than that of S-wave velocity, whereas the anisotropy of P-wave of an olivine crystal is stronger than that of S-wave (*Crampin*, 1978).

Figure 4.8c summarizes the relationship between $\phi - \eta$ and ξ for three scaling relationships. As already noted, it is necessary to constrain $\phi - \eta$ to an accuracy of 10% in order to obtain β and $\delta V = \sqrt{\xi} - 1$ with an accuracy of 1%. The scaling method of *Gung et al.* (2003) is suitable for this purpose because the difference of $\phi - \eta$ between the scaling and other scalings are smaller than 10% ($\xi < 1.2$).

4.5 Smooth Radially Anisotropic Structures

Figure 4.9 shows an example of radially anisotropic structure for the Shikoku Basin region. I chose the scaling relationship for the three anisotropic parameters by *Gung et al.* (2003) as discussed in the previous section. The value of S-wave anisotropy, δV is assumed to be constant from the Moho to the depth of ~ 150 km, lineally complemented to the zero value at the depths of 225 km. The determination of the smoothing parameter, ϵ_{sv} is as same method as that for the isotropic inversion in Section 4.3.1. Figure 4.9a the misfit function (E) and

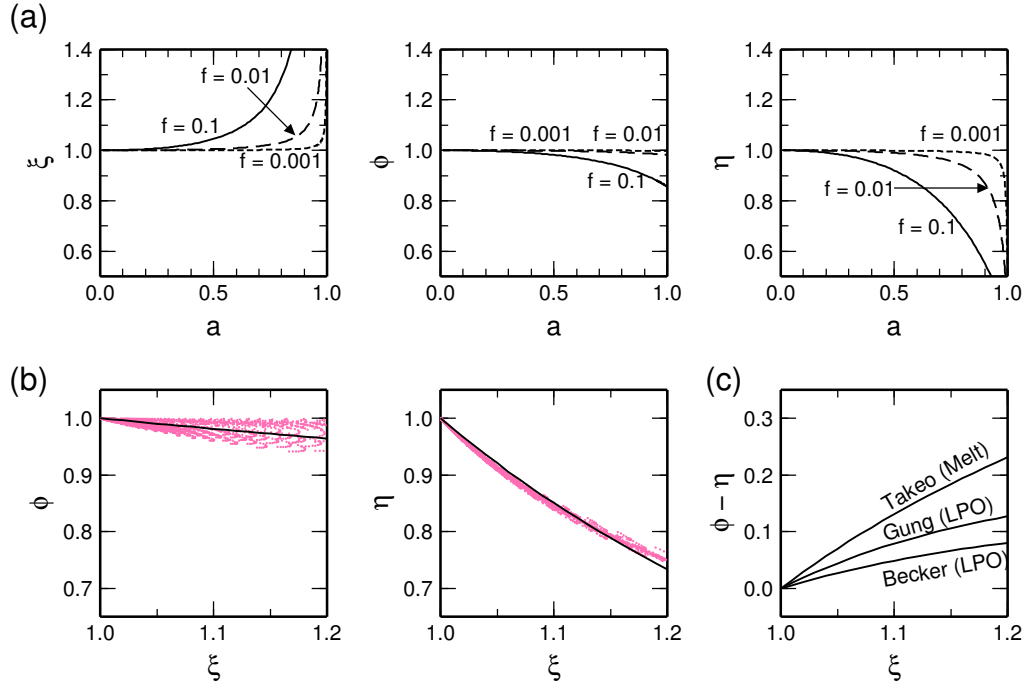


Figure 4.8: (a) Anisotropic parameters for a simple melt layering model when b is set to 0.5. (b) Correlation between anisotropic parameters in the simple melt layering model. Each dot indicates a combination of three anisotropic parameters (a , b , and f). The fitted curves are shown by solid lines. (c) Correlation between $\phi - \eta$ and ξ for three different scaling relationships (*Gung et al.* (2003), *Becker et al.* (2008), and this study.)

the average of V_{SV} uncertainties in 10 layers as a function of ϵ_{sv} . The misfit function is almost constant for ϵ_{sv} less than 10, and the uncertainty increases as ϵ_{sv} decreases. This result means that the fitting does not improve, but the model uncertainty increases, for ϵ_{sv} less than 10. The optimal ϵ_{sv} value is equal to or larger than 10. The solid lines in Figure 4.9b show the model corresponding to $\epsilon_{sv} = 10$ (SB-RA10-ORM) for the radially anisotropic structure beneath the Shikoku Basin. It should be noted that the model is different from the SB-RA10 by *Takeo et al.* (2013), which uses the PREM model (*Dziewonski and Anderson, 1981*) to constrain the structure at depths deeper than 220 km instead of the ORM model by *Maggi et al.* (2006a). The phase velocities of model SB-RA10-ORM show excellent agreement with the phase velocity measurements as shown in Figure 4.9d. However, I obtained a smoother model (SB-RA100-ORM; broken lines in Figure 4.9b) if we choose $\epsilon_{sv} = 100$, but the phase velocities of model SB-RA100-ORM do not fit the phase velocity measurements as shown in Figure 4.9e. I therefore chose $\epsilon_{sv} = 10$ as the final value and SB-RA10-ORM as our preferred final model.

For model SB-RA10-ORM, V_{SV} is 4.5–4.6 km/s at a depth range of 10–40 km, decreases by 6%–10% over depths of 40–70 km and becomes 4.15–4.25 km/s at depths of 70–150 km, which is slower than at deeper depths. These results indicate that a low velocity zone (LVZ) exists at depths greater than ~ 50 km, and that a high velocity LID exists at shallower depths. The thickness of the LID is difficult to define from these results due to a gradual velocity decrease at depths of 40–70 km. I later consider the depth and sharpness of the boundary between the LVZ and LID. The intensity of anisotropy ($V_{SH} > V_{SV}$) is estimated to be 4%–5%. While the assumption of constant anisotropy appears to fit the phase velocity measurements (Figure 4.9d), I will also subsequently discuss possible variations of anisotropy with depth.

Figure 4.10 shows models for four regions: Shikoku Basin, French Polynesia, NW Shatsky and SE Shatsky. The seafloor ages are about 20, 60, 130 and 140 Ma, respectively. The smoothing parameters are the same as SB-RA10-ORM, $\epsilon_{sv} = 10$, for all regions, which give the model uncertainty of $\sim 0.5\%$. The models give phase velocities almost consistent with the phase-velocity measurements as shown in Figure 4.9 and Figures 4.11–4.13. This result means that the depth variation of radial anisotropy is not needed from our measurements. As inferred from the faster 0T mode compared to the isotropic models (Fig. 4.1c and Fig. 4.3–4.5), the radial anisotropy ($V_{SH} > V_{SV}$) exists for all of four regions. The intensity of S-wave radial anisotropy is smallest (3%) for the NW Shatsky region, the largest (6%) for the SE Shatsky region, and the middle (4%–5%) for the Shikoku Basin and French Polynesia regions. The value of V_{SV} is almost same as the value of V_S for the isotropic models (Fig. 4.2). The S-wave velocity is higher than 4.5 km/s at depths shallower than ~ 50 km, whereas it is lower at deeper depths except for the SE Shatsky region, where the velocity is almost constant value of 4.6 km/s from the Moho to the depth of 150 km. The correlation between the S-wave velocities and seafloor ages is obvious at depths of 50–150 km.

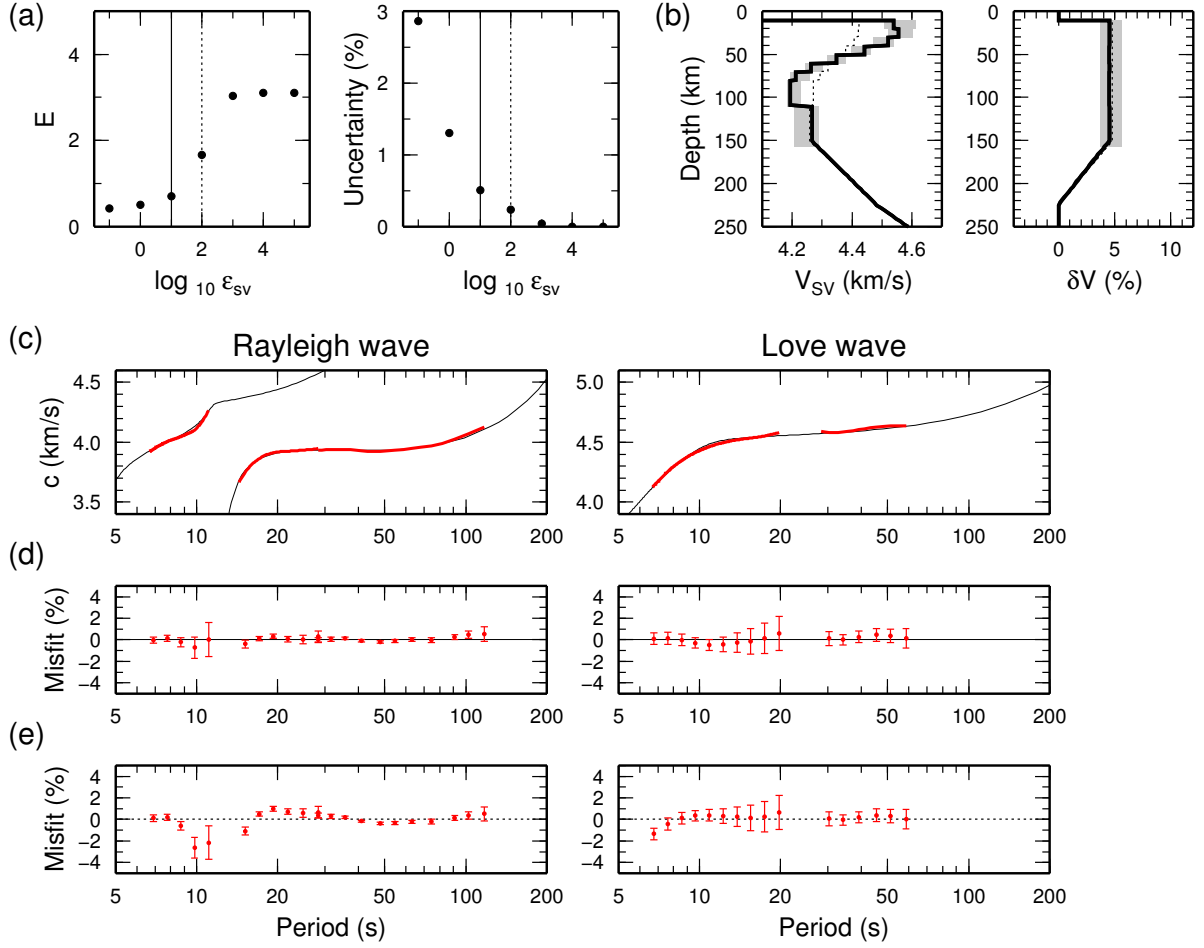


Figure 4.9: Same as Figure 4.1, but for the radially anisotropic model in the Shikoku Basin. The solid lines show our final model, SB-RA10-ORM, whereas the broken lines show a smoother model, SB-RA100-ORM.

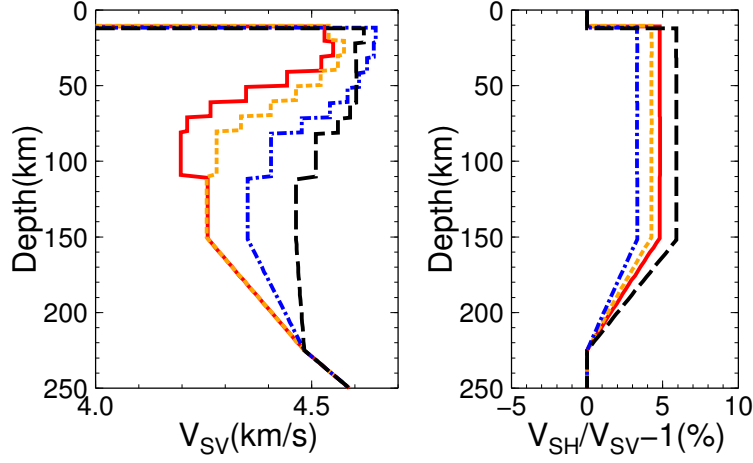


Figure 4.10: Radially anisotropic models for the Shikoku Basin (red solid lines; 20Ma), French Polynesia (orange short-dashed lines; 60 Ma), NW Shatsky (blue chain lines; 130 Ma) and SE Shatsky (black long-dashed lines; 140 Ma) regions.

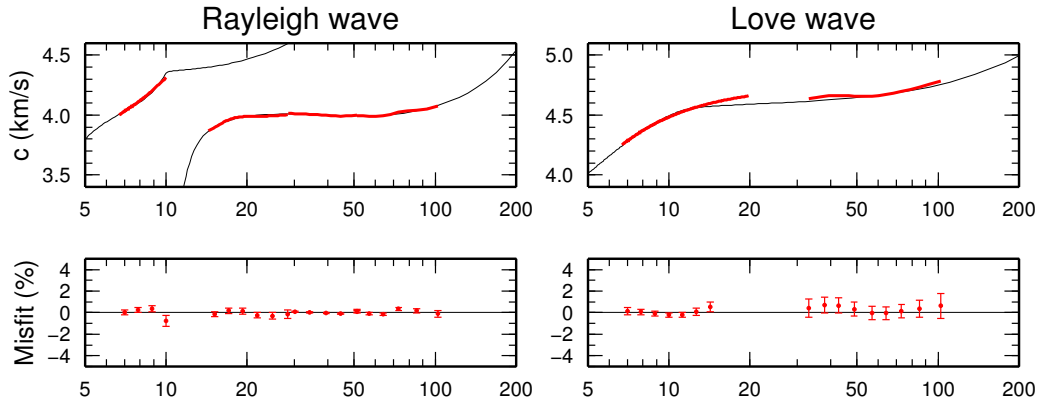


Figure 4.11: Same as Figure 4.9c–d, but for the French Polynesia region.

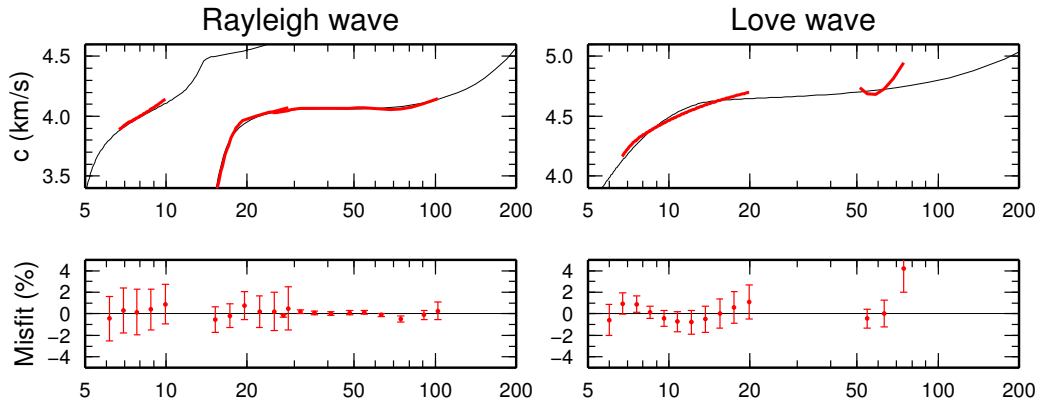


Figure 4.12: Same as Figure 4.9c–d, but for the NW Shatsky region.

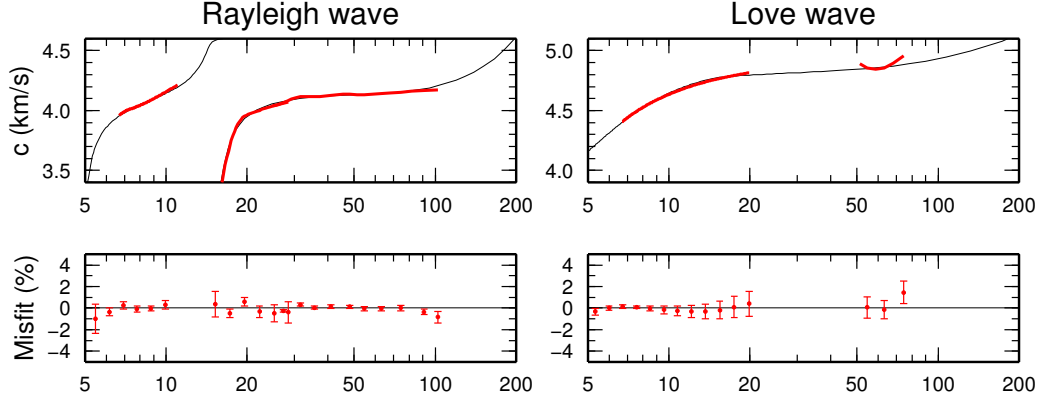


Figure 4.13: Same as Figure 4.9c–d, but for the SE Shatsky region.

4.6 Non-smooth Radially Anisotropic Structures

The presence of a LID over the LVZ has been assumed in structural inversions of surface waves to resolve the LVZ beneath oceanic basins (e.g., *Leeds et al.*, 1974; *Schlue and Knopoff*, 1976). I obtained a similar structure that seems to have a LID at depths of ~ 10 –50 km especially for the Shikoku Basin region (Figure 4.10). The thickness of the LID is, however, difficult to quantify due to the gradual transition from the LID to LVZ at depths of 40–70 km. The estimation of the thickness depend on the assumed smoothing parameter, ϵ_{sv} , and the definition of the LID.

Synthetic tests shown in Figure 4.14 more clearly shows the difficulty of estimating the thickness of the LID. For the initial model, the sharp discontinuity between LID and LVZ was assumed to exist at a depths of 40, 50, 60 and 80 km. The initial crustal model was assumed to be as same as that for the Shikoku Basin region. A model was inverted for each initial model by substituting the phase velocities corresponding to the initial model to the measured phase velocities in equation 4.2 and by using the smoothing parameter as same as that for the smooth models shown in Figure 4.10 ($\epsilon_{sv} = 10$). The obtained models shown by blue chained lines in Figure 4.14 indicate that the transition from LID to LVZ becomes gradual compared to the initial model due to the presence of the smoothing parameter. It is difficult to define the thickness of the LID from the retrieved model with a gradual transition from LID to LVZ. Although more sharp discontinuity can be retrieved by using smaller smoothing parameter ($\epsilon_{sv} = 1$; Fig. 4.15), the retrieved model has unevenness due to the trade-off between adjacent layers. The model roughness is about 1%, and closed to the model uncertainty for $\epsilon_{sv} = 1$ shown in Figure 4.9. This large uncertainty again makes the definition of the LID difficult. The model inversion without using the smoothing parameter is needed for discussing the thickness of the LID or the sharpness of the transition from the LID to the LVZ.

I therefore estimated the possible range of the depth and thickness of the LID–LVZ

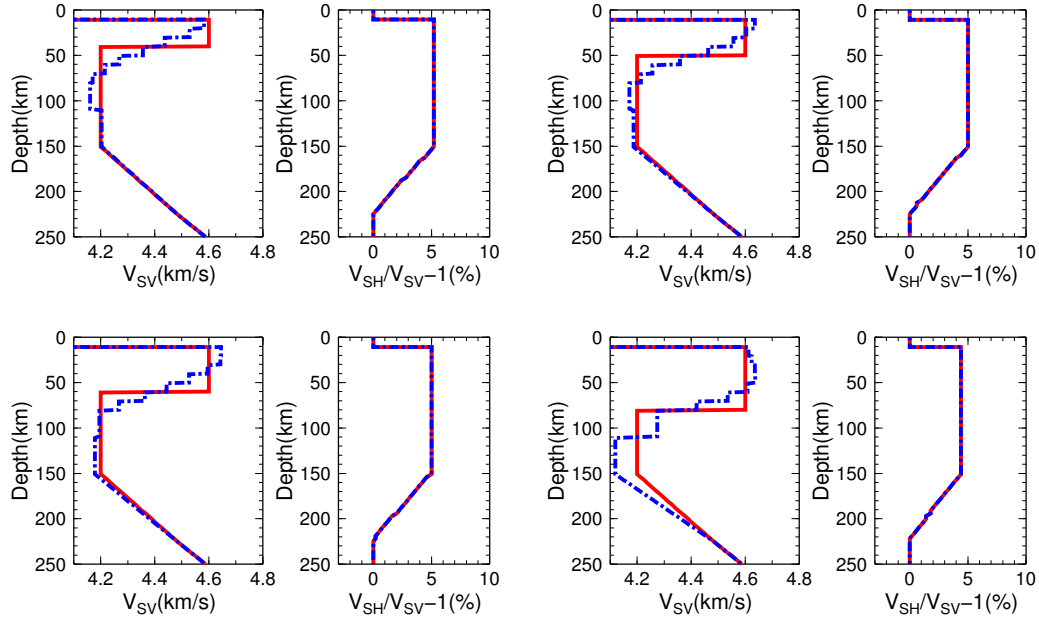


Figure 4.14: Red solid and blue chained lines show the initial model and the model obtained by the synthetic test, respectively. The velocity of initial model sharply decreases at a depth of 40 km (top left), 50 km (top right), 60 km (bottom left) and 80 km (bottom right). The smoothing parameter is as same as the smooth models shown in Figure 4.10 ($\epsilon_{sv} = 10$).

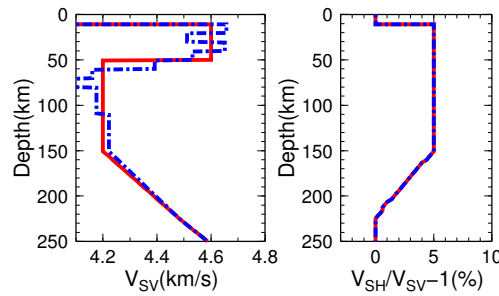


Figure 4.15: Same as Figure 4.14, but for the discontinuity at a depth of 50 km, and a smoothing parameter of $\epsilon_{sv} = 1$.

Table 4.1: Ranges of parameters for the non-smooth radially anisotropic models.

Region	Shikoku Basin	French Polynesia	NW Shatsky	SE Shatsky
Seafloor age (Ma)	15–27	50–70	135	145
V_{LID} (km/s)	4.61–4.68	4.64–4.68	4.66–4.74	4.73–4.79
V_{LVZ} (km/s)	4.35–4.41	4.36–4.41	4.40–4.49	4.54–4.62
z_c (km)	39–48	52–59	63–85	61–91
Δz (km)	0–29	3–40	5–65	4–77
$(\frac{dV}{dz})_{LID}/V(\%/km)$	0.02–0.31	0.02–0.13	-0.11–0.11	-0.02–0.06
(Thermal model)	(-0.22)–(-0.09)	(-0.12)–(-0.05)	(-0.06)–(-0.03)	(-0.06)–(-0.03)
$-(\frac{dV}{dz})_{LLTZ}/V(\%/km)$	0.1–10	0.2–2	0.1–1	0.05–1
(Thermal model)	0.02–0.1	0.03–0.07	0.01–0.04	0.01–0.04
δV_{LID}	1.3–4.1	2.6–4.2	1.1–4.9	5.4–7.2
δV_{LVZ}	4.0–6.2	3.3–5.5	1.8–7.7	3.1–8.7

transition zone (LLTZ). In addition, I estimated the velocity gradient in the LID because the almost constant velocity gradient in the smooth model (Figure 4.10) is inconsistent with the negative velocity gradient predicted from the thermal gradient in the uppermost mantle (e.g., *Shapiro and Ritzwoller, 2004; Faul and Jackson, 2005*). I also estimated the intensity of radial anisotropy in the LID and LVZ to examine possible differences in radial anisotropy. For estimating these parameters, seven model parameters were chosen for the uppermost mantle structure: center depth and thickness of LLTZ (z_c and δz); average velocity in the LID and LVZ ($V_{LID} = (V_{SV}^{LID} + V_{SH}^{LID})/2$ and $V_{LVZ} = (V_{SV}^{LVZ} + V_{SH}^{LVZ})/2$); velocity gradient in the LID ($(dV/dz)_{LID}$); S-wave anisotropy in the LID and LVZ (δV_{LID} and δV_{LVZ}). These values can be used to estimate the velocity gradient in the LLTZ ($(dV/dz)_{LLTZ}$). The depth of the ocean was fixed to the values of the smooth radially anisotropic models (Figure 4.10).

Figure 4.16a shows the result for the Shikoku Basin region when the bootstrap average of phase velocity measurement (\bar{c}_m) was used as data. The uncertainty range of each parameter is further estimated by obtaining 100 models where the l th model is obtained using combinations of l th dispersion curves ($c_0 S^l$, $c_1 S^l$, $c_0 T^l$, $c_{0S'}^l$, and $c_{0T'}^l$) derived by the bootstrap methods. Figure 4.16b–e show the distribution of 100 models and the uncertainty range defined by the 90% confidence interval (the range of 90 models after discarding top and bottom five values for each parameter). Figures 4.17–4.19 show the results for the French Polynesia, NW Shatsky and SE Shatsky regions. The estimated ranges of parameters are also summarized in Table 4.1.

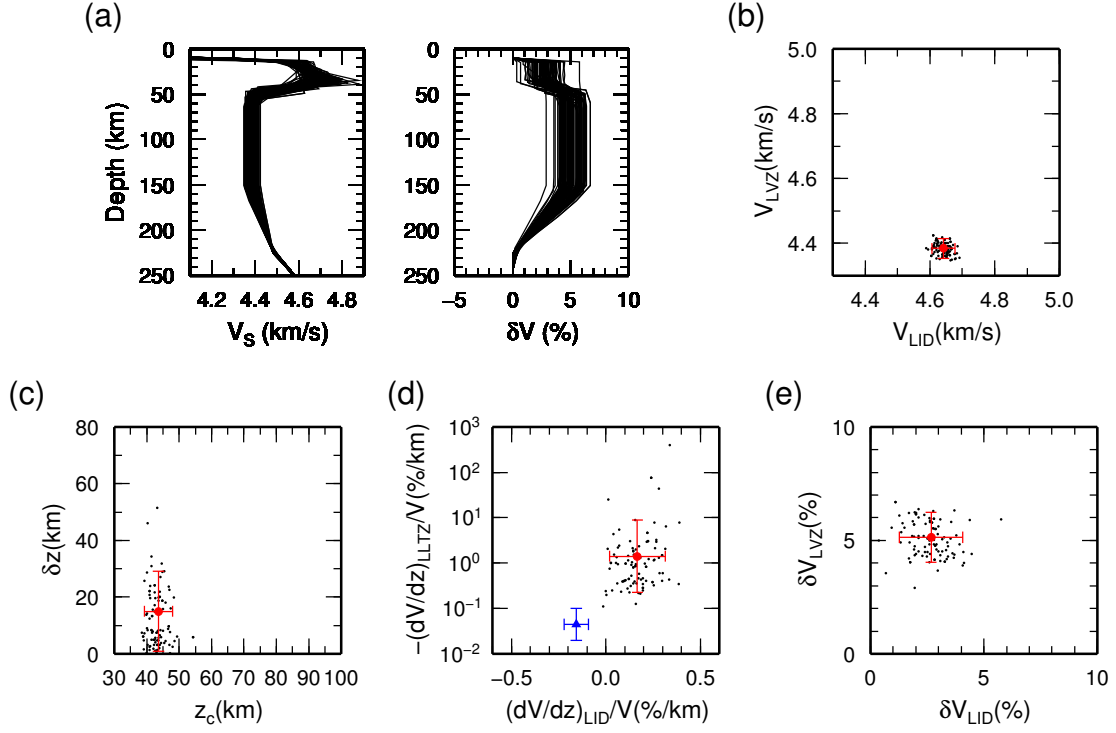


Figure 4.16: (a) One hundred models with LIDs, LVZs and LLTZs obtained by using one hundred combinations of dispersion curves. (b-e) Gray dots show the distributions of the seven model parameters (V_{LID} , V_{LVZ} , z_c , δz , $(dV/dz)_{LID}$, δV_{LID} , δV_{LVZ} , and a parameter calculated from model parameters $[(dV/dz)_{LVZ}]$ for the one hundred models. Red circles with error bars show the uncertainty range defined by the range of 90 models. A blue triangle with error bar in panel (d) shows the range predicted by thermal models.

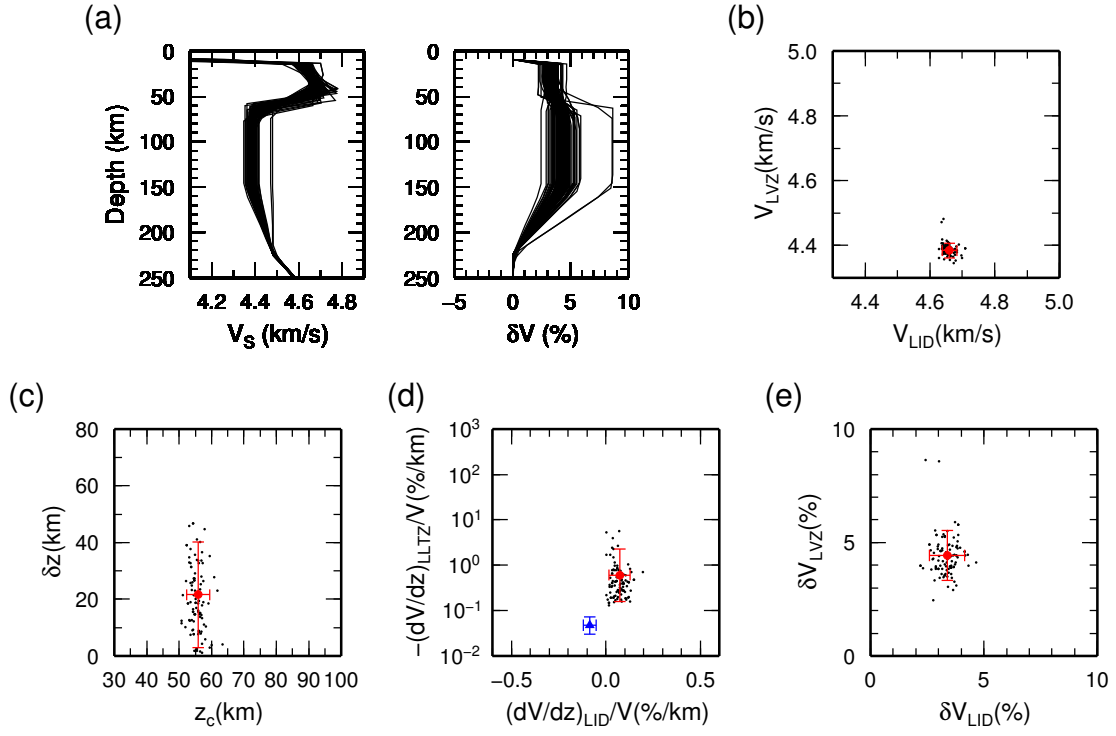


Figure 4.17: Same as Figure 4.16, but for the French Polynesia region.

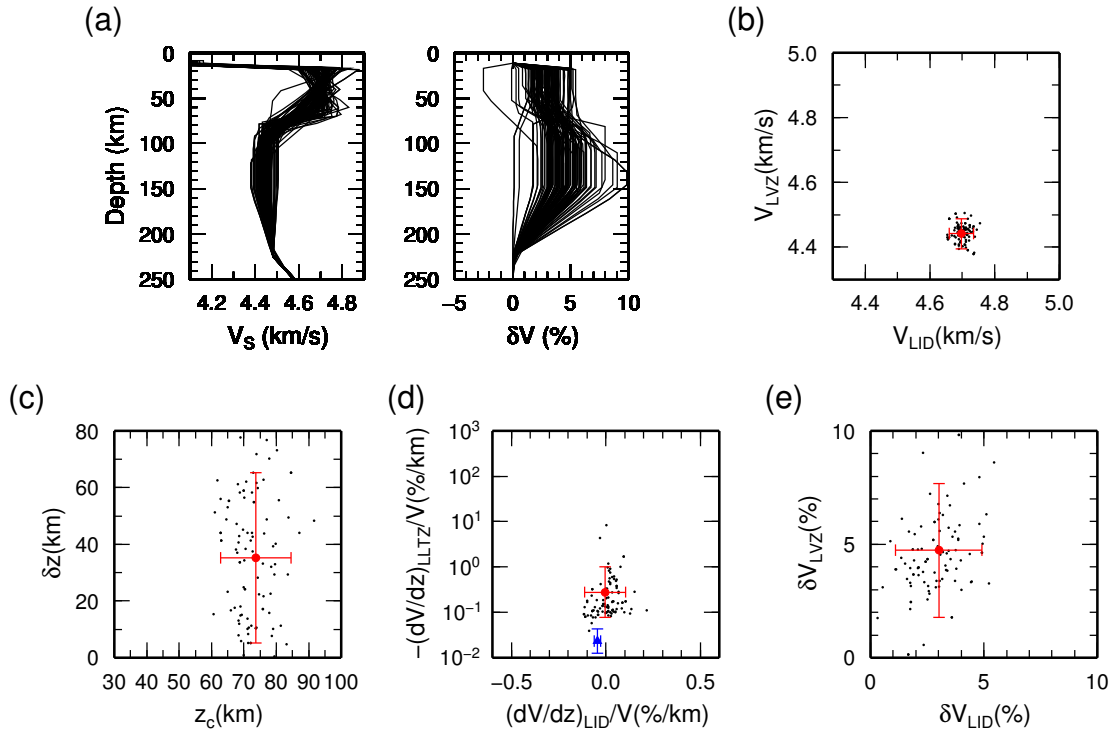


Figure 4.18: Same as Figure 4.16, but for the NW Shatsky region.

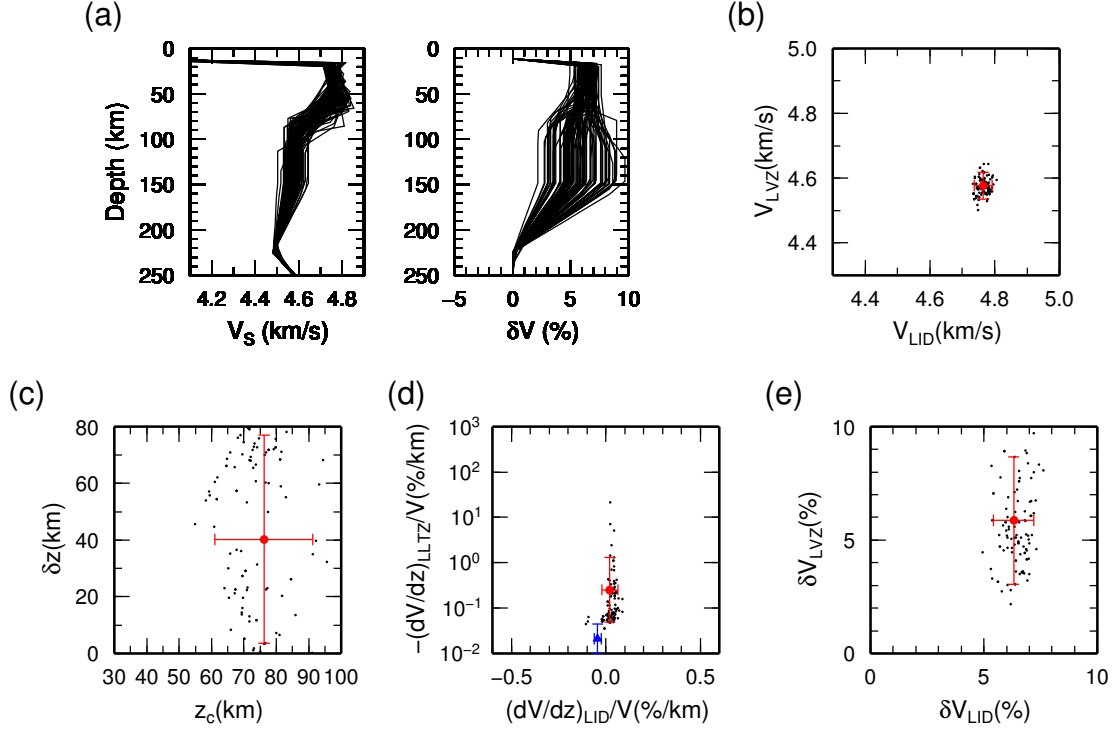


Figure 4.19: Same as Figure 4.16, but for the SE Shatsky region.

4.7 Discussions of the Radially Anisotropic Models

4.7.1 Assumption of 1D Structure

I obtained one-dimensional radially anisotropic structure beneath each seismic array by using average phase velocities of surface waves in the array area. The one-dimensional structures can be considered as the lateral and azimuthal average of the three-dimensional anisotropic structure (*Dziewonski and Anderson, 1981*). Although the trade-off between lateral heterogeneity and azimuthal anisotropy usually exists, the trade-off between lateral heterogeneity and radial anisotropy only exists when the coupling between Rayleigh and Love waves occurs due to the presence of azimuthal anisotropy (*Kawasaki and Koketsu, 1990*). For the surface waves analyzed in this study, coupling may occur between 1S and 0T modes at periods of 7–9 s, where the phase and group velocities of these waves are close to each other (Fig. 3.1–3.2). *Kawasaki and Koketsu (1990)* reported that the azimuthal dependence of phase velocity may be biased $\sim 2\%$ by the presence of coupling if phase and group velocities meet two criteria: (i) the group velocities cross each other, and (ii) the difference in phase velocities is less than 0.05 km/s ($\sim 1\%$). Figure 4.20 shows the phase and group velocities of 1S and 0T modes for the smooth radially anisotropic models obtained in Section 4.5. The crossing between group velocities occurs at a period of ~ 7 s for the Shikoku Basin and NW Shatsky regions, whereas it occurs at a period of ~ 10 s for the

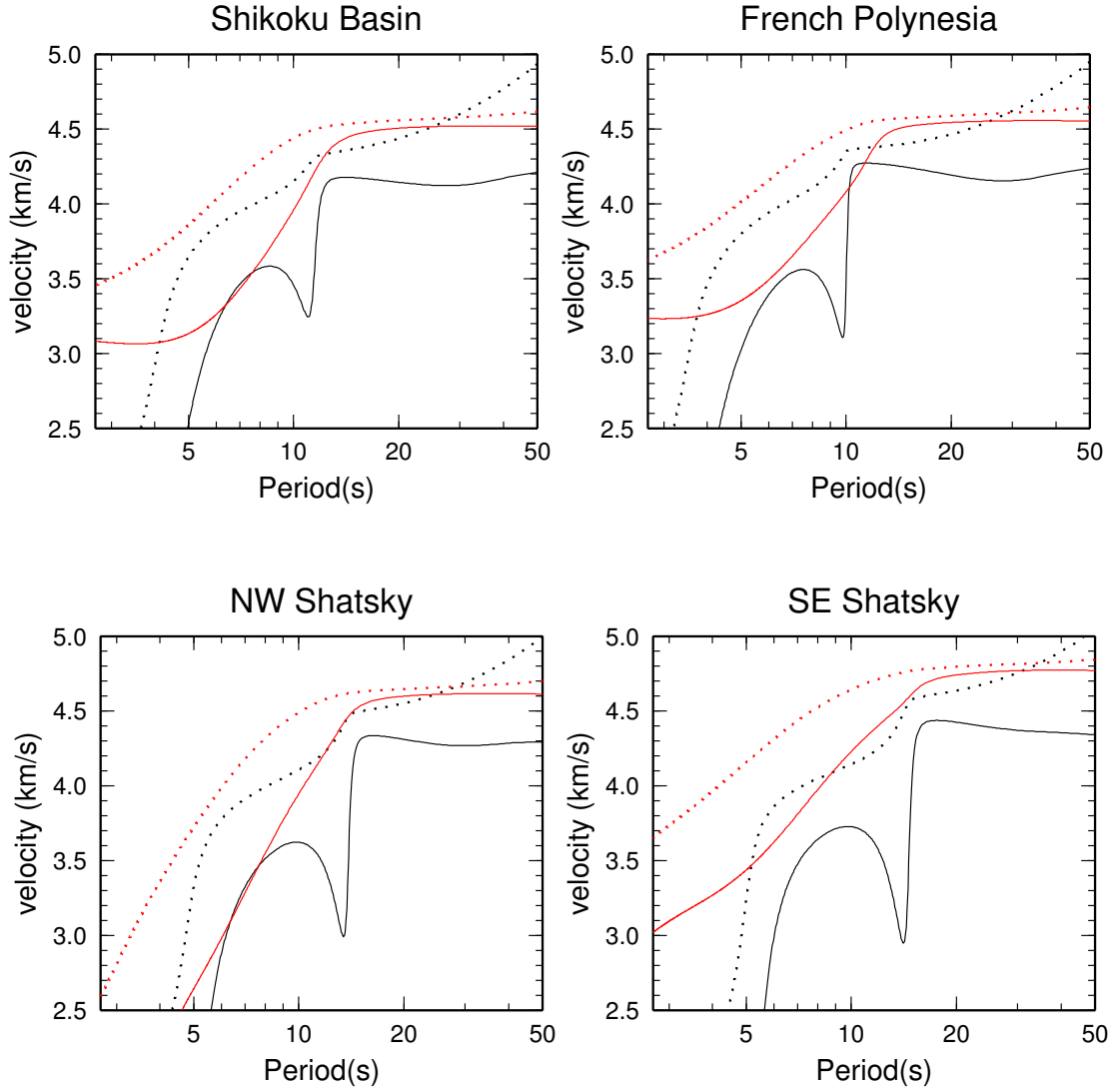


Figure 4.20: Phase (dotted lines) and group (solid lines) velocities of 1S (black) and 0T (red) modes.

French Polynesia region. The difference in phase velocities of at least 2% at these periods, however, indicates that the bias due to the presence of coupling is significantly smaller than 2% (expected to be less than $\sim 1\%$) and can be neglected. Therefore, our structural model most likely represents an azimuthal average of the three-dimensional structure beneath each regions.

The presence of crustal heterogeneity in the Shikoku Basin may lead to an incorrect interpretation of the crustal and uppermost mantle structure at depths shallower than ~ 20 km. Although I simply assumed a crustal thickness of 6 km during the structural inversion, the thickness in the Shikoku Basin determined by refraction surveys is not constant, varying in the range of 4.0–7.5 km, apart from sites of small seamounts that have a crustal thickness of up to 15 km (*Nishizawa et al.*, 2011). The structure I obtained at depths shallower than

20 km is therefore influenced by both crustal and uppermost mantle structures, and needs to be considered with caution. As the main interest in this study is the structure related to the LID and LVZ, I mainly interpret the uppermost mantle structure at depths deeper than 20 km. It should be, however, noted that my estimation of P-wave velocity just below the Moho of 7.8–8.0 km/s is almost consistent with the Pn velocity estimated by refraction survey of 7.9–8.1 km/s (*Nishizawa et al.*, 2011).

The presence of lateral heterogeneity in the uppermost mantle around the Shikoku Basin may also cause an incorrect structural interpretation. *Isse et al.* (2009) found three slow velocity anomalies in the mantle wedge along the IBM arc at depths of ~ 50 –100 km. The northernmost anomaly is sited beneath the northeastern-most station used in this study, and may affect the average phase velocities in the Shikoku Basin. This effect is, however, expected to be small as the phase velocities obtained from five stations in the southern part of Shikoku Basin are consistent (within the error bar) with the phase velocities obtained from seven stations. At depths greater than 100 km, the presence of the subducting Pacific Plate cannot be neglected as shown in the three-dimensional model of *Isse et al.* (2009). As such, I avoid comparing structural models at this depth range with thermal models for oceanic basins.

The lateral heterogeneity is also strong for the French Polynesia region at depths shallower than ~ 20 km. The topography map shown in Figure 2.2 shows several seamounts. The presence of thicker crust beneath high sea-topography is indicated from several refraction surveys in this region (*Grevenmeyer et al.*, 2001; *Patriat*, 2002), although their study area is limited to the area outside the array of stations used in this study. The typical thickness of crust beneath small island is about 15 km. The structure at depths shallower than ~ 20 km may, therefore, be biased from the anomalous crustal thickness.

The topography of other three regions around the Shatsky Rise is homogeneous compared to the Shikoku Basin and French Polynesia regions. Although the topography for the SW Shatsky region shows several seamounts, the effect is expected to be small because they are small (Figure 2.5). The structures beneath these regions can be, therefore, considered to be homogeneous compared that beneath the Shikoku Basin region.

4.7.2 Comparison with Previous Models

I obtained a one-dimensional smooth radially anisotropic structures beneath four regions (Figure 4.10), which can be compared with previous models obtained by surface waves. For example, my model for the Shikoku Basin (SB-RA10-ORM) shows strong vertical variation: V_{SV} is greater than 4.5 km/s at depths of 10–40 km, and less than 4.3 km/s at depths of 60–150 km. *Isse et al.* (2010) previously obtained a three-dimensional model in the Philippine Sea region, including azimuthal and radial anisotropy, using 0S and 0T modes at periods of 40–167 s. The period range of *Isse et al.* (2010) is longer than that of my study, and

they obtained a smoother V_{SV} model beneath the Shikoku Basin, with an almost constant value of 4.3–4.4 km/s at depths of 10–220 km. I compared the phase velocities given by my structural model and that of *Isse et al.* (2010). While the differences are less than 1% for the 0S mode at periods longer than 30 s, the differences are 2%–4% for 0S and 1S modes at shorter periods. This suggests that we need to use phase velocities at periods shorter than 30 s for determining which structural model is closest to the actual structure. As my model better explains the phase velocities of the 1S modes measured in this study, the model is more representative of the actual structure than the model by *Isse et al.* (2010). The V_{SH} structure obtained in this study is also different from that of *Isse et al.* (2010). My model has V_{SH} higher than 4.7 km/s at depths of 10–40 km, and lower than 4.5 km/s at greater depths, whereas the model of *Isse et al.* (2010) has an almost constant V_{SH} of 4.4–4.6 km/s. This discrepancy reflects differences in the phase velocities of 0T mode. The phase velocity obtained in this study is $\sim 2\%$ – 3% higher than the value obtained by *Isse et al.* (2010), which I attribute to damping and smoothing related effects in their analysis.

I further compare the models for four regions with the typical models representative for oceanic regions. Figure 4.21 compares my models with the traditional oceanic uppermost mantle models by *Nishimura and Forsyth* (1989) for the seafloor ages of 4–20, 20–52, 52–110 and >110 Ma. The structures are almost consistent with my models in terms of the dependence on the seafloor age. For example, my model for the Shikoku Basin region at a seafloor age of ~ 20 Ma is within their models for the seafloor age of 4–20 and 20–50 Ma. There are two major differences between my and their models. The values of V_{SV} are lower for the models by *Nishimura and Forsyth* (1989) than my models at depths of ~ 100 – 200 km, where I have less confidence on my models due to larger uncertainty of phase-velocity measurements at periods longer than ~ 80 s. The values of my models may become lower if I can measure phase velocities of 0S mode at periods longer than 100 s with a higher accuracy. The intensity of radial anisotropy is larger for my models than the model by *Nishimura and Forsyth* (1989). It may be caused by the period range of phase-velocity measurement in this study (5–100 s) broader than their study (20–120 s), which enabled us to obtain more reliable radially anisotropic structure in the uppermost mantle.

Figure 4.22 compares my models with the PA5 model by (*Gaherty et al.*, 1996) and the ORM model by (*Maggi et al.*, 2006a). The PA5 model is an average radially anisotropic model for a path between Tonga and Hawaii with seafloor ages of 100–125 Ma. The ORM model is the average of the three-dimensional V_{SV} for the seafloor ages of 30–70 Ma, which was used to constrain structure at depths deeper than 225 km in this study. The LID of the PA5 model is faster than the LID in my models, whereas the LID of the ORM model is slower than the LID in my models. My models are more reliable because I analyzed phase velocities of surface waves in a broader period range including the 1S mode. The intensity of radial anisotropy of the PA5 model is closed to my models for the Shikoku Basin, French Polynesia and NW Shatsky regions, whereas the radial anisotropy for the SE Shatsky region

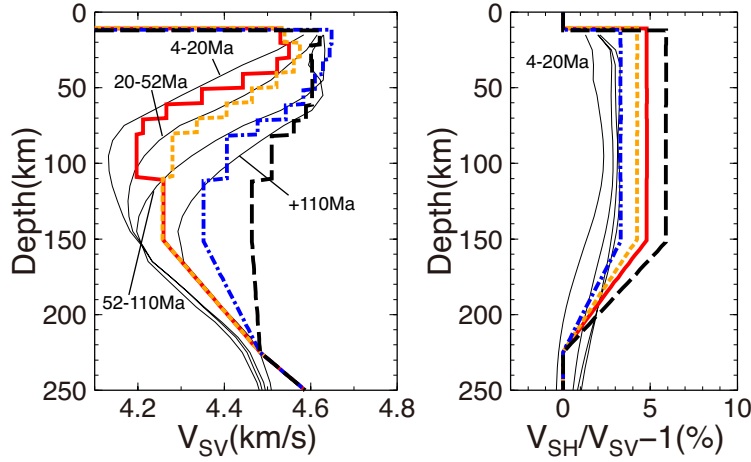


Figure 4.21: Radially anisotropic models by *Nishimura and Forsyth* (1989) for the seafloor ages of 4–20, 20–52, 52–110 and >110 Ma (thin solid lines) with the models obtained in this study for the Shikoku Basin (red solid lines; 20Ma), French Polynesia (orange short-dashed lines; 60 Ma), NW Shatsky (blue chain lines; 130 Ma) and SE Shatsky (black long-dashed lines; 140 Ma) regions.

is relatively high. The difference in the intensity originates from the fast 0T mode for the SE Shatsky region compared to other regions at periods of ~ 10 –80 s (Figure 3.36). The V_{SV} structure beneath the SE Shatsky region (145 Ma) is also fast compared to the structure for the region with the similar seafloor age (NW Shatsky region; 135 Ma), which originates from the velocity difference in 0S modes at periods of ~ 30 –80 s (Figure 3.36). The V_{SV} structure for the NW Shatsky region is more close the PA5 model, a model for the seafloor age of 100–125 Ma. These differences indicate that the structure beneath the SE Shatsky region is anomalous compared to the structure in other regions, although it is also possible that the structures beneath the NW Shatsky and Tonga-Hawaii corridor are anomalous.

4.7.3 Lid, Low Velocity Zone and the Transition Zone

The presence of a LID over the LVZ with a constant velocity has been assumed in structural inversions of surface waves (e.g., *Leeds et al.*, 1974; *Schlue and Knopoff*, 1976), but have not been clearly proved due to the limited depth resolution by surface waves at periods longer than ~ 30 s. Although recent body-wave studies have estimated the depth of the boundary between LID and LVZ by using the converted or reflected waves, there is still large uncertainty for the velocity reduction at the boundary (e.g., *Revenaugh and Jordan*, 1991; *Kawakatsu et al.*, 2009; *Rychert and Shearer*, 2011). The velocity gradient in the LID is also an interesting topic. *Lizarralde et al.* (2004) recently proposed a model with a positive velocity gradient at the top of the LID from the refracted P-wave, which is inconsistent with the negative velocity gradient predicted by the positive temperature gradient, and the

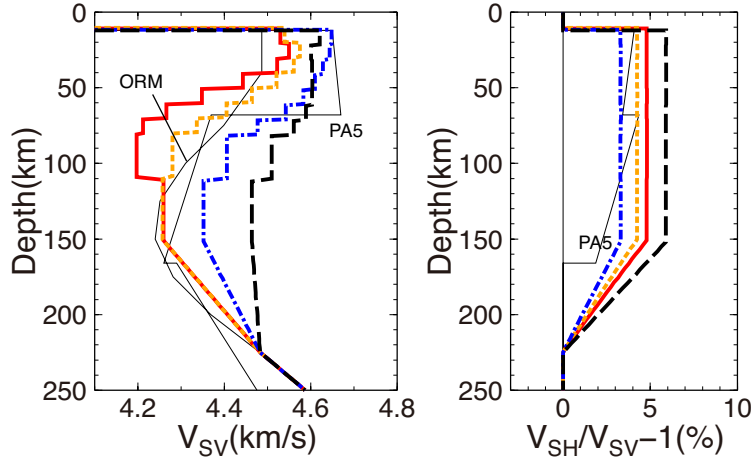


Figure 4.22: A radially anisotropic model for the seafloor ages of 100–125 Ma (PA5) by *Gaherty et al.* (1996) and V_{SV} model for seafloor ages of 30–70 Ma (ORM) by *Maggi et al.* (2006a) with the radially anisotropic models obtained in this study for the Shikoku Basin (red solid lines; 20Ma), French Polynesia (orange short-dashed lines; 60 Ma), NW Shatsky (blue chain lines; 130 Ma) and SE Shatsky (black long-dashed lines; 140 Ma) regions.

thermal and pressure dependence of mantle minerals (e.g., *Stixrude and Lithgow-Bertelloni*, 2005). For determining the velocity gradient in the whole LID, we needed to analyze surface waves at a broadband period range of ~ 5 –100 s to determine structure at depths of ~ 10 –100 km with a good depth resolution, which I could achieve in this study.

I therefore assumed the structure with the LID, LVZ and the transition zone (LLTZ) for evaluating the uncertainty of parameters such as the velocity gradient and the depth of LLTZ in Section 4.6. The results are shown in Figures 4.16–4.19 and are summarized in Table 4.1. For the Shikoku Basin region, for example, the average velocity in the LID is $V_{LID} = 4.61$ – 4.68 km/s, which is $\sim 6\%$ higher than that in the LVZ ($V_{LVZ} = 4.35$ – 4.41 km/s). The LLTZ exists at a depth of $z_c = 39$ – 48 km with a thickness (δz) less than 29 km. These values are almost consistent, but slightly shallower than the G-discontinuity beneath the northern part of the Shikoku Basin observed by *Tonegawa and Helffrich* (2012). They analyzed shear wave reflections and found a velocity drop greater than 6% at depths of 50–70 km with a thickness less than 10 km. The difference between the thickness may be reflecting the difference between regions in the Shikoku Basin. The depth of LLTZ for the NW Shatsky region is 63–85 km, which is also consistent with the value of 78–86 km by *Kawakatsu et al.* (2009) at WP2 station at the northeastern end of the NW Shatsky region in this study.

The velocity gradient in the LID ($(dV/dz)_{LID}/V_{LID}$) is estimated to be -0.1 – $0.3\%/km$, whilst that in the LLTZ ($-(dV/dz)_{LLTZ}/V_{LID}$) is steeper than $0.03\%/km$ (Table 4.1). To compare the obtained velocity gradients with thermal models, I estimated the velocity gradients based on half space cooling models (e.g., *Davis and Lister*, 1974) with various combi-

nations of parameters: thermal diffusivity of $10^{-6} \text{ m}^2/\text{s}$ and ridge temperature of 1200–1700 $^\circ\text{C}$ (*Stein and Stein, 1992*). I used values in the range shown in Table 4.1 for the parameters such as the seafloor age, z_c and δz .

The temperature gradient in the LID is, for example, calculated to be 18–41 K/km for the Shikoku Basin region. Using temperature and pressure relationships for polycrystalline olivine (*Liu et al., 2005*), the velocity gradient in the LID is predicted to be between -0.22 and -0.09 \%/km , which is lower than the range estimated from phase velocity measurements. One possible cause for this difference is crustal heterogeneity in the Shikoku Basin. As the variation of the crustal thickness exists in the Shikoku Basin region with a range of 4–15 km (*Nishizawa et al., 2011*), the structure at depths of 10–20 km cannot be interpreted as the mantle structure as discussed in Section 4.7.1. The presence of crust at the depth range may reduce the average S-wave velocity at the top of the LID and may increase the apparent velocity gradient in the LID. Another possible cause relates to the phase transition from plagioclase peridotite to pyroxene peridotite at depths of ~ 30 km (*Forsyth and Press, 1971*) and/or the presence of orthopyroxene whose pressure and temperature dependence is different from that of olivine at depths shallower than ~ 40 km. *Stixrude and Lithgow-Bertelloni (2005)* solved the equilibrium equation for a realistic mantle composition and calculated a velocity model based on the half-space cooling model. Their model indicates that the effects of the phase transition and the presence of orthopyroxene is difficult to identify from surface-wave velocities, but may produce velocity gradients in the LID about 0.14 \%/km higher than the pure olivine model. The velocity gradient of a realistic mantle model is then between -0.09 and 0.05 \%/km , which is at the lower end of the 90% confidence interval estimated from our surface-wave velocities. There is a similar discrepancy between the observed and model velocity gradient in the LID for other regions: the French Polynesia and SE Shatsky regions. This result invokes that the high velocity gradient is caused by the same mechanism such as the phase transition as discussed above, although the discrepancy is not clear for the NW Shatsky region.

In contrast, the temperature gradient in the LLTZ is estimated to be 8–20 K/km from the half space cooling models for the Shikoku Basin region. The corresponding velocity gradient is then $-(dV/dz)_{\text{LLTZ}} = 0.02\text{--}0.10 \text{ \%/km}$ (Table 4.1). If we use more realistic values of the ridge temperature, 1300–1500 $^\circ\text{C}$ (*Anderson, 2000*), then the gradient is between 0.025 and 0.085 \%/km . If we consider the realistic mantle composition (*Stixrude and Lithgow-Bertelloni, 2005*), the phase transition from orthopyroxene and spinel to garnet at a depth of ~ 60 km may decrease the gradient of thermal models. All these cases suggest that the observed velocity gradient is higher than the values predicted from the thermal models. As the similar discrepancy also exists for other three regions, we need to invoke mechanisms for producing this velocity reduction in the LLTZ in addition to the thermal effect, such as decreasing grain size (*Faul and Jackson, 2005*), partial melting (*Anderson and Sammis, 1970; Kawakatsu et al., 2009*), or the presence of water (*Karato, 2012*) in the LVZ. The sharp

velocity decrease observed by *Tonegawa and Helffrich* (2012) and *Kawakatsu et al.* (2009) may require mechanisms such as partial melting or the presence of water. *Baba et al.* (2010) also found a conductivity increase at a depth of ~ 50 km beneath the Shikoku Basin, and attributed it to the existence of water and/or partial melt at depths of 40–80 km. For any of these mechanisms, the viscosity within the LID is expected to be higher than that in the LVZ (*Fischer et al.*, 2010). I therefore interpret the LID to be the lithosphere, the LVZ to be the asthenosphere, and the LLTZ to be the lithosphere–asthenosphere boundary (LAB) region.

The depth of LLTZ becomes deeper with the increasing seafloor age as summarized in Table 4.1: 40–50 km for the Shikoku Basin region (20 Ma), 50–60 km for the French Polynesia region (60 Ma), and 60–90 km for the NW and SE Shatsky regions. It indicates that the thickness of lithosphere grows from 5–6 km (the thickness of initial crust) to ~ 40 km during the first 20 million years after the emergence of the oceanic crust, and gradually increases to ~ 80 km during the additional ~ 100 million years.

The thickness of LLTZ is difficult to constrain from surface waves due to broad sensitivity of surface waves to S-wave velocity structures. The uncertainty is especially large for the older seafloor regions, where the depth of LLTZ is deeper and the surface waves at long period has sensitivity at a broader depth range than at short periods for the shallower structures (Figure 3.3). The range is much larger than the narrow and thin range of less than ~ 10 km estimated by using conversion of body waves for the limited regions (e.g., *Kawakatsu et al.*, 2009; *Kumar and Kawakatsu*, 2011; *Tonegawa and Helffrich*, 2012). It should be noted, however, the estimated range is comparable to the range estimated by using reflection of S-waves for broader region in the Pacific Ocean by *Rychert and Shearer* (2011).

4.7.4 Possible Depth Changes in Radial Anisotropy

Our smooth radially anisotropic models (Figure 4.10) show that V_{SH} is 3%–6% larger than V_{SV} . This type of radial anisotropy is conventionally interpreted to be due to olivine LPO and/or the presence of thin layers or pockets of melt. During horizontal shearing, the fast axes (a-axes) of olivine crystals align along the horizontal flow direction and/or the slow axes (b-axes) align vertically, leading to the azimuthal average of V_{SH} becoming faster than V_{SV} (*Estey and Douglas*, 1986). Some studies have concluded that the presence of thin layers or pockets of partial melt cause radial anisotropy at wavelengths longer than the structure (e.g., *Backus*, 1962; *Forsyth*, 1975; *Schlue and Knopoff*, 1976). Although the melt distribution tends to dip from the horizontal slip plane under shear stress in laboratory experiments, melt can concentrate along the slip plane if the olivine b-planes are aligned along the slip plane due to the formation of LPO (*Kohlstedt and Zimmerman*, 1996).

For several decades, a number of investigations have focused on examining vertical variations in radial anisotropy (e.g., *Schlue and Knopoff*, 1976; *Cara and L  v  que*, 1988). Al-

though I attempted to determine the depth dependence of radial anisotropy using broadband surface waves, models with constant anisotropy can almost completely explain the phase velocity measurements (Figure 4.9 and Figures 4.11–4.13). Amplitude difference of anisotropy in the LID and LVZ is difficult to estimate due to a tradeoff between the two parameters as evidenced by the negative trend in Figure 4.16 for the Shikoku Basin region or the difficulty of determining radial anisotropy in the LVZ as evidenced by the large uncertainty in Figure 4.19 for the SE Shatsky region. However, the distribution of anisotropy in the LID and LVZ indicates the possibility of greater anisotropy in the LVZ than in the LID for the Shikoku Basin region. The uncertainty range of $\delta V_{LVZ} - \delta V_{LID}$ is 0% to 5%. This result is consistent with the large radial anisotropy identified within the LVZ beneath oceanic basins by tomographic studies (*Ekström and Dziewonski, 1998; Nettles and Dziewonski, 2008*). The stronger radial anisotropy in the LVZ can be interpreted to result from the presence of thin layers or pockets of partial melt in the asthenosphere (*Schlue and Knopoff, 1976; Kawakatsu et al., 2009*), or by enhanced LPO due to strain accumulation in the asthenosphere (*Podolefsky et al., 2004; Becker et al., 2008; Behn et al., 2009*). However, in order to determine the change of radial anisotropy at depths shallower than 100 km, we need to analyze the 1T mode at periods shorter than ~ 25 s as indicated by the sensitivity kernel in Figure 3.3.

Chapter 5

1D AZIMUTHALLY ANISOTROPIC STRUCTURES

5.1 Introduction

The pattern of azimuthal anisotropy for a given elastic velocity can be described by 2θ and 4θ terms for V_{PH} , 2θ term for the V_{SV} , 4θ term for the V_{SH} (*Backus, 1965; Smith and Dahlen, 1973; Montagner and Nataf, 1986*), where θ is the azimuth (Appendix A). As the Rayleigh waves are mostly sensitive to V_{SV} , the 2θ pattern dominates the azimuthal anisotropy of the Rayleigh waves (*Montagner and Nataf, 1986*). I therefore fitted the azimuthal dependence of phase velocities of Rayleigh waves by 2θ in Chapter 3.

The present chapter describes the inversion for the depth variation in the azimuthal anisotropy of V_{SV} for each regions including the model parameters (§5.2), the resultant azimuthally anisotropic structures (§5.3), an additional S-wave splitting analysis for the French Polynesia region (§5.4), and the discussions (§5.5). The S-wave splitting analysis is needed to reveal the lateral heterogeneity in azimuthal anisotropy in the French Polynesia region indicated by a previous study (*Barruol et al., 2009*). The analysis determines the dependence of the “velocity of horizontally-polarized and vertically-propagating S-wave” on the polarization azimuth (e.g., *Ando, 1984; Fukao, 1984*). The estimated azimuthal anisotropy is theoretically same as the dependence of the “velocity of vertically-polarized and horizontally-propagating S-wave” (V_{SV}) on the propagation azimuth estimated from Rayleigh waves (e.g., *Montagner et al., 2000*). The result of shear-wave splitting analysis is used to discuss the laterally heterogeneity of azimuthal anisotropy beneath the French Polynesia region in Section 5.5.1. The section also includes the discussion about the validation of laterally homogeneous structure beneath other regions. The effect of the azimuthal anisotropy of V_{PH} needs to be considered especially when we use the 1S mode. The model including the effect will be discussed in Section 5.5.2. I then discuss the depth variation in the azimuthal anisotropy in Section 5.5.3, and the interpretation for the azimuths of maximum S-wave velocity in Section

5.2 Model Parameters and Inversion Method

The azimuthal dependence of Rayleigh waves was fitted by the 2θ term in Chapter 3 based on the clear domination of 2θ term for the high quality measurements such as those at a period of 34 s for the French Polynesia region (Fig. 3.38) and at a period of 20 s for the NW Shatsky region (Fig. 3.26). I therefore estimate the 2θ term of V_{SV} .

I describe the azimuthal dependence of shear-wave velocity, V_{SV} , by $V_{SV}^0(z)(1+A'_C(z)\cos 2\theta+A'_S(z)\sin 2\theta)$, as a function of depth (z), and estimate $A'_C(z)$ and $A'_S(z)$ in each of eight layers in the uppermost mantle at depths of 12–220 km by assuming a constant value for each layer. The crust is again assumed to be isotropic based on weak anisotropy compared to that in the mantle reported by previous studies (e.g., *Christensen and Salisbury, 1975; Dunn and Toomey, 2001*) (see §4.2 for the detail). The model parameters are assumed to be constant for four layers at depths of 40–220 km for the SW Shatsky region, where I only analyzed surface waves at periods shorter than 25 s. The model azimuthal anisotropy of Rayleigh waves is then given by,

$$c_m(\omega) = c_m^0(\omega) \left[1 + \tilde{A}_C(\omega) \cos 2\theta + \tilde{A}_S(\omega) \sin 2\theta \right], \quad (5.1)$$

where,

$$\tilde{A}_C(\omega) = \int_z [K_\beta(z, \omega)] A'_C(z) dz, \quad (5.2)$$

and

$$\tilde{A}_S(\omega) = \int_z [K_\beta(z, \omega)] A'_S(z) dz, \quad (5.3)$$

where K_β is the sensitivity of phase velocity to the S-wave velocity structure (§3.2). The sensitivity kernel is obtained from the isotropic model (Fig. 4.6) for the SW Shatsky and the smooth radially anisotropic models (Fig. 4.10) for other four regions. The use of sensitivity kernels for the isotropic or radially anisotropic model is valid if the second-order perturbation can be neglected, i.e., the intensity of anisotropy is less than $\sim 10\%$.

The misfit function is defined by,

$$E'_{AA} = \sqrt{\sum_{m,\omega} \left[\left\{ \frac{\bar{A}_C^m(\omega) - \tilde{A}_C^m(\omega)}{\Delta A_C^m(\omega)} \right\}^2 + \left\{ \frac{\bar{A}_S^m(\omega) - \tilde{A}_S^m(\omega)}{\Delta A_S^m(\omega)} \right\}^2 \right] / \sum_m 2N_m}, \quad (5.4)$$

where N_m is the number of measurements for the mode m , $\bar{A}_C^m(\omega) = \bar{A}_2^m(\omega) \cos 2\bar{\phi}_{\max}(\omega)$ and $\bar{A}_S^m(\omega) = \bar{A}_2^m(\omega) \sin 2\bar{\phi}_{\max}(\omega)$ are the bootstrap average of the estimated azimuthal anisotropy of phase velocity, $\Delta A_C^m(\omega)$ and $\Delta A_S^m(\omega)$ are the error on the phase velocity measurements.

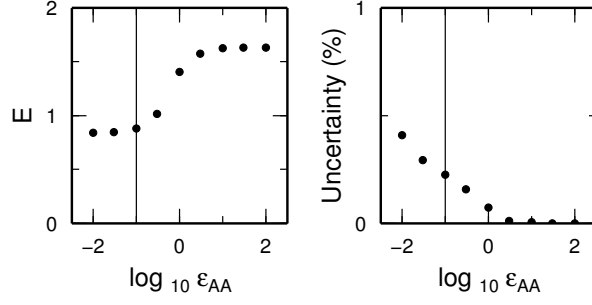


Figure 5.1: An example of trade-off between the minimum misfit function, E_{AA} , and the average uncertainty of model parameters ($A_{C,S}^i$; $i = 1, \dots, 8$) a function of ϵ_{AA} for the SE Shatsky region.

The smoothing term is again introduced to reduce the uncertainty related to the trade-off between adjacent layers, which is given by,

$$E'_{AA} = E_{AA} + \epsilon_{AA} R_{AA}, \quad (5.5)$$

$$R_{AA} = \sum_{i=1}^{N-1} \left[\left(A_C^{''i+1} - A_C^{''i} \right)^2 + \left(A_S^{''i+1} - A_S^{''i} \right)^2 \right], \quad (5.6)$$

where ϵ_{sv} is a constant, $A_C^{''i}$ and $A_S^{''i}$ are A'_C and A'_S in the i th layer and $N = 8$ is the number of layers. The model uncertainty was estimated by the measurements obtained by the bootstrap method (Appendix B) where one hundred values ($A_C^{m,l}$ and $A_S^{m,l}$; $l = 1, \dots, 100$) were obtained for mode m . For the SW Shatsky region, where the measurement at periods longer than 20 s does not exist, I assumed that the model is constant over the depth range of 40–220 km from the fifth layer to the eighth layer.

5.3 Smooth Azimuthally Anisotropic Structures

Figure 5.1 shows the misfit function (E_{AA}) and the average of model uncertainties in the eight layers as a function of ϵ_{AA} for the SE Shatsky region. As the misfit function gradually decreases with ϵ_{AA} , it is difficult to choose an appropriate smoothing parameter. I choose the value of $\epsilon_{AA} = 0.1$ somewhat arbitrary to obtain models with the uncertainty of peak-to-peak intensity ($2A_2$) of 0.5% for all five regions.

Figures 5.2–5.6 show the fitting between the measured and model intensities of surface-wave azimuthal anisotropy, and the model intensity of S-wave azimuthal anisotropy for five regions. The fitting is incomplete especially for the values with large uncertainties, which cannot be fitted even if a smaller smooth value is used. The largest deviation exists for the Shikoku Basin region at a period of ~ 30 s. The measurements is difficult to fit by the one-dimensional azimuthally anisotropic model. Although the estimated intensity is consistent for two methods (Fig. 5.2), the fastest azimuths are inconsistent for two methods

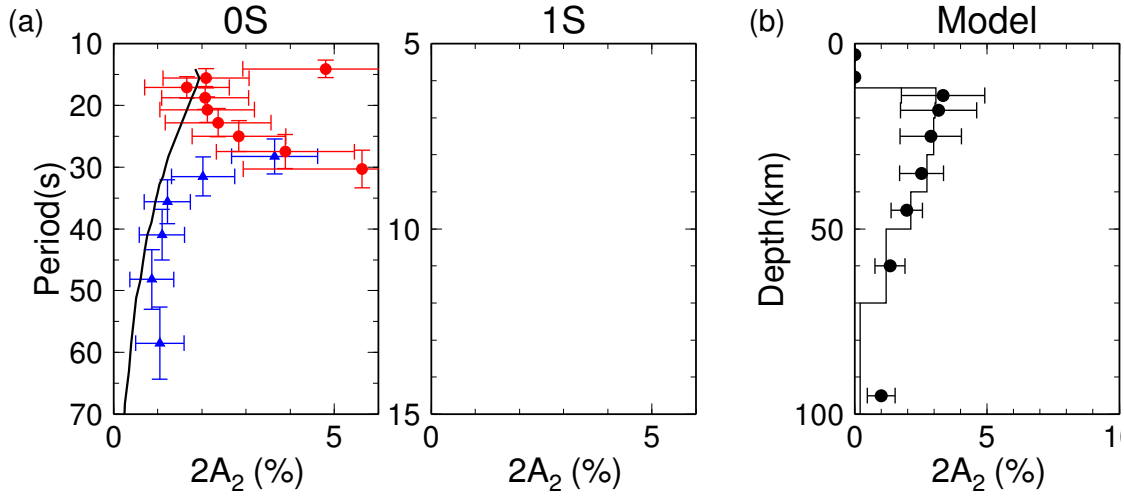


Figure 5.2: Intensity of azimuthal anisotropy for the Shikoku Basin region. (a) Each point shows the peak-to-peak intensity of azimuthal anisotropy, $2A_2$, for the phase velocities of Rayleigh waves as a function of period. Horizontal and vertical error bars show the uncertainty and the range of band-pass filter, respectively. The solid line shows the theoretical values the models shown in (b). (b) The model for the peak-to-peak intensity of azimuthal anisotropy of S-wave velocity (V_{SV}) corresponding to $\epsilon_{AA} = 0.1$.

as previously shown in Figure 3.29. One possible interpretation is that the measurements are biased due to insufficient azimuthal coverage for this region (Fig. 3.25 left and Fig. 3.38 left) compared to other regions. The estimation of the intensity of anisotropy may be too much constrained by the small variation at a limited azimuthal range of 120° – 210° for both methods. For the ambient noise analysis, such a small apparent variation may be produced by the source heterogeneity (see detail in §3.3.5) at periods longer than ~ 30 s, where the wavelength becomes about the half of the interstation distance. For the teleseismic event analysis, the apparent variation may be produced by the strong ray bending at a period of ~ 40 s caused by the low-velocity anomaly beneath the Mariana back-arc spreading region between the array and the seismicity (*Isse et al.*, 2006b). As it is difficult to specify the cause of the variation from the current datasets, I regards the obtained models as the rough representations of the azimuthal anisotropy within the uppermost mantle especially for the Shikoku Basin region.

Figure 5.7 summarizes the obtained one-dimensional azimuthally anisotropic structure for five regions including the intensity and the azimuth of maximum S-wave velocity (V_{SV}). The intensity tends to decrease with depth especially for the NW and SW Shatsky regions. The fastest azimuths are shown in Figure 5.8 for the Shikoku Basin and three regions around the Shatsky Rise. Those for the French Polynesia region are shown in Figure 5.9. The fastest azimuth is NW-SE direction for the Shikoku Basin, French Polynesia and NW Shatsky regions, whereas it is W-E direction for the SE Shatsky, and NE-SW direction for the SW

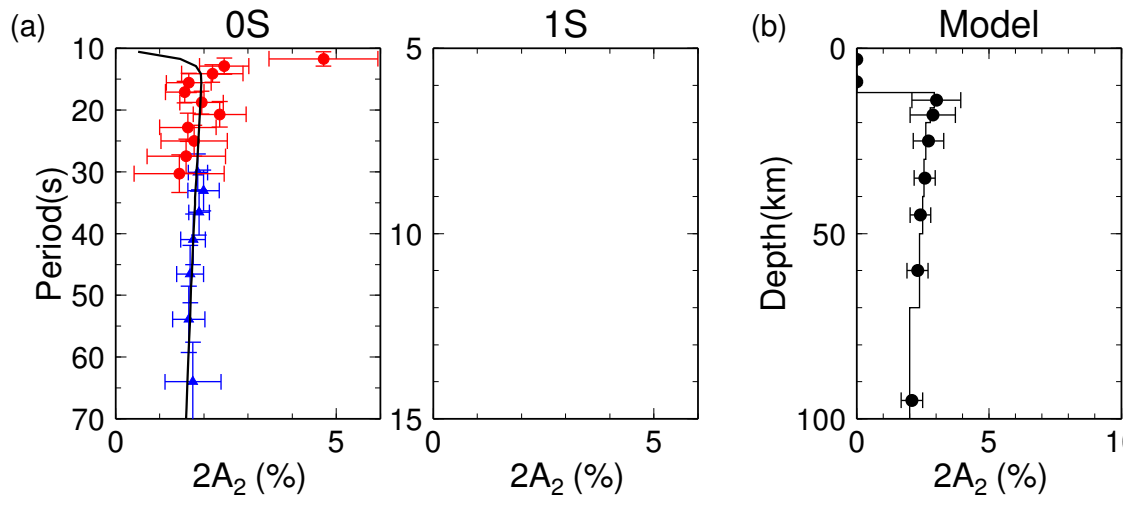


Figure 5.3: Same as Figure 5.2, but for the French Polynesia region.

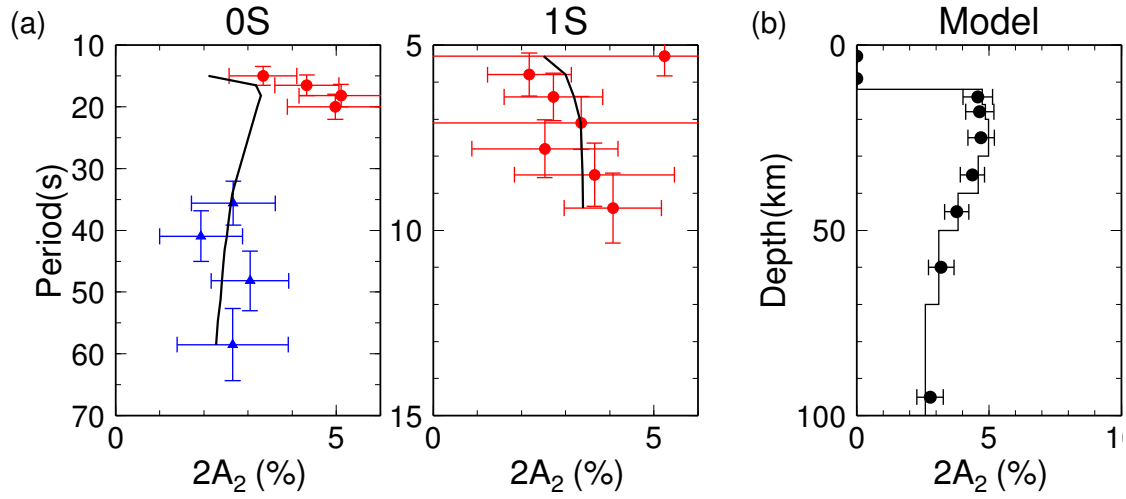


Figure 5.4: Same as Figure 5.2, but for the NW Shatsky region.

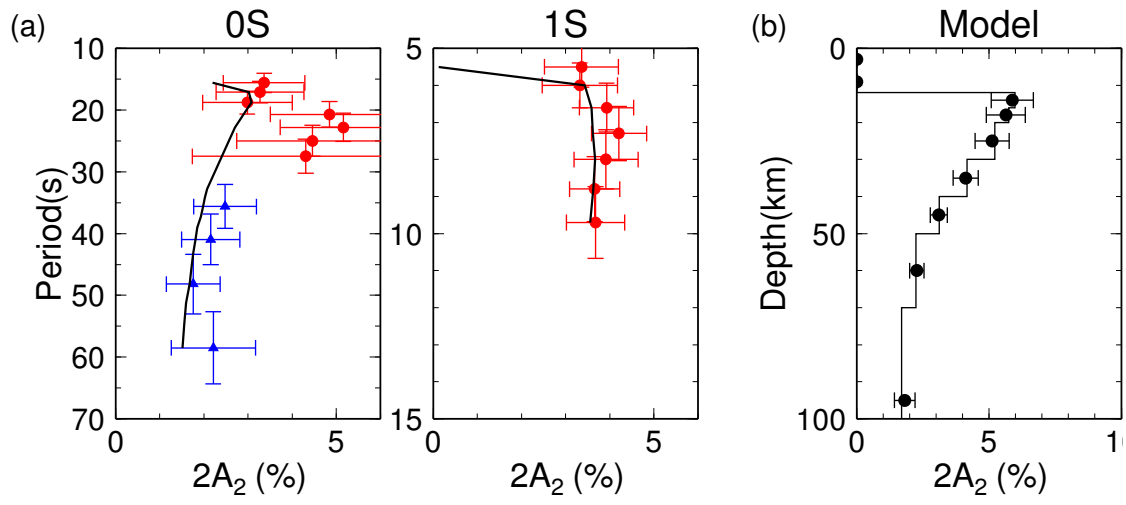


Figure 5.5: Same as Figure 5.2, but for the SE Shatsky region.

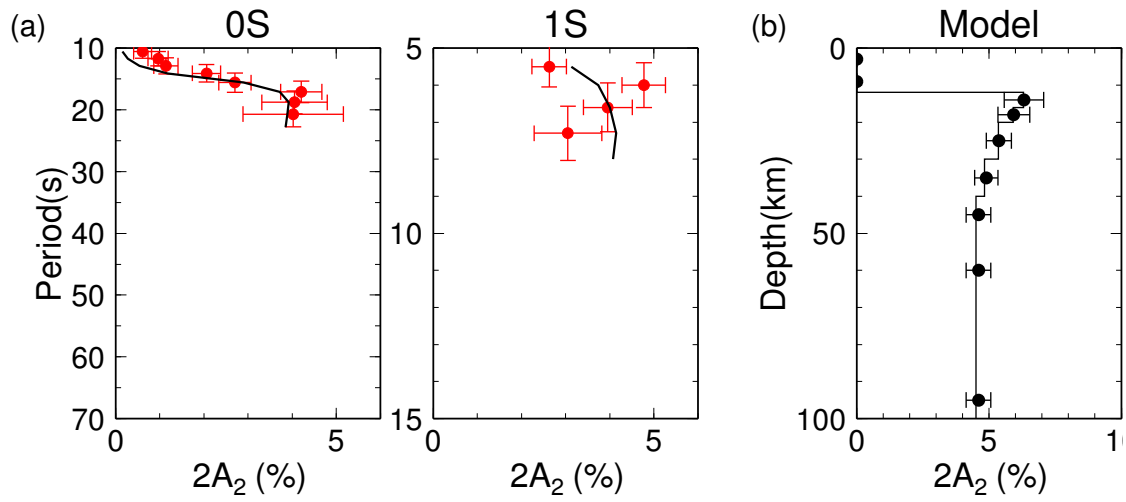


Figure 5.6: Same as Figure 5.2, but for the SW Shatsky region.

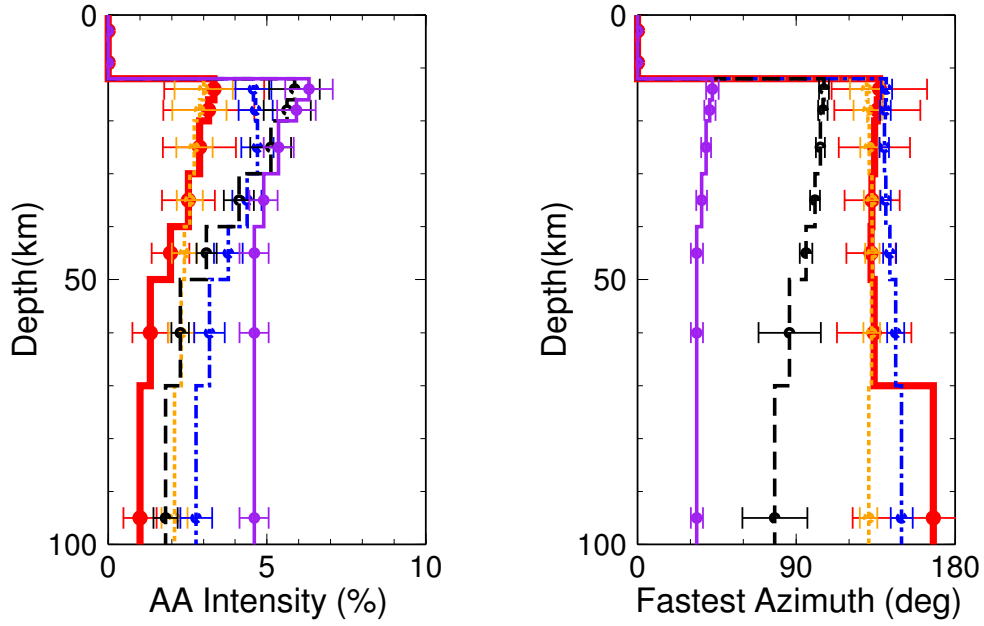


Figure 5.7: Azimuthally anisotropic models for the Shikoku Basin (red solid lines; 20Ma), French Polynesia (orange short-dashed lines; 60 Ma), NW Shatsky (blue chain lines; 130 Ma), SE Shatsky (black long-dashed lines; 140 Ma) and SW Shatsky (purple solid lines; 155 Ma) regions. The intensity of V_{SV} anisotropy (left) and the azimuth of maximum velocity (right).

Shatsky regions.

5.4 Shear Wave Splitting Analysis

The splitting of S-wave occurs when it propagates through an anisotropic layer, which is useful to reveal the lateral heterogeneity of azimuthal anisotropy. I applied the method by *Silver and Chan* (1991) to the records for the French Polynesia region to reveal the lateral heterogeneity of azimuthal anisotropy within the array. The events were first chosen with three criteria: (i) the moment magnitude greater than 5.5 and (ii) the epicentral distance longer than 9000 km or the hypocenter depth deeper than 200 km. The events with epicentral distances longer than 9000 km show the arrival of SKS and/or SKKS wave, whose splitting mainly reflect the azimuthal anisotropy beneath the station integrated from the core-mantle-boundary to the surface. The events with shorter epicentral distances show the arrival of direct S wave, whose splitting reflect the azimuthal anisotropy beneath both the hypocenter and the station. The S-wave from a event with a depth shallower than 200 km should not be used to avoid the effect of near-source anisotropy (e.g., *Long and van der Hilst*, 2005)

The waveforms of horizontal components were then band-pass filtered with a period range of 10–20 s, and were discarded if the signal-to-noise ratio is lower than 2, where the signal

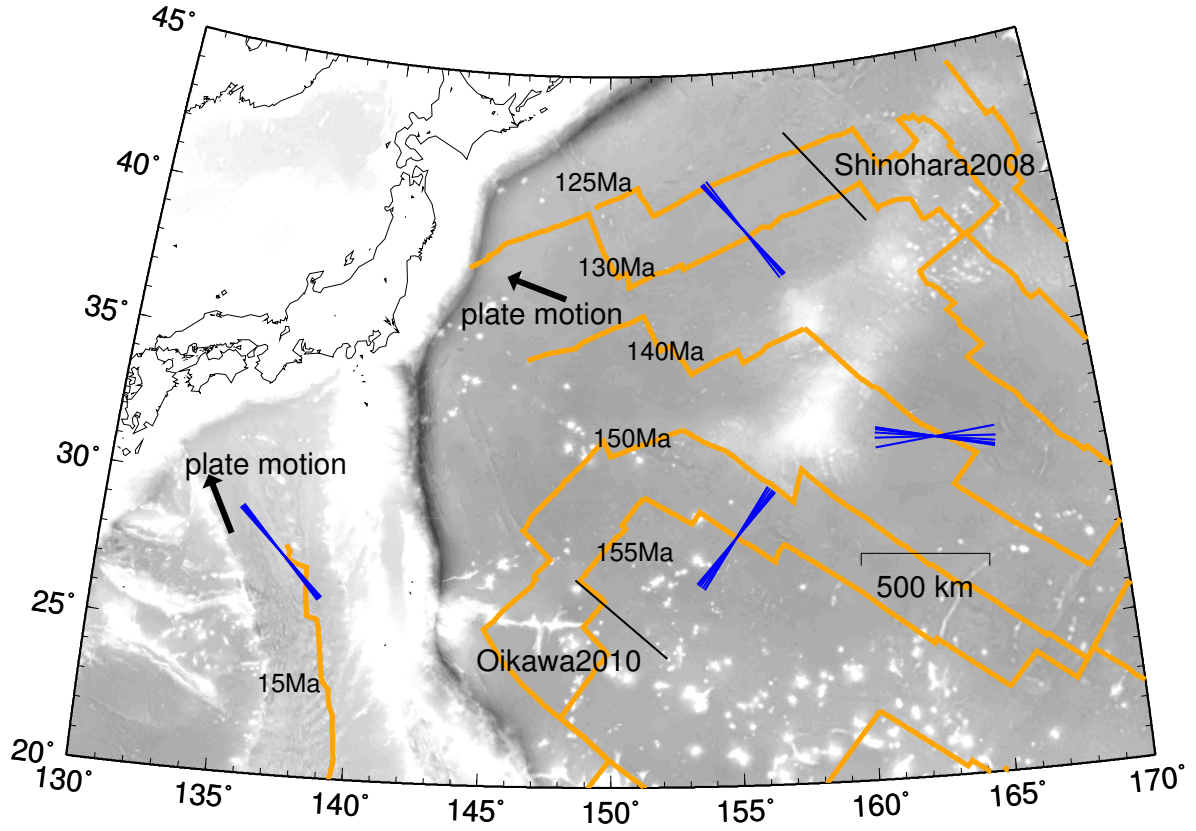


Figure 5.8: Blue bars show the azimuths of maximum S-wave velocity V_{SV} in each of six layers at depths of 12–70 km for the Shikoku Basin (SB) region, and NW, SE and SW Shatsky regions. A black bar labeled Shinohara2008 shows the fastest azimuth of Pn and Sn velocity by *Shinohara et al.* (2008), whereas the bar labeled Oikawa2010 shows the azimuth of a survey line that has faster Pn velocity than a line perpendicular to it (*Oikawa et al.*, 2010).

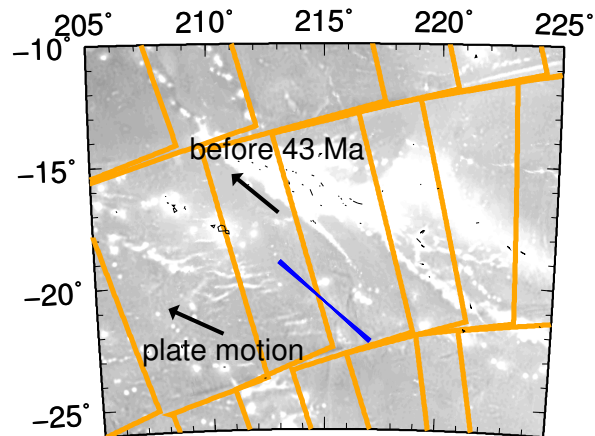


Figure 5.9: Same as Figure 5.8, but for the French Polynesia region.

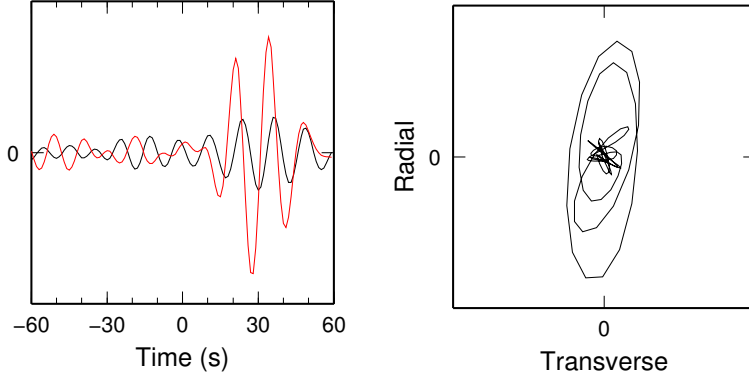


Figure 5.10: An example of normalized waveforms showing splitting of SKKS wave at station 1 in the French Polynesia region for an event occurred at 1:13, 18th February 2010 (UT). The epicentral distance is 143° . (Left) The radial and transverse components for the time-window of signal (0–60 s), and that for calculating noise level (-60–0 s). (Right) The particle motion of the waveforms shown in left.

amplitude is the root mean square amplitude of a 60-s long record centers at the peak of arrived signal, and the noise amplitude is that of a 60-s long record prior to the time-window for the signal amplitude. The range of band-pass filter is chosen to analyze the period range of minimum noise level for BBOBSs (Fig. 2.6). Figure 5.10 shows an example of SKKS waveform, whose particle motion is elliptical due to splitting.

Silver and Chan (1991) proposed various strategies to search for the optimal splitting parameters, the splitting time (δt) and the azimuth of maximum S-wave velocity (ϕ_{\max}), that give the linear particle motion after the correction of splitting. I chose the strategy that minimizes the ratio between the smaller eigen value and the summation of eigen values, $\lambda_{\text{ratio}} = \lambda_2/(\lambda_1 + \lambda_2)$, to search the optimal splitting parameters. By choosing an optimal combination of parameters, the linear particle motion before the splitting can be reconstructed as shown by an example in Figure 5.11.

The uncertainty of splitting parameters are usually large as indicated by the broad distribution of small λ_{ratio} shown in Figure 5.11. I reduced the uncertainty by averaging λ_{ratio} of all events for each station as done by *Wolfe and Silver* (1998). Figure 5.12 shows examples of the averaged values. The distribution of small λ_{ratio} is narrow and has less trade-off between two splitting parameters compared to the distribution for each event (Figure 5.11). In addition, we can estimate the uncertainty of splitting parameters by the bootstrap method (Appendix B): I estimated one hundred parameters by selecting one hundred combinations of events randomly with allowing overlaps, and defined the one standard deviation as the uncertainty.

Figure 5.13 shows the estimated splitting parameters for each station. The number of available events were 8–14, in which more than half events showed splitting as summarized in Table 5.1 (see locations of epicenters in Fig. 5.14). The splitting time is 1.0–1.3 s for

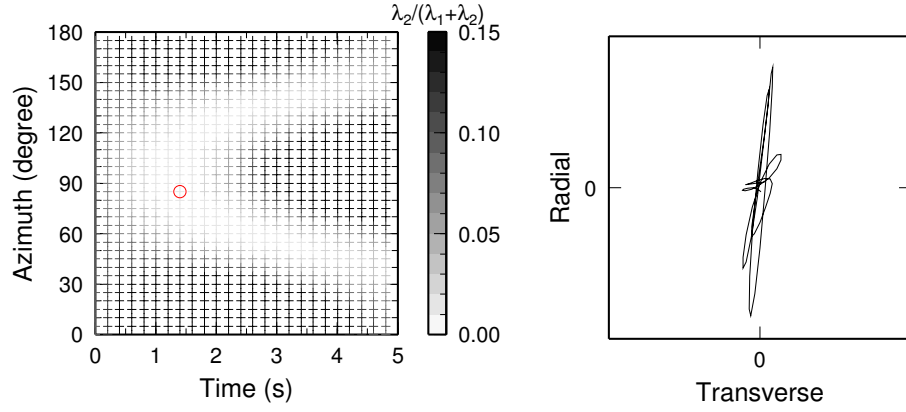


Figure 5.11: An example of estimation of splitting parameters for the station and event same as Figure 5.10. (Left) The ratio between small eigen value and the summation of eigen values, $\lambda_2/(\lambda_1 + \lambda_2)$, as a function of assumed lag time and assumed azimuth of maximum S-wave velocity. (Right) The particle motion after the correction of splitting based on the parameters that give minimum of $\lambda_2/(\lambda_1 + \lambda_2)$ (red circle in the left panel).

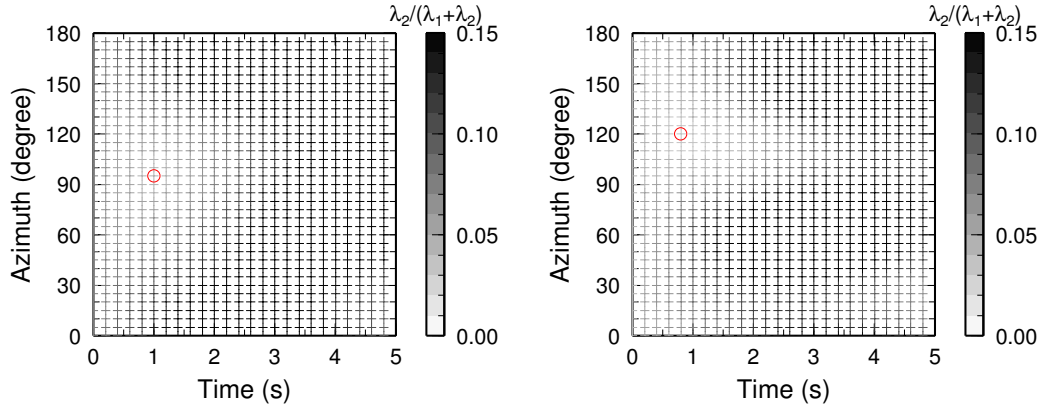


Figure 5.12: The ratio between eigen values, $\lambda_2/(\lambda_1 + \lambda_2)$, averaged for all events at station 1 (left) and 3 (right) in the French Polynesia region.

Table 5.1: Station location and splitting parameters with the numbers of events.

Station	Latitude	Longitude	ϕ_{\max} ($^{\circ}$)	δt (s)	Split Events	Unsplit Events
1	-19.47 $^{\circ}$	-148.05 $^{\circ}$	96 \pm 5	1.0 \pm 0.2	4	4
2	-20.96 $^{\circ}$	-146.44 $^{\circ}$	108 \pm 16	1.1 \pm 0.4	5	3
3	-19.93 $^{\circ}$	-146.02 $^{\circ}$	118 \pm 7	0.9 \pm 0.3	7	5
4	-18.42 $^{\circ}$	-144.99 $^{\circ}$	148 \pm 14	1.1 \pm 0.7	8	4
5	-17.50 $^{\circ}$	-144.51 $^{\circ}$	152 \pm 38	2.3 \pm 1.8	7	4
6	-18.81 $^{\circ}$	-142.29 $^{\circ}$	127 \pm 17	1.1 \pm 0.9	5	6
7	-19.94 $^{\circ}$	-142.69 $^{\circ}$	137 \pm 7	1.1 \pm 0.3	9	5
8	-20.95 $^{\circ}$	-143.76 $^{\circ}$	150 \pm 21	1.3 \pm 0.6	9	2
9	-22.17 $^{\circ}$	-144.70 $^{\circ}$	107 \pm 10	1.2 \pm 0.2	9	3

almost all stations except for the station 5, which gives 2.6 ± 1.8 s. The uncertainty of the azimuth is also large for station 5, $152^{\circ} \pm 38^{\circ}$. For other stations, the uncertainty for the splitting time is 0.2–0.9 s, and the uncertainty of the azimuth is less than 22° . The azimuth is almost parallel to each other, although it is slightly northward for the northeastern stations (stations 4–8), and is slightly westward for the northwestern station (station 1).

5.5 Discussions of the Azimuthally Anisotropic Models

5.5.1 Lateral Heterogeneity of Isotropic and Anisotropic Structures

I interpreted the phase-velocity anomalies by considering azimuthal anisotropy in Chapter 3. Here I consider another possible interpretation of the lateral heterogeneity of phase-velocity anomalies. Figure 5.15 shows the phase-velocity anomalies of the 0S mode for the eastern array of SW Shatsky region as a function of longitude. The phase-velocity anomalies at periods of 19 s are about 3% in the eastern part of eastern array, whereas the anomalies are almost zero at the western part of the eastern array. The variation in phase velocity of the 0S mode at periods of 19 s becomes about half the variation in S-wave velocity at depths of 20–50 km. A phase-velocity anomaly of about 3%, therefore, would indicate an S-wave velocity anomaly of about 6% at depths of 20–50 km in the uppermost mantle.

Both lateral heterogeneity (Fig. 5.15) and azimuthal anisotropy (Fig. 3.28) can explain the phase-velocity anomalies, and the identification of the cause of the phase-velocity anomalies from current data is impossible. I, however, consider that the azimuthal anisotropy is the main cause of the phase-velocity anomalies. An S-wave velocity anomaly of 6% corresponds to the change of rock composition or the temperature variation of 600 K if we use the temperature derivative of olivine crystals by *Liu et al.* (2005). Such large lateral heterogeneity over

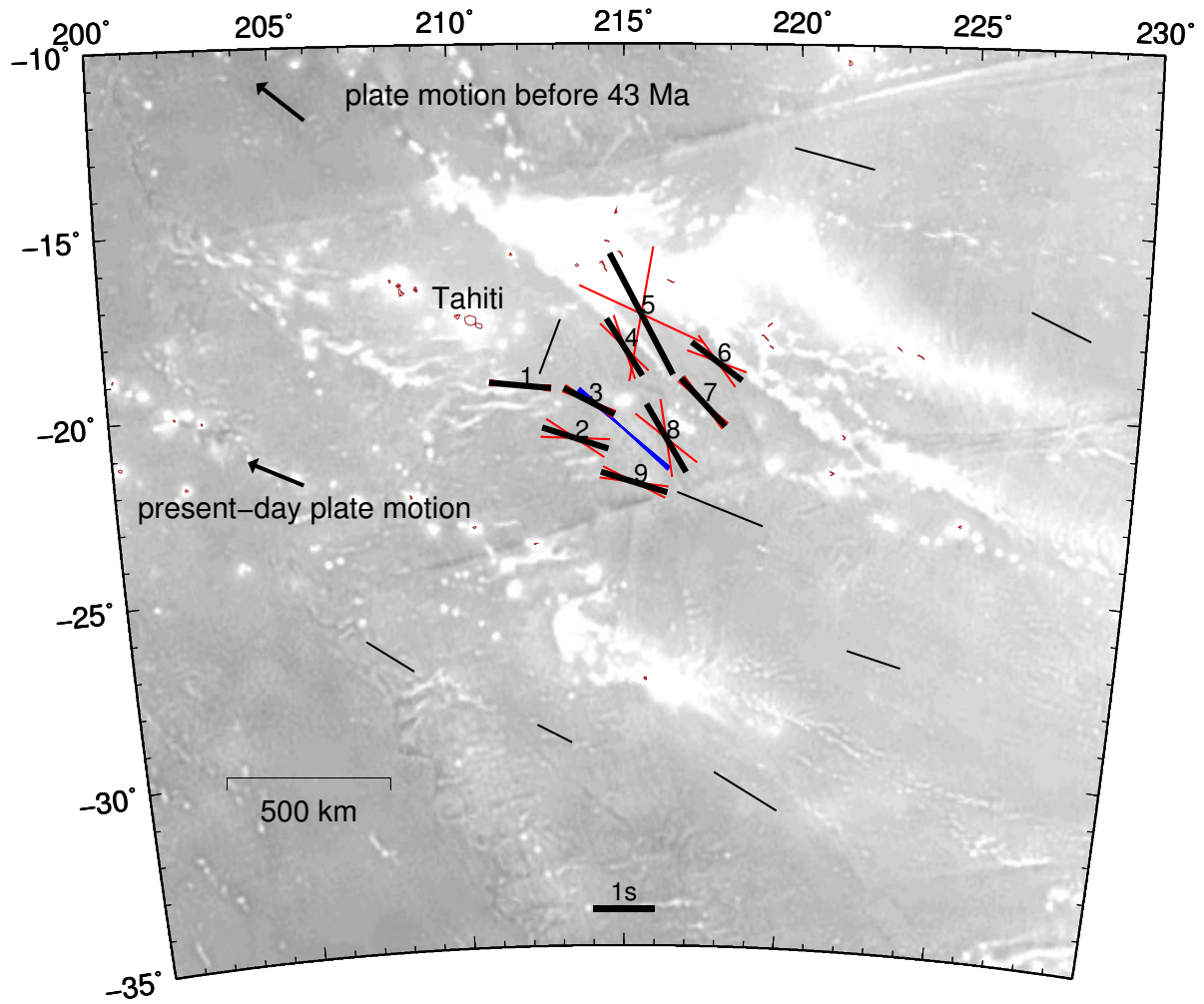


Figure 5.13: The azimuth of maximum S-wave velocity estimated by the shear-wave splitting analysis in this study (thick black bars with the red bars showing the uncertainty) and by *Barruol et al.* (2009) (thin black bars). The lengths of bars show the splitting time. Blue bars show the azimuth at depths of 12–70 km estimated from surface waves.

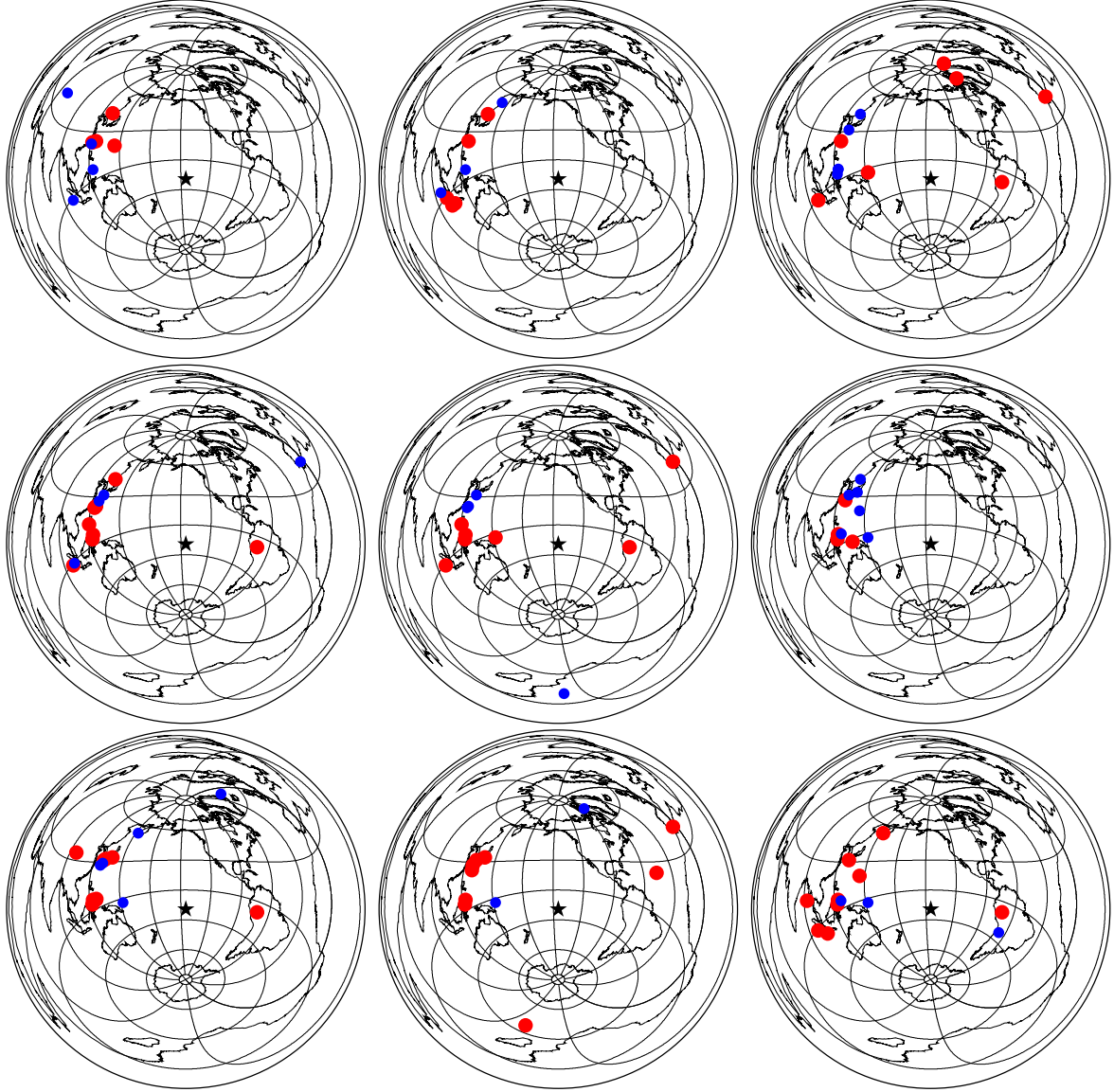


Figure 5.14: The epicenters of split (red) and unsplit (blue) events. The star shows the location of the station array.

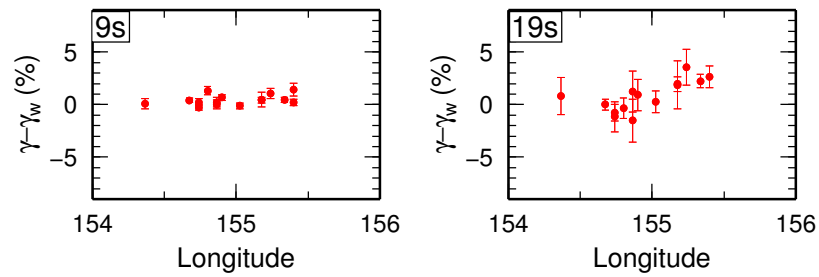


Figure 5.15: Phase-velocity anomalies of the 0S mode in the eastern array as a function of longitude at the center between two stations.

a horizontal distance of 50-100 km is not expected in this region of almost uniform age and water depth. In comparison, large azimuthal anisotropy of up to 10% is observed in various oceanic regions by refraction surveys, especially in the region with large shear deformation due to fast spreading (e.g., *Song and Kim*, 2012) including the western array of PLATE project (*Oikawa et al.*, 2010). Pn anisotropy in both the eastern and western arrays has been estimated to be 8%–10% by using high frequency phases generated by earthquakes in the western Pacific trenches (*Shintaku et al.*, submitted). The seafloor in the eastern array, where I estimated azimuthal anisotropy in the SW Shatsky region, has a high half spreading rate of 5 cm/yr (*Nakanishi et al.*, 1989, 1992; *Müller et al.*, 2008). The presence of strong azimuthal anisotropy is, therefore, not surprising in this region.

The trade-off between lateral heterogeneity and azimuthal anisotropy is expected to be smaller for other four regions because of larger number of available stations compared to that for the SW Shatsky region. The presence of crustal lateral heterogeneity should be, however, discussed for the Shikoku Basin and French Polynesia regions. In these regions, the sea topography is highly heterogeneous and the crustal thickness is thicker when the topography is high (e.g., *Patriat*, 2002; *Nishizawa et al.*, 2011) as already discussed in Section 4.7.1. The heterogeneity of the crustal thickness causes strong heterogeneity at depths shallower than ~ 20 km. The effect to the azimuthal anisotropy is, however, expected to be small in this study because I only used the 0S mode for the estimation of azimuthal anisotropy, which has little sensitivity to S-wave velocity at depths shallower than ~ 20 km (Figure 3.3).

The lateral heterogeneity of azimuthal anisotropy should be also discussed for the French Polynesia region. *Barruol et al.* (2009) analyzed S-wave splitting by using BBOBS records of the PLUME project (*Barruol*, 2002; *Suetsugu et al.*, 2005) to investigate the lateral variation in azimuthal anisotropy. They revealed that the fastest azimuth is almost consistent with the current plate motion as already shown by onland records (*Fontaine et al.*, 2007) except for the region southwest of an active hotspot (at the southeast of the Tahiti island) where the azimuth is almost perpendicular to the plate motion (Figure 5.13). Based on the calculation of mantle flow, they concluded that the fastest azimuth is reflecting the mantle flow disturbed by the presence of a plume beneath the Tahiti island. The reliability of their measurements are, however, insufficient because the SKS wave from only one event showed splitting at the station southwest of the Tahiti island in their study.

I estimated the azimuthal anisotropy by analyzing the S-wave splitting from BBOBS records of the TIARES project (*Suetsugu et al.*, 2012). As 4–9 events showed splitting of S, SKS or SKKS waves for each station (Table 5.1), the obtained pattern shown in Figure 5.13 is more reliable compared to the result at the southeast of the Tahiti island estimated from one splitting event by *Barruol et al.* (2009). The azimuths for the southwestern stations of 2, 3 and 9 are 107° – 118° (287° – 298°), which are consistent with the direction of current plate motion, 296° (HS3-NUVEL-1; *Gripp and Gordon*, 2002), as already inferred by previous S-wave splitting studies in this area (*Fontaine et al.*, 2007; *Barruol et al.*, 2009). The azimuths

for the northeastern stations of 4–8 are slightly northward of 127° – 152° (307° – 332°), whereas those for the northwestern station of 1 is slightly westward of 96° (276°). This result indicates that the mantle flow beneath the area of this study may be perturbed by the presence of the plume beneath the Tahiti island as discussed by *Barruol et al.* (2009).

There is an agreement between the azimuths of maximum S-wave velocity estimated from surface waves and from these from the S-wave splitting. The fastest azimuth estimated from surface waves is $130^\circ \pm 15^\circ$ between the values for both southwestern stations (station 1–3 and 9) of 96° – 118° and the values for the northeastern stations (station 4–8) of 127° – 152° . It can be interpreted by averaging the two areas for the different azimuthal dependence of phase velocities with the same intensity: $A_2 = 1$ and $\phi_{\max} = 110^\circ$ for the first half area, and $A_2 = 1$ and $\phi_{\max} = 140^\circ$ for the second half area. The azimuthal dependence of phase velocity is then $\cos 2(\phi - 110^\circ)$ and $\cos 2(\phi - 140^\circ)$ for two areas, and $\cos(140^\circ - 110^\circ) \cos 2[\phi - (110^\circ + 140^\circ)/2] = 0.86 \cos 2(\phi - 125^\circ)$ for the average. Although there may be existing heterogeneity of azimuthal anisotropy beneath the French Polynesia region, we can estimate the average of fastest azimuths with a small reduction in the intensity of azimuthal anisotropy of up to $\sim 14\%$ if the variation in the azimuths is less than 30° .

The fastest azimuth for the station 1 is largely different from the average for all other stations. If we discard the result for station 1 and consider the uncertainty for the estimation, all the fastest azimuths for stations 2–9 fall within the range between 117° and 134° , whereas the value for the station 1 is $96^\circ \pm 5^\circ$ (Table 5.1). It indicates that the fastest azimuth estimated by surface waves may be affected by strong lateral variation in the fastest azimuths near station 1. I therefore re-estimated the azimuthal anisotropy of surface waves by discarding the records of station 1. Figure 5.16 shows the result as well as the model obtained by using all the stations. The intensity of azimuthal anisotropy is $\sim 20\%$ larger for the model without station 1 than the model for all stations at depths shallower than 70 km. The fastest azimuth is also slightly changed from the value for all stations of $312^\circ \pm 4^\circ$ ($132^\circ \pm 4^\circ$) to the value without station 1 of $318^\circ \pm 4^\circ$ ($138^\circ \pm 4^\circ$) at depths shallower than 70 km. These results indicate that the intensity of azimuthal anisotropy and the fastest azimuth is changed due to the lateral variation in the fastest azimuth near station 1 at shallow depths.

5.5.2 Effect of P-wave Anisotropy

The azimuthal anisotropy of P-wave and S-wave can be predicted theoretically for a given elastic constants (*Backus*, 1965; *Montagner and Nataf*, 1986). The pattern of azimuthal anisotropy can be described by 2θ and 4θ terms for V_{PH} , 2θ term for the V_{SV} , 4θ term for the V_{SH} , where θ is the azimuth. The 2θ term dominates the anisotropic pattern of V_{PH} for the case of LPO in the upper mantle with the horizontal alignment of a-axes of olivine crystals (*Backus*, 1965; *Crampin*, 1978, 1982; *Montagner and Nataf*, 1986). This anisotropy

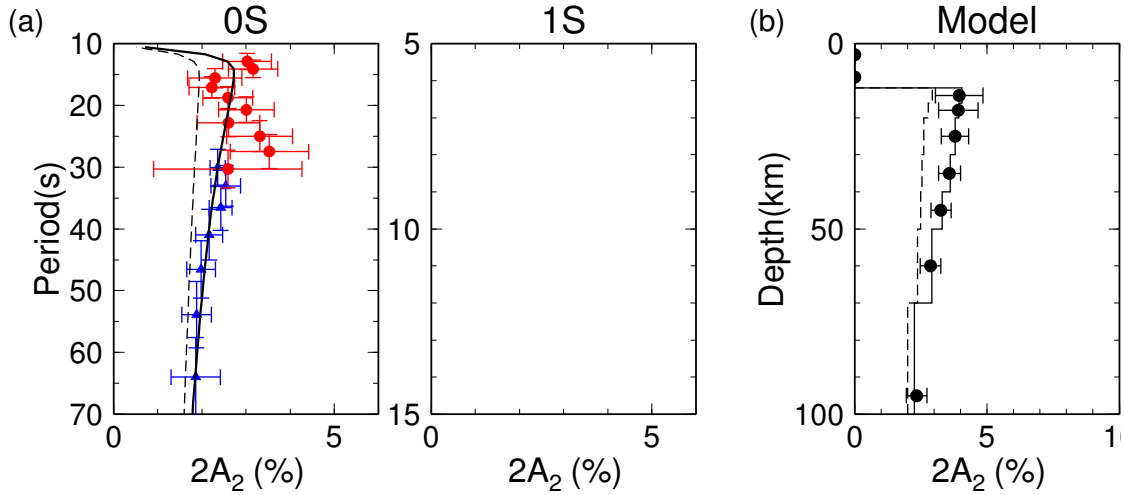


Figure 5.16: Same as Figure 5.2, but for the French Polynesia region except for the north-western station (station 1 in Figure 2.2). Dashed lines correspond to the model obtained by using all nine stations shown in Figure 5.3.

corresponds to the azimuthal anisotropy of Pn wave observed by refraction surveys (e.g., *Raïtt et al.*, 1969; *Morris et al.*, 1969; *Shinohara et al.*, 2008). The fastest azimuth of V_{PH} is as same as that of V_{SV} (e.g., *Backus*, 1965). There is no azimuthal anisotropy for V_{PV} because it is the velocity of vertically propagating P-wave with the vertical oscillation. Although the Rayleigh waves mainly reflect the azimuthal anisotropy of V_{SV} , the azimuthal anisotropy of V_{PH} also affects that of Rayleigh waves. The azimuthal dependence of the Rayleigh wave is, thus, dominated by the 2θ term.

Montagner and Nataf (1986) showed the sensitivity of azimuthal anisotropy of surface waves to the azimuthal anisotropy of V_{SV} and V_{PH} structures. The sensitivity kernels are as same as those for the V_{SV} and V_{PH} shown in Figure 5.17. The azimuthal anisotropy of Rayleigh waves estimated in Chapter 3, therefore, reflects the azimuthal anisotropy of V_{SV} structure and slightly reflects that of V_{PH} at depths shallower than V_{SV} . In addition, the azimuthal anisotropy of Rayleigh wave due to V_{PH} anisotropy countervail that due to V_{SV} anisotropy as indicated by the negative sensitivity to V_{PH} at depths deeper than ~ 40 km in Figure 5.17. The overall effect of V_{PH} can be fortunately neglected if the azimuthal anisotropy is almost constant from the Moho to the depths of ~ 100 km because the positive and negative sensitivity to V_{PH} cancel each other.

The sensitivity to V_{PH} at shorter periods, however, invokes the importance of V_{PH} anisotropy again. As shown in Figure 5.18, the 1S mode at a period of 6 s has a negative sensitivity to V_{PH} beneath the Moho, whose intensity is $\sim 30\%$ of that to V_{SV} . If the intensity of V_{PH} anisotropy is as same as that of V_{SV} anisotropy, for example, the intensity of the anisotropy of 1S mode becomes $\sim 70\%$ of that without the presence of V_{PH} anisotropy.

I therefore estimated one-dimensional azimuthally anisotropic models with considering

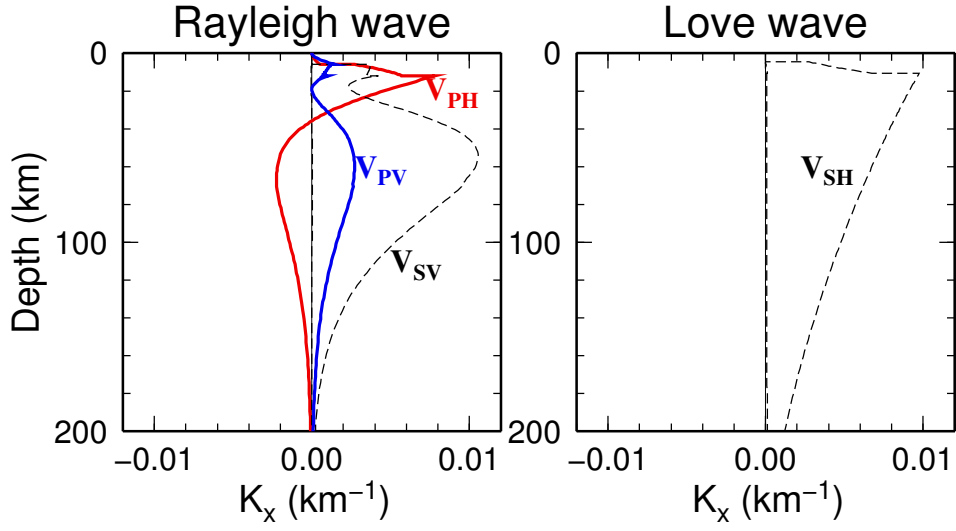


Figure 5.17: Sensitivity of the parameter p to the phase velocities of 0S and 0T modes at a period of 40 s (K_p) for the PREM-OCEAN6 model (§3.2). The independent parameters here are V_{SV} , V_{SH} , V_{PV} , V_{PH} , η and ρ , which are different from the independent parameters in Figure 4.7 ($\beta = V_{SV}$, $\alpha = V_{PH}$, $\xi = (V_{SH}/V_{SV})^2$, $\phi = (V_{PV}/V_{PH})^2$, η and ρ). The sensitivity to η and ρ are not shown as they do not affect the azimuthal anisotropy.

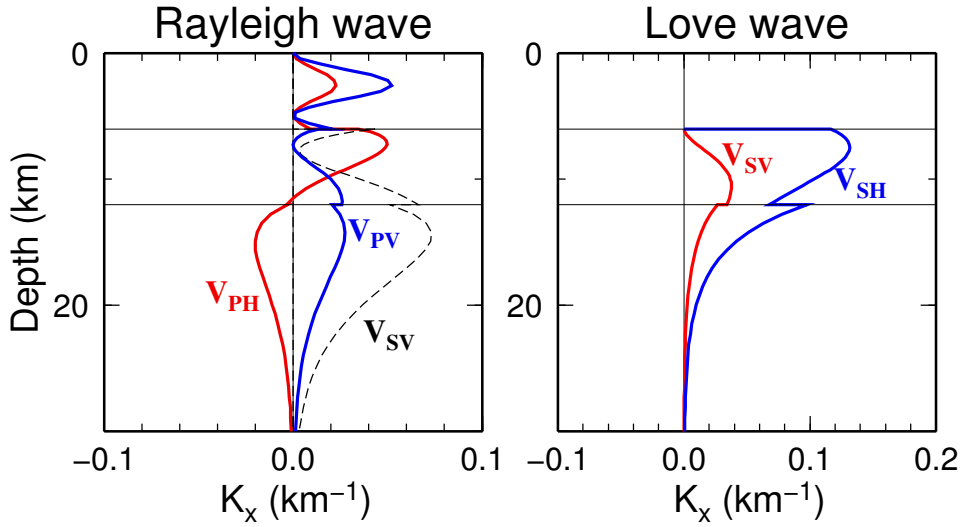


Figure 5.18: Same as Figure 5.17, but for the 1S and 0T mode at a period of 6 s. Two horizontal lines show the depth of the seafloor and Moho.

the effect of V_{PH} anisotropy. The intensity of V_{PH} anisotropy is scaled to be 1.3 times larger than that of V_{SV} anisotropy based on the observed ratio between P-wave and S-wave azimuthal anisotropy in the northwestern Pacific Ocean by a refraction survey (*Shinohara et al.*, 2008). The azimuthal anisotropy of Rayleigh waves given in equations (5.2–5.3) then becomes,

$$\tilde{A}_C(\omega) = \int_z [K_\beta(z, \omega) + 1.3K_{PH}(z, \omega)] A'_C(z) dz, \quad (5.7)$$

and

$$\tilde{A}_S(\omega) = \int_z [K_\beta(z, \omega) + 1.3K_{PH}(z, \omega)] A'_S(z) dz, \quad (5.8)$$

where K_β and $K_{PH} = K_\alpha(z, \omega) - 2K_\phi(z, \omega)$ are the sensitivity of phase velocity to V_{SV} and V_{PH} structures (§3.2).

Figure 5.19 shows the one-dimensional azimuthally anisotropic structure of V_{SV} with the assumption of V_{PH} anisotropy 1.3 times larger than V_{SV} anisotropy. The fastest azimuth is as same as the previous models obtained without considering the V_{PH} anisotropy in Figure 5.7 in the range of uncertainty. The intensity of V_{SV} anisotropy is also as same as the previous models for the Shikoku Basin and French Polynesia regions, where I only analyzed the 0S mode whose sensitivity to V_{PH} can be neglected when the depth variation in the azimuthal anisotropy is small. The intensity of V_{SV} anisotropy, on the other hand, becomes larger for three regions around the Shatsky Rise. The increase of the intensity is $\sim 1\%$ at depths shallower than 20 km, and is not large compared to the uncertainty of 0.5%–1% for the NW and SE Shatsky regions. In contrast, the increase of the intensity is $\sim 50\%$ from Moho to depths deeper than 50 km for the SW Shatsky region, where I only analyzed surface waves at periods shorter than 25 s. The intensity in this region, therefore, may depend on the assumed ratio between V_{SV} and V_{PH} anisotropy, which has large uncertainty. Although I assumed the ratio of 1.3 in this study based on the ratio obtained by a refraction survey (*Shinohara et al.*, 2008), the ratio is estimated to be ~ 2.0 from the elastic constants of pure olivine crystal (e.g., *Crampin*, 1982).

The intensity of V_{PH} anisotropy assumed from the ratio between V_{PH} and V_{SV} anisotropy of 1.3 is $\sim 9\%$ for the eastern array of the SW Shatsky region. This value is larger than the 2θ component of V_{PH} anisotropy estimated from teleseismic Pn-waves in the eastern array of about 5%–7% (*Shintaku et al.*, submitted). The difference between values may be reflecting the inappropriate assumption of the ratio between V_{PH} and V_{SV} anisotropy or the difference between the sensitivity to the structure: their estimation might have sensitivity to structure at depths deeper than ~ 30 km, whereas the measurements in this study have less sensitivity to the depth range.

The estimated V_{SV} and assumed V_{PH} anisotropy at depths of 10–20 km is $\sim 5\%$ and $\sim 7\%$ for the NW Shatsky region. These values are 1%–2% larger than those obtained by a refraction survey (*Shinohara et al.*, 2008), 4% and 5%, near the WP2 station at the northeastern end of the NW Shatsky region in this study (see Figure 5.8 for the location). The difference may be coming from the uncertainty of the ratio between V_{PH} and V_{SV}

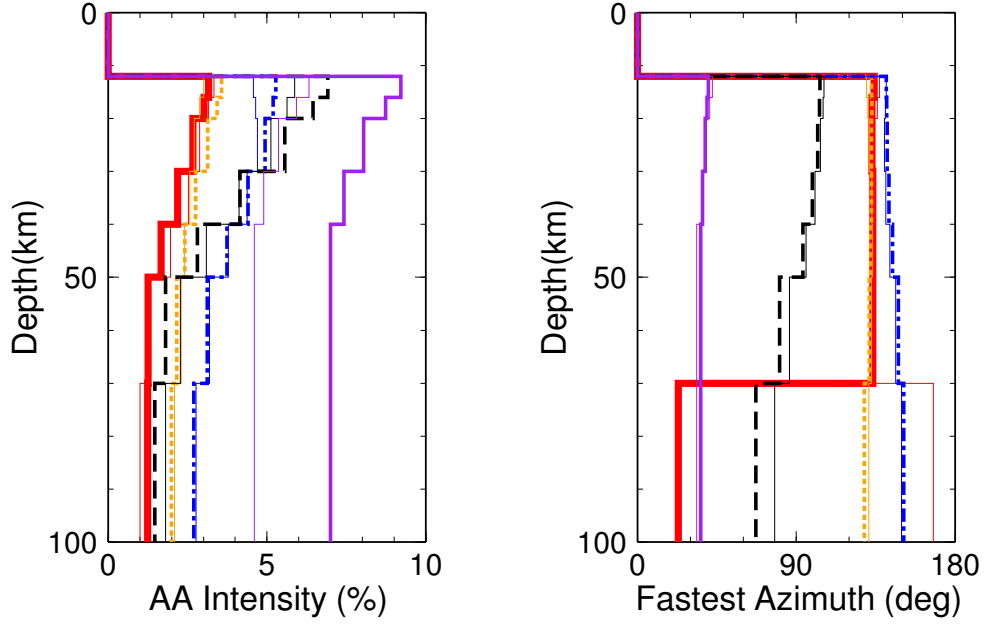


Figure 5.19: Azimuthally anisotropic models when azimuthal anisotropy of V_{PH} is assumed with the intensity 1.3 times larger than that of V_{SV} for the Shikoku Basin (red solid lines; 20Ma), French Polynesia (orange short-dashed lines; 60 Ma), NW Shatsky (blue chain lines; 130 Ma), SE Shatsky (black long-dashed lines; 140 Ma) and SW Shatsky (purple solid lines; 155 Ma) regions. The intensity of V_{SV} anisotropy (left) and the azimuth of maximum velocity (right). Thin solid lines show the model obtained without V_{PH} anisotropy shown in Figure 5.7 with the color same as the models with V_{PH} anisotropy. The model uncertainties are omitted to simplify the figure, which is 0.5%–1% for the intensity and is 5–10 degree for the fastest azimuth similar to the values shown in Figure 5.7.

anisotropy or the large uncertainty for the azimuthal anisotropy of 1S mode (Figure 5.4) due to small number of available pairs between stations (eleven pairs) in this study. More detailed discussion should be done after the analysis of ten BBOBSs (including six BBOBS-NXs) planned to recover in 2014.

5.5.3 Depth Changes in Azimuthal Anisotropy

The depth change in azimuthal anisotropy has been focused by previous studies. The fastest azimuth seems to change from the direction perpendicular to magnetic lineation in the lithosphere (e.g., *Raith et al.*, 1969; *Francis*, 1969) to the direction parallel to the current plate motion in the asthenosphere (e.g., *Tanimoto and Anderson*, 1984), although the lateral resolution of the surface-wave tomography studies is ~ 2000 km, which is lower than the scale of lateral heterogeneity in the magnetic anomaly and anomalous crust of ~ 500 km. The intensity of azimuthal anisotropy is estimated to be up to 10% at depths shallower than ~ 20 km by refraction surveys (e.g., *Oikawa et al.*, 2010) (see a compile by *Song and Kim* (2012)), which is larger than the intensity at deeper depths of $\sim 2\%$ roughly determined by surface-wave tomography studies, although the quantitative estimation of the intensity is difficult for the tomography studies (*Smith et al.*, 2004).

I estimated the intensity of azimuthal anisotropy somewhat quantitatively for laterally homogeneous regions in this study. The estimated azimuthally anisotropic models (Figure 5.7) can be, therefore, used to discuss the depth change in the azimuthal anisotropy and its relationship with the magnetic lineation reflecting the seafloor spreading. The fastest azimuths seems almost constant for all regions if we consider the larger uncertainty at depths deeper than 50–70 km (Figure 5.7). This result indicates that the fastest azimuths is almost constant throughout the lithosphere at depths shallower than 50–80 km estimated from the one-dimensional radially anisotropic structures in Section 4.6 and as summarized in Table 4.1.

The results by the synthetic test shown in Figure 5.20 reveal the depth resolution of the azimuthal anisotropy. The measurement error for the SE Shatsky region is used for the estimation of the uncertainty. The smoothing parameter is as same as the values shown in Figure 5.7 ($\epsilon_{AA} = 0.1$). The depth change in the fastest azimuth can be retrieved for the initial model with a change at a depth of 50 km (Fig. 5.20 top), whereas the fastest azimuth cannot be retrieved perfectly for the change at a depth of 70 km (Fig. 5.20 bottom left) and cannot be retrieved for the change at a depth of 120 km (Fig. 5.20 bottom right). The intensity of anisotropy can be retrieved almost perfectly except for the depth where the change in the fastest azimuth is sharp (at depths of ~ 50 km in Fig. 5.20 top right). These results indicate that the azimuthally anisotropic structure at depths of ~ 10 – 100 km can be constrained quantitatively from the measurements in this study.

The azimuthal anisotropy in the asthenosphere could not be estimated except for the

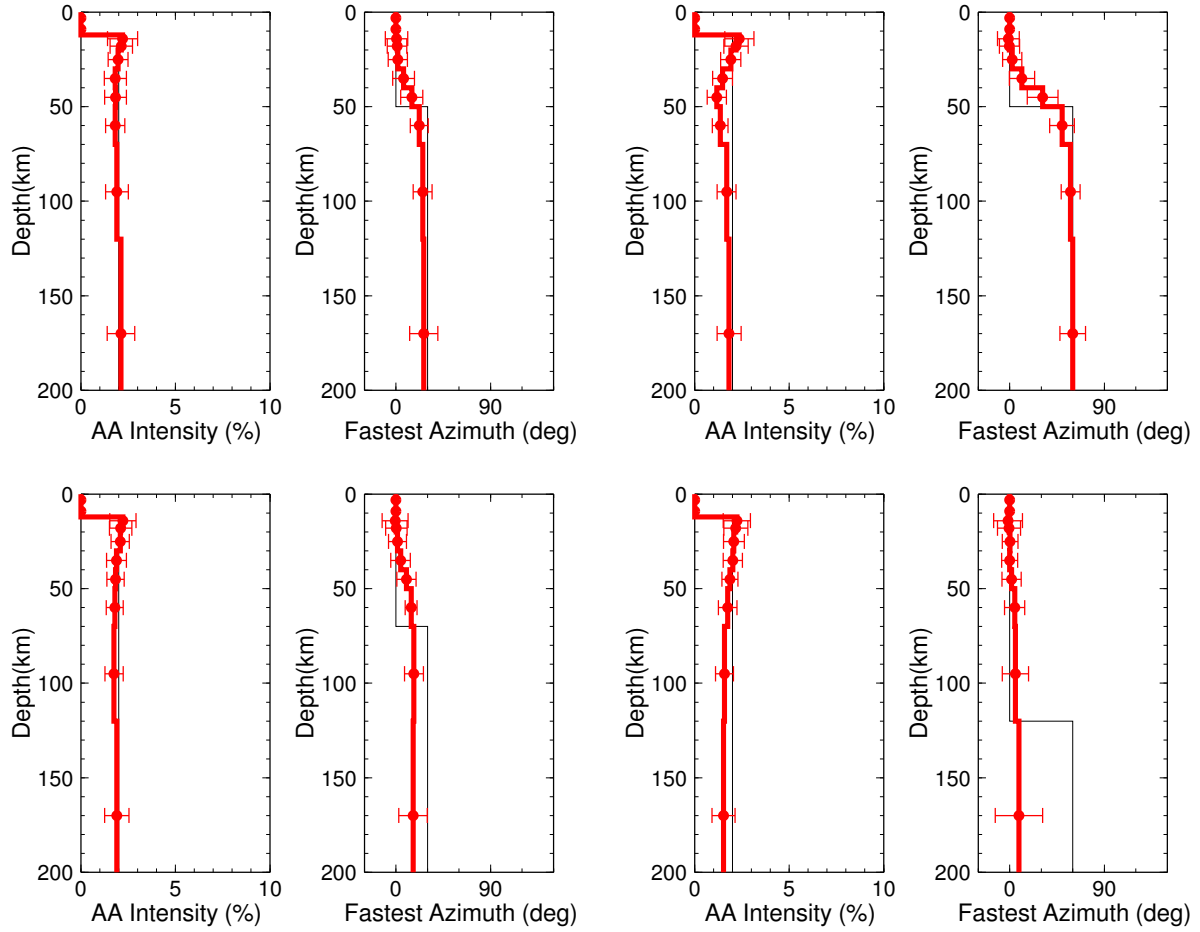


Figure 5.20: The initial (thin black) and retrieved (thick red) models by the synthetic test. The fastest azimuth of initial model is changed from 0 to 30 (top left) and 60 (top right) degree degree at a depth of 50 km, 30 degree at a depth of 70 km (bottom left) and 120 km (bottom right).

French Polynesia region. For the French Polynesia region, the quality is good for the estimated azimuthal anisotropy of 0S mode at periods longer than ~ 50 s (Figure 5.3), which has sensitivity to depths deeper than 60 km, the depth range of the asthenosphere in this region (Table 4.1). For the Shikoku Basin region, on the other hand, the azimuthal anisotropy of 0S mode is small at periods longer than ~ 40 s, and indicates that the azimuthal anisotropy is small at depths deeper than 50 km, the asthenosphere in this region. For the NW and SE Shatsky regions, the azimuthal anisotropy in the asthenosphere is difficult to determine due to the thick lithosphere (~ 80 km; Table 4.1) and the large uncertainty of the anisotropy of 0S mode (Figures 5.4–5.5). The uncertainty may become smaller especially for the NW Shatsky region after the final recovery of BBOBSs and BBOBS-NXs by NOMan project in 2014. The azimuthal anisotropy in the asthenosphere for the SW Shatsky region cannot be estimated because I only analyzed Rayleigh waves at periods shorter than 25 s, which has sensitivity to depths shallower than ~ 50 km. The detailed interpretation about the fastest azimuths will be in the next section after the discussion about the depth changes in the intensity of anisotropy.

The intensity of azimuthal anisotropy seems to decrease with depth for all regions (Figure 5.7). The estimated decrease becomes larger when I assume the presence of V_{PH} (Figure 5.19), and when I discard the station 1 for the French Polynesia region (Figure 5.16). The decrease is especially significant for the NW and SE Shatsky region, where I could analyze both 0S and 1S modes in a broadband period range of 5–70 s (Figures 5.4–5.5).

This estimated decrease of intensity with depth is inconsistent with the monotonic increase of anisotropy with depth suggested by the accumulation of shear strain in the oceanic asthenosphere with the increasing seafloor age (e.g., *Behn et al.*, 2009). Although there is several studies about the accumulation of shear strain in the oceanic uppermost mantle (e.g., *Podolefsky et al.*, 2004; *Becker et al.*, 2008; *Behn et al.*, 2009), they have focused on the shear deformation at deeper than ~ 100 km, where the strong intensity of radial anisotropy have been suggested by surface-wave tomography studies (e.g., *Ekström and Dziewonski*, 1998; *Nettles and Dziewonski*, 2008). We need to focus on calculating the shear deformation at shallower depths in the future studies to interpret the decrease of intensity with depth estimated in this study.

At this moment, I qualitatively interpret that the azimuthal anisotropy is strong at depths shallower than ~ 50 km because the shear deformation accumulates there. The depth range is expected to be the asthenosphere when the seafloor age is less than 20 Ma because the depth of the LLTZ is ~ 39 –48 km for the Shikoku Basin region where the seafloor age is ~ 20 Ma (Table 4.1). The accumulation of the shear at the depth range, thus, indicates that the viscosity in the asthenosphere at the seafloor age younger than 20 Ma is lower than the asthenosphere at older seafloor. Such low viscosity can be produced at the young asthenosphere because the possibility of the partial melt is high at the region as discussed by previous studies (e.g., *Hirschmann*, 2010).

The stronger anisotropy for three regions around the Shatsky Rise may be reflecting the larger half-spreading rate of >4 cm/yr in these regions (*Nakanishi et al.*, 1992) compared to those for the Shikoku Basin and French Polynesia regions (*Okino et al.*, 1999; *Müller et al.*, 2008) as similarly discussed by compiling the results of refraction surveys by *Song and Kim* (2012).

5.5.4 Azimuth of Maximum S-wave Velocity

The fastest azimuths are almost perpendicular to magnetic lineations for the SW Shatsky, NW Shatsky regions. This kind of anisotropy is frequently observed in oceanic regions, and can be interpreted to be caused by the mantle flow perpendicular to the ancient mid ocean ridge recorded as the magnetic lineations (*Raith et al.*, 1969; *Francis*, 1969). The fastest azimuths are, however, not perpendicular to the magnetic lineations for other three regions: the Shikoku Basin, French Polynesia and SE Shatsky regions.

I first interpret the fastest azimuths for the French Polynesia region at depths of 20–50 km in the lithosphere, which is NE–SE direction and is not perpendicular to the magnetic lineation of NNW–SSE. The shear strain frozen in the depth range is considered to be produced by the ancient mantle flow in the ancient asthenosphere 0–20 million year after the seafloor spreading, which is at 40–60 Ma in this region. The obtained result, therefore, means that the ancient mantle flow at 40–60 Ma was not perpendicular to the ancient mid ocean ridge.

One possible interpretation emerges when we realize that the fastest azimuths are parallel to the plate motion before 43 Ma recorded by the lineation of seamounts north of the Tahiti island at 10°S – 14°S and 208°E – 212°E (Figure 5.13). As compiled by *Seton et al.* (2012), the ancient plate motion in this region was not perpendicular to the ancient mid ocean ridge at this moment probably because of passive spreading in this region compared to an active spreading between the Pacific Plate and the Antarctica Plate at the southwest of this region. The fastest azimuth estimated in this study, therefore, implies that the mantle flow is not perpendicular to the magnetic lineation as stated by previous studies (e.g., *Francis*, 1969; *Smith et al.*, 2004), but is parallel to the ancient plate motion 0–20 million years after spreading when the plate motion was not perpendicular to the ancient mid-ocean-ridge. It should be noted that *Toomey et al.* (2007) revealed the obligation of fastest azimuth to the plate motion at depths shallower than ~ 15 km in the East Pacific Rise region, which indicates more complicated mantle flow in the current mid-ocean-ridge with segmentations.

The fastest azimuth at depths deeper than 50 km for the French Polynesia region is expected to be parallel to the current plate motion, but is oblique to the current plate motion with a differential angle of $\sim 20^{\circ}$. The azimuth is as same as that at depths shallower than 50 km and is rather parallel to the ancient plate motion. One possible interpretation is that the flow in the asthenosphere is perturbed by the presence of an active hotspot near the

Tahiti island as already discussed and indicated from the S-wave splitting analysis (§5.5.1). This interpretation seems strange because the effect of anomalous anisotropy near station 1 was larger at depths shallower than 50 km than at deeper depths (Figure 5.16). The perturbation due to the presence of plume beneath a hotspot may be, therefore, different for the shallower and deeper depths: the effect of ancient hotspot at north of the Tahiti island before 45 Ma (*Schlanger et al.*, 1984) at shallower depths, and the effect of current hotspot near the Tahiti island after 10 Ma (*Duncan and McDougall*, 1976) at deeper depths.

The fastest azimuth for the Shikoku Basin region (Figure 5.8) is difficult to interpret because of the complicated tectonic setting in this region: the subduction of the Philippine Sea Plate beneath the southwest Japan and the subduction of the Pacific Plate beneath the northeast Japan and the Philippine Sea Plate. The spreading direction is estimated to have changed from E–W direction at 20–27 Ma to NE–SW direction at 15–20 Ma (*Okino et al.*, 1999). The corresponding azimuthal anisotropy has, however, not been recognized in this region (*Nishizawa et al.*, 2011) probably because of small shear strain due to low half-spreading ratio of 2–5 cm/yr, which is especially low at 15–20 Ma of 2–3 cm/yr (*Okino et al.*, 1999). The another cause of azimuthal anisotropy is the mantle flow related to the plate motion. The current plate motion is in NW direction, and is consistent with the observed fastest azimuths. Although several scientists discussed that the direction was north before 3 Ma (e.g., *Takahashi*, 2006), *Yamazaki et al.* (2010) concluded that the fast northward motion stopped at 15 Ma. *Isse et al.* (2010) also revealed the similar fastest azimuth by a local surface-wave tomography, and concluded that it is caused by the current plate motion. The subduction of the Pacific Plate beneath the Shikoku Basin may also affect the flow in the mantle wedge beneath the Shikoku Basin, which is WNW closed to the obtained fastest azimuths in this region.

The fastest azimuth for the SE Shatsky region is also oblique to the magnetic lineations (Figure 5.8). I here considered two interpretations: the change in the plate motion, and the influence of the Shatsky Rise.

The first interpretation is based on the result for the French Polynesia region, which indicates that the fastest azimuth at depths shallower than 50 km reflects plate motion ~0–20 million years after the seafloor spreading. The fastest azimuth observed in the SE Shatsky region may, therefore, reflect the plate motion at 120–140 Ma. The azimuth in the NW and the eastern array of SW Shatsky regions may similarly reflect the plate motion at 110–130 and 135–155 Ma, respectively. With this interpretation, the difference in the fastest azimuths between these areas correspond to the rapid change in plate motion at 110–155 Ma, from the northeast or southwest direction at ~140–155 Ma, the east or west direction at ~125–140 Ma, to the northwest or southeast direction at ~110–125 Ma. Such motion seems impossible for the current Pacific Plate locked by surrounding subduction zones, but seems possible for the ancient Pacific Plate, a micro plate surrounded by MORs.

A problem for this interpretation arises when we interpret the result by *Oikawa et al.*

(2010). They revealed that the Pn-wave velocity is faster for the NW–SE direction than for the SW–NE direction, and the faster direction is perpendicular to the magnetic lineations at the western array of the SW Shatsky Rise (Figure 5.8). As the seafloor age is same for the eastern and western arrays of the SW Shatsky Rise, the fastest azimuths should be the same if the mantle flow is parallel to the motion of the Pacific Plate at ~ 140 – 155 Ma. The difference in fastest azimuths for the eastern and western arrays indicates that the mantle flow was not parallel to the ancient plate motion, but was perpendicular to the ancient MOR in the SW Shatsky region as discussed by previous studies (e.g., *Raïtt et al.*, 1969; *Francis*, 1969; *Smith et al.*, 2004).

I here modify the interpretation that the ancient mantle flow is parallel to the ancient plate motion, to that the flow is parallel to the ancient plate motion when the velocity of plate motion is high, and is perpendicular to the ancient MOR when the rate of seafloor spreading is high. This interpretation can explain the overall results including three regions around the Shatsky Rise, and the French Polynesia region. For example, the velocity of plate motion was 9–10 cm/yr, faster than the half spreading rate of 2–4 cm/yr in the French Polynesia region (*Schlanger et al.*, 1984), where the fastest azimuths is parallel to the ancient plate motion (Figure 5.13). The half spreading rate is ~ 7 cm/yr, expected to be faster than the plate motion in the western array of the SW Shatsky region, where *Oikawa et al.* (2010) revealed that the Pn-wave propagates faster for the direction perpendicular to the magnetic lineations (Figure 5.8). On the other hand, the half spreading rate is in the intermediate value of ~ 5 cm/yr for the eastern array of SW Shatsky, and NW and SE Shatsky regions (*Nakanishi et al.*, 1992). The fastest azimuth in the SE Shatsky region can be interpreted by the fast plate motion with a velocity greater than 5 cm/yr in the east or west direction.

The second interpretation is the influence of the Shatsky Rise. The fastest azimuths indicates mantle flow radially arose from the Shatsky Rise (Figure 5.8). If an anomalous upwelling existed beneath the Shatsky Rise to form the anomalous seafloor rise, the excess of mass may be cancelled by the horizontal flow radially initiated from the Shatsky Rise. Although this interpretation is simple, the evaluation is difficult because of insufficient knowledge about the flow at the triple junction after the discussion about its stability by *McKenzie and Morgan* (1969). The numerical modeling of the mantle flow around the triple junction as well as the triple junction of triple junctions may progresses the discussion in the future.

Chapter 6

GENERAL DISCUSSIONS

6.1 Intensities of Radial and Azimuthal Anisotropies

The intensity of the azimuthal anisotropy has been quantitatively estimated by refraction surveys for the depth range shallower than ~ 20 km (e.g., *Raitt et al.*, 1969; *Morris et al.*, 1969; *Shinohara et al.*, 2008). In contrast, the azimuthal anisotropy at deeper depths have been estimated by surface-wave tomography studies (*Tanimoto and Anderson*, 1984; *Montagner*, 2002; *Maggi et al.*, 2006b), which are usually constrained only qualitatively as indicated by the dependence of the intensity on the smoothing and dumping parameters (*Smith et al.*, 2004). *Song and Kawakatsu* (2012) recently focused on the relative intensity of the radial and azimuthal anisotropies. From the pattern of the S-wave splitting with the fastest azimuths being parallel to the trench in the subduction zones, they suggested that the radial anisotropy is stronger than the azimuthal anisotropy within or under the subducting plate.

I here compare the intensities of radial and azimuthal anisotropies obtained in Chapters 4–5, which could be estimated more quantitatively in this study by the array analysis methods in Chapter 3 compared to previous tomography studies. Figure 6.1 shows the difference between intensities of the radial and azimuthal anisotropies for four oceanic regions, where the radially anisotropic structure could be estimated: the Shikoku Basin, French Polynesia, NW Shatsky and SE Shatsky regions. The intensity of radial anisotropy is the value for the smooth radially anisotropic models (Figure 4.10) obtained in Section 4.5, whereas the intensity of azimuthal anisotropy is the value for the azimuthally anisotropic models (Figure 5.7) obtained in Section 5.2. The model uncertainty is 0.5%–1% for both radial and azimuthal anisotropies.

Figure 6.1 indicates that the radial anisotropy is stronger than the azimuthal anisotropy especially for the Shikoku Basin and SE Shatsky regions. It should be noted the intensity of azimuthal anisotropy increases at depths shallower than ~ 30 km if we assume the presence of V_{PH} anisotropy (Figure 5.19), although the effect is less than 1%. The azimuthal anisotropy seems stronger than the radial anisotropy at depths shallower than ~ 40 km for the NW

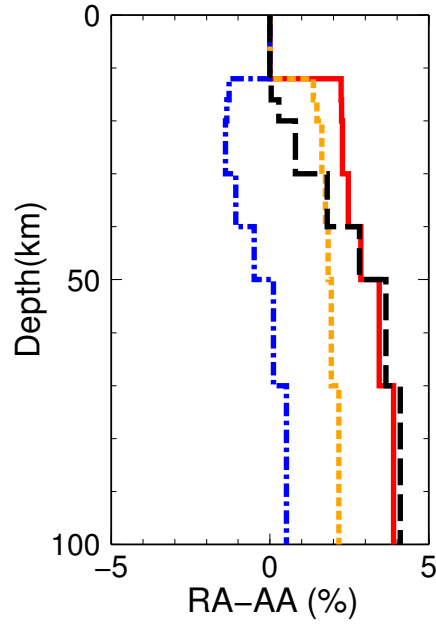


Figure 6.1: The difference between intensity of the radial anisotropy (RA; δV) for the smooth radially anisotropic models (Figure 4.10), and the intensity of azimuthal anisotropy (AA; $2A_2$) obtained without the assumption of V_{PH} anisotropy (Figure 5.7) for the Shikoku Basin (red solid line; 20Ma), French Polynesia (orange short-dashed line; 60 Ma), NW Shatsky (blue chain line; 130 Ma) and SE Shatsky (black long-dashed line; 140 Ma) regions.

Shatsky region. The value is, however, less reliable compared to other regions because of the large uncertainty in the azimuthal anisotropy of 1S mode (Figure 5.4) and the estimated azimuthal anisotropy stronger than the value estimated by a refraction survey in this region (*Shinohara et al.*, 2008) as discussed in Section 5.5.2. The uncertainty will be smaller after the analysis of ten BBOBSs (including six BBOBS-NXs) planned to recover in 2014.

There are two interpretations for the larger intensity of radial anisotropy compared to that of azimuthal anisotropy: the AG-type fabric of olivine crystals, and the effect of the partial melt. Both have potentials to produce the radial anisotropy stronger than the azimuthal anisotropy.

There are various types of fabric for the LPO of olivine crystals: A-, B-, C-, D-, E- and AG- types. *Mainprice* (2007) and *Michibayashi* (2008) summarized the fabrics and the corresponding seismic anisotropy. The seismic anisotropy for the A-, D- and E- types are closed to each other, and can explain the fastest azimuths parallel to the mantle flow. For example, *Estey and Douglas* (1986) and *Nishimura and Forsyth* (1989) considered the A- and D- types to explain the azimuthal anisotropy in the upper mantle, respectively. For these fabrics, the intensity of radial anisotropy is as same as the intensity of azimuthal anisotropy as indicated by the incident-angle dependence of S-wave velocity by *Crampin* (1982). The B- and C- types give the different pattern of seismic anisotropy, and have been focused by researchers especially to explain the complicated patterns of anisotropy estimated by the shear-wave-splitting analysis (e.g., *Jung and Karato*, 2001; *Nakajima and Hasegawa*, 2004; *Terada et al.*, 2013). Although there was no such attention to the AG-type, the AG-type is the fabric that gives the radial anisotropy stronger than the azimuthal anisotropy.

The fabric of AG-type is a fabric closed to the A-type fabric found in the $\sim 10\%$ of natural rocks (*Mainprice*, 2007). For the case of A-type, the fastest axes of olivine crystals (a-axes) align in the direction of flow, whereas the slowest axes (b-axes) align in the direction perpendicular to the flow plane. For the case of AG-type, both a- and c- axes align in the flow plane with more accumulation of a-axes to the direction of flow. The seismic anisotropy of AG-type, therefore, has the pattern similar to the A-type: the fastest azimuths parallel to the direction of mantle flow, and the radial anisotropy of $V_{SH} > V_{SV}$. On the other hand, the intensity of azimuthal anisotropy is weaker for the AG-type than for the A-type because of the less accumulation of a-axes for the AG-type than for the A-type. As the intensity of radial anisotropy of the AG-type is as same as the A-type, the radial anisotropy becomes stronger than the azimuthal anisotropy. The AG-type fabric can, thus, explain the difference between radial and azimuthal anisotropy estimated in this study (Figure 6.1). Although *Jung and Karato* (2001) summarized the temperature and water-content conditions for the A–D types, there is few studies for the condition for the AG-type fabric as pointed out by *Miyazaki et al.* (2013). For example, *Holtzman et al.* (2003) reported the appearance of the AG-type fabric by an experimental study with the presence of partial melt. The future understanding of the AG-type fabric is needed to discuss whether it can exist in the uppermost mantle as

with the case of A–D type fabrics.

The another mechanism to produce the strong radial anisotropy is the effect of partial melting in the asthenosphere. The presence of thin layers or pockets of partial melt can produce radial anisotropy at wavelengths longer than the structure (e.g., *Backus*, 1962; *Forsyth*, 1975; *Schlue and Knopoff*, 1976). On the other hand, there is no azimuthal anisotropy due to the presence of partial melt if the melt distribution is isotropic in the horizontal plane as inferred by experimental studies (e.g., *Kohlstedt and Zimmerman*, 1996). Even if the solid part of the partially molten rock has the A-, D- or E- type fabric, therefore, the radial anisotropy can be stronger than the azimuthal anisotropy in the partially molten asthenosphere.

This interpretation is consistent with the positive difference between the intensity of radial and azimuthal anisotropies shown in Figure 6.1. The figure is, however, obtained by using the intensity of radial anisotropy assumed to be constant at a depth range of 10–150 km. For comparing the intensity in the lithosphere and asthenosphere, Figure 6.2 was made to show the difference between the intensity of azimuthal anisotropy, and the intensity of radial anisotropy in the LID and LVZ (Table 4.1) independently estimated in Section 4.6. Although the uncertainty range is large, it is obvious that the radial anisotropy is stronger than the azimuthal anisotropy especially in the asthenosphere at depths deeper than ~ 50 km for the Shikoku Basin and French Polynesia regions, where the seafloor ages are young (20 and 60 Ma) and the fraction of partial melting may be higher than 0.1% (e.g., *Hirschmann*, 2010). *Kawakatsu et al.* (2009) discussed that the small fraction of partial melt (0.25%–1.25%) can produce the strong radial anisotropy of $\sim 7\%$. The partial melt can, therefore, explain the excess of the intensity of radial anisotropy compared to that of the azimuthal anisotropy for the Shikoku Basin and French Polynesia regions. It can also explain the small difference between the intensities of radial and azimuthal anisotropies for the NW Shatsky region (Figure 6.2), where the fraction of partial melt is expected to be lower because of the older seafloor age of 130 Ma.

The intensity of radial anisotropy in the SE Shatsky region is 3%–5% larger than that of azimuthal anisotropy in this region (Figure 6.2), and 2%–3% larger than the intensity of the radial anisotropy in other regions (Figure 4.10). This cannot be explained by the partial melt because of small fraction of melt predicted for the old seafloor age of 140 Ma. The strong radial anisotropy may be, therefore, caused by the AG-type fabric at depths of ~ 50 km in this region. This result, as well as the high S-wave velocity in the uppermost mantle (see Figure 4.10 and Table 4.1) and the fastest azimuths oblique to the magnetic lineations (Figure 5.8), indicates that the structure beneath the SE Shatsky region is completely different from the structure beneath the oceanic region with a similar seafloor age of 130 Ma, the NW Shatsky region

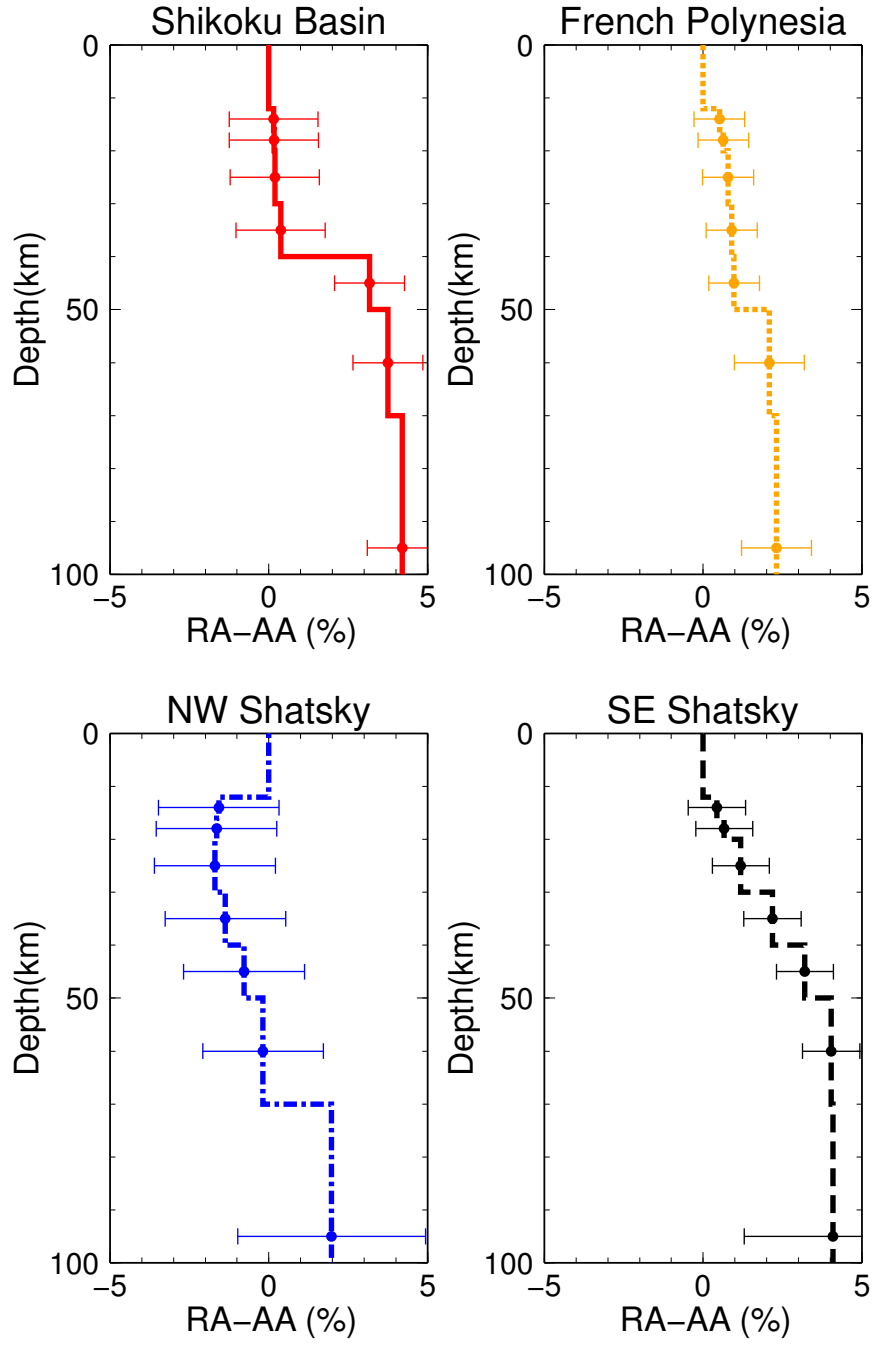


Figure 6.2: Same as Figure 6.1, but the intensity of radial anisotropy is the value summarized in Table 4.1 obtained by assuming a structure with a LID, LVZ and the LLTZ in Section 4.6. The error bars show the uncertainties in the intensities of radial anisotropy (Table 4.1).

6.2 Summary of Results for Each Region

The radially and azimuthally anisotropic models were obtained separately in Chapter 4 and 5, and the difference between them was discussed in the previous section (§6.1). The result for each region is, however, distributed in various sections and not summarized yet. This section, therefore, summarizes the result for each region.

6.2.1 Shikoku Basin

The Shikoku Basin region is the northeastern part of the Philippine Sea plate emerged at 15–30 Ma (*Okino et al.*, 1999). In this study, I estimated the radially and azimuthally anisotropic models beneath the area covered by seven BBOBS stations deployed by the Stagnant Slab Project (§2.2.1).

The radially anisotropic model shows the large velocity reduction at a depth of ~ 50 km, and the intensity of radial anisotropy ($V_{SH} > V_{SV}$) of 4%–5% (§4.5; Fig. 4.10). The structure including the LID, LVZ and the LID-LVZ transition zone (LLTZ) was estimated (§4.6) to discuss the structure of the lithosphere/asthenosphere system (§4.7.3). The depth of the center of the LLTZ was estimated to be 39–48 km (Table 4.1), which was slightly shallower than the value estimated by *Tonegawa and Helffrich* (2012) for the northern part of the Shikoku Basin region. The velocity gradient in the LID is estimated to be larger than the range estimated from the thermal model and the elastic constants of olivine crystals. The difference indicates the importance of considering the phase transition from plagioclase peridotite to pyroxene peridotite at depths of ~ 30 km (*Forsyth and Press*, 1971; *Stixrude and Lithgow-Bertelloni*, 2005). The velocity gradient in the LLTZ is steep compared to the value estimated from a thermal model, and indicates that the velocity reduction is produced by mechanisms other than the temperature such as the presence of partial melting (*Anderson and Sammis*, 1970) and the presence of water (*Karato*, 2012). In any mechanism, the LID and LVZ can be interpreted as the oceanic lithosphere and asthenosphere, respectively. Although the depth change in the radial anisotropy could not be resolved, the anisotropy may be $\sim 0\%$ –5% stronger in the LVZ than in the LID (§4.7.4).

The azimuthally anisotropic structure was also estimated in Section 5.3 from the azimuthal anisotropy of 0S mode estimated in Chapter 3 (§3.3.6, §3.4.2). The azimuth of maximum S-wave velocity was estimated to be NW–SE direction at depths of ~ 20 –50 km (Fig. 5.8) mainly in the lithosphere in this region, which is not perpendicular to the magnetic lineation as expected but is almost parallel to the current plate motion. *Nishizawa et al.* (2011) also reported the absence of anisotropy at depth shallower than ~ 20 km from refraction studies. These results indicate that the anisotropy was formed not by the seafloor spreading, but by the plate motion after the seafloor spreading in this region.

The intensity of azimuthal anisotropy is especially weaker than that of radial anisotropy in the LVZ with a difference of 3%–5% (Fig. 6.2). This result, as well as the possibility of

stronger radial anisotropy in the LVZ than in the LID (Table 4.1), indicates the presence of apparent anisotropy in the LVZ produced by the partial melting (*Schlue and Knopoff*, 1976).

6.2.2 French Polynesia

The French Polynesia region is the hotspot region in the south Pacific Ocean emerged at 50–70 Ma. I analyzed records of nine BBOBSs deployed by the TIARES project (§2.2.2). The analysis for this region is as same as the Shikoku Basin region except for the shear-wave splitting analysis performed only for this region.

The radially anisotropic model shows the velocity reduction at a depth of ~ 60 km, and the intensity of radial anisotropy of $\sim 4\%$ (§4.5; Fig. 4.10). The depth of the center of the LLTZ is at 52–59 km (Table 4.1), which is slightly deeper than the depth for the younger seafloor at the Shikoku Basin region. The velocity gradient in the LID is larger than that predicted by simple olivine models, and indicates the importance of the phase transition similar to the Shikoku Basin region. The velocity gradient in the LLTZ is sharp and indicates the presence of partial melting or water in the LVZ. The intensity of radial anisotropy may be 0%–2% stronger in the LVZ than in the LID.

The azimuth of maximum S-wave velocity was estimated to be NW–SE direction at depths of ~ 20 –100 km in both lithosphere and asthenosphere in this region. The direction is not perpendicular to the magnetic lineation, but is almost parallel to the plate motion from the age of seafloor spreading to current age (Fig. 5.9). This result indicates that the azimuthal anisotropy in the lithosphere does not records the seafloor spreading, but records the plate motion during the age of seafloor spreading at least in this region. More detailed distribution of azimuthal anisotropy was estimated by shear-wave splitting analysis (§5.4). The result indicates the perturbation of azimuthal anisotropy caused by the presence of hotspot activity at north of the analyzed area (§5.5.1; Fig. 5.13).

The intensity of radial anisotropy is 1%–3% stronger than the intensity of azimuthal anisotropy in the LVZ (Fig. 6.2). This result indicates the presence of apparent anisotropy in the LVZ by the presence of partial melting, although the effect seems smaller than that for the younger seafloor in the Shikoku Basin region.

6.2.3 Northwest Shatsky

The NW Shatsky region is the old seafloor in the northwestern Pacific Ocean emerged at 125–135 Ma. I analyzed records of BBOBSs acquired at seven stations by the NOMan project (§2.2.3). The analysis is as same as the Shikoku Basin region, although I also estimated azimuthal anisotropy of 1S mode (§3.3.6) in this region.

The radially anisotropic model shows the velocity reduction at a depth of ~ 70 km, and the intensity of radial anisotropy of 3%–4% (§4.5; Fig. 4.10). The center depth of the LLTZ

is at 63–85 km. The discrepancy between observed and predicted velocity gradients in the LID is not clear in this region. The velocity gradient in the LLTZ is slightly sharper than the value predicted by simple olivine models and indicate the presence of partial melting or water. The intensity of radial anisotropy may be 0%–5% larger in the LVZ than in the LID, although the uncertainty is large (Fig. 4.18).

The azimuth of maximum S-wave velocity was estimated to be almost perpendicular to the magnetic lineations at depths of ~ 10 –100 km (Fig. 5.8). The anisotropy at depths of 10–20 km could constrain by the use of 1S mode in addition to 0S mode analyzed for the Shikoku Basin and French Polynesia regions. The direction is also parallel to the azimuth at depths of ~ 10 –20 km estimated by the previous refraction study (*Shinohara et al.*, 2008). These results indicate that the mantle flow during the seafloor spreading in this region was perpendicular to the ancient mid-ocean-ridge as discussed by previous studies (*Raitt et al.*, 1969; *Francis*, 1969).

The intensity of radial anisotropy is same as the intensity of azimuthal anisotropy in the range of error (Fig. 6.2). It indicates that there is no requirement for the apparent anisotropy caused by the presence of partial melting in this region.

6.2.4 Southeast Shatsky

The SE Shatsky region is the old seafloor emerged at 135–145 Ma. I analyzed records of seven BBOBSs acquired by the NOMan project (§2.2.3). The analysis is as same as the NW Shatsky region.

The radially anisotropic model shows the velocity reduction at a depth of ~ 80 km (§4.5; Fig. 4.10), although the reduction is small compared to other regions. The intensity of radial anisotropy is $\sim 6\%$ and is larger than other regions. These results indicate that the structure beneath SE and NW Shatsky regions are different from each other, although the seafloor ages are closed to each other. The velocity gradient in the LID is larger than the value estimated from simple olivine models (Table 4.1), and indicates the effect of phase transition similarly to the Shikoku Basin and French Polynesia regions. The intensity of radial anisotropy in the LVZ is difficult to constrain (Fig. 4.19) because it exists at depths deeper than ~ 80 km, and the phase-velocity measurements of the Love wave in this study has less sensitivity to the deeper depths.

The azimuth of maximum S-wave velocity was estimated to be W–E direction at depths of ~ 10 –100 km mainly in the lithosphere in this region (Fig. 5.8). The direction is not perpendicular to the magnetic lineation similarly to the French Polynesia region. Although the ancient plate motion is unknown in this old seafloor, the obtained fastest azimuth may be reflecting the ancient plate motion during the age of seafloor spreading.

The intensity of radial anisotropy is 3%–5% larger than that of azimuthal anisotropy especially at depths of ~ 50 km (Fig. 6.2), which corresponds to the lower part of lithosphere

in this region. This result cannot be interpreted by the apparent radial anisotropy under the presence of partial melt. It cannot be explained by the fabric of olivine crystal, A-type, which is usually considered to explain the seismic anisotropy in the uppermost mantle (*Estey and Douglas, 1986; Nishimura and Forsyth, 1989*). Another fabric, AG-type (*Mainprice, 2007*) may explain the anomalous seismic anisotropy in this region.

6.2.5 Southwest Shatsky

The SW Shatsky region is the oldest seafloor in this study emerged at 150–160 Ma. I analyzed records of eight OBSs and nine DPGs obtained by the PLATE project (§2.2.4). The analysis is limited to the ambient noise cross-correlation analysis for this region, and the analysis of teleseismic event will be published elsewhere by other researchers. The obtained structure is, therefore, limited to depths shallower than ~ 30 km.

The radial anisotropy was not required in this region, and 1D crustal models could be obtained in Section 4.3.2. The azimuthal of maximum S-wave velocity was estimated to be NE–SW direction at depths of ~ 10 –30 km from 0S and 1S modes (Fig. 5.8). The direction is almost perpendicular to the magnetic lineations, and indicates that the flow in the mantle was perpendicular to the ancient mid-ocean ridge in this region.

6.3 Broadband Ocean Bottom Seismology in This Study

The broadband array analysis of surface waves in oceanic regions is essential for obtaining the structure of the oceanic lithosphere and asthenosphere as pointed out in Chapter 1. Although there are several previous studies in the EPR region (*Dunn and Forsyth, 2003; Harmon et al., 2007; Yao et al., 2011; Weeraratne et al., 2007*), the period range especially for the Love wave was insufficient to obtain the radially anisotropic structure at depths deeper than 30 km. In addition, previous studies spent less effort to estimate the uncertainty of the measurements, which provides difficulty in interpreting the results. Above all, the structure beneath the EPR region is not suited to discuss the structure within the lithosphere and asthenosphere because of the thin lithosphere at the region of young seafloor age.

I therefore analyzed the seafloor records obtained in five oceanic basins as summarized in Chapter 2. The datasets covers various types of broadband seafloor records available now including those obtained by Japanese researchers in the Shikoku Basin, French Polynesia, NW and SE Shatsky regions as well as the records obtained by U. S. researchers in the SW Shatsky region. The methods developed in this study can be, thus, applied to almost all kind of records obtained in oceanic regions.

The methods for the broadband surface-wave analysis can be divided into two groups, the ambient-noise analysis and the teleseismic surface-wave analysis, as described in Chapter 3. There were many improvements to the existing methods especially for the ambient noise

cross-correlation analysis including the estimation of the clock delay and instrumental responses (§3.3.3), the simultaneous estimation of the average phase velocities of multi-mode surface waves by developing a waveform fitting method (§3.3.4), the correction of the effects of water-depth and source heterogeneity to the phase-velocity anomalies (§3.3.5). As a result, I could measure phase velocities of both Rayleigh and Love waves at periods of ~ 3 –100 s, and could estimate the azimuthal anisotropy of phase velocities of Rayleigh waves at periods of ~ 5 –70 s. The period range is broad compared to previous studies, and could be used to estimate radially and azimuthally anisotropic structures beneath each region at depths of ~ 10 –150 km in Chapters 4–5. The errors of each estimated values were carefully discussed in each section, and also used to estimate the uncertainty of the obtained models in Chapters 4–5.

The estimation of the radially anisotropic structures is described in Chapter 4. After showing the insufficiency of the isotropic models (§4.3) and discussing the scaling relationship between anisotropic parameters (§4.4), both smooth and non-smooth one-dimensional radially anisotropic models were obtained for each region in Section 4.5 and 4.6. The velocity gradient obtained by assuming the non-smooth structure (Table 4.1) was especially used to compare with the thermal models beneath oceanic basins including the velocity gradients in the LID and in the LID–LVZ transition zone (§4.7.3).

The estimation of the azimuthally anisotropic structures is described in Chapter 5. The one-dimensional structures beneath each region was obtained in Section 5.3. By further estimating the azimuthal anisotropy by the S-wave splitting method (§5.4), the lateral heterogeneity of azimuthal anisotropy was discussed in Section 5.5.1. After evaluating the effect of P-wave anisotropy to the estimation of one-dimensional azimuthally anisotropic structures (§5.5.2), the intensity of anisotropy and the fastest azimuths was extensively discussed in Section 5.5.3–5.5.4. The intensities of azimuthal and radial anisotropies were compared in Section 6.1 as the last discussion in this thesis.

The multi-band analyses in this study proved that the broadband array analysis of surface waves contributes to estimate the radially and azimuthally anisotropic models in the uppermost mantle to discuss the structure and flow in the oceanic lithosphere/asthenosphere system. It means I could establish a new field to the structural analysis in the oceanic regions, the broadband ocean bottom seismology, which estimate the anisotropic uppermost mantle structure beneath oceanic regions by the broadband surface wave of seafloor records. This new method can provide uppermost mantle structure at depths deeper than that by refraction surveys and the reliability higher than the surface-wave tomography studies, although the area is limited to the regions in which BBOBSs were deployed.

6.4 Broadband Ocean Bottom Seismology in the Future Studies

Although I summarized the overall analysis of seafloor records in this thesis, there still exist a great number of problems and questions unsolved in this study, which needs to be solved in future studies.

There is one point needed to improve for the ambient noise cross-correlation analysis. I measured the phase velocities of 2S mode at periods of 3–5 s only for the SW Shatsky region as described in Section 3.3.4, which has not been analyzed in previous studies (*Harmon et al.*, 2007; *Yao et al.*, 2011). Although the 2S mode can be recognized in the NW and SE Shatsky regions, the determination of the appropriate phase velocities was difficult due to high noise levels at periods of ~ 1 –10 s in these regions. One possible method to analyze such record is the estimation of crustal and uppermost mantle structure directly from the waveforms. There is a limited variation for the structures that can fit the 0S and 1S modes at a broadband period range of ~ 3 –30 s. The variation in the dispersion curves of the 2S mode should be then limited to those corresponding to the limited structures. By directly fitting the structure to the waveforms including the 0S, 1S and 2S modes, therefore, we may be possible to estimate phase velocity of the 2S mode even if the signal-to-noise ratio of CCF is low.

The amplitude of the ambient noise should be estimated and considered more as described in Section 3.5.2. Although I only analyzed the azimuthal dependence of ambient-noise source distribution to correct the effect to the phase-velocity measurement, more detailed estimation may reveal the source location of ambient noise as done in southern California by *Harmon et al.* (2010). The ratio between the amplitudes of Rayleigh waves in ZZ and RR is also interesting, as it may be reflecting the difference between shallow structures such as the velocity and thickness of shallow crustal layers (e.g., *Tanimoto and Alvizuri*, 2006). The amplitude ratio between the Rayleigh and Love waves is also interesting to consider the excitation mechanism of the microseisms (*Nishida et al.*, 2008a). All of these discussions are beyond the scope of this study, but should be discussed in the future studies.

Several problems exists for the estimation of radially and azimuthally anisotropic structures. The depth change in radial anisotropy could not be resolved in this study, and needs to be constrained by somehow analyzing 1T mode at periods of ~ 5 –25 s as discussed in Section 4.7.4. The depth and the thickness of LLTZ were difficult to constrain especially when the depth is deeper than 60 km such as the NW and SE regions (Table 4.1; §4.7.3). The analysis of reflection or conversion of body waves may reveal those parameters as done for borehole seafloor records by *Kawakatsu et al.* (2009). By combining the body- and surface-wave analyses, as done by *Gaherty et al.* (1996) and *Kato and Jordan* (1999), it may become possible to constrain the structure from the lithosphere to the asthenosphere with less uncertainty. The BBOBS-NXs deployed in the NW Shatsky region will be recovered in 2014,

and may provide horizontal-component records better than other BBOBSs, which is needed to analyze conversion of body waves.

The uncertainty of azimuthal anisotropy of the 1S mode was especially large for the NW Shatsky region, where the available pairs of stations was few in this study. After the recovery of ten instruments in 2014, the uncertainty is expected to be smaller. We can then discuss the depth variation or the lateral variation in azimuthal anisotropy in the future study. The teleseismic surface waves for the SW Shatsky region was not analyzed in this study, but will be analyzed by different researchers. By combining our results with their results, we will be able to discuss the depth variation of azimuthal anisotropy in this region.

The future observation and analysis in other oceanic regions is essential for discussing the universality and the regionality of the oceanic lithosphere/asthenosphere system. By applying the multi-band methods developed in this study to the future records, we can obtain anisotropic structure beneath other oceanic regions and can discuss the difference between oceanic regions. The tomographic inversion for the three-dimensional structure beneath the array is also needed to reveal the lateral heterogeneity within the array. Such attempt has been started in various oceanic regions by the teleseismic event analysis (*Weeraratne et al.*, 2007), and by the ambient noise analysis (not yet published). It should be, however, noted that the intensity of anisotropy is difficult to estimate by the tomographic procedures. For evaluating the intensity of anisotropy qualitatively, it is important to deploy seafloor instruments in the homogeneous region and estimate the anisotropy by assuming the one-dimensional structure.

The station distribution should be carefully considered for planning the future deployment of the seafloor instruments. For example, the azimuthal dependence of 0S mode is expected to appear clearly for the array with a horizontal scale larger than ~ 500 km as indicated by the difference between the azimuthal dependence for a small array in NW Shatsky region (Fig. 3.39) and that for a larger array in the French Polynesia region (Figure 3.38). In contrast, the interstation distance should be small to analyze 1S and 2S modes at periods shorter than ~ 10 s. For the Shikoku Basin and French Polynesia regions, where the interstation distances are longer than ~ 200 km, we could not analyze phase-velocity anomalies of the 1S mode because of the strong 2π ambiguity (§3.3.6). The array size should be, therefore, larger than 500 km for the surface-wave analysis at periods longer than ~ 30 s, whereas the typical interstation distance should be shorter than 200 km for the analysis at periods shorter than ~ 10 s. Both conditions need to be satisfied to analyze surface waves in a broadband period range of ~ 3 –100 s to obtain uppermost mantle structure at depths of ~ 0 –150 km.

Chapter 7

SUMMARY

I proposed a multi-band method in this study, the “broadband ocean bottom seismology”, and applied the method to the array records of broadband seafloor instruments obtained in five oceanic regions summarized in Chapter 2: Shikoku Basin, French Polynesia, NW Shatsky, SE Shatsky and SW Shatsky regions.

In Chapter 3, broadband surface waves at periods of 3–100 s were analyzed by the ambient noise cross-correlation method at periods of 3–30 s (§3.3) and by the teleseismic event analysis at periods of 30–100 s (§3.4). The existing methods are improved to analyze seafloor records that include problems such as high noise level (§3.3.1), unknown clock delays (§3.3.3), unknown instrumental responses (§3.3.3), overlap between different modes of surface waves (§3.3.4). As a result, I could measure average phase velocities beneath each array, and could estimate azimuthal anisotropy of phase velocities beneath each array at a broadband period range of 3–100 s.

In Chapter 4, 1D radially anisotropic models at a depth range of ~ 10 –150 km were estimated for each region. After showing the inefficiency of isotropic models (§4.3.1) and discussing the relationship between anisotropic parameters (§4.4), smooth 1D radially anisotropic models were obtained (§4.5). The uncertainty of model and its dependence on the smoothing parameter were carefully discussed. The non-smooth radially anisotropic models were then obtained (§4.6) to discuss the structure of the oceanic lithosphere/asthenosphere system (§4.7.3). As a result, the thickness of the lithosphere was revealed to thicken with increasing seafloor age. In addition, the discrepancy between the observed and model-predicted velocity gradients were shown for both in the LID and in the LID-LVZ transition zone. The discrepancy indicates the importance of considering the effect of phase transition at a depth of ~ 30 km, and the presence of partial melt or water in the LVZ.

In Chapter 5, 1D azimuthally anisotropic models at a depth range of ~ 10 –1000 km were estimated for each region. The obtained azimuths of maximum S-wave velocities indicate that the flow in the lithosphere, which records ancient mantle flow during the age of seafloor spreading, is not perpendicular to the magnetic lineations in general. This result suggests that the seismic anisotropy in the lithosphere can be used to estimate the direction of ancient

plate motion.

Chapter 6 consists of general discussions. The intensity of radial and azimuthal anisotropy was first compared and discussed in Section 6.1. The larger intensity of radial anisotropy especially in the LVZ indicates that the apparent radial anisotropy may be produced by the presence of partial melt. The anomalous fabric of olivine crystals may also contribute to produce the radial anisotropy stronger than the azimuthal anisotropy.

The multi-band surface-wave analysis established in this study is useful to obtain 1D anisotropic structure beneath oceanic regions, which can be used to discuss the structure of the oceanic lithosphere/asthenosphere system. I propose this new research method as the “Broadband Ocean Bottom Seismology”. The detail of the method is summarized in Section 6.3 as well as the potential of the broadband ocean bottom seismology in the future studies in Section 6.4.

Appendix A

NOTATIONS

The important notations are summarized in Table A.1–A.3 except for the elastic constants, which will be described below.

The elastic constants are defined by the stress divided by the strain. The relationship can be described by:

$$\begin{pmatrix} \sigma_{xx} \\ \sigma_{yy} \\ \sigma_{zz} \\ \sigma_{yz} \\ \sigma_{zx} \\ \sigma_{xy} \end{pmatrix} = \begin{pmatrix} c_{11} & c_{12} & c_{13} & c_{14} & c_{15} & c_{16} \\ c_{21} & c_{22} & c_{23} & c_{24} & c_{25} & c_{26} \\ c_{31} & c_{32} & c_{33} & c_{34} & c_{35} & c_{36} \\ c_{41} & c_{42} & c_{43} & c_{44} & c_{45} & c_{46} \\ c_{51} & c_{52} & c_{53} & c_{54} & c_{55} & c_{56} \\ c_{61} & c_{62} & c_{63} & c_{64} & c_{65} & c_{66} \end{pmatrix} \begin{pmatrix} \epsilon_{xx} \\ \epsilon_{yy} \\ \epsilon_{zz} \\ 2\epsilon_{yz} \\ 2\epsilon_{zx} \\ 2\epsilon_{xy} \end{pmatrix}, \quad (\text{A.1})$$

where σ_{kl} is stress for the plane normal to k -axis and direction parallel to l -axis, c_{ij} is elastic constants, ϵ_{kl} is the strain defined by

$$\epsilon_{kl} = \frac{1}{2} \left(\frac{\partial u_k}{\partial l} + \frac{\partial u_l}{\partial k} \right), \quad (\text{A.2})$$

where u_k is the displacement for the component k . As the elastic constants are symmetric ($c_{ij} = c_{ji}$), 21 independent parameters are needed to described an anisotropic medium generally. Given the large number of independent parameters, it is difficult to avoid the overlap between notations for elastic constants and those other parameters (Table A.1–A.3). The notations in this chapter are, therefore, according to those by *Takeuchi and Saito* (1972) and *Montagner and Anderson* (1989), and are independent from notations in previous chapters.

A radially anisotropic medium can be described by using five elastic coefficients (A , C ,

Table A.1: Notation for surface-wave analysis (§3).

Symbol	Explanation
c	Phase velocity
T	Period
z	Depth
K_p	Sensitivity of phase velocity to parameter p
F_i^k	Fourier spectrum of k th component at i th station
ω	Angular frequency
S_{ij}^{kl}	Cross spectrum between k th and l the components at i th and j th stations
W_{ij}^{kl}	Weighting term for calculation of cross spectrum
s_i^k	Signal in the Fourier spectrum
n_i^k	Noise in the Fourier spectrum
$\Delta\tau$	Time shift between five-day CCF and one-year CCF
$\Delta\phi$	Phase shift between records of OBS and DPG
$\Delta\tau'$	Time shift between positive and negative lag time of CCF
d_{ij}	Distance between i th and j th stations
a_m^{kl}	Amplitude of mode m in the cross spectrum between k th and l th components
c_m	Phase velocity of mode m
g_m^n	B-spline functions for the frequency dependence of phase velocities
p_m^n	Coefficients for the B-spline functions
\bar{c}_m	Average of 100 phase velocities obtained by the bootstrap method
Δc_m	Error of phase-velocity measurement
γ_{ij}^{kl}	Phase-velocity anomaly
ζ_{ij}^{kl}	Amplitude anomaly
γ_w	Effect of water depth to the phase velocity
γ_s	Effect of source distribution to the phase velocity
B	Source distribution of ambient noise
ϕ	Azimuth
$\Delta\gamma$	Uncertainty of phase-velocity anomaly
A_2	Half intensity of azimuthal anisotropy
ϕ_{\max}	Azimuth of maximum velocity
E	Event
N_E^k	Number of station pairs for component k and event E
θ	Perturbation of incident angle from the great circle

Table A.2: Notation for 1D radially anisotropic structural inversion (§4).

Symbol	Explanation
E_{RA}	Root mean square misfit
R_{sv}	Model roughness
ϵ_{sv}	Smoothing parameter
δV	Radial anisotropy of S-wave velocity defined by $V_{SH}/V_{SV} - 1$
V_{LID}	Average S-wave velocity in the LID
V_{LVZ}	Average S-wave velocity in the LVZ
z_c	Depth of the center of the LID-LVZ transition zone
δz	Thickness of the LID-LVZ transition zone

Table A.3: Notation for 1D azimuthally anisotropic structural inversion (§5).

Symbol	Explanation
E_{AA}	Root mean square misfit
R_{AA}	Model roughness
ϵ_{AA}	Smoothing parameter
$\tilde{A}_{C,S}$	Coefficients for the azimuthal anisotropy of the phase velocity of Rayleigh wave
$A'_{C,S}$	Coefficients for the azimuthal anisotropy of S-wave velocity
δt	Splitting time
λ	Eigen value

F , L and N) as:

$$\begin{pmatrix} \sigma_{xx} \\ \sigma_{yy} \\ \sigma_{zz} \\ \sigma_{yz} \\ \sigma_{zx} \\ \sigma_{xy} \end{pmatrix} = \begin{pmatrix} A & A-2N & F & 0 & 0 & 0 \\ A-2N & A & F & 0 & 0 & 0 \\ F & F & C & 0 & 0 & 0 \\ 0 & 0 & 0 & L & 0 & 0 \\ 0 & 0 & 0 & 0 & L & 0 \\ 0 & 0 & 0 & 0 & 0 & N \end{pmatrix} \begin{pmatrix} \epsilon_{xx} \\ \epsilon_{yy} \\ \epsilon_{zz} \\ 2\epsilon_{yz} \\ 2\epsilon_{zx} \\ 2\epsilon_{xy} \end{pmatrix}, \quad (\text{A.3})$$

where the symmetric axis is set to be z-axis (*Takeuchi and Saito, 1972*). The velocities of elastic waves are then given by:

$$V_{SH} = \sqrt{\frac{N}{\rho}}, \quad V_{SV} = \sqrt{\frac{L}{\rho}}, \quad V_{PH} = \sqrt{\frac{A}{\rho}}, \quad V_{PV} = \sqrt{\frac{C}{\rho}}, \quad (\text{A.4})$$

where ρ is density, V_{SH} is the velocity of horizontally propagating and horizontally polarized S-wave, V_{SV} is the velocity of horizontally propagating and vertically polarized S-wave or the velocity of vertically propagating and horizontally polarized S-wave, V_{PH} is the velocity of horizontally propagating P-wave, and V_{PV} is the velocity of vertically propagating P-wave. Three anisotropic parameters are given by:

$$\xi = \frac{N}{L} = \left(\frac{V_{SH}}{V_{SV}} \right)^2, \quad \phi = \frac{C}{A} = \left(\frac{V_{SH}}{V_{SV}} \right)^2, \quad \eta = \frac{F}{A-2L}, \quad (\text{A.5})$$

where ξ denotes the S-wave anisotropy, ϕ denotes the P-wave anisotropy, and η is a parameter that affects the velocities of P- and S-waves with incident angles between 0° and 90° .

The azimuthal anisotropy can be further described by considering eight more elastic constants: B_C , B_S , G_C , G_S , H_C , H_S , E_C and E_S (*Montagner and Nataf, 1986; Montagner and Anderson, 1989*). As a radially anisotropic medium needs five elastic constants, 13 elastic constants are needed to describe an radially and azimuthally anisotropic medium. Although there are 21 independent elastic constants, *Montagner and Anderson (1989)* pointed out that other eight elastic constants are not needed for describing seismic waves under the assumption that the anisotropy is small. The velocities of P- and S- waves can be then given by each solving equations:

$$\rho V_{PH}^2 = A + B_C \cos 2\phi + B_S \sin 2\phi + E_C \cos 4\phi + E_S \sin 4\phi, \quad (\text{A.6})$$

$$\rho V_{SH}^2 = N - E_C \cos 4\phi - E_S \sin 4\phi, \quad (\text{A.7})$$

$$\rho V_{SV}^2 = L + G_C \cos 2\phi + G_S \sin 2\phi. \quad (\text{A.8})$$

The azimuthal dependence of V_{SV} can be obtained by :

$$V_{SV} = \sqrt{\frac{L}{\rho}} \sqrt{1 + \frac{G_C}{L} \cos 2\phi + \frac{G_S}{L} \sin 2\phi} \quad (\text{A.9})$$

$$\sim \sqrt{\frac{L}{\rho}} \left(1 + \frac{G_C}{2L} \cos 2\phi + \frac{G_S}{2L} \sin 2\phi \right). \quad (\text{A.10})$$

The intensity of azimuthal anisotropy of V_{SV} estimated in this study is, therefore, given by:

$$A_2 = \frac{1}{2L} \sqrt{G_C^2 + G_S^2}. \quad (\text{A.11})$$

There is no azimuthal anisotropy for V_{PV} because it is the velocity of vertically propagating and vertically polarized P-wave, which has no azimuth for both propagation and polarization directions. The sensitivities of surface-wave velocities to the azimuthal anisotropy of elastic constants are exactly equal to the sensitivities to the elastic constants of radially anisotropic structure (*Montagner and Nataf*, 1986) under the assumption that the anisotropy is small.

Appendix B

BOOTSTRAP METHOD

Efron (1979) originally proposed the bootstrap method as an method for estimating the uncertainty of an estimated value by resampling the original values used for the estimation. For example, I here consider the case that N values, $\mathbf{x} = (x_1, x_2, \dots, x_N)$, are used for estimating M values f , i.e., $\mathbf{f} = (f_1, f_2, \dots, f_M) = \mathbf{F}(\mathbf{x})$. The bootstrap method can be applied only when all the N values are replaceable to each other. In that case, we can make a bootstrap sample, $\mathbf{x}^* = (x_1^*, x_2^*, \dots, x_N^*)$, composed of N values randomly selected N times from the original N values (\mathbf{x}) with allowing overlaps. The bootstrap sample gives new values (\mathbf{f}^*) by using the estimation procedure same as the original estimation, $\mathbf{f}^* = \mathbf{F}(\mathbf{x}^*)$. If we repeat this process L times, we obtain L different values ($\mathbf{f}_1^*, \mathbf{f}_2^*, \dots, \mathbf{f}_L^*$) from L bootstrap samples ($\mathbf{x}_1^*, \mathbf{x}_2^*, \dots, \mathbf{x}_L^*$). The confidence interval for each model parameters is given by calculating the average and a standard deviation of the L estimated values for each parameter.

The number of bootstrap samples (L) should be large enough to obtain a reliable estimation for the confidence interval. If the number is lower than ~ 100 , the confidence interval becomes unstable, i.e., the interval becomes different if we use different bootstrap samples. If the number is larger than ~ 100 , on the other hand, the change in confidence interval is negligible compared to the estimated uncertainty range, although the computational cost increases. I, therefore, choose $L = 100$ in this study.

The bootstrap method in this study was first appeared for the estimation of measurement error of phase velocities by the ambient noise cross-correlation method (§3.3.4). In this case, the datasets are three or five components of cross-spectra: $\mathbf{S} = (\mathbf{S}^{ZZ}, \mathbf{S}^{RR}, \mathbf{S}^{TT}, \mathbf{S}^{PZ}, \mathbf{S}^{PP})$, where \mathbf{S} denotes the aggregate of cross-spectra of N pairs of stations. The estimated values are the average phase velocities of multi-mode surface waves described by $\mathbf{c} = (c_{0S}(\omega), c_{1S}(\omega), c_{0T}(\omega))$. If the bootstrap sample is made simply from all the cross-spectra, the number of measurements for each component can differ from original number of measurements. The reduction of number for the TT component, however, causes large uncertainty of the phase velocity of Love wave because the wave only appears in the TT component. I, therefore, assumed that the number of measurements for each component in a bootstrap sample

is same as the original number of measurements for the component. One hundred combinations of phase velocities ($\mathbf{c}_1^*, \mathbf{c}_2^*, \dots, \mathbf{c}_{100}^*$) were obtained from one hundred bootstrap samples ($\mathbf{S}_1^*, \mathbf{S}_2^*, \dots, \mathbf{S}_{100}^*$), where $\mathbf{S}_l^* = (\mathbf{S}_l^{*ZZ}, \mathbf{S}_l^{*RR}, \mathbf{S}_l^{*TT}, \mathbf{S}_l^{*PZ}, \mathbf{S}_l^{*PP})$. The bootstrap method is also used for the estimation of azimuthal anisotropy from the phase-velocity anomalies by the ambient noise cross-correlation method (§3.3.6) and the teleseismic event analysis (§3.4.1–3.4.2). In these cases, the bootstrap sample was simply made from all the data because all the datasets are replaceable to each other.

The uncertainty of 1D radially anisotropic models were also estimated by the bootstrap method in Chapter 4. In this case, the datasets are phase velocities of Rayleigh and Love waves for the inversion of the radially anisotropic structure estimated from the ambient noise at periods of 3–30 s, $c_{0S}(\omega)$, $c_{1S}(\omega)$ and $c_{0T}(\omega)$, and from the teleseismic events at periods of 30–100 s, $c_{0S'}(\omega)$ and $c_{0T'}(\omega)$, as summarized in Table 3.1. The 1D model, \mathbf{g} , were obtained from these measurements, $\mathbf{c} = (c_{0S}(\omega), c_{1S}(\omega), c_{0T}(\omega), c_{0S'}(\omega), c_{0T'}(\omega))$, by $\mathbf{g} = \mathbf{G}(\mathbf{c})$. In this case, the measurements are not replaceable to each other because measurements at different period or for different modes have different depth sensitivities to the mantle structure. I, therefore, defined a bootstrap sample from the phase velocities obtained by the bootstrap method in Chapter 3: $\mathbf{c}_1^*, \mathbf{c}_2^*, \dots, \mathbf{c}_{100}^*$. In each bootstrap sample (\mathbf{c}_l^*), the pairs used for the analysis are the same for the measurements from the ambient noise (c_{0S}^l, c_{1S}^l and c_{0T}^l), whereas the events used for the analysis are not same for the measurements from the teleseismic events ($c_{0S'}^l$ and $c_{0T'}^l$). One hundred models ($\mathbf{g}_1^*, \mathbf{g}_2^*, \dots, \mathbf{g}_{100}^*$) were then obtained from those one hundred bootstrap samples. The uncertainty of 1D azimuthally anisotropic models were similarly estimated by the bootstrap method in Chapter 5, although the dataset in this case is the azimuthal anisotropy of phase velocities of Rayleigh waves summarized in Table 3.2.

Appendix C

SIMULATED ANNEALING METHOD

The simulated annealing method is a kind of Monte Carlo algorithm developed for searching a best global fit of a nonlinear problem (e.g., *Kirkpatrick et al.*, 1983; *Ingber*, 1989), i.e., it is a method to search for M model parameters, $\mathbf{x} = (x_1, x_2, \dots, x_M)$, that gives the minimum of the cost function, $E = E(\mathbf{x})$. The cost function is defined by the root-mean-square misfit in this study. The global minimum is given by iterating the four steps. In the first step, a temperature, T , is defined and decreased with increasing number of iteration. In the second step, new model parameters, \mathbf{x}' , are assumed by perturbing the original model parameters, \mathbf{x} , by using a probability distribution such as the Boltzmann or Cauchy distributions. The size of the perturbation is large for the high temperature and small for the low temperature. In the third step, the cost function is calculated for the assumed model parameters. In the fourth step, the model parameters are replaced to the new values ($\mathbf{x}' \rightarrow \mathbf{x}$) if the cost function, $E(\mathbf{x}')$, is lower than the cost function for the original model parameters, $E(\mathbf{x})$, or the difference in the cost functions is small. The threshold for the difference in the cost functions is large for high temperature and small for low temperature. By repeating these four steps infinitely, we can find the model parameters (\mathbf{x}) corresponding to the global minimum of the cost function.

There are four parameters for the very fast simulated annealing method by *Ingber* (1989) used in this study: an initial temperature (T_0), a final temperature (T_f), a constant for calculating the perturbation (k) and the number of iterations (N). The temperature for the n th iteration is given by:

$$T = T_0 \exp\left(-cn^{1/M}\right), \quad (\text{C.1})$$

where the parameter c controls the annealing schedule and give by:

$$c = \frac{\ln T_0 - \ln T}{N^{1/M}}. \quad (\text{C.2})$$

The perturbation to i th model parameter, Δx_i , is obtained from a uniform distribution

Table C.1: Parameters for the simulated annealing method.

	M	N	T_0	T_f	k
Phase velocity measurement (§3.3.4)	~ 30	40000	100	10^{-5}	1
Phase velocity measurement (§3.4.1)	~ 7	5000	0.1	10^{-6}	1
Smooth radially anisotropic inversion (§4.5)	14	20000	10^5	10^{-6}	1
Non-smooth radially anisotropic inversion (§4.6)	10	5000	10	10^{-6}	0.1
Azimuthally anisotropic inversion (§5.2)	16	100000	1000	10^{-6}	0.01

between 0 and 1, $u \in [0, 1]$, by:

$$\Delta x_i = x'_i - x_i = \text{sgn} \left(u - \frac{1}{2} \right) kT \left[\left(1 + \frac{1}{kT} \right)^{|2u-1|} - 1 \right], \quad (\text{C.3})$$

where sgn is a function that gives the sign of the value. After the calculation of new cost function, $E(\mathbf{x}')$, the model parameters are replaced if the new cost function is smaller than the original cost function ($E(\mathbf{x}') < E(\mathbf{x})$). When the new cost function is larger, the model parameters are replaced with a probability give by:

$$\exp \left[-\frac{E(\mathbf{x}') - E(\mathbf{x})}{T} \right]. \quad (\text{C.4})$$

The parameters used in this study are summarized in Table C.1. I tried various combinations of parameters and tested whether the estimated values depend on the initial model parameters. The final parameters for the simulated annealing correspond to the minimum number of iteration (N) among the combinations of parameters that give no dependence of the estimated values on the initial model parameters. The small number of iteration is needed to reduce the computational cost because I repeated the model estimation one hundred times to estimate the model uncertainty by the bootstrap method (Appendix B).

The computational time is especially long for the radially anisotropic inversion in Chapter 4 because it includes the calculation of phase velocities for the assumed structural model by the DISPER80 package (*Saito, 1988*) that takes 1–2 s for the required accuracy and period range in this study. In tomography studies, the computational time is reduced by estimating the phase velocities from the sensitivity kernels (§3.2) with an assumption of linear relationship between the model perturbation and the perturbation in the phase velocities. Although it takes time to calculate the sensitivity kernels, model phase velocity for any structural model can be estimated quickly after obtaining the sensitivity kernels once. If the perturbation from the initial model is large, however, the linear relationship cannot be assumed. The phase velocities and sensitivity kernels should be calculated again based on the new model if the model is far from the initial model. In this study, therefore, I calculated the model phase velocities by using sensitivity kernels at the third step of each iteration to minimize the computational cost, and re-calculated the sensitivity kernels and the model

phase velocities by the DISPER80 package (*Saito*, 1988) only when the model parameters are replaced in the fourth step of each iteration.

Acknowledgements

This work has been done in the University of Tokyo, where I met a number of wonderful people. I first would like to express my appreciation to my supervisor, Hitoshi Kawakatsu. His comments on the current analysis of seafloor records gave me the inspiration for beginning this work. He also gave me many opportunities to meet foreign researchers and to visit foreign institutes, that helped me to have an international scope.

I also need to express my best appreciation to Kiwamu Nishida for the discussion and comments especially about the methods. He encouraged and helped my works from the initial treatment of datasets to the publication of articles. The various discussions about “seismic noise” is not only helpful for this study, but also will be the base for my future studies.

I am also grateful to Takehi Isse for the discussion and comments especially about the results. He gave me many comments as one of surface-wave researchers and as one of ocean-bottom seismologist, and helped me to compare the radially anisotropic models obtained in this study with those obtained by previous studies.

I spent more than five years in the Ocean Hemisphere Research Center, Earthquake Research Institute, the University of Tokyo. I would like to thank all other researchers in the center as well as my advisors for their advice throughout my study and their continuous contribution to the development of and broadband observation by the electromagnetic instruments and seismometers: Hisashi Utada, Hisayoshi Shimizu, Nozomu Takeuchi, Shingo Watada, Kiyoshi Baba, Noriko Tada (also in JAMSTEC), Takashi Tonegawa (now in JAMSTEC) and Koki Idehara (now in a company). I also would like to thank all people in the Earthquake Research Institute for the advice and discussions, especially by the two rheologists: Yasuko Takei and Takehiko Hiraga.

I would like to thank Donald Forsyth in the Brown University for his advice and discussion during my two-month stay there. He gave me an opportunity to analyze newly obtained datasets obtained by the PLATE project. After I came back to Japan, he continued to discuss with me by e-mails and when he came to Japan. I also would like to thank many researchers and friends I met there, especially the students in the Geology Department, Natsumi Shintaku and Takamasa Kanaya, and my floor-mate in the apartment, Karine Ip, for their kindness. I could get used to talk in English through the conversations with those international students.

I am also grateful to many researchers for their advice in the meetings, workshops, my stay in US and their stay in ERI: Yoshio Fukao (JAMSTEC), Kazunori Yoshizawa (Hokkaido University), Mamoru Kato (Kyoto University), Jean-Paul Montagner (IPG Paris), Toshiro Tanimoto (UC Santa Barbara), Nobukazu Seama (Kobe University), Shun-ichiro Karato (Yale University), Karen Fischer (Brown University), Spahr Webb, Goran Ekstrom, James Gaherty, Geoffrey Abers (LDEO, Columbia University), Reiji Kobayashi (Kagoshima University), and all others, although I cannot write them all here. Especially, I learned about the rock deformation during the visit to Mt. Apoi in 2011 and 2013 from Eiichi Takazawa (Niigata University), Katsuyoshi Michibayashi (Shizuoka University), Takehiko Hiraga (ERI), Natsue Abe, Hiroshi Ichihara (JAMSTEC) and Saeko Kita (NIED).

The records for four regions used in this study (Shikoku Basin, French Polynesia, and NW and SE Shatsky regions) were taken by Japanese researchers and technical staffs: Hajime Shiobara, Takehi Isse, Koji Miyakawa (ERI, University of Tokyo), and Daisuke Suetsugu, Hiroko Sugioka, Aki Ito and Takashi Tonegawa (JAMSTEC). The broadband ocean bottom seismometers (BBOBSs) were developed mainly by Toshihiko Kanazawa, and the BBOBS-NXs were developed mainly by Hajime Shiobara. I also participated the observation cruise in the NW Shatsky region by the NOMAN project (KR10-08 in 2010 and KR12-14 in 2012) by R/V KAIREI of JAMSTEC. I could spend fruitful time on the ship with the supports by the crew, the technical staffs and the operation team of ROV KAIKO 7000II. They are all gentle and wonderful.

The records for the SW Shatsky region used in this study were taken by U.S. researchers: Dayanthie Weeraratne (CSUN) and Donald Forsyth (Brown University). They acquired the records by the instruments from the Lamont-Doherty Earth Observatory of Columbia University and Scripps Institution of Oceanography, UC San Diego.

I also would like to thank five reviewers in the University of Tokyo: Robert Geller, Nozomu Takeuchi, Takashi Iidaka, Kimihiro Mochizuki and Kyoko Okino. I could improve this thesis by their helpful comments.

The surface-wave analysis and 1D radially anisotropic inversion for the Shikoku Basin region in Chapter 3–4 are based on an original paper, “Radially anisotropic structure beneath the Shikoku Basin from broadband surface wave analysis of ocean bottom seismometer records”, by Takeo et al., *Journal of Geophysical Research* (*Takeo et al.*, 2013). The surface-wave analysis and 1D inversion for the SW Shatsky region in Chapter 3–5 are based on an original paper, “Estimation of azimuthal anisotropy in the NW Pacific from seismic ambient noise in seafloor records”, by Takeo et al., submitted to *Geophysical Journal International* (*Takeo et al.*, submitted). The clock corrections for the NW and SE Shatsky region in Chapter 3 are based on an original paper, “Time correction and clock stability of ocean bottom seismometer using recorded seismograms”, by Isse et al., accepted by JAMSTEC-R (*Isse et al.*, accepted). Other part of this thesis will be published elsewhere.

I have been financially supported by the Research Fellowship for Young Scientists of

Japan Society for the Promotion of Sciences (JSPS) as well as the Grant-in-Aids for JSPS Fellows (23-8157) and Scientific Research (16075203, 22000003, 24654142). The Department of Earth and Planetary Science, the University of Tokyo, gave me an opportunity to stay in the Brown University with the financial support by the Institutional Program for Young Researcher Overseas Visits of JSPS.

I used various free softwares in this study: the GMT (*Wessel and Smith*, 1991) for drawing figures and maps, SAC2000 (*Goldstein and Snoke*, 2005) for analyzing seismic records, and DISPER80 (*Saito*, 1988) for calculating dispersion curves of surface waves.

Finally, I would like to thank my family and friends for their supports and understandings throughout my studies in these five years.

Akiko Takeo
Tokyo, March 2014

Bibliography

- Adam, C., and A. Bonneville, Extent of the South Pacific Superswell, *J. Geophys. Res.*, *110*(B9), B09,408, doi:10.1029/2004JB003465, 2005.
- Aki, K., Space and time spectra of stationary stochastic waves, with special reference to microtremors, *Bull. Earthq. Res. Inst.*, *35*(3), 415–456, 1957.
- Aki, K., Seismological evidences for the existence of soft thin layers in the upper mantle under Japan, *J. Geophys. Res.*, *73*(2), 585–594, doi:10.1029/JB073i002p00585, 1968.
- Aki, K., and K. Kaminuma, Phase Velocity of Love Waves in Japan (Part 1): Love Waves from the Aleutian Shock of March 9, 1957., *Bull. Earthq. Res. Inst.*, *41*(1), 243–259, 1963.
- Anderson, D. L., Love wave dispersion in heterogeneous anisotropic media, *Geophysics*, *27*(4), 445–454, doi:10.1190/1.1439042, 1962.
- Anderson, D. L., The thermal state of the upper mantle; No role for mantle plumes, *Geophys. Res. Lett.*, *27*(22), 3623, doi:10.1029/2000GL011533, 2000.
- Anderson, D. L., and J. D. Bass, Mineralogy and composition of the upper mantle, *Geophys. Res. Lett.*, *11*(7), 637, doi:10.1029/GL011i007p00637, 1984.
- Anderson, D. L., and C. Sammis, Partial melting in the upper mantle, *Phys. Earth Planet. Inter.*, *3*, 41–50, doi:10.1016/0031-9201(70)90042-7, 1970.
- Ando, M., ScS polarization anisotropy around the Pacific Ocean., *J. Phys. Earth*, *32*(3), 179–195, doi:10.4294/jpe1952.32.179, 1984.
- Araki, E., and H. Sugioka, Calibration of deep sea differential pressure gauge, *JAMSTEC-R IFREE*, (November), 141–148, 2009.
- Baba, K., H. Utada, T. Goto, T. Kasaya, H. Shimizu, and N. Tada, Electrical conductivity imaging of the Philippine Sea upper mantle using seafloor magnetotelluric data, *Phys. Earth Planet. Inter.*, *183*(1-2), 44–62, doi:10.1016/j.pepi.2010.09.010, 2010.
- Baba, K., N. Tada, L. Zhang, P. Liang, H. Shimizu, and H. Utada, Is the electrical conductivity of the northwestern Pacific upper mantle normal?, *Geochemistry, Geophys. Geosystems*, *14*(12), 4969–4979, doi:10.1002/2013GC004997, 2013.

- Backus, G. E., Long-Wave Elastic Anisotropy Produced by Horizontal Layering, *J. Geophys. Res.*, *67*(11), 4427–4440, doi:10.1029/JZ067i011p04427, 1962.
- Backus, G. E., Possible forms of seismic anisotropy of the uppermost mantle under oceans, *J. Geophys. Res.*, *70*(14), 3429–3439, doi:10.1029/JZ070i014p03429, 1965.
- Barruol, G., PLUME investigates South Pacific Superswell, *Eos, Trans. Am. Geophys. Union*, *83*(45), 511, doi:10.1029/2002EO000354, 2002.
- Barruol, G., D. Suetsugu, H. Shiobara, H. Sugioka, S. Tanaka, G. H. R. Bokelmann, F. R. Fontaine, and D. Reymond, Mapping upper mantle flow beneath French Polynesia from broadband ocean bottom seismic observations, *Geophys. Res. Lett.*, *36*(14), 1–5, doi:10.1029/2009GL038139, 2009.
- Beaty, K. S., D. R. Schmitt, and M. Sacchi, Simulated annealing inversion of multimode Rayleigh wave dispersion curves for geological structure, *Geophys. J. Int.*, *151*(2), 622–631, doi:10.1046/j.1365-246X.2002.01809.x, 2002.
- Becker, T. W., B. Kustowski, and G. Ekström, Radial seismic anisotropy as a constraint for upper mantle rheology, *Earth Planet. Sci. Lett.*, *267*(1-2), 213–227, doi:10.1016/j.epsl.2007.11.038, 2008.
- Behn, M. D., G. Hirth, and J. R. Elsenbeck II, Implications of grain size evolution on the seismic structure of the oceanic upper mantle, *Earth Planet. Sci. Lett.*, *282*(1-4), 178–189, doi:10.1016/j.epsl.2009.03.014, 2009.
- Bensen, G. D., M. H. Ritzwoller, M. P. Barmin, a. L. Levshin, F. Lin, M. P. Moschetti, N. M. Shapiro, and Y. Yang, Processing seismic ambient noise data to obtain reliable broad-band surface wave dispersion measurements, *Geophys. J. Int.*, *169*(3), 1239–1260, doi:10.1111/j.1365-246X.2007.03374.x, 2007.
- Bensen, G. D., M. H. Ritzwoller, and N. M. Shapiro, Broadband ambient noise surface wave tomography across the United States, *J. Geophys. Res.*, *113*(B5), 1–21, doi:10.1029/2007JB005248, 2008.
- Bozdag, E., and J. Trampert, On crustal corrections in surface wave tomography, *Geophys. J. Int.*, *172*(3), 1066–1082, doi:10.1111/j.1365-246X.2007.03690.x, 2008.
- Cara, M., and J. J. L  v  que, Anisotropy of the asthenosphere: The higher mode data of the Pacific revisited, *Geophys. Res. Lett.*, *15*(3), 205, doi:10.1029/GL015i003p00205, 1988.
- Christensen, N. I., and M. H. Salisbury, Structure and constitution of the lower oceanic crust, *Rev. Geophys.*, *13*(1), 57, doi:10.1029/RG013i001p00057, 1975.

- Cox, C., T. Deaton, and S. Webb, A deep-sea differential pressure gauge, *J. Atmos. Ocean. Technol.*, 1(3), 237–246, doi:10.1175/1520-0426(1984)001<0237:ADSDPG>2.0.CO;2, 1984.
- Cox, H., Spatial correlation in arbitrary noise fields with application to ambient sea noise, *J. Acoust. Soc. Am.*, 54(5), 1289, doi:10.1121/1.1914426, 1973.
- Crampin, S., Seismic-wave propagation through a cracked solid: polarization as a possible dilatancy diagnostic, *Geophys. J. R. Astron. Soc.*, 53(3), 467–496, doi:10.1111/j.1365-246X.1978.tb03754.x, 1978.
- Crampin, S., Comments on “Possible forms of seismic anisotropy of the uppermost mantle under oceans” by George E. Backus, *J. Geophys. Res.*, 87(B6), 4636, doi:10.1029/JB087iB06p04636, 1982.
- Davis, E., and C. Lister, Fundamentals of ridge crest topography, *Earth Planet. Sci. Lett.*, 21(4), 405–413, doi:10.1016/0012-821X(74)90180-0, 1974.
- Dorman, J., M. Ewing, and J. Oliver, Study of shear-velocity distribution in the upper mantle by mantle Rayleigh waves, *Bull. Seismol. Soc. Am.*, 50(1), 87–115, 1960.
- Duncan, R., and I. McDougall, Linear volcanism in French Polynesia, *J. Volcanol. Geotherm. Res.*, 1(3), 197–227, doi:10.1016/0377-0273(76)90008-1, 1976.
- Dunn, R. A., and D. W. Forsyth, Imaging the transition between the region of mantle melt generation and the crustal magma chamber beneath the southern East Pacific Rise with short-period Love waves, *J. Geophys. Res.*, 108(B7), 2352, doi:10.1029/2002JB002217, 2003.
- Dunn, R. A., and D. R. Toomey, Crack-induced seismic anisotropy in the oceanic crust across the East Pacific Rise (9°30'N), *Earth Planet. Sci. Lett.*, 189(1-2), 9–17, doi:10.1016/S0012-821X(01)00353-3, 2001.
- Dziewonski, A. M., and D. L. Anderson, Preliminary reference Earth model, *Phys. Earth Planet. Inter.*, 25(4), 297–356, doi:10.1016/0031-9201(81)90046-7, 1981.
- Efron, B., Bootstrap methods: Another look at the jackknife, *Ann. Stat.*, 7(1), 1–26, doi:10.1214/aos/1176344552, 1979.
- Ekström, G., and A. M. Dziewonski, The unique anisotropy of the Pacific upper mantle, *Nature*, 394(6689), 168–172, doi:10.1038/28148, 1998.
- Ekström, G., G. A. Abers, and S. C. Webb, Determination of surface-wave phase velocities across USArray from noise and Aki’s spectral formulation, *Geophys. Res. Lett.*, 36(18), 5–9, doi:10.1029/2009GL039131, 2009.

- Estey, L. H., and B. J. Douglas, Upper Mantle Anisotropy: A Preliminary Model, *J. Geophys. Res.*, *91* (B11), 11,393–11,406, doi:10.1029/JB091iB11p11393, 1986.
- Ewing, W. M., W. S. Jardetzky, and F. Press, *Elastic Waves in Layered Media*, 380 pp., McGraw Hill Book Company Inc., 1957.
- Faul, U. H., and I. Jackson, The seismological signature of temperature and grain size variations in the upper mantle, *Earth Planet. Sci. Lett.*, *234*, 119–134, doi:10.1029/2001JB001225, 2005.
- Fichtner, A., B. L. Kennett, H. Igel, and H.-P. Bunge, Full waveform tomography for radially anisotropic structure: New insights into present and past states of the Australasian upper mantle, *Earth Planet. Sci. Lett.*, *290* (3-4), 270–280, doi:10.1016/j.epsl.2009.12.003, 2010.
- Fischer, K. M., H. A. Ford, D. L. Abt, and C. A. Rychert, The Lithosphere-Asthenosphere Boundary, *Annu. Rev. Earth Planet. Sci.*, *38* (1), 551–575, doi:10.1146/annurev-earth-040809-152438, 2010.
- Fontaine, F. R., G. Barruol, A. Tommasi, and G. H. R. Bokelmann, Upper-mantle flow beneath French Polynesia from shear wave splitting, *Geophys. J. Int.*, *170* (3), 1262–1288, doi:10.1111/j.1365-246X.2007.03475.x, 2007.
- Forsyth, D. W., The early structural evolution and anisotropy of the oceanic upper mantle, *Geophys. J. R. Astron. Soc.*, *43* (1), 103–162, doi:10.1111/j.1365-246X.1975.tb00630.x, 1975.
- Forsyth, D. W., and A. Li, Array Analysis of Two-Dimensional Variations in Surface Wave Phase Velocity and Azimuthal Anisotropy in the Presence of Multipathing Interference, in *Seism. Earth array Anal. broadband Seism.*, edited by A. Levander and G. Nolet, pp. 81–97, American Geophysical Union, Washington, D. C., doi:10.1029/157GM06, 2005.
- Forsyth, D. W., and F. Press, Geophysical tests of petrological models of the spreading lithosphere, *J. Geophys. Res.*, *76* (32), 7963, doi:10.1029/JB076i032p07963, 1971.
- Francis, T. J. G., Generation of seismic anisotropy in the upper mantle along the mid-oceanic ridges, *Nature*, *221* (5176), 162–165, doi:10.1038/221162b0, 1969.
- Fukao, Y., Evidence from core-reflected shear waves for anisotropy in the Earth’s mantle, *Nature*, *309* (5970), 695–698, doi:10.1038/309695a0, 1984.
- Furumura, T., Subduction zone guided waves and the heterogeneity structure of the subducted plate: Intensity anomalies in northern Japan, *J. Geophys. Res.*, *110* (B10), B10,302, doi:10.1029/2004JB003486, 2005.

- Gaherty, J. B., T. H. Jordan, and L. S. Gee, Seismic structure of the upper mantle in a central Pacific corridor, *J. Geophys. Res.*, *101*(B10), 22,291–22,309, doi:10.1029/96JB01882, 1996.
- Goldstein, P., and A. Snoke, SAC availability for the IRIS community, *DMS Electron. Newsl.*, *7*(1), <http://www.iris.edu/dms/newsletter/vol7/no1/>, 2005.
- Grevemeyer, I., W. Weigel, S. Schüssler, and F. Avedik, Crustal and upper mantle seismic structure and lithospheric flexure along the Society Island hotspot chain, *Geophys. J. Int.*, *147*(1), 123–140, doi:10.1046/j.0956-540x.2001.01521.x, 2001.
- Gripp, A. E., and R. G. Gordon, Young tracks of hotspots and current plate velocities, *Geophys. J. Int.*, *150*(2), 321–361, doi:10.1046/j.1365-246X.2002.01627.x, 2002.
- Gung, Y., M. Panning, and B. Romanowicz, Global anisotropy and the thickness of continents, *Nature*, *422*(April), 707–711, doi:10.1038/nature01557.1., 2003.
- Gutenberg, B., Wave velocities below the Mohorovicic discontinuity, *Geophys. J. Int.*, *2*(4), 348–352, doi:10.1111/j.1365-246X.1959.tb05805.x, 1959.
- Haney, M. M., T. D. Mikesell, K. van Wijk, and H. Nakahara, Extension of the spatial autocorrelation (SPAC) method to mixed-component correlations of surface waves, *Geophys. J. Int.*, *191*(1), 189–206, doi:10.1111/j.1365-246X.2012.05597.x, 2012.
- Hannemann, K., F. Krüger, and T. Dahm, Measuring of clock drift rates and static time offsets of ocean bottom stations by means of ambient noise, *Geophys. J. Int.*, doi:10.1093/gji/ggt434, 2013.
- Harmon, N., D. Forsyth, and S. Webb, Using ambient seismic noise to determine short-period phase velocities and shallow shear velocities in young oceanic lithosphere, *Bull. Seismol. Soc. Am.*, *97*(6), 2009–2023, doi:10.1785/0120070050, 2007.
- Harmon, N., C. Rychert, and P. Gerstoft, Distribution of noise sources for seismic interferometry, *Geophys. J. Int.*, *183*(3), 1470–1484, doi:10.1111/j.1365-246X.2010.04802.x, 2010.
- Hilde, T., N. Isezaki, and J. M. Wageman, 18. Mesozoic Sea-Floor Spreading in the North Pacific, in *Geophys. Monogr. Ser.*, vol. 19, edited by G. H. Sutton, M. H. Manghnani, R. Moberly, and E. U. McAffee, vol. 19 ed., pp. 205–226, AGU, Washington, D. C., doi:10.1029/GM019p0205, 1976.
- Hirschmann, M. M., Partial melt in the oceanic low velocity zone, *Phys. Earth Planet. Inter.*, *179*(1-2), 60–71, doi:10.1016/j.pepi.2009.12.003, 2010.
- Holtzman, B. K., D. L. Kohlstedt, M. E. Zimmerman, F. Heidelbach, T. Hiraga, and J. Hystoft, Melt segregation and strain partitioning: implications for seismic anisotropy and mantle flow., *Science*, *301*(5637), 1227–30, doi:10.1126/science.1087132, 2003.

- Ingber, L., Very fast simulated re-annealing, *Math. Comput. Model.*, *12*(8), 967–973, doi:10.1016/0895-7177(89)90202-1, 1989.
- Isse, T., D. Suetsugu, H. Shiobara, H. Sugioka, K. Yoshizawa, T. Kanazawa, and Y. Fukao, Shear wave speed structure beneath the South Pacific superswell using broadband data from ocean floor and islands, *Geophys. Res. Lett.*, *33*(16), 2–6, doi:10.1029/2006GL026872, 2006a.
- Isse, T., K. Yoshizawa, H. Shiobara, M. Shinohara, K. Nakahigashi, K. Mochizuki, H. Sugioka, D. Suetsugu, S. Oki, T. Kanazawa, K. Suyehiro, and Y. Fukao, Three-dimensional shear wave structure beneath the Philippine Sea from land and ocean bottom broadband seismograms, *J. Geophys. Res.*, *111*(B6), 1–13, doi:10.1029/2005JB003750, 2006b.
- Isse, T., H. Shiobara, Y. Tamura, D. Suetsugu, K. Yoshizawa, H. Sugioka, A. Ito, T. Kanazawa, M. Shinohara, and K. Mochizuki, Seismic structure of the upper mantle beneath the Philippine Sea from seafloor and land observation: Implications for mantle convection and magma genesis in the Izu-Bonin-Mariana subduction zone, *Earth Planet. Sci. Lett.*, *278*(1-2), 107–119, doi:10.1016/j.epsl.2008.11.032, 2009.
- Isse, T., H. Shiobara, J.-P. Montagner, H. Sugioka, A. Ito, A. Shito, T. Kanazawa, and K. Yoshizawa, Anisotropic structures of the upper mantle beneath the northern Philippine Sea region from Rayleigh and Love wave tomography, *Phys. Earth Planet. Inter.*, *183*(1-2), 33–43, doi:10.1016/j.pepi.2010.04.006, 2010.
- Isse, T., A. Takeo, and H. Shiobara, Time correction and clock stability of ocean bottom seismometer using recorded seismograms, *JAMSTEC-R IFREE*, accepted.
- Jung, H., and S. Karato, Water-induced fabric transitions in olivine., *Science*, *293*(5534), 1460–3, doi:10.1126/science.1062235, 2001.
- Kanamori, H., and K. Abe, Deep structure of island arcs as revealed by surface waves, *Bull. Earthq. Res. Inst.*, *46*(5), 1001–1025, 1968.
- Kanamori, H., and D. L. Anderson, Importance of physical dispersion in surface wave and free oscillation problems: Review, *Rev. Geophys.*, *15*(1), 105, doi:10.1029/RG015i001p00105, 1977.
- Kanazawa, T., M. Shinohara, and H. Shiobara, Recent progress in seafloor earthquake observations and instruments in Japan (in Japanese with English abstract), *J. Seism. Soc. Japan*, *61*, S55–S68, 2009.
- Karato, S.-i., On the origin of the asthenosphere, *Earth Planet. Sci. Lett.*, *321-322*, 95–103, doi:10.1016/j.epsl.2012.01.001, 2012.

- Kato, M., and T. H. Jordan, Seismic structure of the upper mantle beneath the western Philippine Sea, *Phys. Earth Planet. Inter.*, *110*(3-4), 263–283, doi:10.1016/S0031-9201(98)00176-9, 1999.
- Kawakatsu, H., P. Kumar, Y. Takei, M. Shinohara, T. Kanazawa, E. Araki, and K. Suyehiro, Seismic evidence for sharp lithosphere-asthenosphere boundaries of oceanic plates., *Science*, *324*(5926), 499–502, doi:10.1126/science.1169499, 2009.
- Kawasaki, I., and K. Koketsu, Rayleigh-Love wave coupling in an azimuthally anisotropic medium., *J. Phys. Earth*, *38*(5), 361–390, doi:10.4294/jpe1952.38.361, 1990.
- Kirkpatrick, S., C. D. Gelatt, and M. P. Vecchi, Optimization by simulated annealing., *Science*, *220*(4598), 671–80, doi:10.1126/science.220.4598.671, 1983.
- Kohlstedt, D. L., and M. E. Zimmerman, Rheology of partially molten mantle rocks, *Annu. Rev. Earth Planet. Sci.*, *24*(1), 41–62, doi:10.1146/annurev.earth.24.1.41, 1996.
- Korenaga, T., and J. Korenaga, Subsidence of normal oceanic lithosphere, apparent thermal expansivity, and seafloor flattening, *Earth Planet. Sci. Lett.*, *268*(1-2), 41–51, doi:10.1016/j.epsl.2007.12.022, 2008.
- Kumar, P., and H. Kawakatsu, Imaging the seismic lithosphere-asthenosphere boundary of the oceanic plate, *Geochemistry Geophys. Geosystems*, *12*(1), 1–13, doi:10.1029/2010GC003358, 2011.
- Laske, G., J. A. Collins, C. J. Wolfe, S. C. Solomon, R. S. Detrick, J. A. Orcutt, D. Bercovici, and E. H. Hauri, Probing the Hawaiian hot spot with new broadband ocean bottom instruments, *Eos, Trans. Am. Geophys. Union*, *90*(41), 362–363, doi:10.1029/2009EO410002, 2009.
- Leeds, A. R., L. Knopoff, and E. G. Kausel, Variations of upper mantle structure under the Pacific Ocean., *Science*, *186*(4159), 141–3, doi:10.1126/science.186.4159.141, 1974.
- Lin, F.-C., M. H. Ritzwoller, Y. Yang, M. P. Moschetti, and M. J. Fouch, Complex and variable crustal and uppermost mantle seismic anisotropy in the western United States, *Nat. Geosci.*, *4*(1), 55–61, doi:10.1038/ngeo1036, 2010.
- Liu, W., J. Kung, and B. Li, Elasticity of San Carlos olivine to 8 GPa and 1073 K, *Geophys. Res. Lett.*, *32*(16), doi:10.1029/2005GL023453, 2005.
- Lizarralde, D., J. B. Gaherty, J. A. Collins, G. Hirth, and S. D. Kim, Spreading-rate dependence of melt extraction at mid-ocean ridges from mantle seismic refraction data., *Nature*, *432*(7018), 744–7, doi:10.1038/nature03140, 2004.

- Long, M. D., and R. D. van der Hilst, Upper mantle anisotropy beneath Japan from shear wave splitting, *Phys. Earth Planet. Inter.*, 151(3-4), 206–222, doi:10.1016/j.pepi.2005.03.003, 2005.
- Lonsdale, P., Geography and history of the Louisville Hotspot Chain in the southwest Pacific, *J. Geophys. Res.*, 93(B4), 3078, doi:10.1029/JB093iB04p03078, 1988.
- Maggi, A., E. Debayle, K. Priestley, and G. Barruol, Multimode surface waveform tomography of the Pacific Ocean: a closer look at the lithospheric cooling signature, *Geophys. J. Int.*, 166(3), 1384–1397, doi:10.1111/j.1365-246X.2006.03037.x, 2006a.
- Maggi, A., E. Debayle, K. Priestley, and G. Barruol, Azimuthal anisotropy of the Pacific region, *Earth Planet. Sci. Lett.*, 250(1-2), 53–71, doi:10.1016/j.epsl.2006.07.010, 2006b.
- Mainprice, D., Seismic anisotropy of the deep earth from a mineral and rock physics perspective, in *Treatise Geophys.*, edited by G. Schubert, pp. 437–491, Elsevier, Amsterdam, doi:10.1016/B978-044452748-6.00045-6, 2007.
- McKenzie, D. P., and W. J. Morgan, Evolution of triple junctions, *Nature*, 224(5215), 125–133, doi:10.1038/224125a0, 1969.
- McNutt, M. K., Superswells, *Rev. Geophys.*, 36(2), 211, doi:10.1029/98RG00255, 1998.
- MELT Seismic Team, Imaging the deep seismic structure beneath a mid-ocean ridge: The MELT Experiment, *Science*, 280(5367), 1215–1218, doi:10.1126/science.280.5367.1215, 1998.
- Michibayashi, K., Structure sensitivity and elastic anisotropy within peridotites, *J. Geog.*, 117(1), 93–109, 2008.
- Miyazaki, T., K. Sueyoshi, and T. Hiraga, Olivine crystals align during diffusion creep of Earth’s upper mantle., *Nature*, 502(7471), 321–6, doi:10.1038/nature12570, 2013.
- Montagner, J., Upper mantle low anisotropy channels below the Pacific Plate, *Earth Planet. Sci. Lett.*, 202(2), 263–274, doi:10.1016/S0012-821X(02)00791-4, 2002.
- Montagner, J.-P., and D. L. Anderson, Petrological constraints on seismic anisotropy, *Phys. Earth Planet. Inter.*, 54(1-2), 82–105, doi:10.1016/0031-9201(89)90189-1, 1989.
- Montagner, J.-P., and H.-C. Nataf, A simple method for inverting the azimuthal anisotropy of surface waves, *J. Geophys. Res.*, 91(B1), 511–520, doi:10.1029/JB091iB01p00511, 1986.
- Montagner, J.-P., D.-A. Griot-Pommerehne, and J. Lavé, How to relate body wave and surface wave anisotropy?, *J. Geophys. Res.*, 105(B8), 19,015, doi:10.1029/2000JB900015, 2000.

- Mordret, A., M. Landes, N. M. Shapiro, S. C. Singh, P. Roux, and O. I. Barkved, Near-surface study at the Valhall oil field from ambient noise surface wave tomography, *Geophys. J. Int.*, *193*(3), 1627–1643, doi:10.1093/gji/ggt061, 2013a.
- Mordret, A., N. M. Shapiro, S. Singh, P. Roux, J.-P. Montagner, and O. I. Barkved, Azimuthal anisotropy at Valhall: The Helmholtz equation approach, *Geophys. Res. Lett.*, *40*(11), 2636–2641, doi:10.1002/grl.50447, 2013b.
- Morris, G. B., R. W. Raitt, and G. G. Shor, Velocity anisotropy and delay - time maps of the mantle near Hawaii, *J. Geophys. Res.*, *74*(17), 4300–4316, doi:10.1029/JB074i017p04300, 1969.
- Müller, R. D., M. Sdrolias, C. Gaina, and W. R. Roest, Age, spreading rates, and spreading asymmetry of the world’s ocean crust, *Geochemistry Geophys. Geosystems*, *9*(4), 1–19, doi:10.1029/2007GC001743, 2008.
- Nakahara, H., A systematic study of theoretical relations between spatial correlation and Green’s function in one-, two- and three-dimensional random scalar wavefields, *Geophys. J. Int.*, *167*(3), 1097–1105, doi:10.1111/j.1365-246X.2006.03170.x, 2006.
- Nakajima, J., and A. Hasegawa, Shear-wave polarization anisotropy and subduction-induced flow in the mantle wedge of northeastern Japan, *Earth Planet. Sci. Lett.*, *225*(3-4), 365–377, doi:10.1016/j.epsl.2004.06.011, 2004.
- Nakamura, Y., and T. Shibutani, Three-dimensional shear wave velocity structure in the upper mantle beneath the Philippine Sea region, *Earth, Planets Sp.*, *50*, 939–952, 1998.
- Nakanishi, M., K. Tamaki, and K. Kobayashi, Mesozoic magnetic anomaly lineations and seafloor spreading history of the northwestern Pacific, *J. Geophys. Res.*, *94*(B11), 15,437, doi:10.1029/JB094iB11p15437, 1989.
- Nakanishi, M., K. Tamaki, and K. Kobayashi, Magnetic anomaly lineations from Late Jurassic to Early Cretaceous in the west-central Pacific Ocean, *Geophys. J. Int.*, *109*(3), 701–719, doi:10.1111/j.1365-246X.1992.tb00126.x, 1992.
- Nakanishi, M., W. W. Sager, and A. Klaus, Magnetic lineations within Shatsky Rise, north-west Pacific Ocean: Implications for hot spot-triple junction interaction and oceanic plateau formation, *J. Geophys. Res.*, *104*(B4), 7539, doi:10.1029/1999JB900002, 1999.
- Nettles, M., and A. M. Dziewonski, Radially anisotropic shear velocity structure of the upper mantle globally and beneath North America, *J. Geophys. Res.*, *113*(B2), B02,303, doi:10.1029/2006JB004819, 2008.

- Nishida, K., Two-dimensional sensitivity kernels for cross-correlation functions of background surface waves, *Comptes Rendus Geosci.*, *343*(8-9), 584–590, doi:10.1016/j.crte.2011.02.004, 2011.
- Nishida, K., H. Kawakatsu, Y. Fukao, and K. Obara, Background Love and Rayleigh waves simultaneously generated at the Pacific Ocean floors, *Geophys. Res. Lett.*, *35*(16), 1–5, doi:10.1029/2008GL034753, 2008a.
- Nishida, K., H. Kawakatsu, and K. Obara, Three-dimensional crustal S wave velocity structure in Japan using microseismic data recorded by Hi-net tiltmeters, *J. Geophys. Res.*, *113*(B10), B10,302, doi:10.1029/2007JB005395, 2008b.
- Nishimura, C. E., and D. W. Forsyth, The anisotropic structure of the upper mantle in the Pacific, *Geophys. J. Int.*, *96*(2), 203–229, doi:10.1111/j.1365-246X.1989.tb04446.x, 1989.
- Nishizawa, A., K. Kaneda, and M. Oikawa, Backarc basin oceanic crust and uppermost mantle seismic velocity structure of the Shikoku Basin, south of Japan, *Earth, Planets Sp.*, *63*(2), 151–155, doi:10.5047/eps.2010.12.003, 2011.
- Oda, H., and N. Senna, Regional variation in surface wave group velocities in the Philippine Sea, *Tectonophysics*, *233*(3-4), 265–277, doi:10.1016/0040-1951(94)90245-3, 1994.
- Oikawa, M., K. Kaneda, and A. Nishizawa, Seismic structures of the 154-160 Ma oceanic crust and uppermost mantle in the Northwest Pacific Basin, *Earth, Planets Sp.*, *62*(4), e13–e16, doi:10.5047/eps.2010.02.011, 2010.
- Okino, K., Y. Ohara, S. Kasuga, and Y. Kato, The Philippine Sea: New survey results reveal the structure and the history of the marginal basins, *Geophys. Res. Lett.*, *26*(15), 2287, doi:10.1029/1999GL900537, 1999.
- Parsons, B., and J. G. Sclater, An analysis of the variation of ocean floor bathymetry and heat flow with age, *J. Geophys. Res.*, *82*(5), 803, doi:10.1029/JB082i005p00803, 1977.
- Patriat, M., Deep crustal structure of the Tuamotu plateau and Tahiti (French Polynesia) based on seismic refraction data, *Geophys. Res. Lett.*, *29*(14), doi:10.1029/2001GL013913, 2002.
- Peterson, J., Observations and modeling of seismic background noise, *Tech. rep.*, U.S. Department of Interior Geological Survey, New Mexico, 1993.
- Podolefsky, N. S., S. Zhong, and A. K. McNamara, The anisotropic and rheological structure of the oceanic upper mantle from a simple model of plate shear, *Geophys. J. Int.*, *158*(1), 287–296, doi:10.1111/j.1365-246X.2004.02250.x, 2004.

- Press, F., Some implications on mantle and crustal structure from G waves and Love waves, *J. Geophys. Res.*, *64*(5), 565–568, doi:10.1029/JZ064i005p00565, 1959.
- Raitt, R. W., G. G. Shor, T. J. G. Francis, and G. B. Morris, Anisotropy of the Pacific upper mantle, *J. Geophys. Res.*, *74*(12), 3095–3109, doi:10.1029/JB074i012p03095, 1969.
- Revenaugh, J., and T. H. Jordan, Mantle layering from ScS reverberations: 2. The transition zone, *J. Geophys. Res.*, *96*(B12), 19,763, doi:10.1029/91JB01486, 1991.
- Ritzwoller, M. H., N. M. Shapiro, and S.-J. Zhong, Cooling history of the Pacific lithosphere, *Earth Planet. Sci. Lett.*, *226*(1-2), 69–84, doi:10.1016/j.epsl.2004.07.032, 2004.
- Rychert, C. a., and P. M. Shearer, Imaging the lithosphere-asthenosphere boundary beneath the Pacific using SS waveform modeling, *J. Geophys. Res.*, *116*(B7), 1–15, doi:10.1029/2010JB008070, 2011.
- Sager, W. W., D. W. Handschumacher, T. W. Hilde, and D. R. Bracey, Tectonic evolution of the northern Pacific plate and Pacific-Farallon Izanagi triple junction in the Late Jurassic and Early Cretaceous (M21-M10), *Tectonophysics*, *155*(1-4), 345–364, doi:10.1016/0040-1951(88)90274-0, 1988.
- Saito, M., DISPER80: a subroutine package for the calculation of seismic normal-mode solutions, in *Seismol. Algorithms*, pp. 293–319, Academic Press, San Diego, 1988.
- Schlanger, S. O., M. O. Garcia, B. H. Keating, J. J. Naughton, W. W. Sager, J. A. Haggerty, J. A. Philpotts, and R. A. Duncan, Geology and geochronology of the line islands, *J. Geophys. Res.*, *89*(B13), 11,261, doi:10.1029/JB089iB13p11261, 1984.
- Schlue, J. W., and L. Knopoff, Shear wave anisotropy in the upper mantle of the Pacific Basin, *Geophys. Res. Lett.*, *3*(6), 359, doi:10.1029/GL003i006p00359, 1976.
- Schlue, J. W., and L. Knopoff, Shear-wave polarization anisotropy in the Pacific Basin, *Geophys. J. R. Astron. Soc.*, *49*(1), 145–165, doi:10.1111/j.1365-246X.1977.tb03706.x, 1977.
- Sens-Schönfelder, C., Synchronizing seismic networks with ambient noise, *Geophys. J. Int.*, *174*(3), 966–970, doi:10.1111/j.1365-246X.2008.03842.x, 2008.
- Seton, M., R. Müller, S. Zahirovic, C. Gaina, T. Torsvik, G. Shephard, a. Talsma, M. Gurnis, M. Turner, S. Maus, and M. Chandler, Global continental and ocean basin reconstructions since 200Ma, *Earth-Science Rev.*, *113*(3-4), 212–270, doi:10.1016/j.earscirev.2012.03.002, 2012.
- Shapiro, N. M., and M. Campillo, Emergence of broadband Rayleigh waves from correlations of the ambient seismic noise, *Geophys. Res. Lett.*, *31*(7), L07,614, doi:10.1029/2004GL019491, 2004.

- Shapiro, N. M., and M. H. Ritzwoller, Monte-Carlo inversion for a global shear-velocity model of the crust and upper mantle, *Geophys. J. Int.*, *151*(1), 88–105, doi:10.1046/j.1365-246X.2002.01742.x, 2002.
- Shapiro, N. M., and M. H. Ritzwoller, Thermodynamic constraints on seismic inversions, *Geophys. J. Int.*, *157*(3), 1175–1188, doi:10.1111/j.1365-246X.2004.02254.x, 2004.
- Shinohara, M., E. Araki, T. Kanazawa, K. Suyehiro, M. Mochizuki, T. Yamada, K. Nakahigashi, Y. Kaiho, Y. Fukao, and Others, Deep-sea borehole seismological observatories in the western Pacific: temporal variation of seismic noise level and event detection, *Ann. Geophys.*, *49*(2/3), 625–641, 2006.
- Shinohara, M., T. Fukano, T. Kanazawa, E. Araki, K. Suyehiro, M. Mochizuki, K. Nakahigashi, T. Yamada, and K. Mochizuki, Upper mantle and crustal seismic structure beneath the Northwestern Pacific Basin using a seafloor borehole broadband seismometer and ocean bottom seismometers, *Phys. Earth Planet. Inter.*, *170*(1-2), 95–106, doi:10.1016/j.pepi.2008.07.039, 2008.
- Shintaku, N., D. W. Forsyth, C. J. Rau, and D. S. Weeraratne, Pn Anisotropy in Mesozoic western Pacific lithosphere, *J. Geophys. Res.*, submitted.
- Shiobara, H., K. Baba, H. Utada, Y. Fukao, N. S. Plan, and R. Taylor, Ocean bottom array probes stagnant slab beneath the Philippine Sea, *Eos, Trans. Am. Geophys. Union*, *90*(9), 70, doi:10.1029/2009EO090002, 2009.
- Shito, A., D. Suetsugu, T. Furumura, H. Sugioka, and A. Ito, Small-scale heterogeneities in the oceanic lithosphere inferred from guided waves, *Geophys. Res. Lett.*, *40*(9), 1708–1712, doi:10.1002/grl.50330, 2013.
- Silver, P. G., and W. W. Chan, Shear wave splitting and subcontinental mantle deformation, *J. Geophys. Res.*, *96*(B10), 16,429–16,454, doi:10.1029/91JB00899, 1991.
- Smith, D. B., M. H. Ritzwoller, and N. M. Shapiro, Stratification of anisotropy in the Pacific upper mantle, *J. Geophys. Res.*, *109*(B11), 1–22, doi:10.1029/2004JB003200, 2004.
- Smith, M. L., and F. A. Dahlen, The azimuthal dependence of Love and Rayleigh wave propagation in a slightly anisotropic medium, *J. Geophys. Res.*, *78*(17), 3321–3333, doi:10.1029/JB078i017p03321, 1973.
- Snieder, R., Extracting the Greens function from the correlation of coda waves: A derivation based on stationary phase, *Phys. Rev. E*, *69*(4), doi:10.1103/PhysRevE.69.046610, 2004.
- Song, T.-R. A., and H. Kawakatsu, Subduction of oceanic asthenosphere: Evidence from sub-slab seismic anisotropy, *Geophys. Res. Lett.*, *39*(17), L17,301, doi:10.1029/2012GL052639, 2012.

- Song, T.-R. A., and Y. Kim, Anisotropic uppermost mantle in young subducted slab underplating Central Mexico, *Nat. Geosci.*, *5*(1), 55–59, doi:10.1038/ngeo1342, 2012.
- Stein, C. A., and S. Stein, A model for the global variation in oceanic depth and heat flow with lithospheric age, *Nature*, *359*(6391), 123–129, doi:10.1038/359123a0, 1992.
- Stixrude, L., and C. Lithgow-Bertelloni, Mineralogy and elasticity of the oceanic upper mantle: Origin of the low-velocity zone, *J. Geophys. Res.*, *110*(B3), B03,204, doi:10.1029/2004JB002965, 2005.
- Suetsugu, D., H. Sugioka, T. Isse, Y. Fukao, H. Shiobara, T. Kanazawa, G. Barruol, F. Schindelé, D. Reymond, A. Bonneville, and E. Debayle, Probing South Pacific mantle plumes with ocean bottom seismographs, *Eos, Trans. Am. Geophys. Union*, *86*(44), 429, doi:10.1029/2005EO440001, 2005.
- Suetsugu, D., T. Isse, S. Tanaka, M. Obayashi, H. Shiobara, H. Sugioka, T. Kanazawa, Y. Fukao, G. Barruol, and D. Reymond, South Pacific mantle plumes imaged by seismic observation on islands and seafloor, *Geochemistry Geophys. Geosystems*, *10*(11), doi:10.1029/2009GC002533, 2009.
- Suetsugu, D., H. Shiobara, H. Sugioka, A. Ito, T. Isse, T. Kasaya, and N. Tada, TIARES Project Tomographic investigation by seafloor array experiment for the Society hotspot, *Earth, Planets Sp.*, *64*(4), i–iv, doi:10.5047/eps.2011.11.002, 2012.
- Takahashi, M., Tectonic development of the Japanese Islands controlled by Philippine Sea Plate motion, *J. Geog.*, *115*(1), 116–123, 2006.
- Takeo, A., K. Nishida, T. Isse, H. Kawakatsu, H. Shiobara, H. Sugioka, and T. Kanazawa, Radially anisotropic structure beneath the Shikoku Basin from broadband surface wave analysis of ocean bottom seismometer records, *J. Geophys. Res.*, *118*(6), 2878–2892, doi:10.1002/jgrb.50219, 2013.
- Takeo, A., D. W. Forsyth, D. S. Weeraratne, and K. Nishida, Estimation of azimuthal anisotropy in the NW Pacific from seismic ambient noise in seafloor records, *Geophys. J. Int.*, submitted.
- Takeuchi, H., and M. Saito, Seismic surface waves, in *Methods Comput. Phys.*, edited by B. A. Bolt, pp. 217–295, Academic Press, New York, 1972.
- Tanimoto, T., and C. Alvizuri, Inversion of the HZ ratio of microseisms for S-wave velocity in the crust, *Geophys. J. Int.*, *165*(1), 323–335, doi:10.1111/j.1365-246X.2006.02905.x, 2006.
- Tanimoto, T., and D. L. Anderson, Mapping convection in the mantle, *Geophys. Res. Lett.*, *11*(4), 287, doi:10.1029/GL011i004p00287, 1984.

- Terada, T., Y. Hiramatsu, and T. Mizukami, Shear wave anisotropy beneath the volcanic front in South Kyushu area, Japan: Development of C-type olivine CPO under H₂O-rich conditions, *J. Geophys. Res. Solid Earth*, *118*(8), 4253–4264, doi:10.1002/jgrb.50300, 2013.
- Tonegawa, T., and G. Helffrich, Basal reflector under the Philippine Sea Plate, *Geophys. J. Int.*, *189*, 659–668, doi:10.1111/j.1365-246X.2012.05386.x, 2012.
- Toomey, D. R., D. Joussetin, R. a. Dunn, W. S. D. Wilcock, and R. S. Detrick, Skew of mantle upwelling beneath the East Pacific Rise governs segmentation., *Nature*, *446*(7134), 409–14, doi:10.1038/nature05679, 2007.
- Tromp, J., Y. Luo, S. Hanasoge, and D. Peter, Noise cross-correlation sensitivity kernels, *Geophys. J. Int.*, *183*(2), 791–819, doi:10.1111/j.1365-246X.2010.04721.x, 2010.
- Vine, F. J., and D. H. Matthews, Magnetic anomalies over oceanic ridges, *Nature*, *199*(4897), 947–949, doi:10.1038/199947a0, 1963.
- Weaver, R., B. Froment, and M. Campillo, On the correlation of non-isotropically distributed ballistic scalar diffuse waves., *J. Acoust. Soc. Am.*, *126*(4), 1817–26, doi:10.1121/1.3203359, 2009.
- Webb, S. C., T. K. Deaton, and J. C. Lemire, A broadband ocean-bottom seismometer system based on a 1-Hz natural period geophone, *Bull. Seismol. Soc. Am.*, *91*(2), 304–312, doi:10.1785/0120000110, 2001.
- Weeraratne, D. S., D. W. Forsyth, Y. Yang, and S. C. Webb, Rayleigh wave tomography beneath intraplate volcanic ridges in the South Pacific, *J. Geophys. Res.*, *112*(B6), 1–18, doi:10.1029/2006JB004403, 2007.
- Wessel, P., and W. H. F. Smith, Free software helps map and display data, *Eos, Trans. Am. Geophys. Union*, *72*(41), 441–441, doi:10.1029/90EO00319, 1991.
- Wolfe, C. J., and P. G. Silver, Seismic anisotropy of oceanic upper mantle: Shear wave splitting methodologies and observations, *J. Geophys. Res.*, *103*(B1), 749, doi:10.1029/97JB02023, 1998.
- Woods, M. T., and G. F. Davies, Late Cretaceous genesis of the Kula plate, *Earth Planet. Sci. Lett.*, *58*(2), 161–166, doi:10.1016/0012-821X(82)90191-1, 1982.
- Yamazaki, T., M. Takahashi, Y. Iryu, T. Sato, M. Oda, H. Takayanagi, and P. S. Plate, Philippine Sea Plate motion since the Eocene estimated from paleomagnetism of seafloor drill cores and gravity cores, *Earth, Planets Sp.*, *62*(6), 495–502, doi:10.5047/eps.2010.04.001, 2010.

- Yao, H., and R. D. van der Hilst, Analysis of ambient noise energy distribution and phase velocity bias in ambient noise tomography, with application to SE Tibet, *Geophys. J. Int.*, *179*(2), 1113–1132, doi:10.1111/j.1365-246X.2009.04329.x, 2009.
- Yao, H., P. Gouédard, J. A. Collins, J. J. McGuire, and R. D. van der Hilst, Structure of young East Pacific Rise lithosphere from ambient noise correlation analysis of fundamental- and higher-mode Scholte-Rayleigh waves, *Comptes Rendus Geosci.*, *343*, 571–583, doi: 10.1016/j.crte.2011.04.004, 2011.
- Yu, G.-K., and B. J. Mitchell, Regionalized shear velocity models of the Pacific upper mantle from observed Love and Rayleigh wave dispersion, *Geophys. J. R. Astron. Soc.*, *57*(2), 311–341, doi:10.1111/j.1365-246X.1979.tb04781.x, 1979.